A SURVEY FOR COOL WHITE DWARFS AND THE AGE OF THE GALACTIC DISC

Richard Alan Knox

Presented for the Degree of Doctor of Philosophy
The University of Edinburgh
1999

This thesis is my own composition except where indicated in the text.

June 8, 1999

ABSTRACT

The use of white dwarf cooling times is now established as one of the most important methods of determining the age of our Galaxy. Estimates of the age of the Galactic Disk from the study of cool white dwarf samples have remained at approximately 9 Gyr since the technique was first applied over a decade ago, in contrast to globular clusters ages and cosmological timescales, which have been the subject of much revision and debate. Much of the white dwarf work has of necessity relied on all-sky photographic proper motion surveys to provide sufficiently large numbers of white dwarfs in conjunction with quantifiable survey limits, unfortunately resulting in demonstrably incomplete samples.

This thesis describes a survey specifically undertaken to obtain a sample of cool white dwarfs directly from original Schmidt plate material. Concerns regarding the subjectivity of 'eye-blinked' proper motion measures are avoided by using digitised data obtained using the COSMOS and SuperCOSMOS microdensitometers. The observational material is restricted to a single 6° field in which an exceptionally large database of over 300 Schmidt plates exists. As a brief aside, the issue of stacking digitised plate data is examined. In particular, recommendations for the correct weighting algorithm and bad pixel rejection algorithm to adopt are made, following detailed experimentation with a variety of techniques. The plate stacking technique is used for the white dwarf survey material to extend the photometric survey limits, while the optimum proper motion limit to adopt is investigated in detail, with the principal concern being elimination of contaminants while retaining as many genuine proper motion objects as possible. Application of the reduced proper motion population discrimination technique to the resultant proper motion catalogue results in a final sample comprising 56 white dwarf candidates. Follow up spectroscopic observations show the survey has been successful in identifying cool white

dwarfs, gives no indication of contamination in the white dwarf sample by other stellar types, and also provides two further cool white dwarfs to include in the sample which were marginally excluded by the reduced proper motion survey criteria.

Comparison of photographic colours with model predictions allow effective temperatures and bolometric luminosities to be estimated for the sample members. The luminosity function constructed from the sample members is in good agreement with previous work, although the slightly higher space density found for the coolest white dwarfs leads to a modest increase in the age estimate for the Galactic Disc when the luminosity function is compared to theoretical models. The Disc age is found to be 10^{-1}_{+3} Gyr.

Recurring themes in this work are the related questions of sample completeness and sample contamination. These have been addressed in several ways, notably via number counts, the V/V_{max} completeness test and sample distributions on the reduced proper motion diagram. The results of these analyses may be summarised by stating that the sample is consistent with being drawn from a complete sample, shows no statistical evidence of incompleteness, and is unlikely to be contaminated by non-degenerates. Probably the most serious source of error here is the omission of very cool white dwarfs due to the conservative reduced proper motion survey criteria adopted. This concern, along with other considerations regarding the atmospheric constituents of the sample members, imply that a 9 Gyr Disc age may be regarded as a quite robust lower limit from this work.

Contents

Chapter 1

Introduction

The endpoint of stellar evolution for the vast majority of stars is the white dwarf (WD). The first WDs to be discovered were the hot, subluminous companions to the bright stars Sirius and o Eridani. Dubbed 'white' due to their unexpected blue colour, the name could be considered somewhat misleading since WDs are now known to exist with 'yellow' and even 'red' colours. WDs have often been studied as interesting objects in their own right, although their intrinsic faintness makes them awkward targets for observation, and theoretical predictions have often preceded observational confirmation by some margin. In 1958, Luyten bemoaned the fact that the confident and wide-ranging predictions of theorists concerning the mass, composition, size and luminosity of WDs was at that time largely unconfirmed by the sparse observations available: 'It seems to the writer high time that observers with modern giant telescopes plan some extensive series of observations in order to provide a firm basis of observational fact under the quick-sand of current astrophysical theories' (Luyten 1958).

This trend is well illustrated by the concept that WDs can be used to constrain the age of the local galaxy. As long ago as the late 1950s Schmidt (1959) realised that WDs can be considered a reasonably homogeneous class of object cooling in a well understood way, and that there should be a luminosity below which the oldest WDs have not had time to cool. It took nearly thirty years for the predicted fall off in WD numbers at faint luminosities to be explicitly observed (Liebert, Dahn & Monet, 1988 henceforth LDM), a reflection of the particular difficulties inherent in finding faint, cool white dwarfs (CWDs).

Measuring timescales of order the age of the Universe is timely, since many putative cosmologies predict a universe older than some of its constituent bodies. Reliable ages for astrophysical objects can therefore place valuable constraints on cosmological models. A recent example is the discovery of a galaxy at redshift 1.55 estimated to be 3.5 Gyr old (Dunlop et al. 1996). This excludes $\Omega = 1$, $\Lambda = 0$ Einstein-de Sitter cosmologies for any Hubble constant, H_0, greater than $50 \mathrm{kms}^{-1}\mathrm{Mpc}^{-1}$. Modern estimates of H_0 are invariably larger than $60 \mathrm{kms}^{-1}\mathrm{Mpc}^{-1}$ (Freedman 1998). Similar problems are encountered when considering the ages of the old metal-poor globular clusters within our Galaxy. An $\Omega = 1$, $\Lambda = 0$ Universe with $H_0 = 65 \mathrm{kms}^{-1}\mathrm{Mpc}^{-1}$ is 10 Gyr old at the current epoch. The long standing age estimates for Galactic globular clusters have recently been revised downwards by $\sim 15\%$, although current ages of 13-14 Gyr for the oldest globular clusters still provide an excellent constraint on cosmological parameters (Vandenberg 1998). Although the old globular clusters are clearly a sensible target for investigating the age of the Galaxy, deriving reliable ages for them is difficult. For example, D'Antona, Caloi and Mazzitelli (1997) obtain ages for the oldest globular cluster of 11-12 Gyr by employing new stellar model calculations. This age estimate comes very close to removing the conflict with the age of the Universe, and highlights the need for independent measures of the age of the Galaxy.

Cooling models indicate that a WD formed 10 Gyr ago is still bright enough to be a realistic subject for astronomical surveys, and WDs are thus a natural choice for studies in cosmochronometry. Since their luminosity is directly related to their age, the number density of WDs as a function luminosity, or the white dwarf luminosity function (WDLF), contains information about the star formation history of the Galaxy. Two basic ingredients are required to calculate the Disc age from the WDLF:

1. An observational WDLF drawn from a complete, unbiased sample of Disc WDs. Since it is the cut-off in the WDLF that contains the information concerning the Disc age, the sample must contain WDs of sufficiently low luminosity to clearly delineate the cut-off. Extensive observations of the WD sample members are desirable, including trigonometric parallax , spectroscopy and optical and IR photometry, in order to obtain the most reliable WD luminosities.

2. Theoretical WDLF curves calculated for various Disc ages. These should obviously

incorporate realistic WD cooling models, although other inputs such as the progenitor star lifetimes and star formation rates are also required to produce a WDLF.

Modern determinations of the observational WDLF have almost exclusively relied on the proper motion catalogues of the Luyten Palomar survey, since to this day it provides the only database of faint proper motion objects over a large fraction of the sky. The use of the Luyten catalogues has led to completeness worries, in part because much of the survey was conducted using eye-blinked plates and uses eye-measured photometry. The discovery of objects missed by Luyten, notably the very cool WD found by Hambly, Smartt & Hodgkin (1997), questions the suitability of the Luyten catalogues as a database for obtaining complete samples of faint proper motion objects. Indeed, WD samples culled from the LHS catalogue (Luyten 1979) all fail statistical completeness tests. Studies of the observational WDLF to date have found the faint cut-off in space densities to lie between $(-4.3 > \log L/L_{\odot} > -4.7)$, leading to Disc age estimates ranging between 8 and 9.5 Gyr. It has been argued (Ruiz et al. 1995) that the reality of the observed cut-off has been demonstrated by the parallax program of Monet et al. (1992), who have produced a HR diagram showing a clear WD locus which ends at an absolute V magnitude of approximately 16. This appears to be a dubious line of argument however, since the parallax sample was also drawn from the Luyten catalogues and would be expected to show the same incompleteness. A review of previous work on the WDLF is given in Chapter 2.

The purpose of this research is to exploit both the extensive collection of over 300 plates in ESO/SERC field 287 and the power of the COSMOS and SuperCOSMOS measuring machines to produce a deep, complete multi-colour proper motion survey sample. This is the first survey to be conducted with the sole aim of extracting a sample of CWDs from a proper motion catalogue suitable for construction of a WDLF. In Chapter 3 a description of the Schmidt plate material and data reduction is given. In order to increase the depth of the survey, an important consideration when searching for intrinsically faint objects, the technique of digital plate stacking was employed. An investigation into plate stacking is presented in Chapter 4. The extraction of a proper motion, and subsequently a CWD sample from the Schmidt plate data is described in Chapter 5, and follow up observations of CWD candidates discussed in Chapter 6. The final CWD sample is analysed in Chapter 7, with the resulting WDLF and fitted Disc age presented in Chapter 8. The work is

summarised in Chapter 9, after which a glossary is supplied containing abbreviations and acronyms.

Chapter 4 has been published as a paper entitled 'Digital stacking of photographic Schmidt plates with SuperCOSMOS' in Monthly Notices of the Royal Astronomical Society (MNRAS). A second paper, with the same title as this thesis, has been accepted for publication in MNRAS and is a summary of the material presented in Chapters 3, 5, 6, 7 and 8 of this work.

Chapter 2

Literature Review

Early this century Walter Adams (1914, 1915) reported unexpected results from his spectroscopic observations of the faint companions of Sirius and o Eridani. The combination of high temperatures, low luminosities and unexceptional solar type masses implied a class of object of extremely high density and small radius distinct from other known stars. The name white dwarf was a natural suggestion for such a star, having a radius smaller than the planet Uranus and looking whiter than the sun. In one of the first applications of the nascent quantum theory to astrophysics, Fowler (1926) demonstrated that the pressure exhibited by degenerate electrons was sufficient to support such a star against gravity.

Techniques employed for discovering WDs invariably exploit either the blue colour or the intrinsic faintness of these objects, or both together. If only hot blue objects are sought, the relative paucity of blue objects makes trawling through ultraviolet excess surveys via spectroscopic observations a practical proposition (eg Fleming, Liebert & Green 1986). Indeed, 15% of the objects found in the recent Edinburgh-Cape Blue Object Survey were found to be WDs (Kilkenny et al. 1997). In general however, the number of non-WD stars at a given colour make the use of the relative faintness of WDs essential. For most of this century the only wide-field medium available to astronomers has been the photographic plate, and it is through photographic plates that most WDs have been discovered. The usual method of discovery of WDs from plate data dates back to the beginning of this century, when Hertzsprung proposed that measures of apparent magnitude and proper motion could be combined to estimate absolute magnitudes (Reid 1997). This technique,

now known as the method of 'reduced proper motions' (RPM) or occasionally as the 'method of mean absolute magnitudes', is particularly suited to the task of extracting WDs from a collection of survey objects. The reduced proper motion (RPM) is defined by

$$H = m + 5\log_{10}\mu + 5 \tag{2.1}$$

where m is apparent magnitude and μ proper motion. A reduced proper motion diagram (RPMD) is a plot of colour against RPM. It is a powerful way of combining proper motions and photometry to distinguish stellar population groups. Equation 2.1 can be re-written using the relationships $m = M - 5 + 5\log d$ and $\mu = V_T/4.74d$ to give

$$H = M + 5\log_{10} V_T - 3.4 \tag{2.2}$$

where M is the absolute magnitude, V_T the transverse velocity (in kms^{-1}) and d the distance in parsecs. Since M and V_T are both intrinsic properties of the star, so too is H. To see the significance of H, suppose that every star had an identical V_T; H would then clearly be simply M plus a constant and the distribution of a particular population group in H at a particular colour would depend solely on the spread of the populations' colour-magnitude relation at that colour. Of course there is a distribution in $5\log_{10} V_T$ for each population, but since the tangential velocities are distributed around a most probable value (Wanner 1972) the RPM serves as an estimate of M, ie. $M = a + bH$ (a and b constants). The resulting locus for each population in the RPMD is then the convolution of its colour magnitude distribution with its $5\log_{10} V_T$ distribution over the diagram's colour range. To allow population discrimination in some colour region it is therefore only required that the various population loci do not overlap significantly in that region of the RPMD. The RPMD is analogous to the Hertzsprung-Russell diagram, which explains why it is particularly suited to detecting WDs, which occupy a distinct region several magnitudes below the MS on the HR diagram. All that will be required of Galactic kinematics in this work is that the distribution of $5\log_{10} V_T$ in the field of interest allows WD population discrimination on the RPMD. It will be immediately apparent whether this is the the case or not by inspecting a RPMD and checking for a distinct locus of objects below the main sequence and subdwarf groups. The use of the RPM method is by no means restricted to WD searches, and has also been employed to delineate other stellar populations (eg. Evans 1992, Ryan 1989, Jones 1972a).

One prolific contributor to the list of known WDs is Willem Luyten, who spent much of his working life producing proper motion catalogues from which WDs may be culled using the RPM technique. Discussion here will be primarily restricted to Luyten's survey, simply because it is from his catalogues that samples bearing direct comparison with that described in this thesis have been extracted. The majority of Luytens WDs were found on plates taken on the Palomar 48 inch Schmidt Telescope. Initially, proper motions were measured using a 'hand-blinking' technique. This method involved projecting two plates of the same area of sky but taken several years apart alternately onto some form of viewing apparatus. The operator then inspects every image in turn to check for movements attributable to a proper motion. Photometry was also eye-measured, with colours obtained by comparing magnitudes on plates taken through different filters. Luyten assigned a 'colour-class' based on his measured magnitudes, labelling each object with the appropriate spectral type. WD candidates were extracted from the proper motion samples by assigning a cut-off value in RPM for each colour class. Any object with RPM exceeding the cut-off was given a preliminary WD status pending further observation. As the survey work progressed, the number of WD candidates identified became sufficiently large that a separate list entitled 'White Dwarfs' was published (Luyten 1970). It was from lists such as these that targets for firm identifications via spectroscopy were drawn. These lists were by no means free of contamination, and were not expected to be so: 'Probably no more that forty percent of the stars with colour "k" will prove to be genuine degenerates' (Luyten 1977). This quote, taken from a second expanded list of WD candidates published by Luyten, refers to the problem of contamination by high velocity main sequence stars and subdwarfs. The RPM loci of WDs and subdwarfs start to become entangled for redder stars, and the problem is exacerbated by poor colour determinations. Greenstein (1975) also noted this trend when describing the success rate of finding WDs from targets selected from the Lowell proper motion catalogue (eg. Giclas, Burnham & Thomas 1978). The plate blinking process of Luyten was automated in the 1970s, leading to the publication of the Luyten Half Second (LHS hereafter, Luyten 1979) ($\mu > 0\farcs5$ yr^{-1}) and NLTT ($\mu > 0\farcs2$ yr^{-1}) catalogues, for which the majority of plate data had been 'machine-blinked'. The currently accepted WDLF (Liebert, Dahn & Monet 1988, henceforth LDM) sample is drawn from the LHS catalogue, which with an average limiting magnitude of $m_{ph} = 21.2$ (Luyten 1963) extends deep enough to sample extremely subluminous stars. One question that is difficult to answer, given the haphazard way objects have been ob-

served and classified, is the role candidate selection may play in any WD sample drawn from these surveys. This is a separate issue to the question of proper motion or photometric completeness of the surveys, which will be discussed below. The point is simply that, given the labour intensive nature of spectroscopic observations, observers may have limited themselves to candidates of high RPM less likely to be subdwarf contaminants. Thus for surveys with large scatters on the RPM-colour plane due to measurement errors in photometry or proper motion, spectroscopic observation of every potential WD is likely to be too time consuming to undertake. While this source of incompleteness may be essentially unquantifiable, especially given the eclectic nature of some spectroscopically confirmed WD samples, it may nevertheless be significant.

Dawson (1986) in the course of his work on the halo population luminosity function, assessed the completeness of the LHS catalogue. Two fundamental constraints on the completeness are image crowding within 10° of the galactic equator , and an upper proper motion limit of $2\farcs5$ yr^{-1} ($3''$yr^{-1} at the north Galactic pole) imposed on the survey as a labour saving device. Dawson considered the region out-with the Galactic plane accessible to the Palomar telescope ($\delta \geq -33°, |b| < 10°$), and concluded that the catalogue is 90% complete for stars brighter than $m_R = 18$. While such assertions are difficult to prove definitively, Dawson's extrapolations from samples with more restricted observational limits in proper motion and magnitude (which are assumed to be complete) yield numbers within $\sim 10\%$ of those found in LHS. However, what is not clear is how the completeness varies as a function of the observed parameters of the star. In an investigation of the Luyten common proper motion binary (CPMB) stars, which will be discussed in more detail below, it was found that the catalogue incompleteness increases with increasing magnitude and decreasing proper motion (Oswalt & Smith 1995, Smith & Oswalt 1994). While this is not a particularly surprising result, since smaller motions and fainter objects may be expected to be more difficult to detect, in a survey specifically searching for low luminosity objects systematic incompleteness for faint stars is clearly not desirable. Detection problems also exist for high proper motion objects, as was recently demonstrated by the discovery of a $1\farcs3$ yr^{-1} WD not included in LHS (Hambly, Smartt & Hodgkin 1997) using a number of digitized plates in the same field. This is a reasonably faint object ($V = 19.04$) but well within the LHS limiting magnitude, and would have been included in the LDM sample as their faintest WD had it been discovered by Luyten. Crucially, this

object was discovered serendipitously in a field in which the authors happened to possess plate material, and therefore if only one in ten fields contain such omissions from the LHS catalogue the implications for the WDLF are severe.

The steady accumulation of spectroscopically confirmed WDs in the 1970s encouraged attempts to improve on Weidemanns (1967) pioneering work on the WDLF. Despite the larger samples available, the WDLFs of Kovetz & Shaviv (1976) and Sion & Liebert (1977) did not sample the WDLF to fainter magnitudes than Weidemanns earlier work. This may in part be due to their adoption of Weidemanns method of constructing LFs, which insisted on adopting a minimum apparent magnitude within which the sample could be considered relatively complete. While such precautions are clearly necessary, Sion & Liebert found that imposing a limit of $m_V < 13.5$ excluded most of their sample, leaving only 85 stars from a total of 424. Extending the limit to $m_V < 14.5$ improved the situation, and the resulting LFs were in good agreement with Weidemann. Furthermore, it was noted that no down turn in the LF was observed in the absolute magnitude range $13 < M_V < 15$, and that searches to fainter apparent magnitudes were required to sample the LF cut-off. It was not long after that observations of Luyten WD candidates fainter than $m_R \sim 16$ began to reveal a number of very cool WDs, notably the second ever degenerate found with Luyten colour class "m" (Liebert et al. 1979a). The first suggestions of an empirically observed cut-off in the WDLF were made following these observations (Liebert et al. 1979b, henceforth LDGS). It was found that there was an apparently large discrepancy between the predicted number of WDs from theoretical WDLFs and the number detected. The search was restricted to the region of sky confidently surveyed by Luyten (essentially the same as considered by Dawson in his study described above) and objects within 10pc of the sun. The models of Kovetz & Shaviv (1976) were used to predict the number of expected WDs in integer bolometric magnitude bins by normalising them to the hot, blue WD number densities of Green (eg 1986). The observed numbers, although small, were equal to or in excess of predictions for stars fainter than $M_{bol} = 15$, at which point the predicted number continued to rise while the number detected fell away. Since they were now sampling to apparent magnitudes equal to and larger than $M_{bol} = 15$, LDGS argued that they would have detected the predicted "VLL" (very low luminosity) WDs within 10pc had they been present. Considerations of potential incompleteness in the Luyten surveys, which were "likely to be more than 50% complete for 1″ motion stars with $m_R \leq 16$ within

the restricted 10pc interval" still lead to 2σ shortfall in the observed numbers. In addition, the lack of VLL WDs observed in CPMB systems (a proven and powerful search technique for faint proper motion stars since all objects with significant motions were scrutinised for a faint companion by Luyten) lent additional weight to the argument. Given the small sample number (12 objects within the 10pc range) and uncertainties in the predicted WD number density however, LDGS restricted themselves to the statement that the observed WDLF appeared to peak within $14 \leq M_{bol} \leq 16$ and represented a probable deficit in very low luminosity degenerates.

Probably the best known and most widely accepted WDLF was published in 1988 by LDM. A preliminary version of this work was used by Winget et al. (1987) to estimate the Disc age to be (9.3 ± 2.0) Gyr. The LDM sample consists of 43 WDs, and represents a more extensive exploitation of the LHS database than LDGS. The 43 stars included in LDM are the spectroscopically confirmed WDs in the LHS catalogue with:

1. $\mu \geq 0''.8$ yr^{-1}
2. $\delta > 20°$
3. $M_V \geq 13.00$

The assumptions made concerning the LHS database when constructing the LDM WDLF were threefold. Firstly, an incompleteness factor of 20% is assumed in the LHS for $\delta > 20°$ due to avoidance of the Galactic plane. Secondly, with the exception of the Galactic plane region, the LHS catalogue is assumed to be complete for stars brighter than 19 magnitude in V, and for proper motions $\geq 0''.8$ yr^{-1}. The faintest LDM star has $V = 18.81$, while the WD found recently by Hambly, Smartt and Hodgkin (1997) with $V = 19.04 \pm 0.12$ would presumably have been included in the LDM had it been found by Luyten, since it passes the LDM inclusion criteria stated above. The third assumption, that the LHS catalogue is complete for proper motions up to $10''$yr^{-1}, is questionable given the $2''.5$ yr^{-1} machine limit mentioned above, although LDM point out that a reduction to $2''$yr^{-1} for the assumed proper motion completeness limit makes little difference to the derived LF.

The LDM sample even then benefited from an extensive range of observations. The absolute V magnitudes of many sample members were well defined due to a combination of

accurate trigonometric parallaxes and accurate photometry. Comparison with theoretical LFs required conversion of absolute V magnitudes to bolometric magnitudes however, a procedure discussed in detail in LDM since it had a significant bearing on the resulting WDLF. Obtaining effective temperatures ($T_{\rm eff}$) by comparing observed colours to theoretical models (eg Kaprandis 1985) allowed derivation of bolometric luminosities. This procedure requires basic knowledge of the WD atmosphere under consideration, since the $T_{\rm eff}$ - colour relationship is dependent on whether the WD has an atmosphere that is hydrogen-rich (designated a 'DA' white dwarf) or helium-rich (generally termed 'non-DA')[1]. Consequently, a problem existed for stars with $T_{\rm eff} \leq 5500$ K, since the hydrogen Balmer lines are too weak to be detected spectroscopically and thus the principal atmospheric constituent was unknown. Empirical indications that DA stars became progressively less numerous with decreasing temperature (Sion 1984) coupled with predictions that convective mixing could cause such an effect led LDM to adopt helium $T_{\rm eff}$ fits to their coolest WDs. It was noted however that accretion of interstellar hydrogen onto WDs could make a DA atmosphere model appropriate. The adoption of a 'hydrogen temperature scale' led to $T_{\rm eff}$ predictions much lower than for helium atmospheres. A previously acknowledged problem existed with these low temperatures in that they led to mass estimates, via the well determined absolute magnitudes and theoretical mass-radius relations (Hamada and Salpeter 1961), much lower than that expected. This inconsistency implied that higher effective temperatures were appropriate, and furthermore that these considerations place a serious constraint on how cool the WDs can be. LDM argued that this constraint meant the adoption of the Kaprandis helium atmospheres was reasonable for the coolest WDs, and that the results could not be significantly altered by choosing hydrogen atmospheres instead.

Although bolometric corrections (BCs) from model atmospheres for cool DA stars were available at the time (Greenstein 1976), the same was not true for cool helium atmospheres. The uncertainty in this BC represents a dominant source of error in the final WDLF. LDM approached the problem by adopting two distinct methods of calculating M_{bol} and arguing the resulting LFs bracketed the true distribution. The first method assumed BCs appropriate to a black body, resulting in larger BCs and hence brighter WDs than

[1] A detailed discussion of WD spectral characteristics and classification may be found in Wesemael et al. (1993)

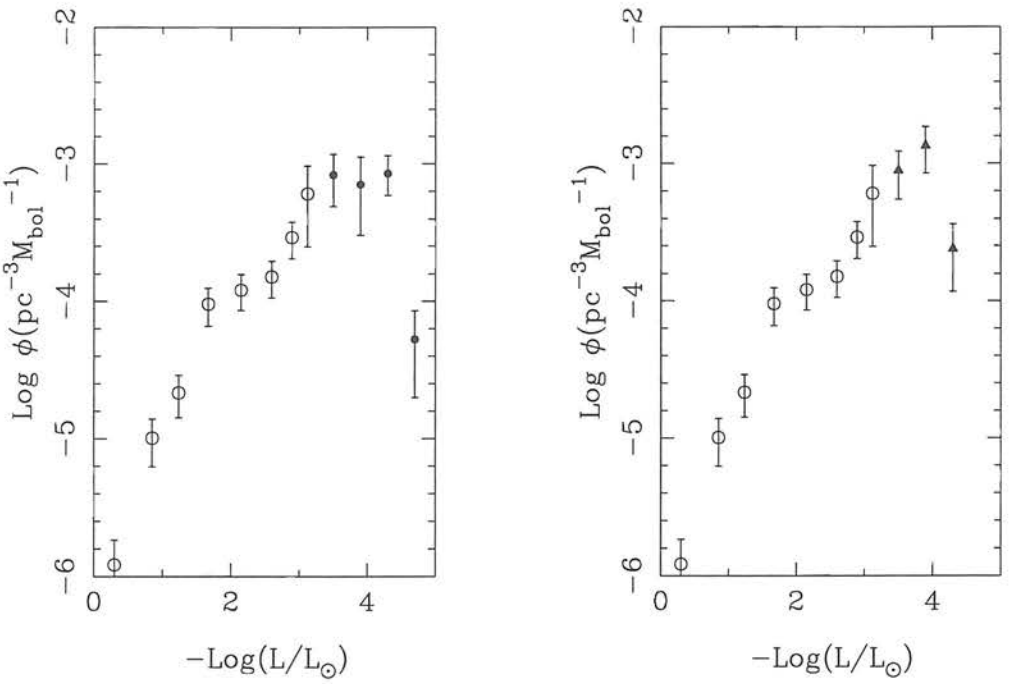

Figure 2.1: The LDM WDLF. Points in open circles are drawn from the hot WD survey of Fleming, Liebert and Green (1986). The left panel shows the LF calculated assuming no bolometric correction (ie. $M_{bol} = M_V$); in the right hand panel the LF displayed was constructed assuming black-body bolometric corrections.

the second method, which assumed a common WD radius and calculated M_{bol} using the fitted effective temperature. The WDLFs derived using the two methods are shown in Figure 2.1, where the primary result of LDM - that the down turn in the WDLF occurs in the range ($-4.6 < \log L/L_\odot < -4.2$) - is easily seen. These LFs were constructed using the "$1/V_{max}$" method, as have subsequent WDLFs. This method is described in Chapter 7. Also shown in Figure 2.1 is the LF for hot WDs of Fleming, Liebert and Green (1986, hereafter FLG). This LF was constructed from the large sample of hot WDs culled from the Palomar-Green ultraviolet excess survey. Because such surveys are only magnitude limited (ie. proper motions are not required) and hot WDs are easier to find in large numbers, the FLG survey is often used as a benchmark for the completeness of cooler WD samples.

The total number density of WDs had been of interest since very faint CWDs had been seen as a means of resolving the believed inconsistency between the observed local mass density and dynamically estimated mass densities. The number density derived by LDM

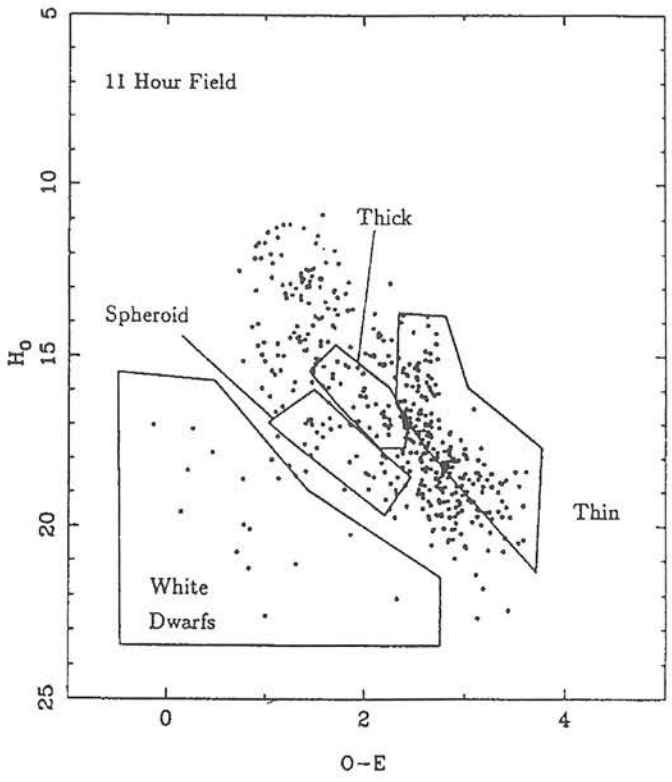

Figure 2.2: RPMD taken from Evans (1992) showing polygons used for thin disc, thick disc, spheroid and WD populations.

of 0.003pc^{-3}, in broad agreement with previous published estimates (Eggen 1983, Liebert, Dahn & Sion 1983), corresponded to only 2% of the estimated shortfall in mass at that time (Bahcall 1984).

The first WDLF to be derived using digitised Schmidt plate data was published by Evans (1992, 1989). This work is interesting in that it features the only modern (post-LDM) WDLF constructed using a sample not drawn directly from the Luyten surveys. The proper motion stars were extracted from APM digitised data of four fields (Evans 1988) and consisted of stars with motions between $\sim$ 0.04 and $\sim$ $0''.4$ yr^{-1}, the exact limits depending on the time baseline separating the first and second epoch plates in each field. Evans undertook a detailed investigation into the potential of the RPM method for population discrimination in his sample, constructing theoretical RPMD featuring several stellar types. Incorporated into the model RPM loci were published colour magnitude relations, estimates for the kinematical properties of the various population groups and the measurement errors inherent in the data. These loci allowed Evans to identify RPMD regions specific to the various populations allowing contamination free population discrim-

ination. An example is shown in Figure 2.2. 123 WDs were identified in this way, allowing construction of a LF in good agreement with LDM. The cut-off was not sampled due to a lack of confidence in the population discrimination at redder WD colours, again reflecting the problems involved in finding red WDs.

One of the most effective methods of searching for CWDs, as has already been mentioned, is by surveying CPMB systems. Their wide separations mean there are no evolutionary complications associated with mass exchange, and the proximity of a CWD to a brighter primary with identical proper motion makes discovery more likely (eg LDGS) than for an isolated degenerate. As part of an investigation into CPMBs containing WDs conducted over a number of years, a new WDLF comprising 50 CPMB WDs was published (Oswalt, Smith, Wood & Hintzen 1995, OSWH hereafter). Again, these stars are drawn principally from the Luyten surveys, although a serious departure from the LDM method is that objects with much lower proper motions are included. OSWH went to some lengths to analyse the completeness of the catalogues they used, principally by investigating number counts as a function of apparent magnitude and proper motion. Oswalt, Hintzen & Luyten (1988) used the prediction that since tangential velocities are distributed around a most probable value, there should be an inverse correlation between proper motion and distance (see Section 5.3.2). Assuming uniform space density, cumulative number counts (from the direction of large μ) should follow a μ^{-3} law. However, it was found that the dataset was systematically incomplete, following a $\mu^{-1.6}$ relation instead. A similar pattern of systematic incompleteness was found as a function of apparent magnitude (Smith & Oswalt 1994). Because the degree of incompleteness, although increasing with lower proper motion and fainter apparent magnitude, appeared to behave consistently as a function of those variables, it was argued that the incompleteness was quantifiable and could be corrected for. The so-called 'completed LF technique' (Oswalt & Smith 1995) corrected for the estimated incompleteness in each (m_{pg},μ) bin by assigning weights in the $1/V_{max}$ prescription. Therefore, although OSWH stated that their sample was "$\sim$ 10% complete", completion factors boosting individual space densities by up to $\sim$ 100 times were used to correct for the incompleteness. An important tool to the observational astronomer studying WDs came with the publication of an extensive grid of model atmosphere predictions for both DA and non-DA WDs, including UBVRIJHK photometry and BCs as function of $T_{\rm eff}$ (Bergeron, Wesemael & Beauchamp 1995). The WD cooling sequences of Wood

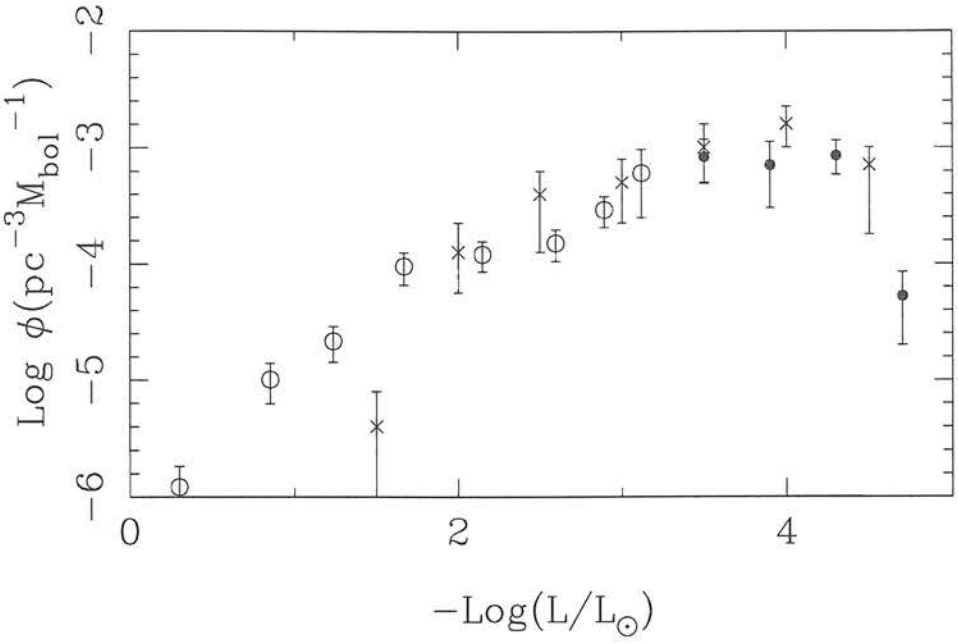

Figure 2.3: The OSWH LF (crosses) compared with the LDM constructed using no BC (solid dots, see left panel of Figure 2.1) and the FLG points in open circles.

(1995) were combined with this work to predict absolute visual magnitudes. These models allowed OSWH to interpolate within the model grid using their CCD (V-I) colours to derive luminosities for their sample. Since insufficient observational material was available to constrain the masses, $0.6M_\odot$ was assumed for every object. The OSWH LF is shown in Figure 2.3, where the LDM with no BC LF is plotted for comparison. Despite the comparison LF being the 'faintest' consistent with the LDM dataset, the turn-down in the OSWH LF appears to occur at fainter luminosities. Despite this, improvements in the theoretical LFs meant the estimate of the Disc age remained essentially unchanged at $9.5^{+1.1}_{-0.8}$ Gyr. OSWH did calculate a higher WD space density – when their data was combined with the LDM sample and account taken of the fraction of LDM WDs that are binary members, the total space density was found to be $7.6^{+3.7}_{-0.7} \times 10^{-3}$ stars pc^{-3}, more that double that found by LDM.

Although OSWH used new model atmospheres which resolved the bolometric correction problems experienced by LDM, defining atmospheric composition for the coolest stars was still unreliable using only optical spectra and $V - I$ colour. A detailed investigation

into some outstanding problems related to the chemical evolution of CWDs by Bergeron, Ruiz & Leggett (1997, hereafter BRL) exploited extensive spectroscopic and BVRIJHK photometric observations of 110 CWDs. BRL were able to combine trigonometric parallax measures and the spectroscopy and photometry to constrain the temperature, surface gravity and atmospheric constituents of CWDs, and from them masses and luminosities. Interesting results from this study include the discovery of a "non-DA gap" in the range $5000 < T_{\rm eff} < 6000$ K, and that most WD atmospheres are well described by either pure hydrogen or pure helium models. The authors went on to use the fitting techniques devised in BRL to redetermine stellar parameters for the LDM WD sample and then construct a revised WDLF (Leggett, Ruiz & Bergeron 1998, hereafter LRB). The observational database for the LDM sample had been greatly enlarged, notably to include the near-infrared photometry which LRB state is important in constraining the WD principal atmosphere constituent. LDM listed 31 objects in their sample with "reasonably determined stellar parameters" (their Table 2), of which 18 were re-evaluated by LRB. Of this 18, six were reclassified with different atmospheric composition. As pointed out by LRB, the difference in luminosity between a DA or non-DA WD of low temperature is significant – approximately 40% for the quoted example of a WD with $V-I \sim 1.3$. The LRB WDLF predicts a much lower space density of very faint ($\log L/L_{\odot} \sim -4.5$) WDs than OSWH, leading to a Disc age estimate of 8 ± 1.5 Gyr. The LRB WDLF is displayed in Figure 2.4, with the OSWH data plotted for comparison. The factor of twenty discrepancy between the two LFs in the last bin is attributed by LRB to the inadequate observational data available to OSWH. LRB claim OSWH have underestimated the errors associated with both the ambiguity of atmosphere constituents of the coolest WDs, and the difficulties of obtaining accurate photometry of binary members. The LRB estimation of the total space density was essentially the same as LDM. The LDM sample is now clearly the best studied WD sample available that is suitable for constructing a LF. A question still exists regarding the completeness of the sample however, since LRB concluded that the sample *was* incomplete, although they argued that the agreement between their space densities and the FLG LF was within the given errors.

All recent (post LDM) determinations of the WDLF have been described above; all appear to indicate an age for the local Disc of approximately 9 Gyr, with errors and discrepancies at the level of one or two Gyr. A more recent survey routinely finding

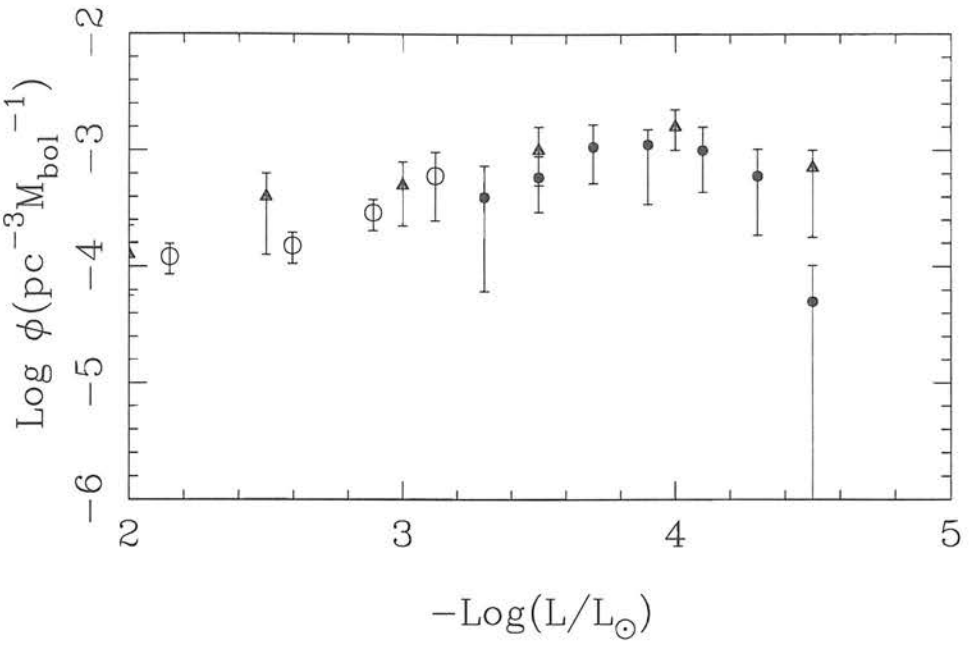

Figure 2.4: The LRB redetermination of the LDM LF (filled circles) with The OSWH LF (filled triangles) for comparison. The FLG points are in open circles.

CWDs in the southern sky is worthy of mention, although the survey method does not appear appropriate for acquiring complete samples suited to construction of a WDLF. The survey uses an eye-blinking technique to locate proper motion stars on plates taken by the ESO Schmidt telescope. Earlier, the same group had discovered the object "ER8" serendipitously in a plate-blinking search for supernovae which also yielded faint proper motion stars as a by product (Ruiz et al. 1986). The luminosity of ER8 ($\log L/L_\odot = -4.41$ according to BRL) make it one of the faintest known WDs, forming part of the population argued to be under-represented by LDGS. Its serendipitous discovery is reminiscent of the aforementioned CWD (Hambly, Smartt & Hodgkin 1997), although its position out-with the area of the Luyten Palomar surveys means it casts fewer doubts on the completeness of the LHS catalogue for faint high proper motion objects. Nevertheless, LDM were aware of ER8, and argued that unless the luminosity of ER8 (which was not well constrained at the time) was extremely low, many such objects would be required to bring the space density beyond the LF cut-off up to the level at the peak near $\log L/L_\odot = -4$. The ESO group subsequently revised their survey to look specifically for proper motion objects (Méndez et al. 1992), and have found a number of new CWDs (Ruiz & Takamiya 1995, Ruiz

1996). An object of particular interest is ESO 439-26 (Ruiz et al. 1995), which highlights the important role WD mass can play. The object is of extremely low luminosity, and hence may be expected to be extremely old. Detailed observations including parallax measurements indicated however that the low luminosity was due to the mass of ESO 439-26, and its cooling age was predicted to be only ~ 6 Gyr. According to Ruiz & Takamiya (1995), the eight CWDs they had discovered at that time implied that the space density of the coolest WDs was several times larger that that predicted by the LDM LF. While this obviously has implications for Disc age estimates, the small numbers of WDs makes the conclusion tentative, and the unclear survey limits may make space densities uncertain.

A means of avoiding the problems associated with samples selected via proper motion is to obtain volume limited samples in the direction of high extinction nebulae. A study of this type by Festin (1998) has resulted in the discovery of 7 WDs, mostly faint, leading to a space density estimate of 0.015 pc^{-3}, five times the LDM number density. Festin argued that his result, in conjunction with the findings of Ruiz & Takamiya (1995), implied that the LDM sample is likely to be missing CWDs due to incompleteness in the LHS catalogue; although the small numbers in both samples make a definitive statement on the issue impossible.

Any estimate of the Disc age from observational WDLFs inevitably relies on predictions of WD cooling theory. Since this is not a thesis about WD physics, and a detailed discussion of the subject is beyond the scope of this work, the reader is referred in the first place to the review by D'Antona and Mazzitelli (1990). The pioneering work of Mestel (1952) has been augmented continually over subsequent years, and the modern numerical evolutionary sequences of Wood (1992, 1995), the best currently available, feature considerable deviations from the Mestel cooling law at high and low temperatures arising from neutrino cooling and core crystallization respectively. Dominant errors in evolutionary time scales arise from uncertainties in core composition and envelope thickness, and are at the level of Gyrs. These errors are discussed along with other inputs to theoretical WDLFs by Wood (1992) in some detail. Theoretical WDLFs are also discussed further in Section 8.3.

Finally, the age of the Galactic Disc has also been investigated using other methods (eg. Jimenez 1998 and references therein), resulting in a broad consensus that the lower limit for the Disc age lies between 8 and 12 Gyr.

Chapter 3

Schmidt Plate Data Reduction

3.1 Introduction

In the course of a long term quasar variability study (eg. Véron & Hawkins 1995) over 300 Schmidt plates have been taken in ESO/SERC field 287 (F287). Analysis of such a large amount of photographic material has been made a practical possibility with the advent of plate scanning machines. The Edinburgh plate scanning machine, SuperCOSMOS, is the most recent in a series of machines designed to exploit the material in the Edinburgh plate library. The SuperCOSMOS machine has only recently come fully online, with the consequence that the bulk of the data used in this project consists of data produced by COSMOS, the predecessor to SuperCOSMOS. The performance of COSMOS is inferior to SuperCOSMOS and defines, along with the intrinsic properties of the photographic plate material itself, the observational limits on this work.

3.2 UKST Photographic Material

The Schmidt camera design, developed by Berhard Schmidt in the 1930s, uses a thin glass corrector plate with a complex profile to correct for spherical abberation arising from the use of a spherical primary mirror. Good quality images several degrees on a side can be obtained with such an instrument in a single exposure, making Schmidt telescopes ideal

Emulsion	Grain Type	Filter	Waveband	Approximate Limiting Magnitude
IIIa-J	fine	UG1	U	21.0
IIIa-J	fine	GG395	B_J	22.5
IIIa-F	fine	AAOV	V	–
IIIa-F	fine	RG630	R	21.5
IV-N	fine	RG715	I	19.5
4415	very fine			

Table 3.1: Principle filter/emulsion combinations used in this work. The 4415 tech pan film is a recent development and has been used for recent U, V and R passbands

for survey work. The 1.2m UKST is located at the Anglo-Australian Observatory (AAO) at Siding Springs, New South Wales (see UKST Handbook, Tritton 1983 for details of what follows). A number of UKST survey projects are currently underway (Morgan et al. 1992), including the nearly complete second epoch $\delta < -20°$ survey and the all southern sky near-infrared survey.

UKST plates are 1mm thick, 356mm square glass plates coated with Kodak photographic emulsion; the UKST plate scale of 67.14arcsec/mm translates to a $6.4° \times 6.4°$ field size . Emulsions of varying spectral sensitivity are used in conjunction with broad band filters to produce filter/emulsion combination passbands approximating the passbands of standard photometric systems. Table 3.1 tabulates the chief filter/emulsion combinations used in this work and gives the corresponding photometric passband and limiting magnitude obtainable. A recent alternative to the glass plate is the 4415 fine grained tech pan film[1], offering higher resolution and a better signal to noise ratio. The relationships between photographic passbands and standard Cousins passbands have been investigated by several authors (eg. Blair and Gilmore 1982, Bessell 1986), although for objects of moderate colour only the B_J passband presents serious departures from the standard passbands.

Spurious images can appear on a developed Schmidt plate in a variety of ways; for

[1]'Plate' will still be used as a generic term for photographic material, although what follows is equally applicable to tech pan films

example the optical properties of the telescope lead to diffraction spikes and ghost images associated with bright images while satellite trails and flaws in the emulsion are not uncommon. On each plate an intensity step wedge, consisting of blocks exposed to light sources of known relative intensity, provides a means of transmission to intensity calibration.

3.3 The Measuring Machines and Image Analysis Software

A full description of the COSMOS microdensitometer was given by MacGillivray and Stobie (1984). COSMOS used a cathode ray tube and associated optics to focus light on the plate emulsion, and measured the transmitted light with a photomultiplier. The 'flying spot' scanning arrangement lead to the pixel data being output in strips across the emulsion surface, the pixel size being 8, 16 or 32 microns. COSMOS scanned the central $5.35° \times 5.35°$ of the field, fully covering the unvignetted portion of the image.

In the first instance, COSMOS data for this project was output in the unwieldy mapping mode (MM) format, which stores transmission values for every 16 micron pixel. Image processing by the COSMOS image analysis software converted this dataset into a list of parameters for every object detected, known as IAM data. It is in this format that virtually all subsequent data analysis has been performed, and it is therefore worth briefly describing the action of the IAM software (see also Stobie 1986).

The relationship between transmission, T, and intensity, I was derived using the scan of the intensity step-wedge region of the plate. From this data, the calibration curve $\log I$ against density ($\log(1/T)$), which should be reasonably linear on a well exposed plate for unsaturated pixels, was used to construct a look-up table for each of the 128 COSMOS digital transmission steps. A median filtering technique was used to produce a sky background map across the scanned area. A 'detection' was deemed to have occurred when a pixel's intensity value was above a given threshold (eg 10% above background), and an image was defined as a specified number of connected signal pixels. Initially, 20 parameters per object were recorded in the IAM dataset, although this increased to 32 when deblending algorithms (Beard, MacGillivray & Thanisch 1990) were included in the image analysis software. These parameters included image centroids (both unit weighted and

intensity weighted) and image size and orientation information. An instrumental magnitude, COSMAG, was also calculated using the sum of the intensity above sky background across the image. It was this quantity, given explicitly by

$$\mathrm{COSMAG} = -250 \log(\sum_i (I_i - I_{sky})) \tag{3.1}$$

that was used for photometric calibration. A discussion of the details of obtaining reliable magnitudes from this quantity is given in Section 3.5.

The new machine, SuperCOSMOS (Hambly et al. 1998), has recently come into full operation. This machine operates with a pixel size of 10 microns and scans substantially faster than the old COSMOS machine. Improvements in astrometry with the advent of SuperCOSMOS are of little relevance to this work since it is limited by the COSMOS scanned data. SuperCOSMOS photometry will again be discussed in Section 3.5, although it is noted here that the image analysis software used on the MM data is essentially identical, again yielding a COSMAG parameter for calibration to a CCD sequence.

3.4 The F287 Database

The orientation of F287 with respect to the Milky Way is particularly suited to studies of the Galactic Disk. An ideal field orientation avoids the serious image crowding difficulties associated with looking directly through the Disk. A field perpendicular to the Disk is also non-optimal, as it samples less Disk volume than orientations inclined to the galactic pole. F287, with galactic coordinates $l^{II} = 355°$, $b^{II} = -47°$ is a reasonable compromise between these two considerations. At present over 300 direct plates have been taken in F287. Material exists in all U, B, V, R and I passbands, although the bulk of the collection is in the form of a survey in B and R consisting of ~ 4 plates taken annually. Figure 3.1 shows in detail the distribution over time of the B_J and R plate collections.The observations start in earnest in 1977 for the B_J plates and in 1980 for the R. While the smaller collection of I plates could in theory also be used for proper motion work, their limited depth means they are of little practical use in this regard.

Once several plates in a single field have been scanned, it is possible to co-add the resulting MM data to form a 'stacked' image of greater depth than the single plate digitised

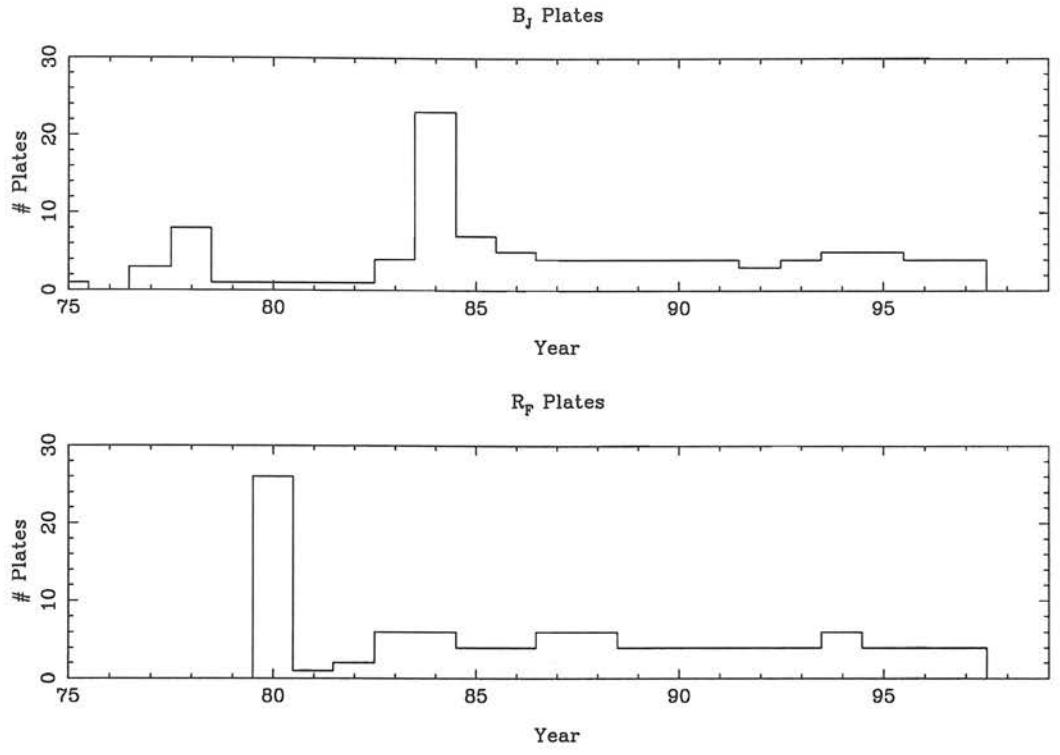

Figure 3.1: Number of plates per year in F287 in the B_J (top) and R (bottom) passbands

images. This stacking procedure is discussed and investigated in detail in Chapter 4. The database presented in Figure 3.1 is an obvious candidate for stacking in a proper motion survey, since at least 4 plates are available in most years and the use of 4 plate stacks rather than single plate data will yield deeper photometric survey limits with no reduction in the proper motion time baseline. For this reason 4 plate stacks have been used in this survey rather than single plate data.

The F287 data available for this survey at its inception consisted of the COSMOS scanned data – all plates taken before 1993 were scanned on the COSMOS machine. The quasar survey for which the scans were originally intended also used 4 plate stacks, and images had been paired across epochs (see Section 3.6) in some passbands. The F287 data was in the following form when this project started:

- B_J stacks – COSMOS IAM files of the 16 1977 – 1992 stacks (unpaired)
- R and I stacks – COSMOS IAM data fully paired up to 1992
- Calibrated photographic U, B_J , V, R, I magnitudes

Year	B_J	R	Year	B_J	R	Year	B_J	R
1977	1		1984	4	2	1991	1	1
1978	1		1985	2	1	1992	1	1
1979			1986	1	1	1993	1	1
1980		5	1987	1	1	1994	1	1
1981			1988	1	1	1995	1	1
1982			1989	1	1	1996	1	1
1983	1	1	1990	1	1			

Table 3.2: The number of B_J and R 4 plate stacks per annual epoch.

During the course of this project the SuperCOSMOS machine has come fully online and has scanned all the B_J and R plates taken between 1992 and 1996. The distribution of 4 plate stacks over time is shown in table 3.2.

3.5 Photometry

As discussed in Section 3.4 calibrated photographic photometry already existed in F287 before this project started (Hawkins 1983). These magnitudes were derived using the COSMAG image parameter from COSMOS scans. This quantity varies monotonically with true magnitude, and is therefore suitable for use in constructing calibration curves using a CCD sequence. A sequence of $\sim$ 200 stars with CCD magnitudes measured in a variety of passbands now exists in F287 (Hawkins et al. 1998), although single channel photoelectric photometry was used in the early work. These known magnitudes in standard passbands were transformed via colour terms to the photographic passbands and compared with the COSMAGs of the sequence objects to produce calibration curves. It was found with COSMOS data that using a position dependent calibration solution significantly reduced the photometric errors, indicating that field effects were a problem, albeit a soluble one.

Previous work on these data has focused primarily on searching for variable objects, and has therefore been concerned with relative photometric accuracy rather than accurate

transformations to known passbands. Since this *will* be an issue in this work, the COSMOS measured magnitudes have been investigated. It was found that while the 'internal' consistency of a particular objects calibrated magnitude across the various plate material is very good, there seems to exist a constant systematic offset from the true value for each measurement. To illustrate this effect, the rms scatter of COSMOS measured magnitudes for a random selection of objects is shown in Figure 3.2 as a function of magnitude. This rms is calculated by extracting the 16 (or less) COSMOS calibrated R magnitudes, finding the mean and then the rms scatter about that mean. The plot shows that the photometry is self-consistent to a few hundredths of a magnitude.

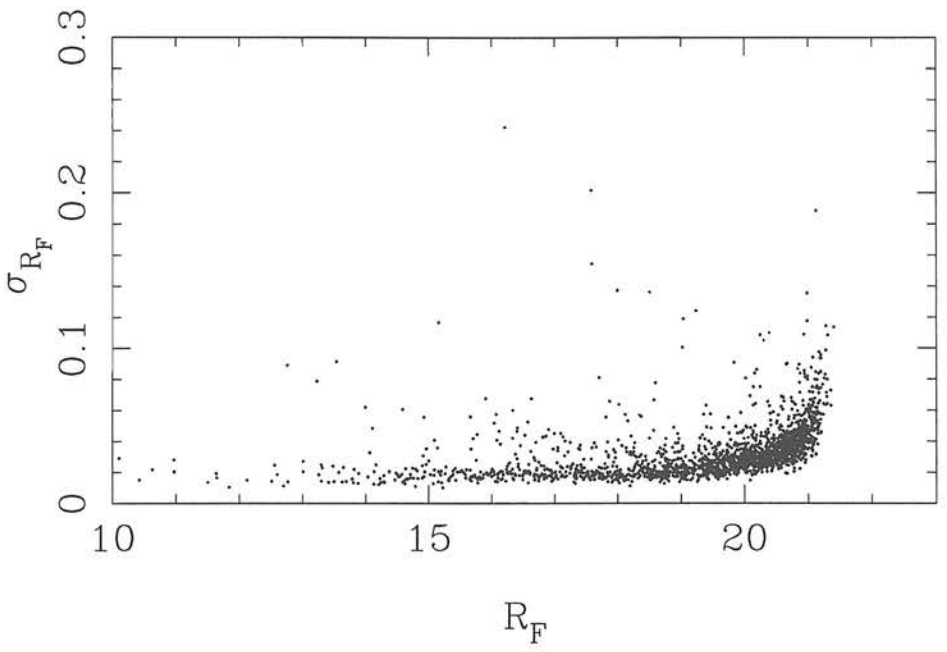

Figure 3.2: The rms scatter of COSMOS measured R magnitudes per object (see text) as a function of magnitude.

If one plots the residual of the fitted magnitude to the CCD magnitude for the sequence stars however (Figure 3.3), it is immediately apparent that the real errors in the photometry are much larger than this. The values of $(R_{CCD} - R_{COSMOS})$ are calculated for each sequence objects measure on each stack. Since the CCD magnitude is plotted on the ordinate, the measures for each sequence object appear on a horizontal line. Again, the rms internal consistency for a particular object is within a few hundredths of a magnitude. Interestingly however, there is a systematic deviation of the mean ΔR from the $\Delta R = 0$

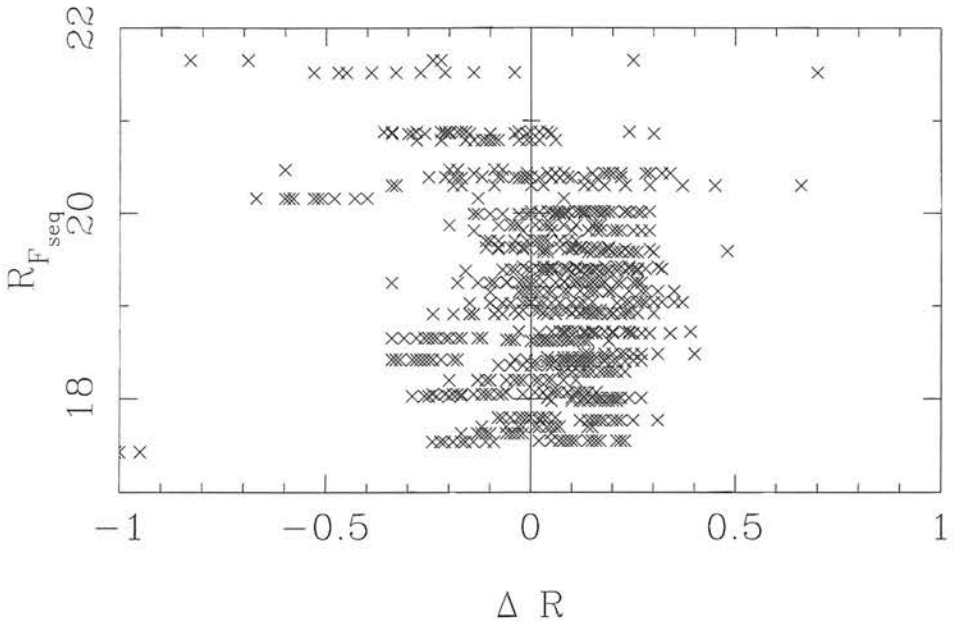

Figure 3.3: The distribution $(R_{CCD} - R_{COSMOS})$ as a function of average COSMOS magnitude for each object. Measurements of the same object appear in a line, and are in general not centered around $\Delta R = 0$

line for virtually every sequence object at the tenth of a magnitude level. The reason for these systematic deviations is not clear, although extensive investigations appear to rule out field effects. Systematic errors in the CCD sequence are clearly a possibility, and it is evident that the internal consistency of calibrated magnitudes is an inadequate indicator of the errors on those magnitudes. In addition, on comparison of the COSMOS calibrated photometry (most notably in B_J) with new CCD data, there was found to be a small zero-point offset between the data values. The importance of these systematics is negligible in the first 'sample selection' phase of this project (Chapter 5), since errors in the photometry will only affect an objects position on the RPMD. Here small photometry zero point shifts are irrelevant and the systematics featured in Figure 3.3 at the level of 0.1 Magnitudes will be swamped by the scatter introduced by eg. population kinematics. Of more concern would be having systematic errors in the photometry when trying to fit UBVRI magnitudes to model atmosphere predictions. For this reason, the photometry of objects selected from the RPM survey are investigated using SuperCOSMOS data.

While faint object photometry does not benefit from the improved SuperCOSMOS dy-

namic range, the finer image sampling and lack of field effects (Hambly 1998) should result in more reliable magnitudes. The procedure used is essentially the same as described above for the COSMOS, except that field effects are small and are neglected and the COSMAG measures are fit straight onto standard passbands using an empirically calculated colour term. The steps involved in the photometric calibration in a particular passband are:

- Locate sequence stars with the appropriate CCD passband magnitude measurement in the SuperCOSMOS IAM data file
- Fit a calibration curve to a plot of COSMAG vs CCD magnitude
- Inspect residuals as a function of magnitude and colour - adjust fit and allow for colour correction if required
- Apply fit to program stars

An example of the calibration procedure is shown in Figure 3.4, with the initial rejection of spurious sequence star detections (top left – top right) and the residual plots as a function of magnitude and colour. The results of this fitting procedure are an improvement on the COSMOS measures, notably in that they do not exhibit zero point offsets. However, the same behaviour as shown in Figure 3.3 is observed when calibrating independent SuperCOSMOS data, perhaps indicating that errors in the CCD sequence are to blame.

3.6 Astrometry

Two independent measures of proper motion have been made for this survey in F287 – one for the set of R stacks and one for the B_J . The data used here is the output of the COSMOS or SuperCOSMOS image analysis software run on each stack (the IAM data). The first step in calculating proper motions is to put every stacks' IAM data onto the same coordinate system. This is achieved by a global transformation followed by local transformations, performed by splitting the stack area into a grid of 16x16 small areas (Hawkins 1986). Every object in each area is used to define the local transformation (since fainter objects are more numerous, they essentially define the astrometric coordinate system). Objects are then paired up between epochs. The software used in this work operates using a fixed

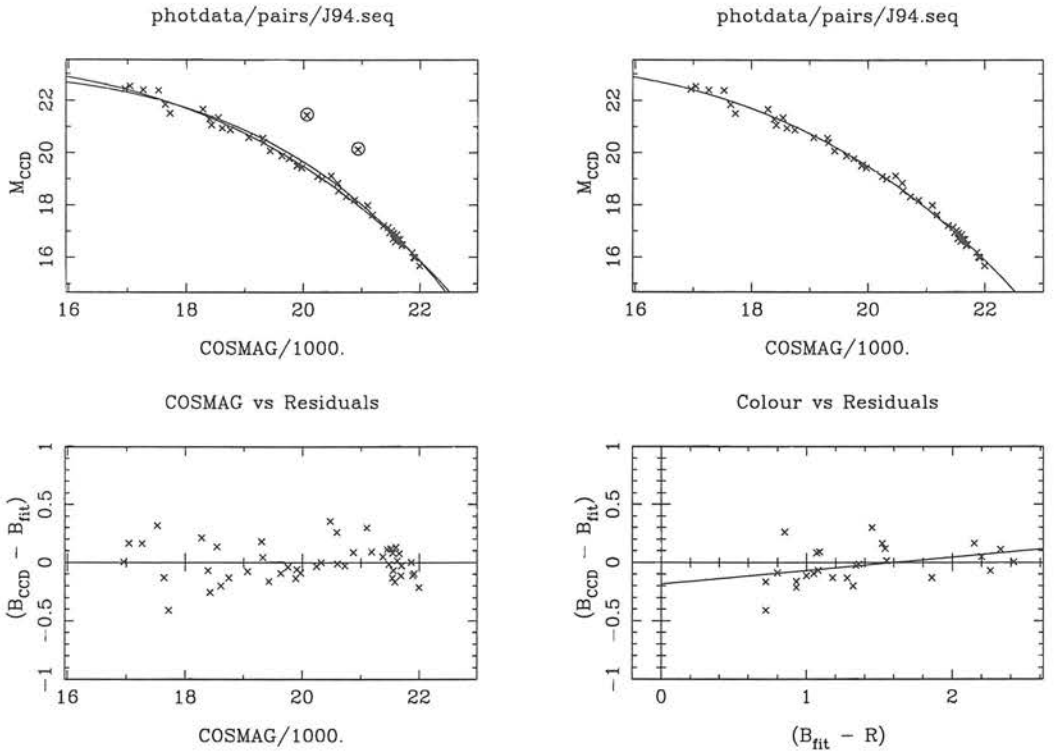

Figure 3.4: Example calibration curve and residual plots for SuperCOSMOS photometric calibration

'box size' (200 microns) in which it looks for a pair. Thus in the first instance a high proper motion limit is imposed on the survey – this issue will be addressed in detail in Section 5.5. The pairing procedure yields a list of x and y coordinates (1 set for each stack the object is found on) for each object. Calculating proper motions is then simply a matter of performing a linear regression fit to each object's x and y coordinates as a function of time. However, erroneous pairing inevitably occurs between stacks, and we therefore wish to perform some form of bad point rejection to reduce contamination by spurious proper motions. In order to reject deviant points (and calculate parameters such as σ_μ and χ^2) an estimate of the error associated with each measure of position is required. We assume this error is simply a function of magnitude and that it will vary from stack to stack, but not across the survey area. Figure 3.5 shows how the typical deviation from the average position (over the 20 stacks) changes with magnitude. The deviations follow a non zero locus as a function of magnitude which may be qualitatively explicable by differential galactic rotation or may be an artifact of the scanning machine. Individual deviations from this locus are assumed to be caused by random measuring error, giving rise to normally distributed errors about the locus. Positional errors are determined in 10 magnitude bins, and are taken to be the standard deviation of the aforementioned normal distribution (eg.

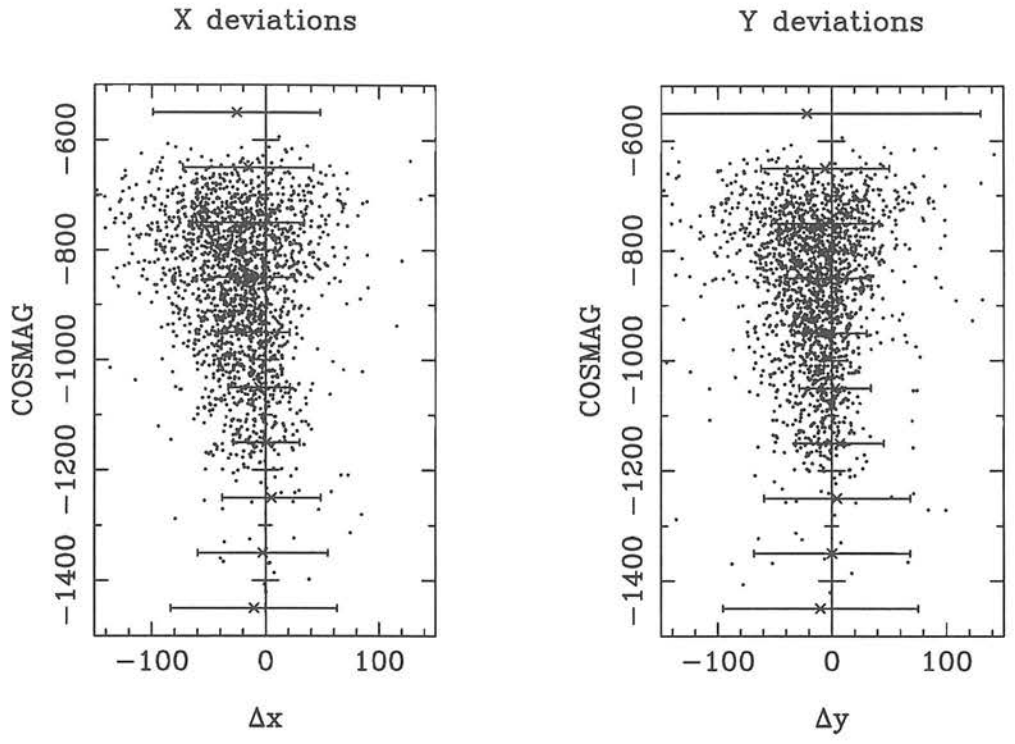

Figure 3.5: Dot plot of object deviation on a particular stack from the average object position as a function of COSMAG. The deviations are in COSMOS $\frac{1}{10}\mu m$ units.

see error bars in Figure 3.5). It is necessary to perform an iterative 3σ rejection procedure here to reject spurious pairings or high proper motion objects which are not reflecting the true positional error sought. The calculated errors are much as one might expect from Figure 3.5: decreasing for brighter objects (more negative COSMAG) until factors such as saturation and blended images makes positional measures more uncertain. These calculations allow an error to be assigned to an image position according to its COSMAG and the stack on which the image is found.

A straight line fit can now be applied to the x and y data for each object, the gradient of which is taken to be the measured proper motion, μ_x and μ_y respectively. An example is shown in Figure 3.6, the points showing the deviation at each epoch from the average object position with error bars calculated as above. Deviant points arising from spurious pairings are often encountered in this data. These points often lie far from the other data and will give rise to spurious high proper motion detections if not removed. We therefore iteratively remove points lying 3σ from the fitted line. This can occasionally lead to further problems if there are several bad points associated with the object, and the result of

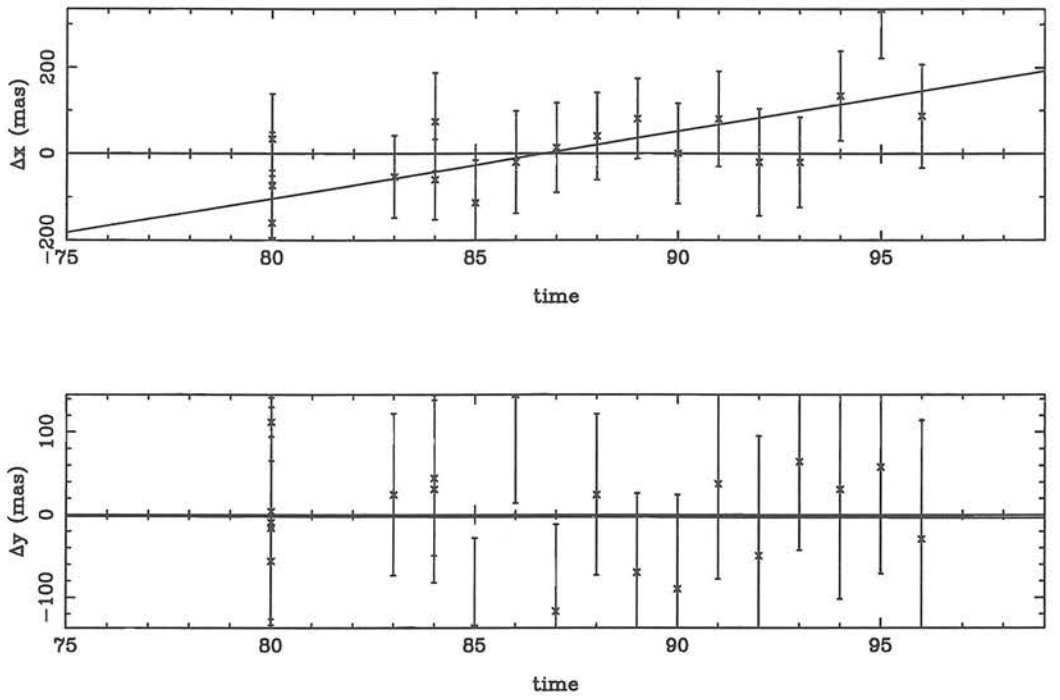

Figure 3.6: An example of a linear regression fit to a set of object positions. The vertical axis is deviation of measured position on a given stack from the mean object position, with year this century on the horizontal axis

several iterations can be a larger spurious motion detection. This source of contamination is generally eliminated by insisting sample objects are detected on virtually every stack. A check on the validity of the positional error estimation scheme described above can be made by calculating the reduced χ^2 of the linear regression fits. One would expect the bulk of calculated χ^2 to be approximately unity for all magnitudes if the positional errors are correct. Figure 3.7 shows that indeed the values of χ^2 are clustered around one, with a scatter of 'underestimates' in the errors for pathological multiple bad-point objects etc. A crude check on the applicability of the positional errors calculated here across the survey area can be made by producing scatter plots such as Figure 3.7 for various portions of the plate. All regions of the plate examined in this way produced scatters about $\log \chi^2 \sim 0$ similar to Figure 3.7, which uses objects found on the bottom left of the survey area (ie. small x and y). Although this survey deals only with relative proper motions, and makes no claim to absolute astrometric accuracy, Luytens LHS proper motion catalogue (Luyten 1979) provides a useful independent check of the motions calculated here (see Table 3.3).

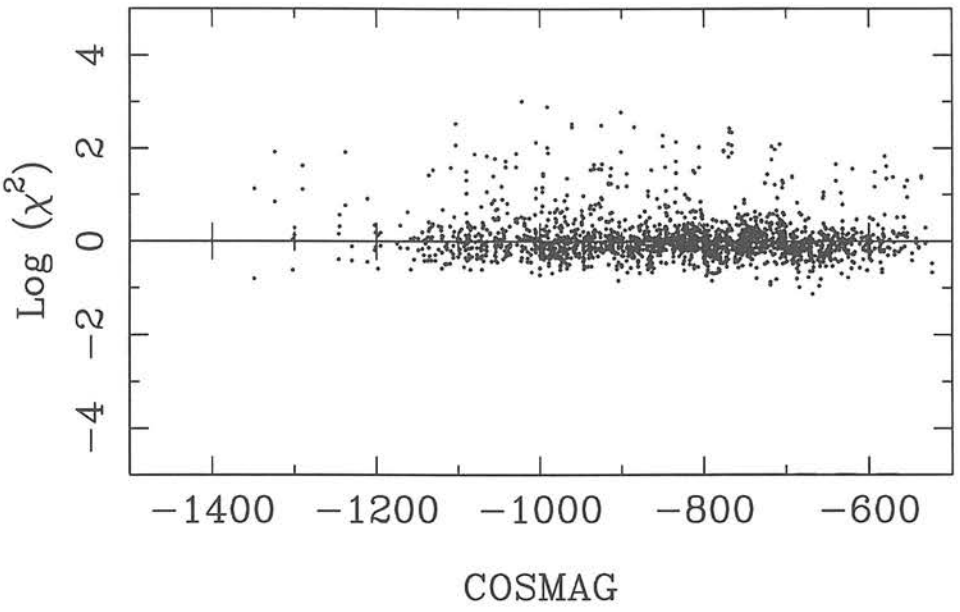

Figure 3.7: The distribution of reduced χ^2 as a function of magnitude showing the positional error estimates used are reasonable

Object	LHS data				this survey			
	RA(2000)	DEC	μ	ϕ	RA(2000)	DEC	μ	ϕ
LHS3666	21 24 15	-46 42.4	.738	97	21 24 16	-46 41.5	.698	90
LHS3671	21 25 22	-44 27.5	.621	237	21 25 27	-44 27.5	.627	237

Table 3.3: A comparison of the LHS astrometry with data from this survey for the two LHS stars in F287.

Chapter 4

Plate Stacking

4.1 Introduction

Continually improving CCD technology inevitably means the case for using photographic Schmidt plates in survey work will become progressively less compelling with time. However, the unrivalled field of view of Schmidt telescopes coupled with the advent of high speed scanning machines such as SuperCOSMOS (Miller et al. 1992; Hambly et al. 1998) still allow Schmidt plates to provide a wealth of information in wide fields (MacGillivray & Thomson 1992). The chief disadvantage of photography compared with modern CCD imaging is that the quantum efficiency of the photographic emulsion is typically between one and two orders of magnitude smaller than that of the CCD. The problem of lack of depth in photographic imaging is addressed in this Chapter by demonstrating a technique for stacking digitised Schmidt plates. This is not a new idea – previously, plate stacking has been done both photographically (eg. Malin 1988 and references therein) and digitally (eg. Hawkins 1991; Kemp & Meaburn 1993; Schwartzenberg et al. 1996), generally in faint galaxy and quasar projects. There are still many fields with large numbers of plates where the stacking process will yield valuable data on all manner of faint objects. In addition, where sufficient plate material exists, stacking may be done at several epochs yielding information on time dependent phenomena, eg. long term variability and proper motions. Table 4.1 shows a 'top–ten' of United Kingdom Schmidt Telescope (UKST) fields having sufficient suitable plates for stacking in the three photographic passbands J, R and I.

Rank	Field Centre		No. of plates available (as at June 18, 1999)		
	RA	DEC	J	R	I
1	21 28	−45 00	99	100	40
2	00 54	−73 00	29	5	59
3	05 20	−66 48	2	2	67
4	18 24	−33 58	31	30	3
5	05 30	−72 12	2	2	56
6	10 38	+00 08	12	33	13
7	05 12	−70 00	37	7	3
8	20 48	−35 00	22	19	4
9	06 04	−70 00	4	6	32
10	04 20	−70 00	5	6	29

Table 4.1: 'Top-ten' UKST Fields for plate stacking

The SuperCOSMOS machine is currently scanning all the UKST survey plates (Morgan et al. 1992) and is routinely archiving pixel data for subsequent analysis. Many private projects are also underway, scanning collections of plates in small numbers of fields.

4.2 Theoretical background and the stacking technique

Since astrometric and photometric data for bright objects are readily available from scans of single plates, the primary purpose of plate stacking must be to maximise the signal to noise of faint images. It is also desirable to devise a stacking scheme that accounts for the often large variations in plate quality, the sources of which are many and varied (Tritton 1983), but the effects of which may be quantified by analysis of the scanned plates' pixel data. Furthermore, it is advantageous in many circumstances to implement bad-pixel rejection algorithms to avoid spurious photographic image defects (eg. due to satellite trails or emulsion flaws) propagating through the stacking procedure (note that time-dependent information, for example positions of high proper motion objects, will be destroyed by such rejection).

The action of photons on the photographic emulsion is to produce dark grains (after development) as a function of exposure time. The photographic process is highly non-linear (eg. Altman 1977) – a plot of the density of dark grains versus log(exposure) typically shows a 'toe', a linear part with gradient conventionally denoted γ and a 'shoulder' where saturation due to the finite number of available grains in the emulsion is approached. Sky limited astronomical photographs are usually exposed so as to yield a background density towards the lower end of the linear part of the characteristic curve, along with good contrast (ie. high γ). Plate scanning in general produces a transmission value T for each pixel. Photographic densities D are, by definition (see, for example, Altman 1977), the logarithm of the reciprocal transmission values, ie. $D = \log_{10}(1/T)$. Calibration of transmission T to relative intensity I is achieved via the step–wedge region of the plate, where spots of known relative intensity are exposed for the duration of the main exposure. Valid stacking procedures could be performed in T, D or I units provided the noise characteristics of the data in those units are correctly quantified and taken into account. However, it is preferable to work in units whose associated error distribution is Poissonian. Then, errors propagate naturally in the stacking process when adding data values.

It can be shown that a density measurement is essentially a count of the number of dark grains (Nutting 1913). Fluctuations in measured density arise both from photon shot noise and the distributions in grain size and position. While the distributions of these grain properties are not Gaussian, the fluctuations in observed density do follow a normal distribution closely, as may be expected from the central limit theorem. Modelling by Selwyn (1935) also predicted Gaussian behaviour for density fluctuations, with the distribution rms (henceforth σ_D) proportional to the inverse square root of the aperture size. In the specific case of the science–grade emulsions used on Schmidt plates, Furenlid et al. (1977) have verified the Gaussian nature of the fluctuations in D. The non-linear relationships between T and D or D and I should then lead to skewed distributions for fluctuations in T and I. Stacking in units of T or I would therefore require cumbersome non–linear weights as a function of data value to correctly propagate the errors. A natural choice therefore is to co-add pixel data in densities ($\log_{10}(1/T)$), and since the associated errors are normally distributed the following simple plate weighting algorithm is appropriate.

Consider a faint image on two plates to be co-added. Plate one has background noise σ_1 and the image has signal above background H_1, with plate two having corresponding characteristics σ_2 and H_2. The pixel data is added such that

$$(-\log_{10} T)_{stack} = w_1(-\log_{10} T)_1 + w_2(-\log_{10} T)_2, \tag{4.1}$$

with weights w_1 and w_2 constrained by $w_1 + w_2 = 1$. The (very good) approximation is made that for faint images that the noise is constant across the profile of the image, and the signal to noise at the peak of the stacked image is then found to be

$$s : n = f(w_1, w_2) = \frac{w_1 H_1 + w_2 H_2}{\sqrt{w_1^2 \sigma_1^2 + w_2^2 \sigma_2^2}}, \tag{4.2}$$

assuming normally distributed errors adding in quadrature. Putting $w_2 = 1 - w_1$, the signal to noise is maximised by setting $\partial f / \partial w_1 = 0$. The weights are then determined by

$$w_1 = \frac{(\sigma_2^2/H_2)}{(\sigma_1^2/H_1) + (\sigma_2^2/H_2)} = \frac{(H_1/\sigma_1^2)}{(H_1/\sigma_1^2) + (H_2/\sigma_2^2)}. \tag{4.3}$$

Bland-Hawthorn & Shopbell (1993) have argued that due to the presence of threshold and saturation limits in photographic emulsions, density fluctuations obey a limited Poisson distribution which introduces skewness that must be corrected for in the weights. It can be argued however that this source of error is negligible for our purposes, since only faint images lying safely in the linear region of the characteristic curve (demonstrated to be least affected by this effect) are of concern in this procedure.

The weighting scheme described here optimises the signal to noise by taking the mean, but takes no account of potential contamination by spurious images and bad pixels. In the presence of bad data, the median is a more robust (but less efficient) estimator of the 'true' mean, and will yield a cleaner stacked image than the weighted mean but with lower signal to noise. Tukey and others (eg Hoaglin, Mosteller & Tukey 1983) have developed more elaborate techniques for stacking images which provide more of the efficiency of a mean estimator while retaining the 'pixel rejection' characteristics of a robust median estimator. A detailed discussion of the theory of image stacking and these estimators in particular may be found in Irwin (1996) and Carter (1993) and references therein. Tukey's biweight function is reported to be one of the best of these robust estimators, and is applied to the plate data as a comparison to the conventional weighted average/pixel rejection combination algorithms.

4.3 The stacking Procedure

4.3.1 Details of pixel weighting

A high quality plate from the stacking sample is chosen to be used as a master or reference plate. A small section (1280x1280 10μm pixels) of the pixel data from the centre of this plate was extracted for analysis, in which 5 blank regions of sky (50x50 pixels) were identified. Values of σ_D and the background density D were calculated for each individual sky region, using iterative 3σ rejection in the log T distribution to discard non–sky pixels arising from plate defects or images. The global plate value of each parameter was taken to be the median average across the 5 sky regions.

In order to obtain a well defined faint image signal value (corresponding to the H parameter discussed in Section 4.2) a 'mini-stack' of some 50 objects near the plate limit was used. Objects lying about 1 magnitude above the plate limit were identified in the small (1280x1280) section of pixel data used to determine the background parameters described above. These faint images were inspected and spurious or extended objects were rejected; in addition, the stellar magnitude parameter was examined over the full run of plates to be stacked, and any object showing variation at a level greater then 3σ above the measured plate–to–plate differences was rejected. Pixel data of the good images were then extracted and the plate background subtracted. Positions for these objects accurate to $\sim 1\mu$m calculated using the SuperCOSMOS image analysis software (Chapter 3) were used to co-add the objects, registering the images with one another on a 1μm grid to create a finely sampled stacked array. Orthogonal strips were extracted from the centre of this combined image, which in general fit a Gaussian profile well (Figure 4.1). The average height of these Gaussian fits was taken to be the parameter H for the master plate.

Both plate stacking and the weighting technique described here require that all slave plates be re-sampled onto the coordinate system of the master plate. Standard SuperCOSMOS software achieves this by dividing each plate pixel map into a 16 by 16 grid and using all object images within each sub-section to define a geometric transformation (rotation, translation and scale) between coordinate systems. The (2 cm) grid size was chosen so that jumps in pixel position across grid boundaries was limited to a small fraction

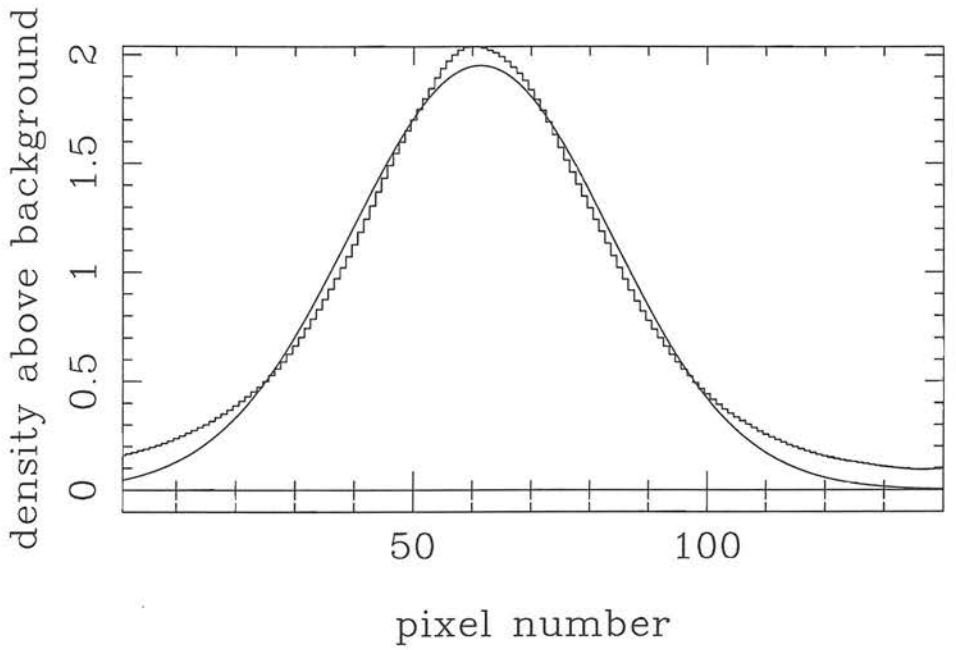

Figure 4.1: Histogram of a cut through a stack of faint images with Gaussian fit over-plotted

of a pixel and was thus negligible compared to other sampling errors. After coordinate transformation and bilinear interpolation to re-sample the data the above analysis was then simply repeated using the same blank sky regions and faint objects on the remaining plates. The resulting σ_D and H values for the each slave plate were used to assign a weight relative to the master according to Equation 4.3.

4.3.2 Details of bad pixel rejection

A comprehensive set of image combining algorithms incorporating weighting and bad pixel rejection are provided in the task 'imcombine' running under the IRAF[1] environment. In this section the results of using these various algorithms in conjunction with the weighting scheme described above on a set of 16 IIIaJ UKST Schmidt plates (see Table 4.2) is presented .

[1]IRAF is distributed by the National Optical Astronomy Observatories, which is operated by the Association of Universities for Research in Astronomy Inc., under contract with the National Science Foundation of the United States of America.

Plate Number	Date	Exposure Time(mins)	Grade	Relative Weight
15563	24/05/93	65	bI	0.53
15795	05/10/93	60	bU	0.46
15796	06/10/93	100	bU	0.68
15801	07/10/93	90	aU	0.93
16177	06/07/94	110	a	0.84
16180	07/07/94	110	a	0.62
16183	08/07/94	110	a	0.53
16230	10/08/94	110	a	0.67
16700	29/07/95	60	aHD	0.31
16728	20/08/95	60	cXD	0.24
16731	23/08/95	60	aE	0.67
16741	25/08/95	70	aD	0.53
17117	25/05/96	90	aU	0.83
17167	07/08/96	60	aI	0.52
17173	11/08/96	60	a	1.0 (master plate)
17189	13/08/96	60	aDE	0.45

Table 4.2: The 16 IIIaJ UK Schmidt plates used in this work

The small field used in these experiments was carefully chosen to contain plate blemishes and spurious images on one of the plates (see Figure 4.2), features which would ideally be removed in any stacking process. The problem of bad pixel rejection should become progressively less serious as the number of plates to be stacked increases, and the most effective pixel rejection algorithm may also change. The 16 plates have therefore also been analysed in sub-stacks of 4 and 8 plates.

The image combination algorithms used were as follows:

(1). no rejection

(2). median taken at each pixel

(3). minmax rejection(1 high, 1 low)

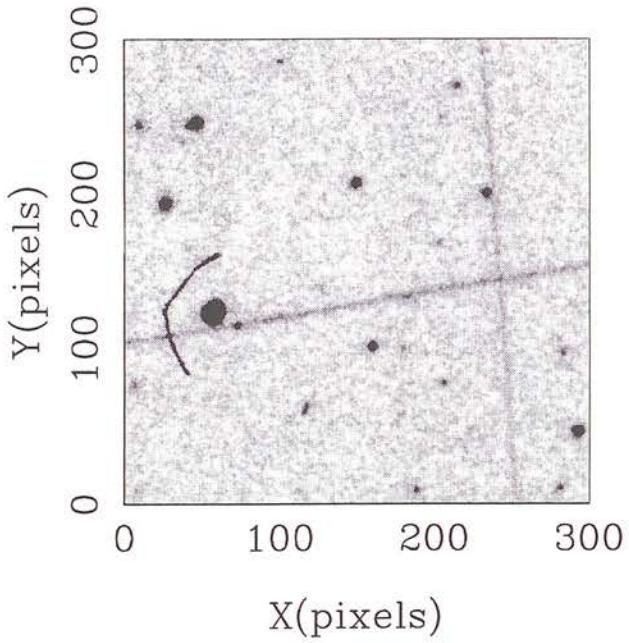

Figure 4.2: Pixel map of a region of plate J15796 containing two satellite trails crossing and a dust speck

(4). sigma clipping (3 σ rejection)

(5). average sigma clipping (3 σ rejection)

(6). no weighting, no rejection

(7). Tukey's biweight

All except (2), (6) and (7) combined unrejected pixels by simple co-addition using weights, and any rejection was on a purely pixel by pixel basis except for (5). The average sigma clipping algorithm uses an entire strip of image data to calculate a noise model as a function of signal which is then applied to each pixel in turn (see the online help pages for 'imcombine' for details).

Correct application of these algorithms of course requires that the images have the same noise parameters. The data is therefore scaled both additively and multiplicatively such that the global noise fluctuations in each plate are equal, allowing rejection of bad pixels. Note however that, due to sometimes large differences in seeing between plates, data in the presence of images can never be scaled to look identical. It is therefore expected that

there will be variations in signal at the peak of faint images, inevitably resulting in a loss of signal to noise by the action of any pixel rejection algorithm.

4.4 Example Results

The weighting algorithm was tested by stacking 2 plates with weights varying around those calculated using the technique described above. The calculated weights were found to maximise the signal to noise in faint images.

The relative merit of these stacking methods was assessed by considering both the signal to noise in the resultant stack and the success of the pixel rejection in removing unwanted features. Each stack was reanalysed using the technique described in Section 4.3.1 and its signal to noise taken to be H/σ_{D}. The results are shown in Table 4.3. While the performances of the various rejection algorithms are assessed in Section 4.5, the fundamental question of whether spurious features are likely to contaminate stacked data is addressed by simulating the action of the SuperCOSMOS image analysis software on the data . The 'pisafind' task in PISA (Draper & Eaton 1996) performs isophotal analysis on image data and is equivalent to the analogous SuperCOSMOS routine. The SuperCOSMOS norm of defining a 2.5σ detection as a signal and defining 8 connected signal pixels as an object detection is adopted.

Pixel and PISA thresholded image ellipse plots are shown for selected stacks. The results of stacking 4 plates are shown in Figure 4.3 through to Figure 4.10. The results of sigma clipping rejection in 8 and the full 16 plate stacks are shown in Figure 4.11 through to Figure 4.14. The full stack results with no rejection are shown in Figure 4.15 and Figure 4.16.

Certain applications of image analysis software may require a relaxation of the criteria for object detection. Figure 4.17 shows the ellipse plot for 4 plates stacked with no pixel rejection with the object detection criteria relaxed to 6 interconnected 2 σ signal detections. The result of applying the same detection criteria to a 4 plate stack with average sigma clipping rejection is shown if Figure 4.18.

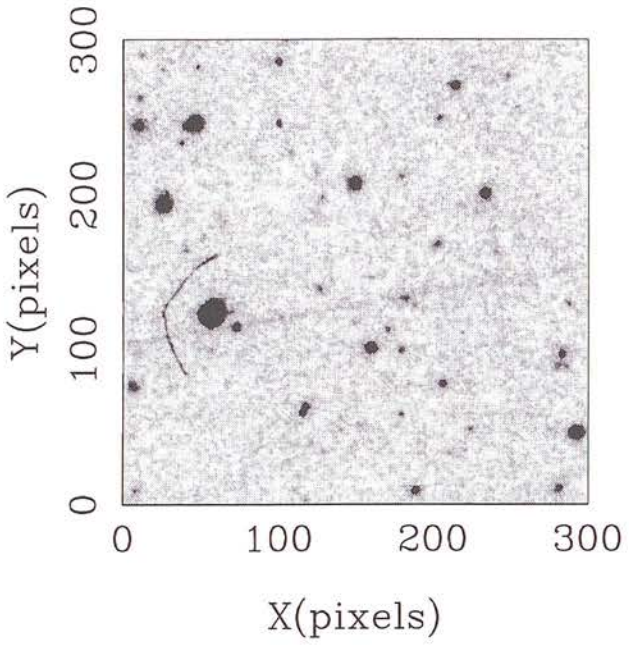

Figure 4.3: 4 plate stack pixel map - no rejection used

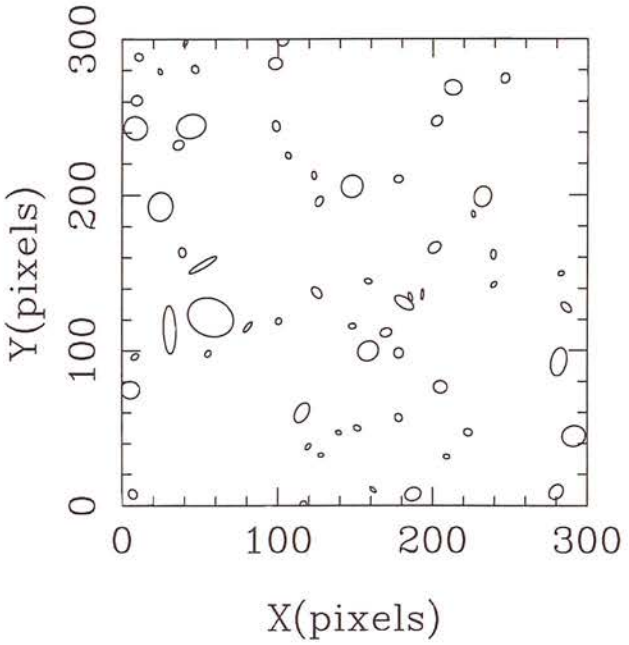

Figure 4.4: PISA ellipse plot of Figure 4.3 pixel map - no rejection

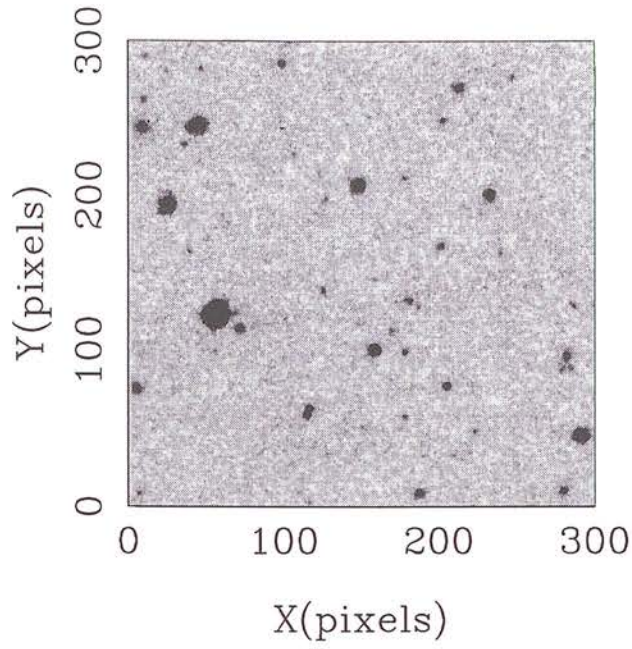

Figure 4.5: 4 plate stack pixel map - average sigma clipping rejection

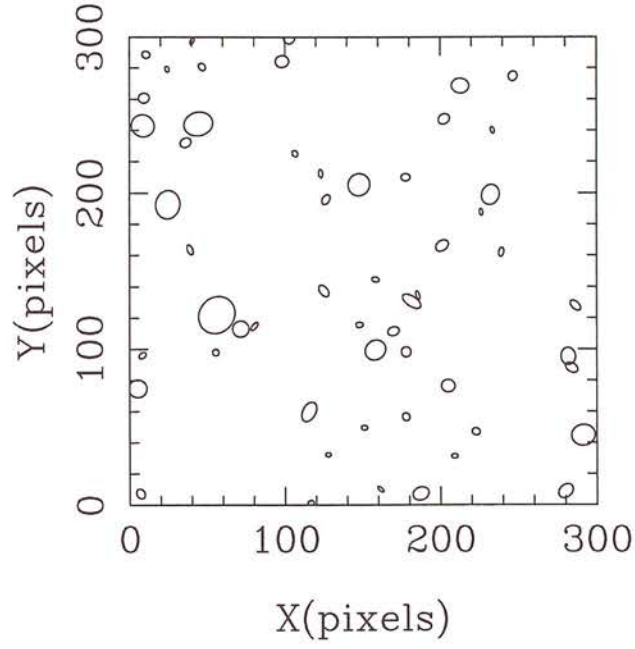

Figure 4.6: PISA ellipse plot of Figure 4.5 pixel map - average sigma clipping rejection

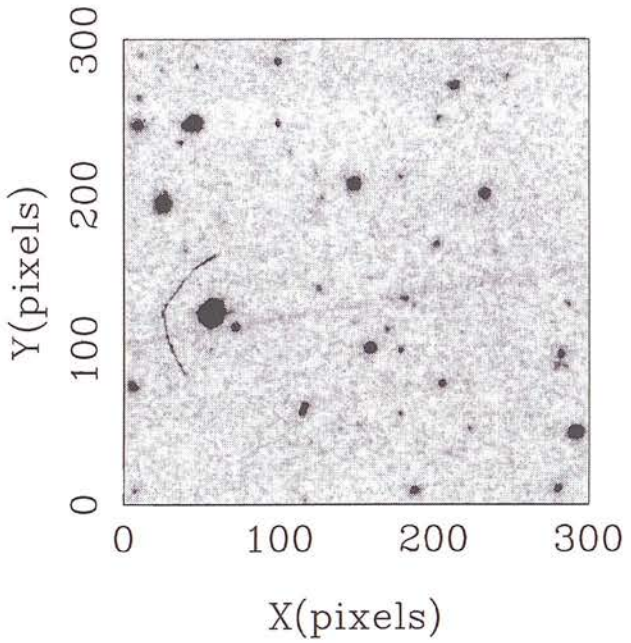

Figure 4.7: 4 plate stack pixel map - sigma clipping rejection

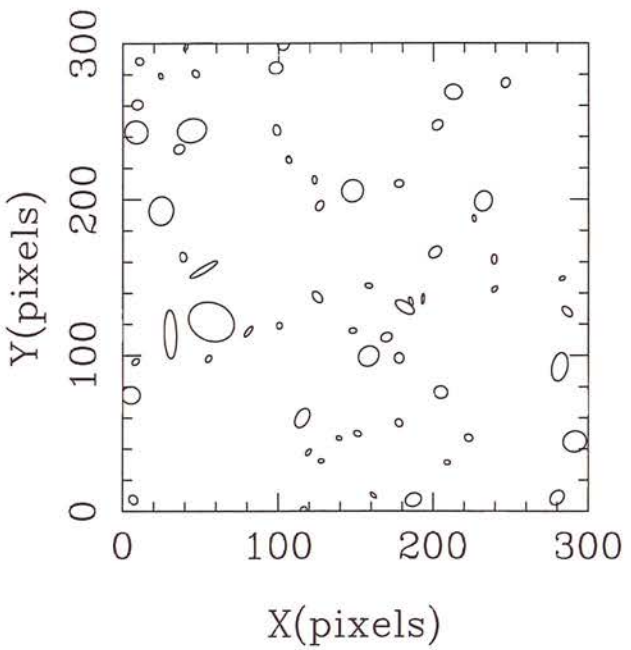

Figure 4.8: PISA ellipse plot of Figure 4.7 pixel map - sigma clipping rejection

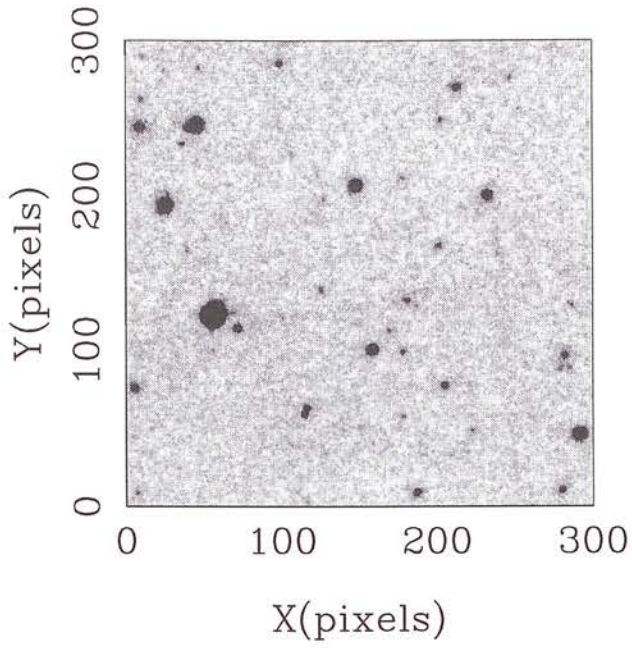

Figure 4.9: 4 plate stack pixel map - minmax rejection

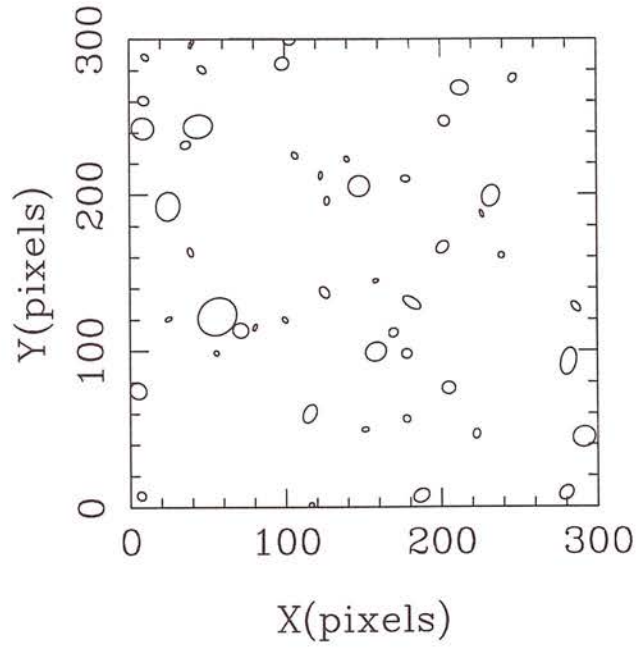

Figure 4.10: PISA ellipse plot of Figure 4.9 pixel map - minmax rejection

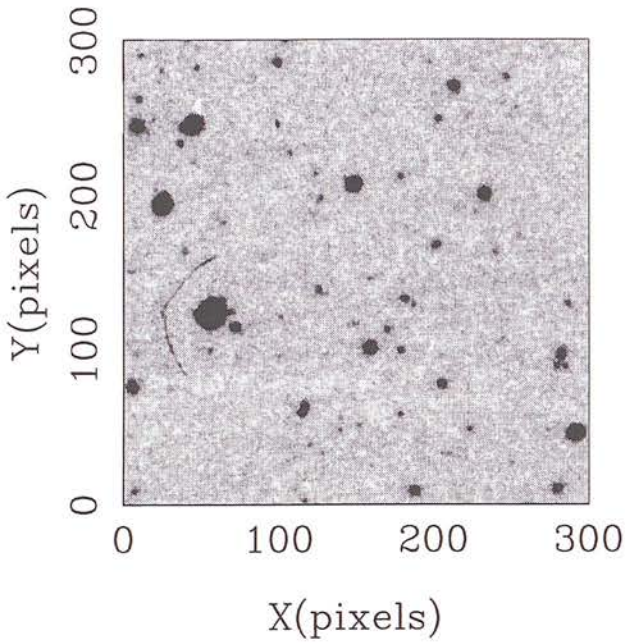

Figure 4.11: 8 plate stack pixel map - sigma clipping rejection

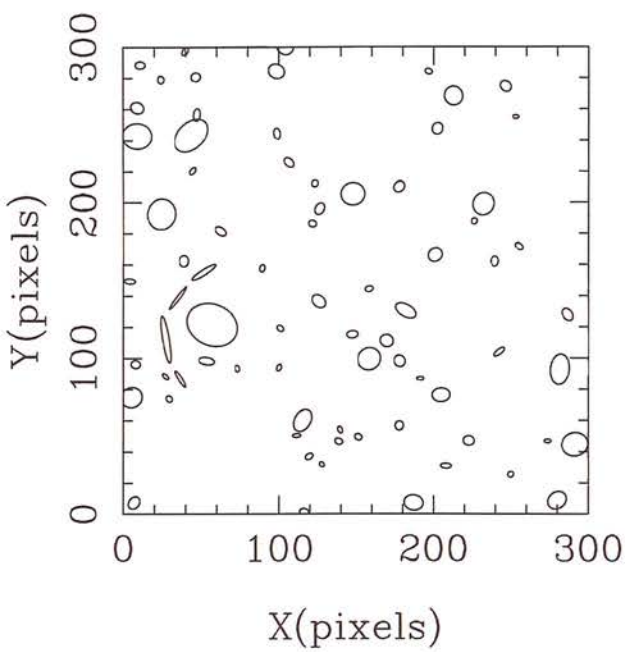

Figure 4.12: PISA ellipse plot of Figure 4.11 pixel map - sigma clipping rejection

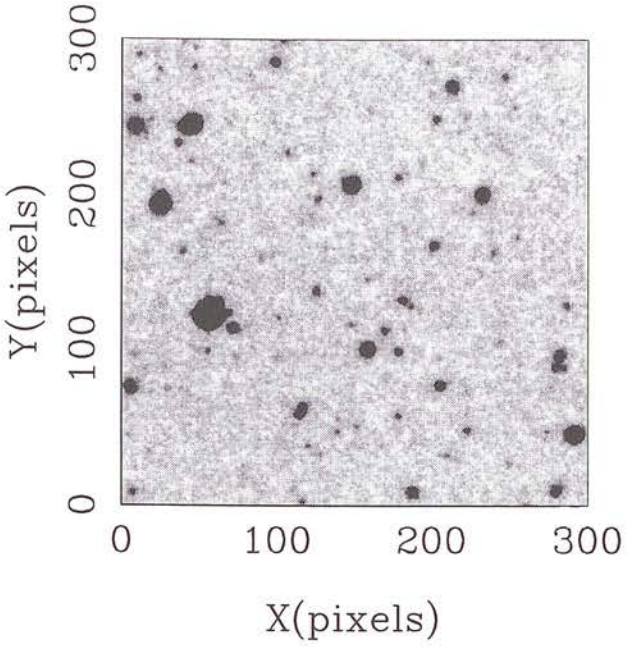

Figure 4.13: 16 plate stack pixel map - sigma clipping rejection

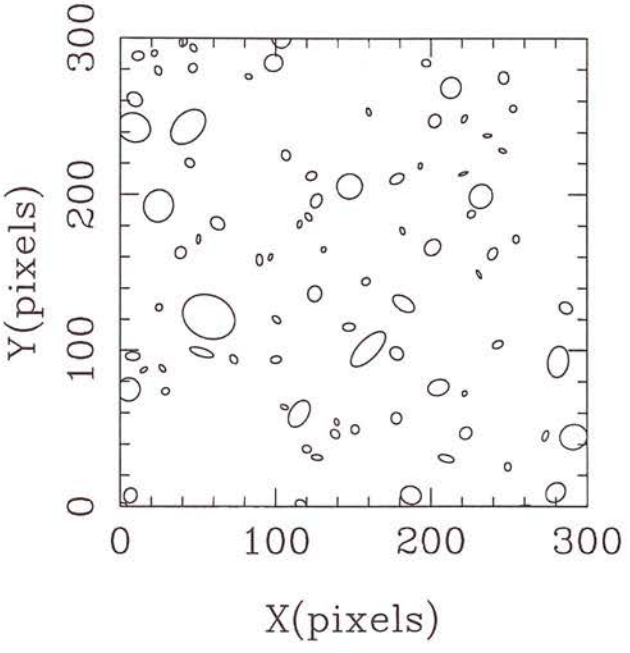

Figure 4.14: PISA ellipse plot of Figure 4.13 pixel map - sigma clipping rejection

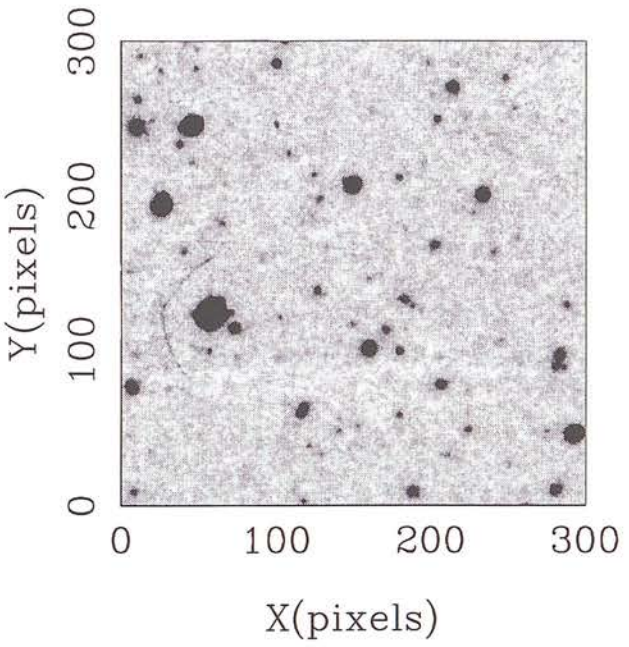

Figure 4.15: 16 plate stack pixel map - no rejection

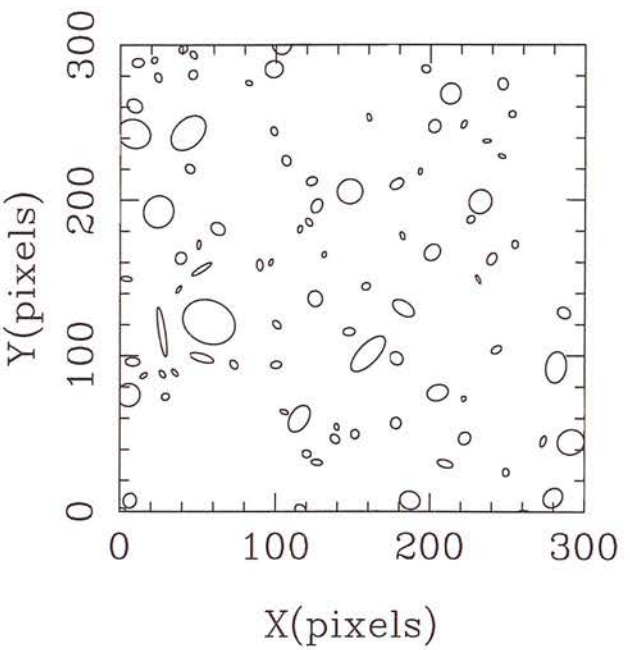

Figure 4.16: PISA ellipse plot of Figure 4.15 pixel map - no rejection

Stacking algorithm	4 plate stack s:n	8 plate stack s:n	16 plate stack s:n
(1) No rejection	12.8	18.7	23.3
(2) Median	10.3	14.9	18.1
(3) Minmax	10.3	16.6	21.4
(4) Sigma clipping	12.1	17.6	22.0
(5) Average sigma clipping	11.0	16.8	21.7
(6) No weighting, no rejection	11.1	16.8	20.9
(7) Tukey's biweight	–	–	18.8

Table 4.3: Results of signal to noise analysis on stacks (*note:* plate J15796 containing the image defects had a s:n ratio of 5.0 and the master plate had a s:n ratio of 8.9)

The weighting algorithm itself was tested by stacking the same two plates several times with various relative weightings. The s:n in each resultant stack (measured as described above) is plotted against plate weight in Figure 4.19, with the prediction for optimum weighting from our algorithm also plotted.

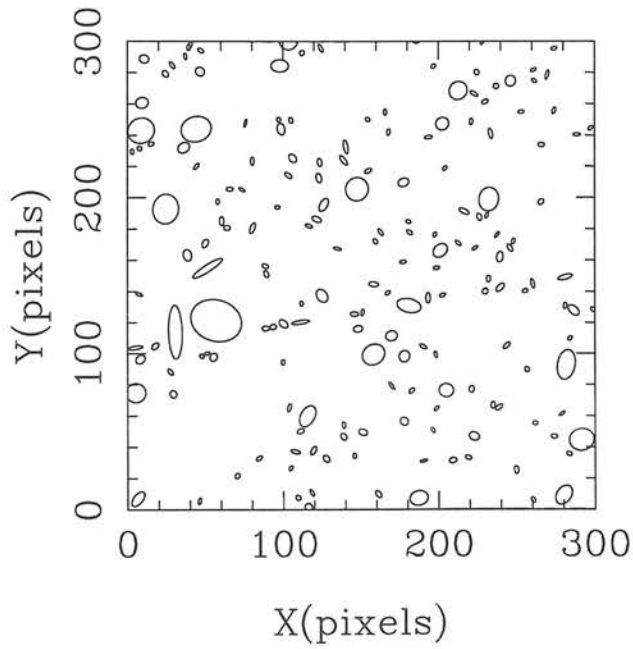

Figure 4.17: 4 plate stack with no rejection PISA ellipse plot using relaxed object detection criteria

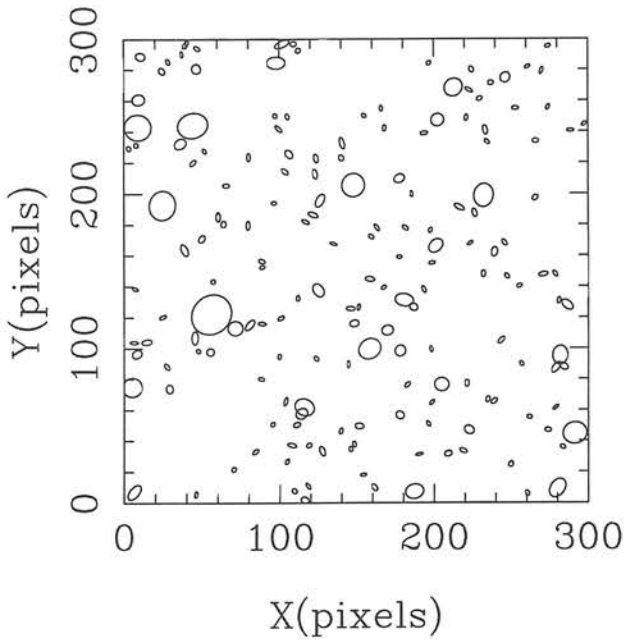

Figure 4.18: 4 plate stack with average sigma clipping rejection PISA ellipse plot using relaxed object detection criteria

4.5 Discussion

All rejection algorithms inevitably lead to a reduction in signal to noise since they can only *reduce* the signal at the peak of faint images as discussed in Section 4.3.2. It is clear from Table 4.3 that simply taking the median compromises the stack quality, while with the expected exception of minmax rejection being poor for a small number of plates the remaining rejection algorithms tend to perform equally well in terms of signal to noise.

Although Tukey's biweight is effective in removing spurious features from the stack, the stack signal to noise is only marginally better than the median for 16 input images. The biweight technique may be improved by using a noise model to calculate sigma (as average sigma clipping does) , although since the biweight always incorporates all data values into the final image (however weighted down) it cannot perform as well as an algorithm that efficiently rejects bad data outright.

Close inspection of the ellipse plots reveals that even with a 4 plate stack both minmax

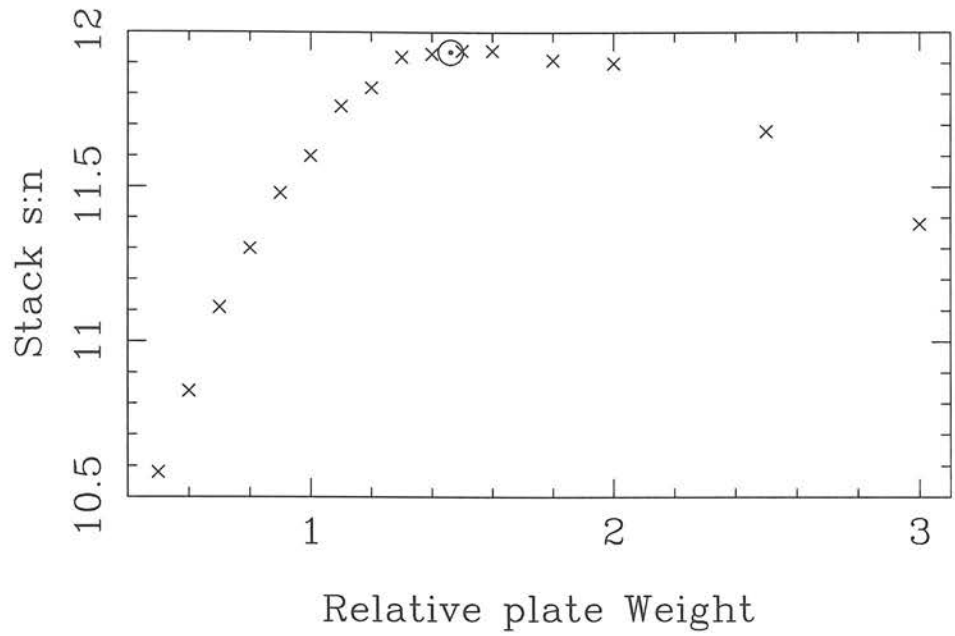

Figure 4.19: Resulting s:n ratio as a function of plate weighting for a stack of two test plates. The weighting algorithm calculated an optimum relative weight shown by the dotted circle

and average sigma clipping remove both the satellite trails and the dust speck very effectively . The latter is to be preferred however since data are not automatically discarded, leading to increased signal to noise in the final stack. In the case of no rejection the spurious features are propagated through the stacking procedure as expected, and are plainly visible even in the 16 plate stack in both the pixel and ellipse plots. The simple sigma clipping algorithm is unsurprisingly very poor at recognising spurious pixels in both the 4 and 8 plate stacks, although 16 plates appears to be sufficient for the 'pixel-by-pixel' technique to work adequately.

The performance of the various rejection algorithms can be assessed more quantitatively by subtracting the various stacked images from the purely weighted optimal signal to noise stack (number 1 in Table 4.3). The resulting image is zero where no pixel rejection has occured, thus showing the regions where the rejection algorithm has been active very clearly. A 12000 pixel area (containing no bright stars but several spurious images) has been extracted from these subtracted (16 plate) images for each rejection algorithm, plus the median and Tukey's biweight images. For a perfect algorithm, a histogram of the

data values from this sub-image should have a large peak at zero, corresponding to the optimum signal to noise where no rejection is required. There should also be a group of outlying points (generally at $\Delta D < 1$ since spurious images are more common than emulsion scratches) where the rejection algorithm has discarded a bad data value. The 'average sigma clipping' algorithm emulates this behaviour most effectively (see Figure 4.20), although the population with positive ΔD indicates that some rejection of good data is occuring (as expected for 3σ clipping). The straight sigma clipping algorithm (Figure 4.21) has been less effective in eliminating the the large body of bad data at $\Delta D = -1 \times 10^{-3}$ in Figure 4.20, although rejection of good data is perhaps less of a problem. The other three algorithms successfully reject deviant data (Figures 4.22, 4.23 and 4.24), but the plots show clearly that the stack signal to noise has suffered as a result of the action of these algorithms since all the good data points have been shifted to varying extents from their optimum value.

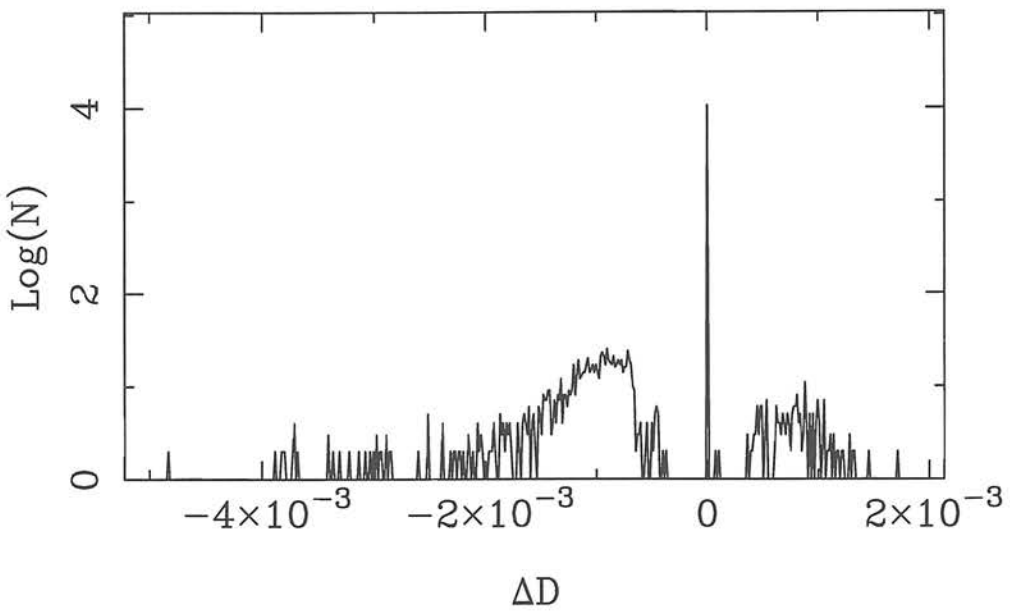

Figure 4.20: Rejection histogram (see text) for the 'average sigma clipping' algorithm

The relaxed detection criteria used in producing Figure 4.17 have resulted in a clear increase in satellite trail images when compared to Figure 4.4. Spurious images introduced by random sky fluctuations have also increased in number. The average sigma clipping rejection performs well in eliminating bad images even in this case.

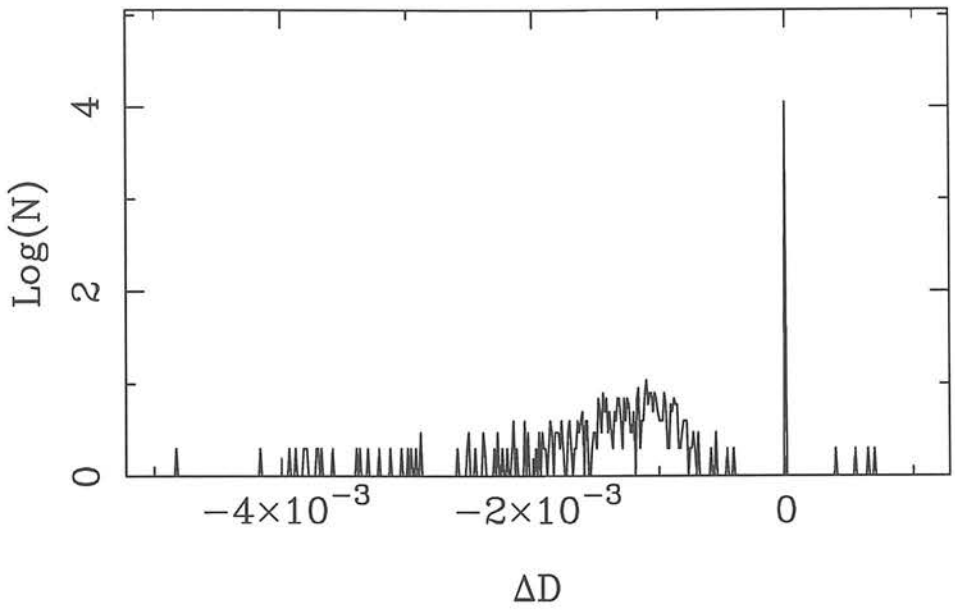

Figure 4.21: Sigma clipping rejection histogram.

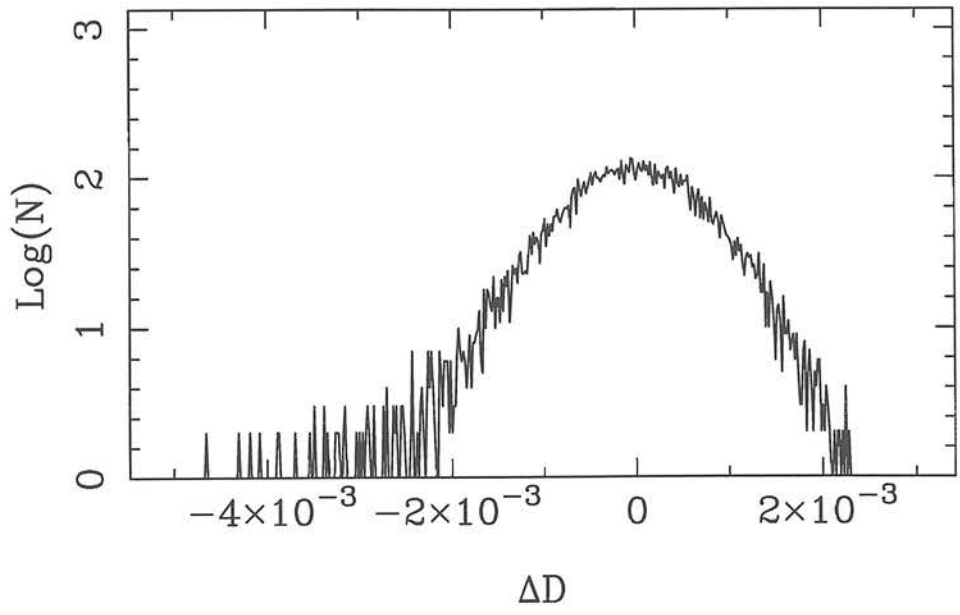

Figure 4.22: Median image rejection histogram

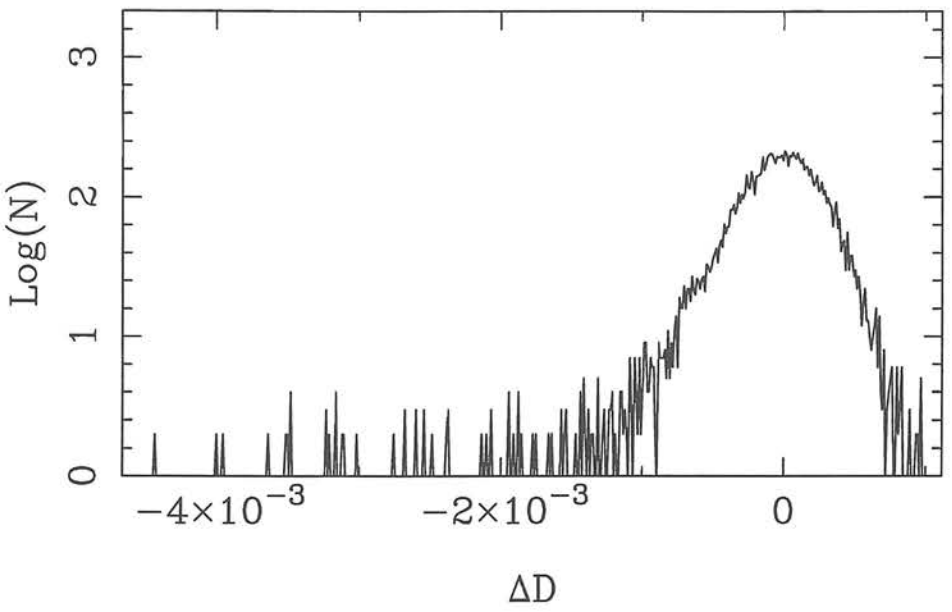

Figure 4.23: Minmax rejection histogram.

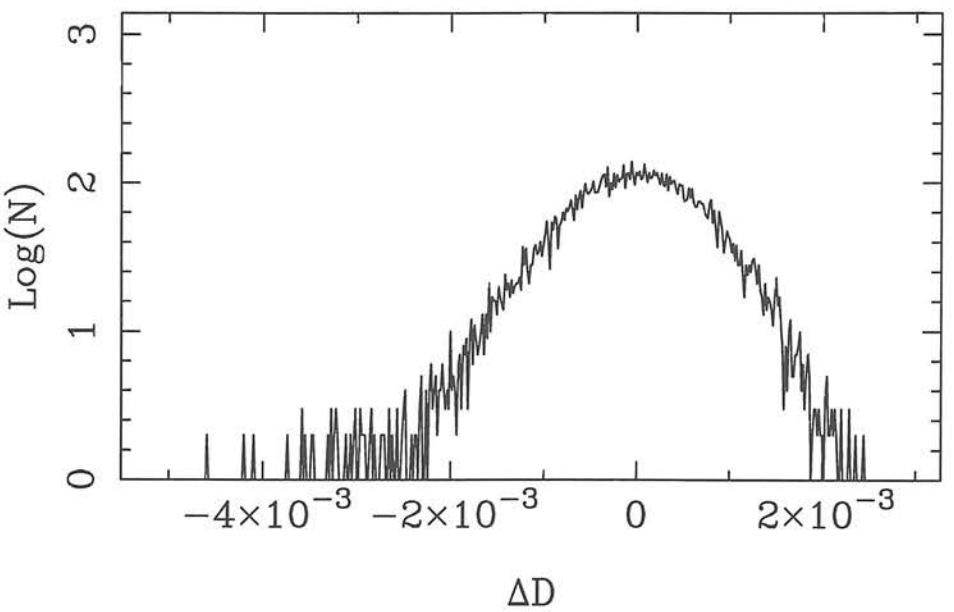

Figure 4.24: Tukey's biweight rejection histogram.

The validity of the weighting algorithm has been confirmed by the two plate stacking experiment. Figure 4.19 shows a broad maximum on the weighting axis providing optimum stack signal to noise, which the algorithm locates successfully.

Table 4.3 appears to indicate that near optimal signal to noise is obtainable by a simple no weighting stacking procedure. This will generally be true if, as in this paper, one is working with a universally high quality plate collection. It should be emphasised however that weighting becomes increasingly important for more heterogenous plate material, where a single low quality plate added at equal weight can seriously compromise stack quality.

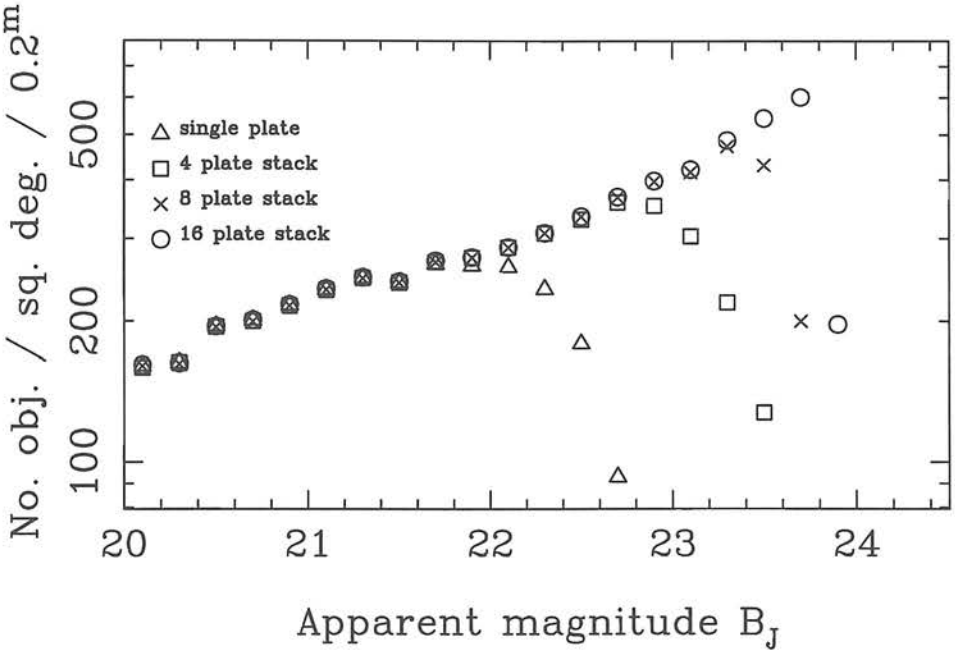

Figure 4.25: Number counts vs. magnitude for various stacks, all with weighting but no rejection

Finally, the question of the increase in depth attainable by stacking plates is addressed. Assuming Poissonian counting errors, the signal to noise should go as $n^{\frac{1}{2}}$ for identical plates, and therefore the increase in limiting magnitude will be $2.5 \log_{10} n^{\frac{1}{2}}$. Figure 4.25 was kindly produced by Nigel Hambly, and shows number-magnitude counts for a single plate, and also a 4,8 and 16 plate stack. Taking the 100% completeness limit to be the point at which a given number-magnitude count turns over, the single plate reaches $B_J \sim 22$. This is around 0.5 magnitudes brighter than the nominal 'limiting magnitude' quoted in

the UKSTU handbook (Tritton 1983). Following an $n^{\frac{1}{2}}$ law, the 4,8 and 16 plate stack limits should be $B_J^4 \sim 22.8$, $B_J^8 \sim 23.1$, $B_J^{16} \sim 23.5$ respectively. This in good agreement with the Figure 4.25, given that the 16 plates in question are not identical in terms of their signal to noise ratios (eg. see the relative plate weights in Table 4.2.)

4.6 Conclusion

The use of any pixel rejection algorithm leads to reduction in signal to noise in faint images in the resultant stack. Thus pixel rejection should only be used in applications where spurious images are likely to pose a serious problem. In addition, while all rejection algorithms tend to work reasonably effectively for a stack of many plates, there is little need for pixel rejection in large stacks since a deviant point in one plate is unlikely to be significant when averaged into all the other plate data.

The prime motivation for stacking digitised Schmidt plates is to detect faint objects over a wide field of view. The plate stacking regime described here optimises the signal to noise ratio in faint objects by analysing the noise characteristics of each plate and weighting them accordingly. These weights used in conjunction with an 'average sigma clipping' bad pixel rejection algorithm yield a stacked image of near-optimal depth and free of spurious contaminant images. The gain in depth is found to be in accordance with the expected $\Delta M \sim 2.5 \log_{10} n^{\frac{1}{2}}$ law.

Chapter 5

Cool White Dwarf Survey

5.1 Introduction

A survey utilising reduced proper motions requires photometric magnitudes in at least 2 passbands and proper motion measures. Since each object included in the survey sample must fall inside all survey detection limit criteria, it is important to extend the survey limits as far as possible to maximise the final sample size.

The implications of adopting a particular survey limit may be appreciated by considering the effects they have on the distance to which cool degenerates can be detected. A $0.6M_{\odot}$ CWD with hydrogen atmosphere and an effective temperature of 4000K is predicted to have absolute magnitudes of $\sim$ 17 and $\sim$ 15.5 in the B and R passbands respectively (Bergeron, Wesemael & Beauchamp 1995). Assuming a modest tangential velocity of $V_T = 50$ km s^{-1}, the limiting distances imposed on a survey for such objects by the two photometric limits and one proper motion limit may be calculated. For illustrative purposes some results from the following Chapter are anticipated here, and the maximum distance observable as a function of the absolute magnitude of the objects sought is plotted in Figure 5.1 for photometric limits of 22.5 (dot-dash), 21.2 (dotted) and 19.0 (dashed). Horizontal lines denote maximum distances imposed by proper motion limits assuming $V_T = 50$ km s^{-1}, which are obviously independent of object absolute magnitude. The 22.5 and 21.2 photometric limit curves denote the B and R limits for this work, while the 19.0

curve is the quoted magnitude limit for the LDM survey sample.

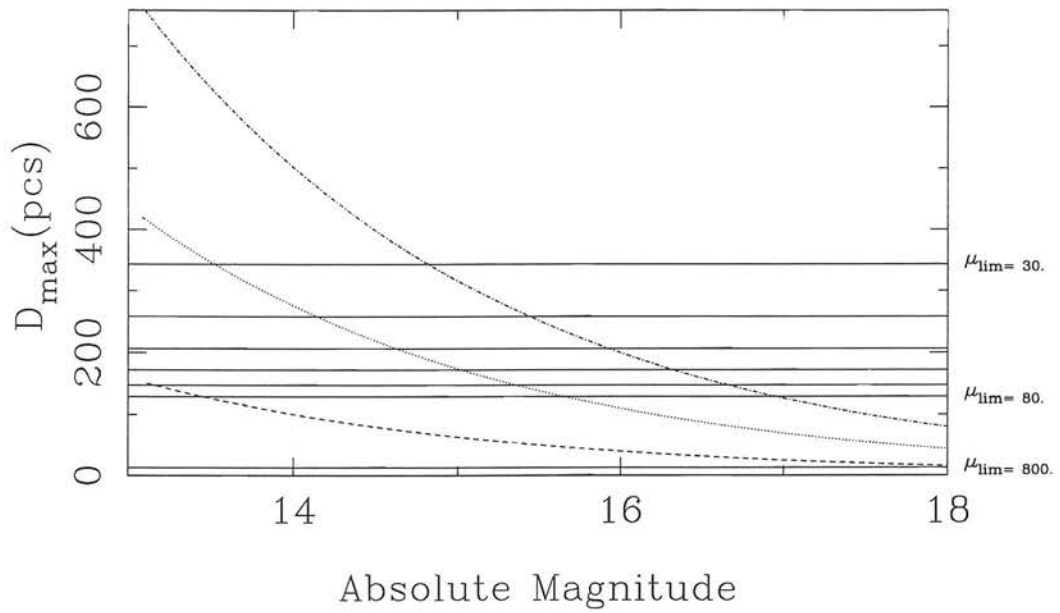

Figure 5.1: The maximum object detection distances imposed by various survey limits as a function of absolute magnitude of survey object. Dotted line: apparent magnitude limit of 21.2, dot-dash line: apparent magnitude limit of 22.5, dashed line: apparent magnitude limit of 19.0, full horizontal lines: proper motion limits assuming survey object with V_T = 50 km s^{-1}; the 800, 80 and 30 mas yr^{-1}limit lines are labelled.

It may be seen from Figure 5.1 that the LDM survey, with a proper motion limit of 0.″8 yr^{-1} and V magnitude limit of 19.0, is always proper motion limited for stars with V_T = 50 km s^{-1} and absolute magnitude smaller than 18. Of course the proper motion detection limit increases linearly with a stars' tangential velocity, although 50 km s^{-1} marks the approximate peak of the V_T distribution and substantially higher velocity stars are rare (Sion et al. 1988). The proper motion limit imposed is $\sim$ 13 pc, which corresponds to a survey volume of 4600pc^3 assuming half the sky was covered. It is interesting to compare the volume surveyed by LDM for faint degenerates to the volume available to this survey. For the 4000K CWD described above, it may be seen from Figure 5.1 that it is the R magnitude limit at M_R = 15.5 which defines the limiting distance for detecting such objects, unless the proper motion limit is greater than $\sim$ 80 mas yr^{-1}. Using the R photometric limit, the limiting distance is $\sim$ 140 pc. If the extent of the survey field

is defined by eg. the most northerly object being found on at least 15 of the 20 stacks in both the B and R datasets, then the solid angle of the field surveyed is found to be 0.0086 steradians. The volume surveyed for the 4000K CWDs can then be calculated to be $\sim 7500\mathrm{pc}^3$. So, despite surveying over 700 times the sky area of a survey which goes approximately two magnitudes deeper and detects proper motions an order of magnitude smaller; LDM samples 40% less volume when searching for 4000K CWDs.

From the above discussion it is clear that great gains in surveyed volume can be made by extending survey limits, and that therefore every effort should be made to do so. Also, given that the proper motion limit will be in the region of a several tens of mas yr^{-1}, Figure 5.1 indicates that the limiting distances defined by the proper motion and photometric limits for CWDs are approximately equal. It is therefore important to extend every survey limit as far as possible to maximise the final sample size, although since the photometric limits are essentially defined by the plate material the only real control over them is to alter the stacking scheme. To fully exploit the deep stacks then, it is desirable to use a low proper motion limit. Unfortunately the RPMD method of population discrimination is rather sensitive to contamination by spurious proper motions, and it is therefore worthwhile being very careful about the exact survey proper motion limit used.

5.2 Photometric Survey Limits

Neglecting interstellar absorption and Disk scale height effects, stellar number counts should vary with magnitude according to the relation

$$\log N(m) = 0.6m + c \tag{5.1}$$

(Mihalas and Binney 1981). Logarithmic number count plots from this survey data do indeed increase linearly with increasing magnitude, as shown for the R data in Figure 5.2 , before dropping precipitously. This cut-off is attributed to the survey detection limit, and the position of the turnover is used to determine photometric survey limits. The limits used are 21.2 in R and 22.5 in B.

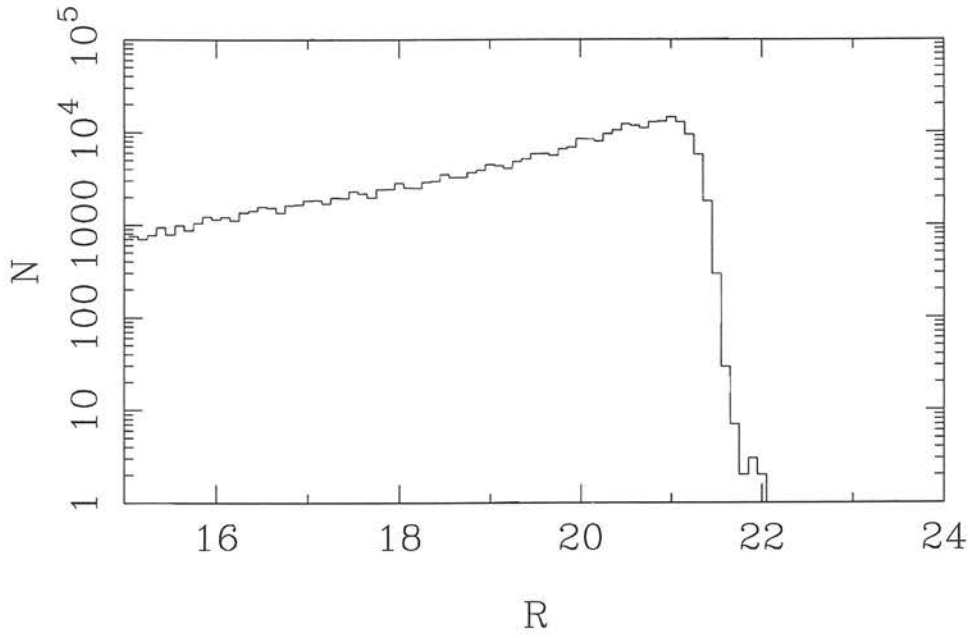

Figure 5.2: Number counts as a function of apparent R magnitude

5.3 The Survey Proper Motion Limit

Proper motions have been calculated for every object detected in the field as described in Section 3.6. Most objects in the field however will have proper motions significantly smaller than the positional accuracy of our data, and are effectively 'zero proper motion objects' (a brief discussion regarding the justifiability this assumption is given at the end of Section 5.3.2). The obvious way of extracting real motions from the survey sample would be by accepting only objects with motions deviating from zero by more than eg. $5\sigma_\mu$. Unfortunately this method would lead to complications later when calculating space densities, for which universal survey limits are desirable. The task in defining a survey proper motion limit is to maximise the sample size while keeping contamination from spurious proper motions to an acceptable level. What constitutes an 'acceptable level' is a difficult question, and will be addressed in detail in this section. Two points are clear from the outset: first, since the positional errors are a function of magnitude the proper motion limit should also be investigated as a function of magnitude; secondly, the extent of contamination arising from random measurement errors will rise in some way, governed

by these errors as the proper motion limit is lowered.

5.3.1 A Survey Proper Motion Limit from error Distribution Analysis

In this section the characteristics of the 'noise' in the proper motion distribution is analysed by assuming all objects are 'zero proper motion objects' and the calculated proper motions arise purely from random measurement error. The 'true' values of μ_x and μ_y measured by linear regression are therefore zero, and the random measurement errors give rise to a normal error distribution in μ_x and μ_y about zero. We are of course interested in the total proper motion,

$$\mu = \sqrt{{\mu_x}^2 + {\mu_y}^2} \tag{5.2}$$

and its distribution. Transforming from $P(\mu_x, \mu_y)$ (where $P(\mu_x)$ and $P(\mu_y)$ are normal distributions with common σ) to $P(\mu, \phi)$ using the Jacobian, such that

$$P(\mu_x, \mu_y) = P(\mu, \phi)\frac{1}{|J|} \tag{5.3}$$

where

$$J = \frac{\partial(\mu_x, \mu_y)}{\partial(\mu, \phi)} = \begin{vmatrix} \frac{\partial \mu_x}{\partial \mu} & \frac{\partial \mu_x}{\partial \phi} \\ \frac{\partial \mu_y}{\partial \mu} & \frac{\partial \mu_y}{\partial \phi} \end{vmatrix} = \mu, \tag{5.4}$$

(using $\mu_x = \mu cos(\phi)$ and $\mu_y = \mu sin(\phi)$) the total proper motion is found to follow a Rayleigh distribution of form

$$P(\mu) = \frac{\mu}{\sigma^2} e^{-\frac{\mu^2}{2\sigma^2}}. \tag{5.5}$$

This survey utilises two independent measures of proper motion in the same field, one from the stacks of B_J plates and the other from the R stacks. A useful means of reducing the final proper motion survey limit will be to compare these two measures and reject inconsistent motions. Comparison of independent measures of proper motion needs to be incorporated into this analysis if it is to be useful in predicting sample contamination later. The measured B_J and R motions and their associated error distributions are therefore characterised

$$P(\mu_b) = A_b \mu_b e^{-C_b \mu_b^2} \tag{5.6}$$

and

$$P(\mu_r) = A_r \mu_r e^{-C_r {\mu_r}^2} \tag{5.7}$$

respectively. The algorithm used to select sample objects on the basis of proper motions

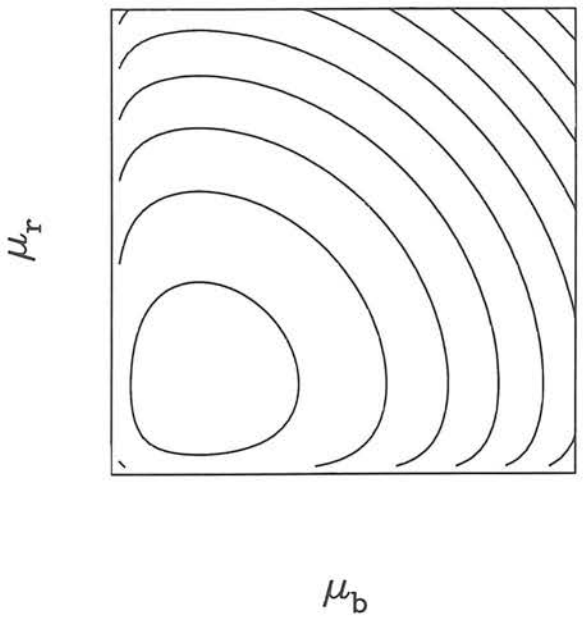

Figure 5.3: The form of the $P(\mu_b)P(\mu_r)$ distribution.

will use three sequential cuts to eliminate spurious motions. Firstly, the averaged proper motion must exceed the proper motion limit μ_{lim}, ie:

$$\frac{\mu_r + \mu_b}{2} > \mu_{lim}. \tag{5.8}$$

Secondly, the difference in proper motion must not exceed a second survey parameter $(\Delta\mu)$:

$$|\mu_b - \mu_r| < (\Delta\mu), \tag{5.9}$$

and finally the difference in position angle must not exceed a third survey parameter $(\Delta\phi)$:

$$|\phi_j - \phi_r| < (\Delta\phi). \tag{5.10}$$

An object must satisfy all three of these criteria to be included in the sample. The desired outcome of this analysis is the ability to predict the expected contamination from spurious motions for a survey with parameters μ_{lim}, $(\Delta\mu)$and $(\Delta\phi)$ given the 'zero proper motion object' error distribution can be described by equations 5.6 and 5.7. In order to do this we consider the combined probability distribution $P(\mu_b)P(\mu_r)$ on the μ_b– μ_r plane, which will in general look like Figure 5.3 with a maximum corresponding to the peaks in the $P(\mu_b)$ and $P(\mu_r)$ distributions. The survey criteria described above effectively limit

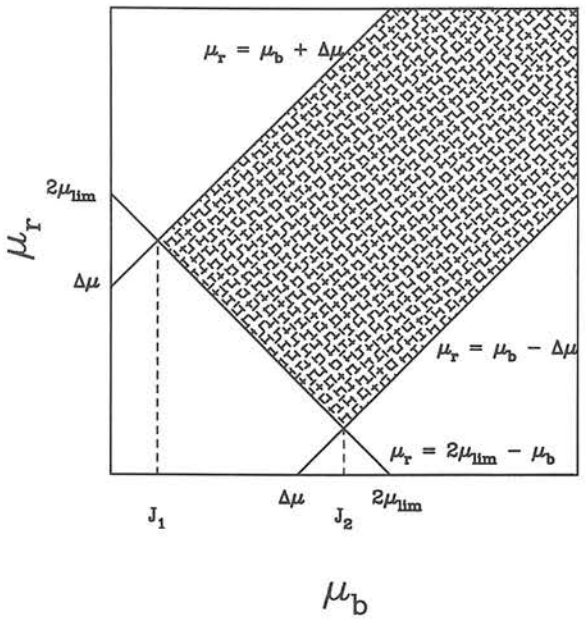

Figure 5.4: Objects will only be selected for the survey sample if their proper motions lie in the hatched region of the diagram.

the selected sample to a specific area on the μ_b– μ_r plane, shown in Figure 5.4. Given a realistic estimate of the (normalised) $P(\mu_b)$ and $P(\mu_r)$ distributions an integration over the hatched region is Figure 5.4 yields an estimate for the fraction of objects, X, belonging to the error distribution likely to contaminate the sample. The integral

$$X = \int_{J_1}^{J_2} \int_{2\mu_{lim}-\mu_b}^{\mu_b+(\Delta\mu)} P(\mu_b)P(\mu_r)d\mu_r d\mu_b + \int_{J_2}^{\infty} \int_{2\mu_b-(\Delta\mu)}^{\mu_b+(\Delta\mu)} P(\mu_b)P(\mu_r)d\mu_r d\mu_b \qquad (5.11)$$

where

$$J_1 = \frac{2\mu_{lim} - (\Delta\mu)}{2} \qquad (5.12)$$

and

$$J_2 = \frac{2\mu_{lim} + (\Delta\mu)}{2} \qquad (5.13)$$

is easily calculated numerically for arbitrary $\mu_{lim}$and $(\Delta\mu)$. Since this analysis concerns zero proper motion objects whose spurious motion arises purely from machine measurement error, we may assume no preferred position angle, and the resulting fraction X will be cut by a further $(2(\Delta\phi))/360$ ($(\Delta\phi)$in degrees) by the position angle selection criterion, ie.

$$X_{final} = \frac{X}{2(\Delta\phi))/360}. \qquad (5.14)$$

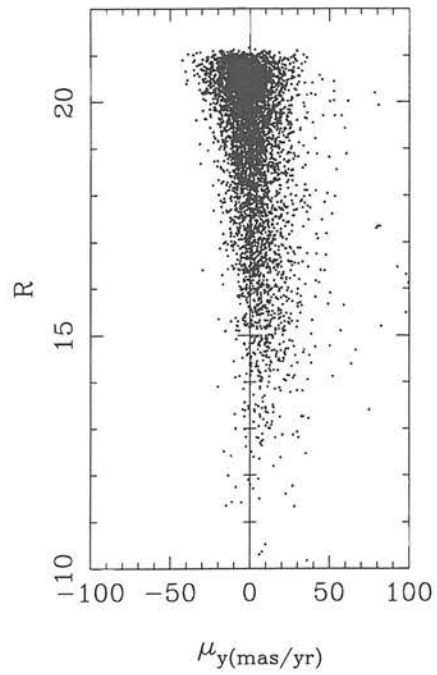

Figure 5.5: A scatter plot of the y component of $\mu_r$as a function of R magnitude taken from the centre of the R field.

The calculation described above requires knowledge of the P(μ_b) and P(μ_r) 'zero proper motion' error distributions. A dot plot of μ_y as a function of magnitude in Figure 5.5 again illustrates both the changing width of the distribution with magnitude and the off zero shift mentioned in discussing Figure 3.5. The existence of this zero point offset in the proper motions as a function of magnitude adds seriously to the complexity of the analysis described above. However, since the deviations from zero are small and absolute astrometry is not required here the deviations from zero can be removed (and added back on later if desired). Having shifted the motions in x and y into distributions centred on zero they can now be added according to equation 5.2. If equation 5.11 is to be used to calculate numbers of contaminants it is important that $P(\mu_b)$ and $P(\mu_r)$ can be simultaneously rescaled from normalised distributions. The B and R data are therefore paired so that $P(\mu_b)$ and $P(\mu_r)$ contain the same objects and thus the same number of objects. This pairing procedure also allows the implementation of object rejection on the basis of eg. magnitude or number of stacks on which the object is found. The distribution of measures of μ_r is shown in Figure 5.6. For the purposes of this analysis

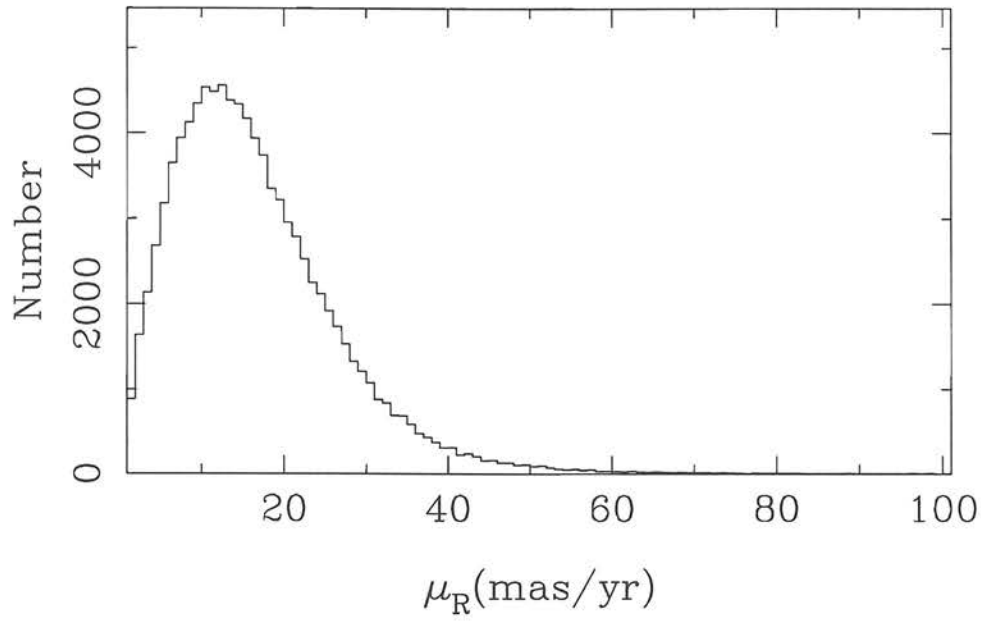

Figure 5.6: The distribution of measured $\mu_r$for objects with $R > 20$ and found on at least 15 stacks.

this proper motion data is thought of as consisting of two distinct distributions: the 'zero proper motion object' error distribution, on which a distribution of real proper motions is superposed. Any attempt to determine the error distribution from measured distribution must use only the low proper motion data where the random errors of interest dominate systematics introduced by real proper motions. In the example to be shown here the first 15 bins (1 mas yr^{-1}bins) of the normalised μ_r distribution in Figure 5.6 is taken to be representative of the error distribution. These 15 data points are fitted with an assumed error distribution like equation 5.7, with a similar procedure adopted for the B_J data. These fits are shown along with the measured data in Figure 5.7, with the real data rising above the error fits representing real proper motions. Since the error distributions exclude real motions they must be renormalised before use in equation 5.11. The rescaling factor to be used in calculating numbers of contaminants is taken to be the number of objects contained in the error distributions. This number will in general be different for the B_J and R data, so the average is used. Numerical methods can now be used to predict the number of contaminant spurious proper motions for a range of μ_{lim}, $(\Delta\mu)$ and $(\Delta\phi)$ using equations 5.11 and 5.14. The result of a series of calculations is shown in Figure 5.8. The predicted contamination falls rapidly below one object as μ_{lim} exceeds

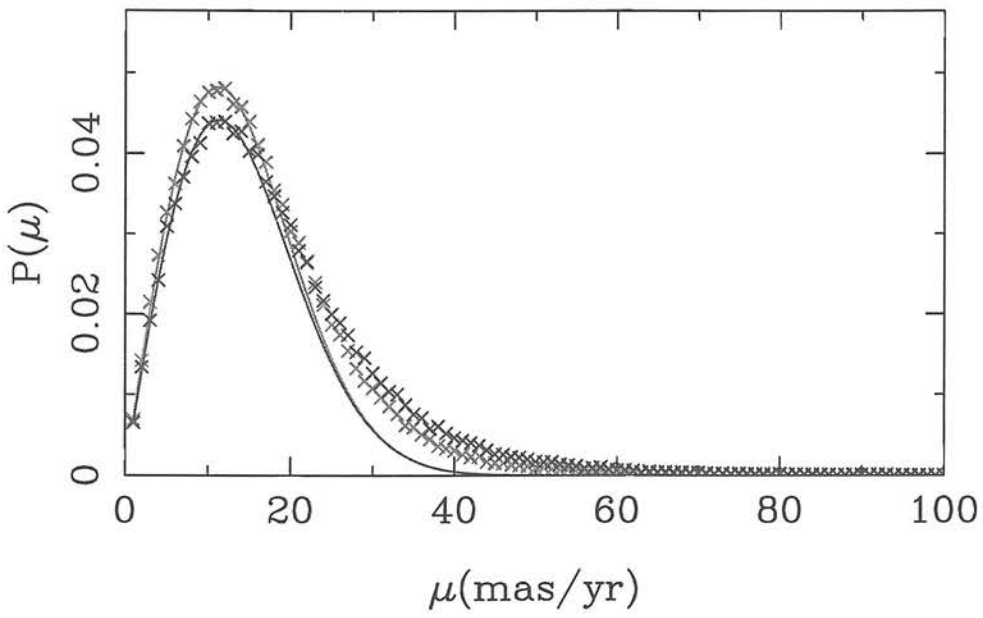

Figure 5.7: Normalised B_J (dark line and crosses) and R (grey line and crosses) measured data(crosses) and fitted error distributions (lines). This example uses the first 15 data points to determine the error distribution.

$\sim$ 42 mas yr^{-1}. Care must be taken however that the error distributions are not overly sensitive to the number of points in the measured μ_b and μ_r distributions used in their calculation. The error distributions were therefore recalculated using the first 30 bins in the measured μ_b and μ_r distribution (see Figure 5.9) and the predicted contamination plot redrawn using these new distributions (Figure 5.10). The separate predictions from the two calculations of the μ_{lim} at which the survey contamination drops to below 1 object are consistent to within $\sim$ 3 mas yr^{-1}. Presented in Table 5.1 are the results of calculating the μ_{lim} at which the predicted number of contaminant objects falls below one for a range of magnitude cuts, $(\Delta\mu)$ and derived $P(\mu_b), P(\mu_r)$ distributions. Table 5.1 indicates that the $(\Delta\mu)$ survey parameter has a small bearing on the μ_{lim} where $N_{contam} \sim 1$. The $(\Delta\mu)$ criterion can therefore be relaxed substantially to ensure no real motions are rejected. A similar argument is applicable to the $(\Delta\phi)$ parameter, where the small advantage gained by tightening the $(\Delta\phi)$ criterion again becomes increasingly outweighed by the potential for rejection of real proper motions. The variation in calculated μ_{lim} as a function of magnitude is certainly measurable, but is not pronounced enough to warrant a further sub-

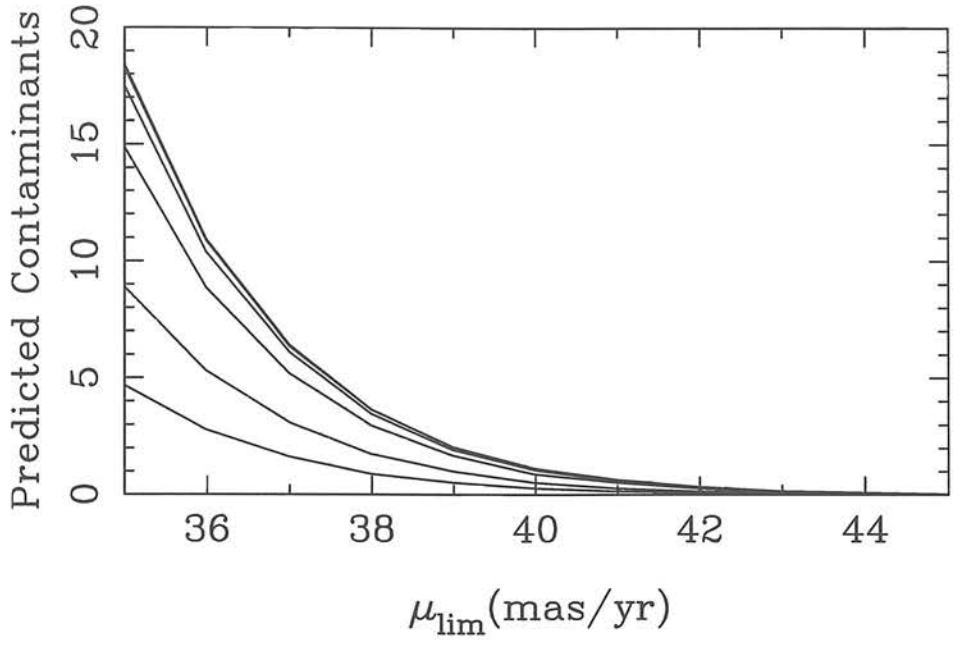

Figure 5.8: The results of numerical integration predicting the number of contaminant objects in the survey sample as a function of survey proper motion limit. The lower of the lines used a $(\Delta\mu)$ of 5 mas/yr, with $(\Delta\mu)$ rising to 50 mas/yr for the top line ($(\Delta\phi)$ was set to 90 throughout). These calculations were based on error distributions determined from the first 15 proper motion bins of the measured μ_b and μ_r distributions.

division of the sample by magnitude since the existing bins seem to characterise Figure 5.5 reasonably well, and repeated reduction of bin size will lead to increasingly noisy μ_r, μ_b distributions and less reliable estimates of the $P(\mu_b)$, $P(\mu_r)$ error distributions. Any estimate of $P(\mu_b)$ and $P(\mu_r)$ from the measured proper motion distributions is affected by the existence of real proper motions, the action of which is to increase the predicted distribution at high μ. Thus in the absence of contamination arising from non-normally distributed errors, the values calculated in Table 5.1 could be thought of as conservative estimates of μ_{lim}.

5.3.2 An Estimate of Proper Motion Limit from Number Counts

If the assumption is made that there is an inverse correlation between distance and proper motion, a simple estimate of expected number counts as a function of proper motion can

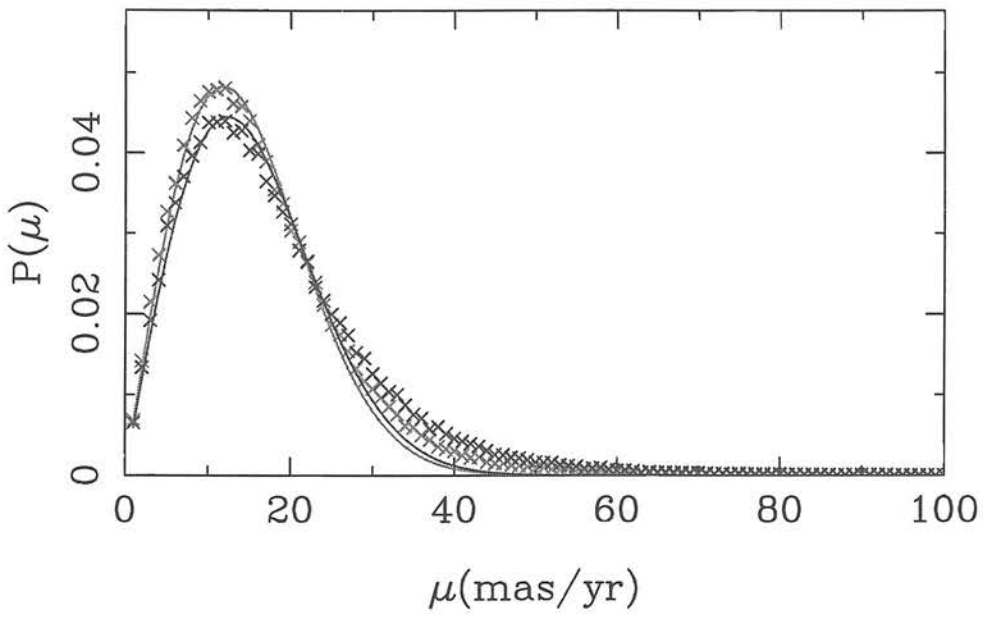

Figure 5.9: Normalised B_J (dark line and crosses) and R (grey line and crosses) measured data (crosses) and fitted error distributions (lines). Here the first 30 data points to determine the error distribution.

be made. If the local disk has a constant stellar density, n, the number of stars, $\sum$N, counted out to a given distance, d, for a survey covering Ω steradians is

$$\sum N = \frac{\Omega}{4\pi}\frac{4}{3}\pi d^3 n \tag{5.15}$$

or

$$\log \sum N \propto -3 \log \mu \tag{5.16}$$

A plot of log cumulative number count (from large to small μ) versus log μ should therefore be a straight line of gradient -3 in this idealised situation. In principle a proper motion limit for this survey could be obtained by determining the point at which our measured proper motions deviate from this relation due to the existence of spurious motions. In Figure 5.11 the cumulative number counts are plotted as a histogram. If the points between $\log \mu = 1.9$ and $\log \mu = 2.5$ are fit with a straight line the resulting gradient is (-2.998 ± 0.071), in excellent agreement with the idealised predicted slope of -3. The fit is shown as a dashed line. This finding compares favourably with a similar analysis of Luyten (1969, 1974, 1979) and Giclas (1971, 1978) common proper motion binary stars, which on an analogous plot describe a straight line of significantly shallower gradient that the

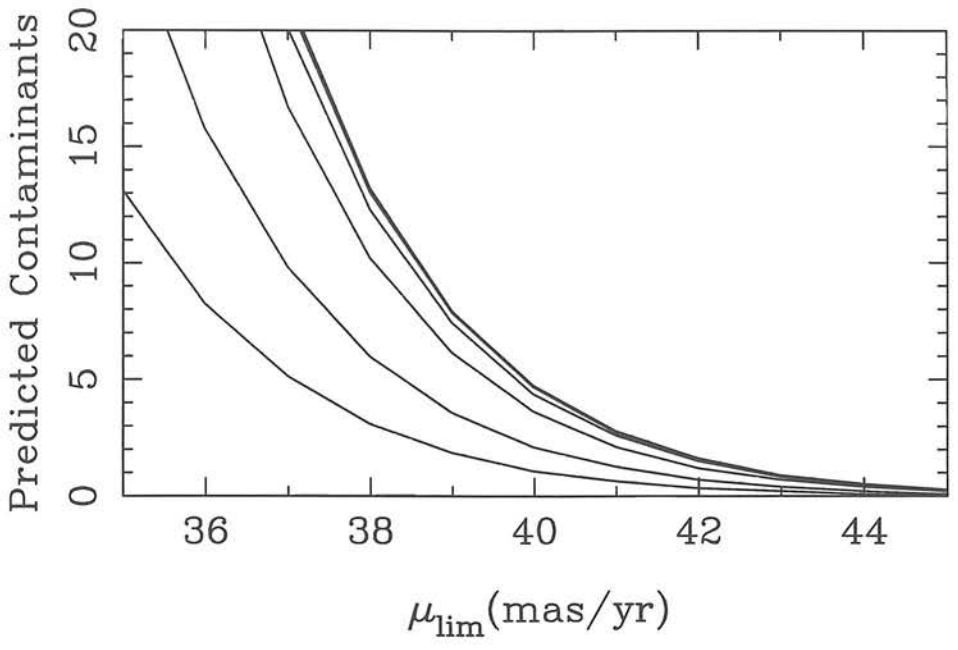

Figure 5.10: An equivalent plot to Figure 5.8 using error distributions calculated using 30 measured μ bins rather than 15

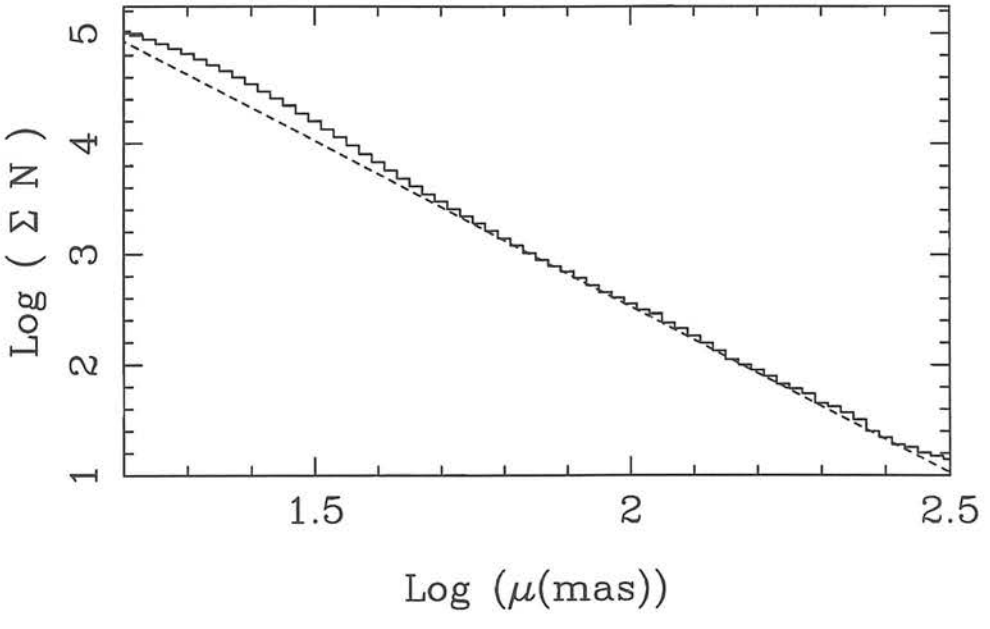

Figure 5.11: Cumulative number counts plot showing deviation from simple model at $\mu \sim 50$ mas yr^{-1}.

R magnitude cut	No. of μ_b,μ_r data points used	μ_{lim}(mas/yr) for varying ($\Delta\mu$)			
		($\Delta\mu$)=5	($\Delta\mu$)=10	($\Delta\mu$)=30	($\Delta\mu$)=50
$R > 20.5$	15	40	41	42	43
	25	41	43	44	44
$20.5 > R > 20$	15	34	35	36	36
	25	34	35	36	36
$20 > R > 17$	15	30	31	32	32
	22	32	33	33	33
$R < 17$	15	31	32	33	33
	25	34	35	36	36

Table 5.1: Calculated μ_{lim} where predicted number of contaminants falls below 1 object. Column two represents the number of bins in the measured μ_b and μ_r distributions used to derive the $P(\mu_b)$, $P(\mu_r)$ distributions.

expected -3 indicating increasing incompleteness with decreasing proper motion (Oswalt & Smith 1995).

Towards lower proper motions the data rises above the line, indicating the onset of contamination at $\mu \sim 50$ mas yr^{-1}, lending credence to the findings of the previous analysis. Specifically, Figure 5.11 contains evidence that the assumption made in the previous analysis – that objects with small (< 25 mas yr^{-1}) should have proper motion estimates dominated by the measurement errors – is justified. The excess of objects with respect to the line arises because objects of small real motion, the 'zero proper motion' objects, have larger proper motion estimates caused by the machine error. Indeed, even for brighter (and therefore presumably closer) stars, 66% are expected to have proper motion less than 10 mas yr^{-1} (Chiu 1980). Inspection of Figure 5.6 shows clearly that the large majority of stars have measured proper motion greater than 10 mas yr^{-1} due to measurement errors.

5.3.3 Proper Motions Limits and the Reduced Proper Motion Diagram

The RPMD is, for all sample objects lacking follow up observations, the sole means of stellar population discrimination. For this reason it is worthwhile inspecting the RPMD of samples produced using various survey limits. The principle concern is that the white

dwarf locus be as distinct as possible at all colours while maximising the sample size.

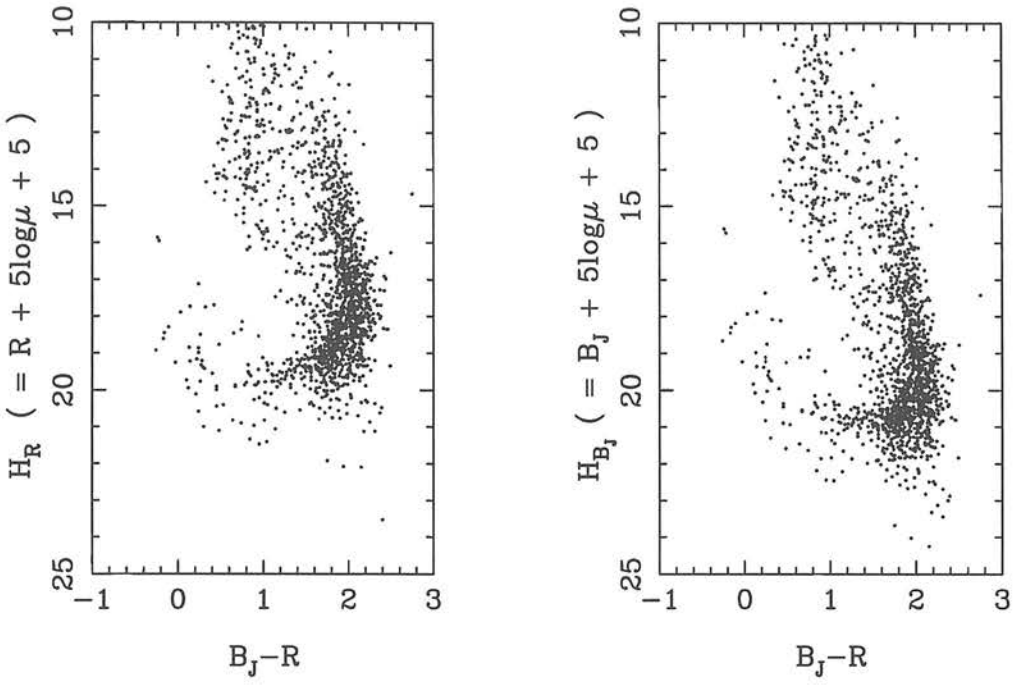

Figure 5.12: A RPMD of a sample with μ_{lim}= 50 mas yr^{-1} for all objects.

It can be argued that there is little purpose in lowering μ_{lim} for bright objects to anything near the level of potential contamination. Consider searching for an intrinsically faint star such as a reasonably cool white dwarf, with an absolute R magnitude of $\sim$ 14, amongst survey objects with apparent R magnitudes as faint as $\sim$ 19. Such an object, having a (conservative, LDM) tangential velocity of 40km/s, would have a proper motion of $\sim$ 80 mas yr^{-1} – well beyond the predicted contamination limit. This argument becomes even more forceful for both intrinsically fainter and apparently brighter objects, implying that a prudent μ_{lim} is desirable for all but the faintest survey objects[1].

Only for the faintest objects is the survey truly proper motion limited. For example, Figure 5.1 demonstrates which limits are important for an object with the faintest possible apparent B_J and R magnitudes at varying absolute magnitudes. It is in this faint regime that the lowest possible μ_{lim} is desired.

Figure 5.12 is a RPMD produced with a μ_{lim} of 50 mas yr^{-1} at every magnitude. The

[1]This argument is equivalent to lowering the surveys photometric limits in Figure 5.1

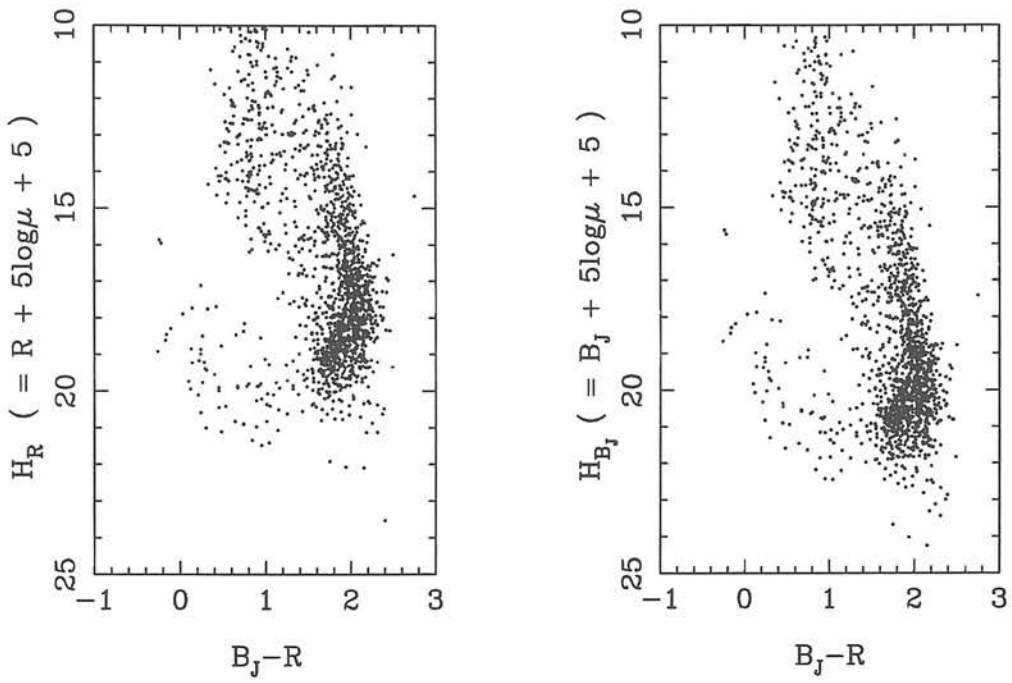

Figure 5.13: A RPMD of a sample with μ_{lim}= 50 mas yr^{-1} for objects with $R < 20.5$ and μ_{lim}= 60 mas yr^{-1} for fainter objects.

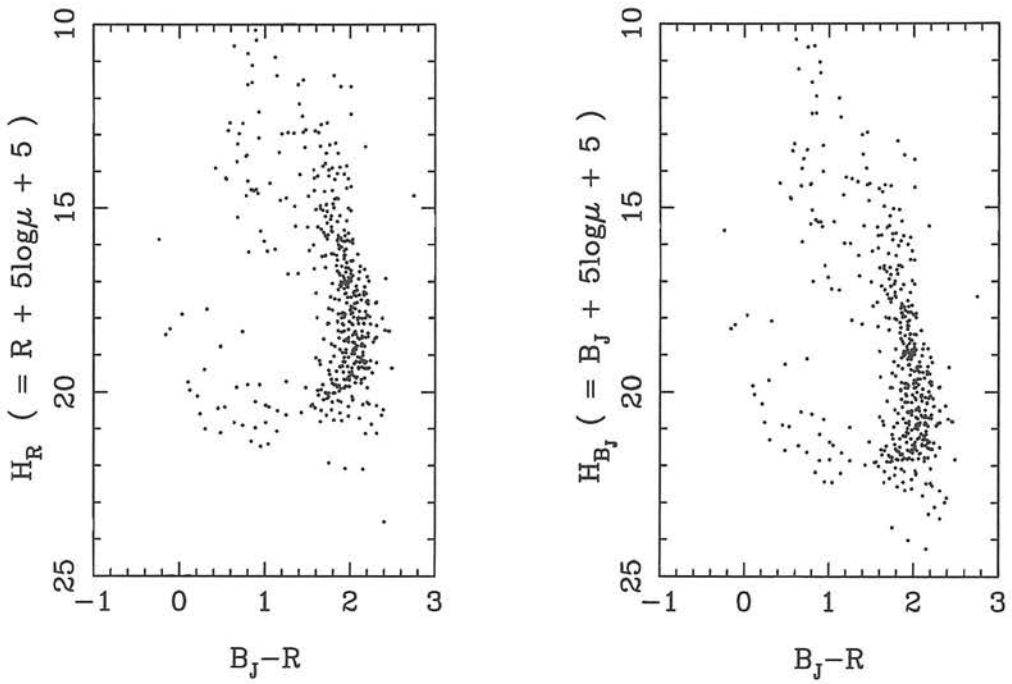

Figure 5.14: A RPMD of a sample with μ_{lim}= 80 mas yr^{-1} for all objects.

main sequence and white dwarf loci are visible, as is a dense group of objects between the two at $H_R \sim 19.5$. This group of objects probably consists of two groups. Firstly of course, the most likely sample contaminant is a faint object creeping through just over the proper motion limit just at this point. Secondly, one would expect a large population of objects to lie on the RPMD where the μ and R distributions are most populated , ie. at μ_{lim} and at faint R (an object with $\mu = 50$ mas yr^{-1} and $R = 21$ has $H_R = 19.5$), and it should therefore not be automatically assumed that every object lying at this point in the RPMD is suspect. A cause for concern however, is the way this population bridges the gap between the main sequence and the white dwarf population, a property one would expect from a contaminant locus rather than the detection of bona fide proper motions. If a more conservative limit of μ_{lim}= 60 mas yr^{-1} is adopted for objects with $R > 20.5$ the RPMD (Figure 5.13) looks more promising, with the 'contaminant locus' all but gone, leaving only the expected mild confusion (Evans 1992) between populations at their faint extremity. The adoption of an extremely conservative μ_{lim} of 80 mas yr^{-1} for all objects leads to an even more well defined RPMD (Figure 5.14), where the white dwarf population discrimination is almost without exception unambiguous.

5.4 White Dwarf Sample Selection

The survey parameters to be used to select the preliminary sample (ie. a sample subject to further object by object scrutiny and potential rejection, with the possibility of further objects being included the sample which lie just outside the RPM cut on one or both RPMDs) have been chosen with reference to the findings of Section 5.3. Sections 5.3.2 and 5.3.1 suggest a $\mu_{lim}$of 50 mas/yr, a ($\Delta\mu$)of 50 mas yr^{-1}and a ($\Delta\phi$)of 90 degrees should essentially eliminate contamination arising from normally distributed measurement errors. It was found, however, that the white dwarf locus is insufficiently distinct in the RPMD obtained using these survey parameters. A slight restriction of $\mu_{lim}$for objects with $R \geq 20.5$ does much to solve the population discrimination problem. Therefore the survey parameters given above, with the exception of a $\mu_{lim}$of 60 mas yr^{-1} for object with $R \geq 20.5$, appears to be an acceptable compromise between sample maximisation and potential contamination and population discrimination problems.

The RPM can be expressed in terms of tangential velocity ,V_T, and absolute magnitude, M :

$$H = M + 5\log_{10} V_T - 3.379. \tag{5.17}$$

Evans (1992) has produced theoretical RPMDs by using expected $5\log_{10} V_T$ distributions and absolute magnitude - colour relations for various populations. Although these theoretical predictions were made for specific fields and incorporated error estimates peculiar to that work, they serve as a useful guide to the expected distribution of stellar populations on the RPMD. The RPMD white dwarf population locus is found to be an unambiguous population discriminator for all colours bluewards of $(O-E) \sim 1.8$, with an increasing chance of contamination from the spheroid main sequence population redwards of this colour. Transforming from (O-R) to (B-R) (Evans, 1989 - equation 13), spheroid population contamination should become a problem redwards of $(B-R) \sim 1.6$ which in turn corresponds to $(B_J - R) \sim 1.2$. Indeed on inspection of Figure 5.13, the white dwarf locus does begin to become confused at this colour. This contamination occurs solely from the direction of small RPM, and the RPMD can still be used with some confidence as a population discriminator for objects with high measured RPM redwards of $(B_J - R) \sim 1.2$. In order to accommodate these contamination considerations, the preliminary survey white dwarf sample is defined as those objects bluewards (in both plots) of the lines in Figure 5.15. The lines cut the top of the white dwarf locus at $(B_J - R) \sim 1.2$ but allow slightly redder objects with higher RPMs into the sample. The white dwarf locus is unambiguous bluewards of $(B_J - R) \sim 1.2$.

Every object in the sample must appear in at least 15 stacks in each passband. The positional data as a function of time have been scrutinised for every object selected as a white dwarf candidate, and those with dubious motions rejected. While such a process may seem rather arbitrary, it was necessary to incorporate this screening stage in the sample extraction because simple automated rejection algorithms such as the 3σ rejection routine used here cannot be guaranteed to eliminate spurious motions. Some examples are shown in Figures 5.16 and 5.17. All three objects shown successfully satisfied all the survey criteria. The object plotted at the top of Figures 5.16 and 5.17 (KX27) shows a clear, genuine motion in both x and y in both passbands and was included in the final sample without hesitation. The middle object (KX18) has larger positional uncertainties and a smaller overall motion, but still shows consistent, smooth motions and was also

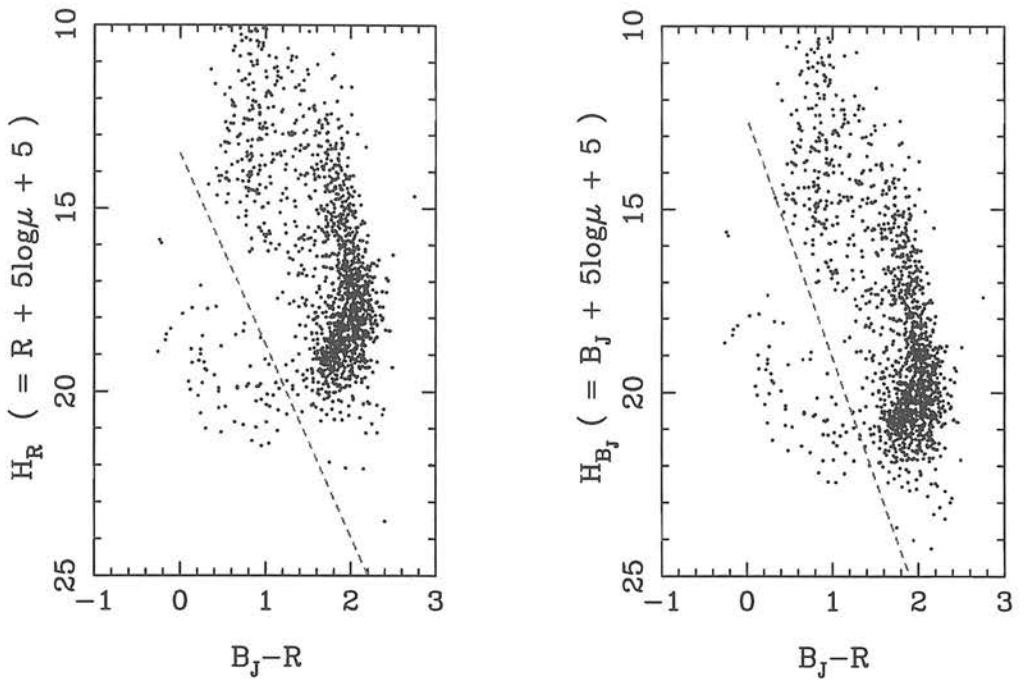

Figure 5.15: RPMD of the survey sample showing the white dwarf population divider used.

included. The final object shows evidence of large non-linear deviations in the last four epochs of the x measures in both passbands. Although the bad-point rejection algorithm has removed at least one datum from each x plot (as shown by the multiple straight line fits), this object shows no evidence of proper motion based on the first 16 data points and certainly cannot be considered a reliable proper motion object candidate. This object, along with 9 others, were rejected based on arguments such as these. While a procedure is unsatisfactory in terms of its lack of objectivity, it is certainly preferable to inclusion of such objects in the final sample, or the introduction of extremely stringent survey limits which would doubtless exclude genuinely interesting objects. The digitised images have also been inspected.

Object	RA(2000)	DEC(2000)	U	B	V	R	I	$\overline{\mu}$	$\overline{\phi}$
KX 1	21 16 9.3	-42 33 48	21.51	21.59	—	20.14	19.61	0.143	155
KX 2	21 17 37.1	-45 36 50	20.91	21.54	—	20.47	—	0.070	101
KX 3	21 17 39.2	-47 21 39	21.43	21.81	—	20.78	20.43	0.067	83
KX 4	21 18 31.1	-46 23 10	20.46	20.45	—	19.22	18.84	0.209	118
KX 5	21 19 23.0	-45 34 35	20.17	20.89	20.44	20.27	20.09	0.052	128
KX 6	21 19 20.7	-45 35 15	21.86	21.90	21.20	20.68	—	0.062	166
KX 7	21 19 18.1	-45 52 3	20.62	21.23	20.79	20.41	20.62	0.069	356

Object	RA(2000)	DEC(2000)	U	B	V	R	I	$\overline{\mu}$	$\overline{\phi}$
KX 8	21 19 6.9	-46 20 4	20.08	20.69	20.33	20.08	20.23	0.062	156
KX 9	21 20 59.1	-45 5 17	21.86	22.04	21.31	20.93	20.38	0.090	184
KX10	21 21 24.5	-43 35 0	22.42	22.34	21.41	20.86	20.80	0.070	73
KX11	21 20 54.0	-46 43 43	—	22.33	21.40	20.78	19.79	0.084	242
KX12	21 21 58.0	-43 8 18	20.64	21.18	20.35	19.76	18.62	0.054	146
KX13	21 22 9.3	-43 39 18	21.10	21.65	20.97	20.79	20.36	0.114	126
KX14	21 23 4.4	-45 26 15	—	22.23	21.25	20.69	20.09	0.222	139
KX15	21 23 19.7	-45 28 32	19.03	19.00	18.37	17.83	17.64	0.135	149
KX16	21 24 56.3	-43 26 53	20.66	21.18	20.52	20.06	19.79	0.087	246
KX17	21 25 4.4	-42 44 4	17.23	17.69	17.56	17.27	17.21	0.125	192
KX18	21 25 52.8	-42 40 31	20.00	20.61	20.14	20.02	19.85	0.068	119
KX19	21 25 49.6	-45 15 4	19.30	20.26	20.02	20.12	20.02	0.057	259
KX20	21 25 30.1	-46 30 37	15.44	16.21	16.12	16.32	16.32	0.080	107
KX21	21 26 20.0	-45 45 32	20.88	21.42	20.76	20.50	20.02	0.098	117
KX22	21 27 50.5	-42 28 39	19.97	20.46	—	19.59	19.52	0.085	156
KX23	21 28 3.6	-44 45 27	19.41	19.80	19.19	18.88	18.45	0.097	144
KX24	21 28 58.8	-43 2 16	20.53	20.60	19.80	19.17	19.02	0.055	222
KX25	21 29 28.1	-44 7 57	20.06	20.78	20.59	20.30	20.47	0.082	144
KX26	21 29 52.5	-45 19 49	21.37	21.44	20.73	20.09	19.90	0.086	159
KX27	21 30 5.9	-46 39 22	17.73	18.31	17.97	17.83	17.65	0.288	137
KX28	21 30 21.2	-43 54 47	20.50	21.12	20.72	20.56	20.60	0.127	215
KX29	21 31 11.8	-43 48 27	19.29	18.77	18.50	18.21	17.87	0.061	150
KX30	21 32 17.1	-46 44 9	22.40	22.04	21.22	20.58	20.29	0.144	71
KX31	21 32 54.7	-45 30 59	20.04	20.46	19.93	19.75	19.41	0.051	269
KX32	21 33 41.2	-43 42 47	16.97	17.51	17.45	17.45	17.50	0.050	285
KX33	21 35 8.4	-45 7 4	22.44	22.25	21.33	20.70	20.20	0.119	132
KX34	21 35 12.8	-44 36 27	17.41	17.89	17.56	17.30	16.97	0.126	289
KX35	21 35 32.9	-45 24 36	19.14	19.66	19.24	19.21	19.02	0.051	109
KX36	21 35 34.6	-46 23 6	20.19	20.84	20.51	20.32	19.89	0.113	125
KX37	21 35 39.5	-47 28 19	16.84	17.87	—	17.90	17.94	0.131	135
KX38	21 36 15.2	-42 46 54	17.97	18.67	18.64	18.46	18.48	0.090	267
KX39	21 36 49.0	-42 28 48	22.43	22.12	—	20.54	—	0.085	221
KX40	21 37 22.6	-45 39 41	20.43	20.77	20.69	20.36	20.03	0.065	120
KX41	21 37 46.7	-44 23 23	20.16	19.57	18.71	18.07	17.70	0.358	159
KX42	21 38 55.4	-46 58 48	20.50	20.23	19.34	18.88	18.45	0.189	159
KX43	21 39 5.2	-42 52 39	18.58	19.44	19.42	19.35	19.36	0.072	128
KX44	21 39 14.0	-42 30 16	21.86	22.28	—	20.72	20.64	0.071	289
KX45	21 41 0.3	-44 57 50	20.40	20.81	20.42	20.25	19.92	0.051	94
KX46	21 41 22.6	-47 4 38	21.62	21.50	21.05	20.33	19.73	0.181	201

Object	RA(2000)	DEC(2000)	U	B	V	R	I	$\overline{\mu}$	$\overline{\phi}$
KX47	21 41 24.5	-42 36 8	19.75	20.56	20.51	20.06	19.73	0.084	109
KX48	21 41 27.6	-42 55 14	22.51	22.16	21.33	20.64	20.24	0.067	175
KX49	21 42 11.4	-43 49 2	21.70	21.77	21.01	20.56	20.26	0.073	145
KX50	21 43 20.6	-46 52 6	21.24	21.36	20.88	20.09	19.60	0.083	221
KX51	21 42 47.4	-42 38 51	20.81	20.68	20.26	19.20	18.87	0.167	112
KX52	21 43 15.1	-42 56 4	20.44	20.96	20.41	20.16	19.87	0.075	135
KX53	21 43 24.6	-43 17 22	—	22.30	21.44	20.64	20.55	0.069	108
KX54	21 43 44.5	-43 45 29	20.29	21.01	20.80	20.43	20.20	0.052	129
KX55	21 43 58.8	-44 23 16	20.92	21.55	21.33	20.79	21.23	0.085	117
KX56	21 44 19.6	-45 34 10	21.36	21.46	—	20.14	19.61	0.168	147
KX57	21 40 46.3	-45 56 13	—	22.12	21.04	20.16	19.61	0.111	257
KX58	21 24 54.4	-43 36 24	21.78	20.98	19.95	19.22	18.65	0.123	154

Table 5.2: COSMOS and SuperCOSMOS measured parameters for the 58 CWD sample members. The positions are those found on the J3376 B_J plate (1977 epoch)

The final sample consists of 56 objects which fully satisfy the photometric, proper motion and RPM/colour survey limits. A further two objects, which satisfy the photometric and proper motion limits but fall marginally outside the RPM/colour cut shown in Figure 5.15 have also been included after favourable follow up observations detailed in Chapter 6.

As was mentioned in Section 3.5, while the COSMOS magnitudes are adequate for the preceding sample selection work, the more detailed object by object analysis to follow requires optimum accuracy from the photographic photometry. SuperCOSMOS U, B, V, R, I photometry has therefore been analysed for the 58 sample objects. Where a good consistent SuperCOSMOS magnitude was obtained, as was generally the case, this was used in place of the old COSMOS measures. The SuperCOSMOS photometry data reduction matched COSMAG measures straight to standard passbands by using an empirically determined colour correction (see Figure 3.4), and the photometry is therefore in standard Kron-Cousins system rather than photographic passbands. In the few cases where the SuperCOSMOS measures seemed dubious (eg. two measures differing by more than a few tenths of a magnitude), the COSMOS measurement could be used as a reference,

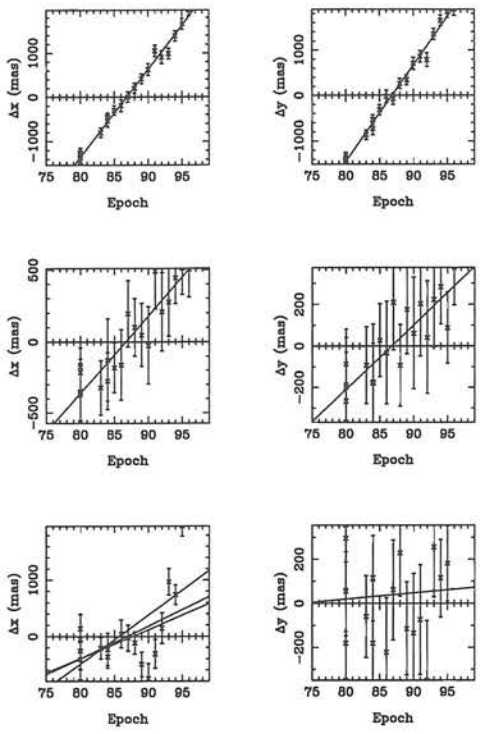

Figure 5.16: Some example proper motion plots from the R plate stacks. The top plot shows data for object KX27, the middle for KX18 and the lower for a rejected object

since zero point effects were only a serious issue for the B_J passband which is well covered by SuperCOSMOS data.

The positions and adopted observational parameters for the full WD sample are tabulated in Table 5.2.

5.5 Very high proper motion, faint object sensitivity limits

In previous Sections the checks made to establish a clean astrometric and photometric catalogue were discussed in some detail. The availability of plates over such a wide epoch range as detailed in Table 3.2 has also allowed a search for faint and/or very high proper motion objects to be undertaken in F287. This work has been accomplished using both the pairing code and generous assistance of Nigel Hambly. This search is important for a number of reasons. For example, it is crucial to firmly establish what the upper limit of detectable proper motion is for the methods used, and also to check if significant numbers

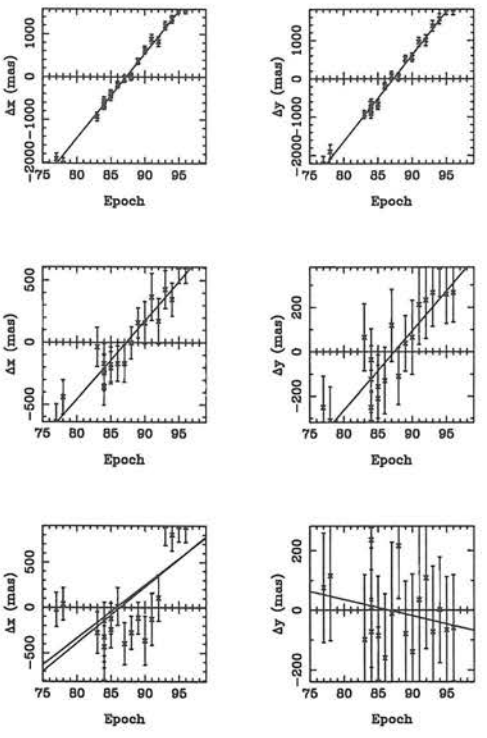

Figure 5.17: Proper motion plots complementary to Figure 5.16 from the J plate stack data

of objects have been missed because of this limit or because of the pairing algorithm used. Also, it is important to check at fainter magnitudes for very dim, high proper motion objects since it is the coolest (and therefore faintest) objects that constrain the age determination based on the turn–over in the WDLF. It is also interesting to search for very faint, high proper motion halo WDs in the light of the current debate concerning the origin of the dark lensing bodies detected in microlensing experiments (eg. Isern et al. 1998 and references therein).

Three experiments were performed to investigate high proper motion and/or faint objects:

1. Within the restricted epoch range 1992 to 1996, ie. five separate epochs, each consisting of a stack of four R plates, completely independent software was used, employing a 'multiple–pass' pairing technique aimed specifically at detecting high proper motion objects. This software has successfully detected a very cool, high proper motion degenerate WD 0346+246 elsewhere (Hambly, Smartt & Hodgkin 1997). The pairing

algorithm described previously used a 200μm search radius over 19 yr resulting in an upper limit of $\sim$ 1 arcsec yr^{-1}, whereas in the multiple–pass test a maximum search radius of 650μm over a 4 yr baseline was used, theoretically enabling detection of objects with annual motions as high as $\sim$ 10 arcsec. The highest proper motion object detected in the catalogue was relatively bright (R $\sim$ 14), with $\mu \sim 0.8$ arcsec yr^{-1}. This experiment revealed two $\mu \sim 0.8$ arcsec yr^{-1} objects , the one mentioned above and another slightly fainter object (R $\sim$ 15) ; no objects were found with motions larger than this. The colours and reduced proper motions of the two objects indicate that they are M-type dwarfs. The second object was undetected in the catalogue due to a spurious pairing, an increasingly likely scenario for high proper motion objects detected without a multiple pass algorithm since they move substantially from their master frame position. All the expected objects having $\mu > 0.2$ arcsec yr^{-1} detected in the catalogue were also found by this procedure.

2. Using the procedure described Section 3.6, but with a relaxed minimum number of epochs, high proper motion objects were searched for. With a 200μm pairing requirement over a maximum epoch separation of 7 yr, the upper limit of proper motion was $\sim$ 1.9 arcsec yr^{-1}. The two objects having $\mu \sim 0.8$ arcsec yr^{-1} found in the previous experiment were also recovered here; again, no objects were found with motions larger than this.

3. To investigate the possibility of fainter objects, the R band material was stacked in groups of 16 plates at epochs 1980, 1983 to 1986, 1987 to 1991 and 1992 to 1996. Obviously, over any individual four year period an object having a proper motion greater than $\sim$ 1 arcsec yr^{-1} will have an extended image and will not be detected to the same level of faintness as a stationary star; nonetheless, the $\sim 0.75^{\rm m}$ increase in depth afforded by going from 4 to 16 plate stacks (Figure 4.25) at least allows an investigation of the possible existence of objects having $\mu \sim 0.5$ arcsec yr^{-1} down to R $\sim$ 23 (100% complete to R $\sim$ 22) over an area of 25 square degrees. In this experiment, all the objects expected from the catalogue were recovered; in addition, one star was found having R $\sim$ 20, $\mu = 0.47$ arcsec yr^{-1} at PA = 179° and RA,DEC = 21h30m8.553s, −44°46'24.09 (J2000.0). This object is the M–type dwarf 'M20' discovered in the photometric survey of Hawkins & Bessell (1988) and has $B_J \sim 23$. The faintness in the blue passband is the reason that this object is

absent from the catalogue. Once more, no other high proper motion, fainter stars were found.

These results of these three experiments argue that there is no large population of objects having $\mu \gtrsim 1$ arcsec yr^{-1} down to faintness limits of R $\sim$ 22 and $B_J \sim 23$. Furthermore, the cut–off in the WD sequence seen in the reduced proper motion diagrams is real, and not an artefact of incompleteness.

Chapter 6

Follow-up Observations

6.1 Introduction

While the RPMD technique is a powerful population discriminator, it is desirable to obtain follow up observations of a sub-set of sample members. The principal motivation for this is to explicitly demonstrate the applicability of the RPM survey technique by confirming the WD status of the sample objects via spectroscopy. Spectroscopic observations redwards of the WD cut in the RPMD may also be used to investigate the possibility of ultra-cool white dwarfs existing in the sample; and as a corollary to this, such observations allow clearer population delineation in the RPMD. In addition, photometric observations through standard filters ensure confidence in photographic-to-standard photometry transformations and provide useful independent checks of stellar parameters (eg $T_{\rm eff}$) derived from fits to photometry.

6.2 Spectroscopy

This project was allocated 3 nights of observing time in 1996 between the 8th and 10th of August, and a further 3 nights in 1997 between the 5th and 7th of August on the 3.9m Anglo-Australian Telescope for spectroscopic observations of selected objects in the proper motion sample. In this Section the observing strategy, the observations themselves, and

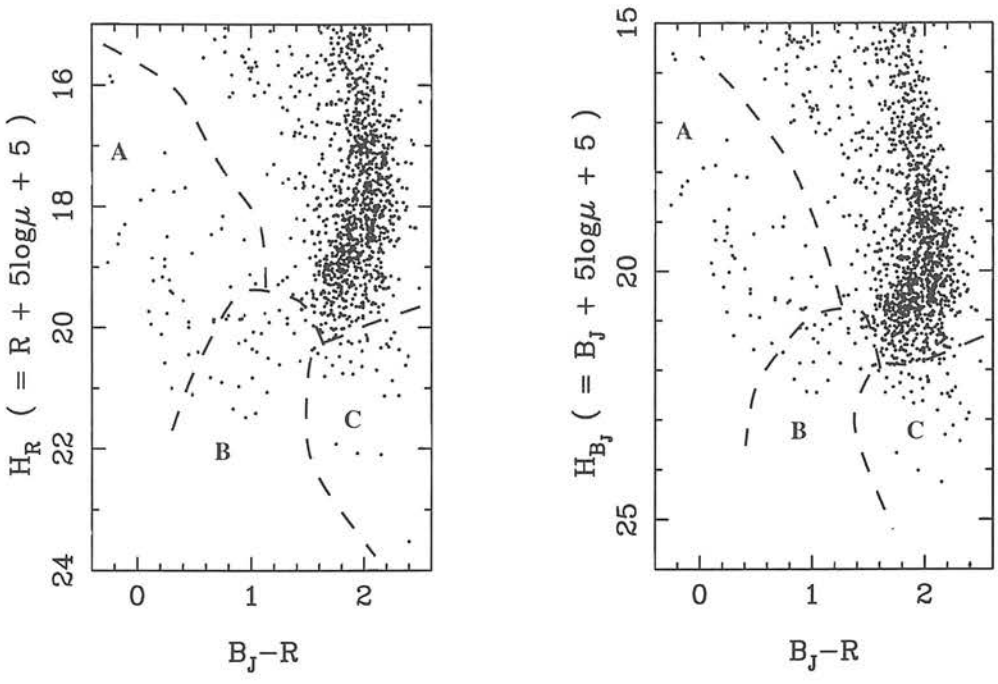

Figure 6.1: Schematic of the regions of the RPMD considered for spectroscopy target selection.

subsequent data reduction and analysis are described.

6.2.1 Observing Strategy and Target Selection

The purpose of these observations was to define as clearly as possible the constituents of the lower portion of the RPMD, from the blue end of the WD locus down to the high H objects below the M-dwarf main sequence stars. Even with the AAT, one of the largest telescopes in the southern hemisphere, high signal to noise spectroscopy of such faint (B $\sim$ 22, R $\sim$ 20.5) candidates was not a practical proposition. The target stars considered for spectroscopy can broadly be categorised as belonging in one of three regions of the RPMD, shown in Figure 6.1.

Region A contains bluer WDs, which are of less interest than the redder candidates for two reasons. Firstly, these relatively young stars will have substantially less bearing on final estimates of the Disk age from the WDLF since they lie far from the predicted cut-off. Secondly, they lie clearly within the WD locus and therefore their status as WDs

is in little doubt. However, it is desirable to obtain a representative sample of this region to confirm the reality of the WD locus along it's full extent, and since these bluer objects tend to be brighter it is not necessary to sacrifice undue amounts of telescope time in this process.

Region C consists of stars lying below the bulk of main sequence objects. Stars generally inhabit this region by dint of their large proper motion rather than apparent faintness, thus reasonably high signal-to-noise spectroscopy of a subsample of these objects should not be too time consuming. Observing at least some of these objects is particularly important because, since ultra-red WDs have never been observed, their locus on the RPMD is not known empirically. Although only a few objects in region C lie on a locus extrapolated from the bluer WD population, the group of objects at lower H are worthy of investigation because of the potential interest of discovering an ultra-cool group of degenerates, and more practically because observations in this region help to define the red extent of the WD locus.

The most pressing objective of these observations was to identify CWDs near the predicted LF cut-off, and attempt to delineate the RPMD in this region. The objects in region B inhabit the cool, intrinsically faint end of the WD locus, and almost without exception have large apparent magnitude. Selection of targets in region B was therefore based primarily on apparent magnitude, since effective use of limited telescope time was optimised by observing the brightest objects first. Clearly an ideal observing strategy would sample this region extensively, examining objects in the full range of apparent brightnesses down to the survey limit. In practise, however, the faintest candidates were simply not bright enough to obtain usable spectroscopic data with the AAT, even allowing for the modest signal-to-noise required for WD identification. The objectives of the spectroscopic work were therefore necessarily limited, and consisted of investigating the stellar type of as many CWD candidates as possible while adequately sampling regions A and C.

A star lying near the cut-off region of the RPMD clearly showing the absence of strong metal features that would be present even in a low-metallicity subdwarf is very likely a CWD. Ideally, a signal-to-noise of at least ten is desired to convincingly demonstrate this absence. The procedure used for identifying candidates is discussed in detail in Section 6.2.3. This procedure does not require absolute spectrophotometry, but makes use

of the broad shape of the continuum and the position of features. A wavelength range of $\sim 4000 - 7500$Å allows detection of the strong G-band and MgI features of K dwarfs and subdwarfs and also includes the broadened hydrogen Balmer series of hotter WDs.

6.2.2 Observations and Data reduction

A spectral coverage of $\sim 4100 - 7200$Å was obtained with the RGO spectrograph and 300B grating in conjunction with the Tek CCD (~ 3Å per pixel). LTT standards were observed throughout each usable night, although over 50% of the time was lost to cloud. Poor seeing during much of the rest of the available time made detection of faint candidates difficult. The details of the following data reduction description apply both to the 1996 and 1997 datasets.

The data reduction was performed in the IRAF environment with aid of the IRAF users guides (Massey 1992, Massey, Valdes & Barnes 1992). The data was trimmed and bias corrected and the flat field exposures averaged in conjunction with a rejection algorithm that uses the known noise characteristics of the Tek CCD. The normalised flat field image was obtained by fitting the combined flat field exposure image (collapsed in the spatial direction) to six cubic splines along the wavelength direction and taking the ratio of the fit to the combined image. This procedure removes large scale wavelength dependent structure in the flat fields as well as pixel to pixel variations. At the blue end of the exposure, very low counts made the flat field image noisy, and the portion of the image with noise $> 1\%$ was replaced with pixels set to unity. Wavelength calibration was achieved via CuAr lamp exposures containing lines of known wavelength. A quadratic fit of pixel number to wavelength resulted in an rms of 0.48 Å with no systematic residuals, and was adopted as the dispersion solution. Flux calibration using standard stars with known SED was applied to the extracted spectra. An extinction correction was also applied, the consistency of which was confirmed by inspecting several calibrated spectra of the standard star LTT7987 at varying airmass.

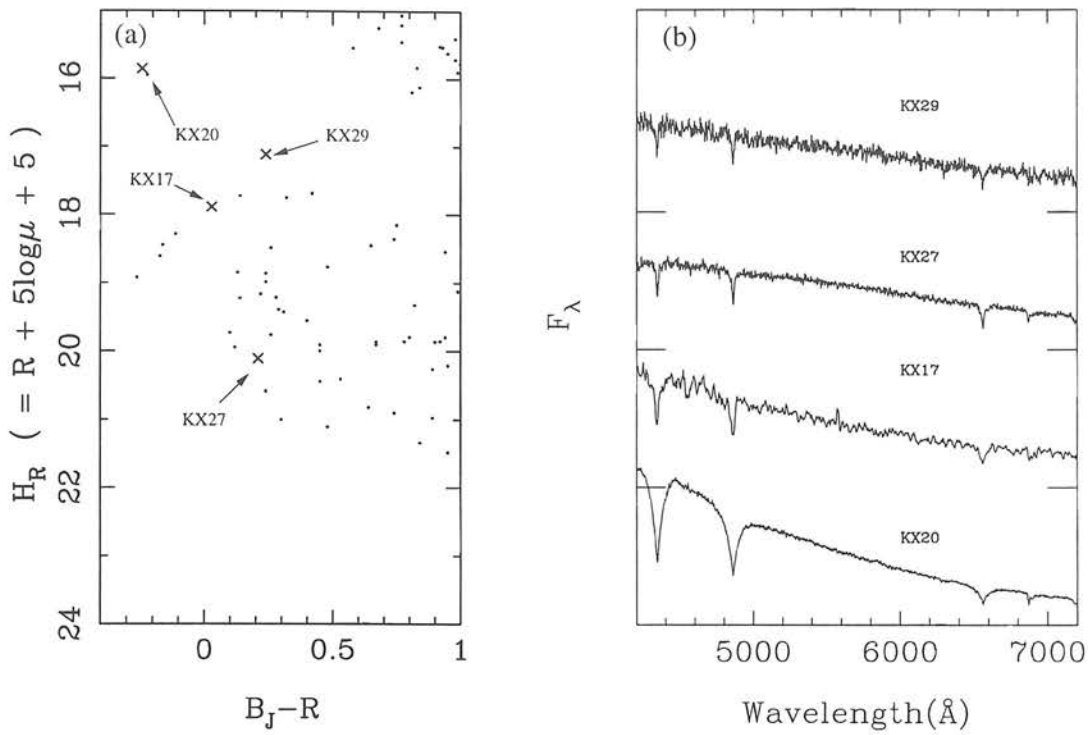

Figure 6.2: Observations in region A. The positions of the observed objects on the RPMD are shown in (a), where they are labelled and denoted by a cross. The AAT spectra obtained are shown in (b).

6.2.3 Results and Analysis

Spectra of four hotter WDs showing clear hydrogen features were obtained. These stars lie firmly in region A of Figure 6.1. Their exact position on the RPMD is highlighted in Figure 6.2 (a), a blown up version of the H_R RPMD centred around region A.

Figure 6.2 (b) displays the AAT spectra obtained for the four candidates highlighted in Figure 6.2 (a). The KX17 spectrum was noisy and has been smoothed. A principal characteristic of hot WD spectra when compared to main sequence stars is the large line width and equivalent width of the spectral lines (Jaschek and Jaschek 1987 p.385). Greenstein and Liebert (1990) produced plots of estimated equivalent width and fwhm for Hα as a function of colour for around 100 WDs. Measurements of the Hα line in the

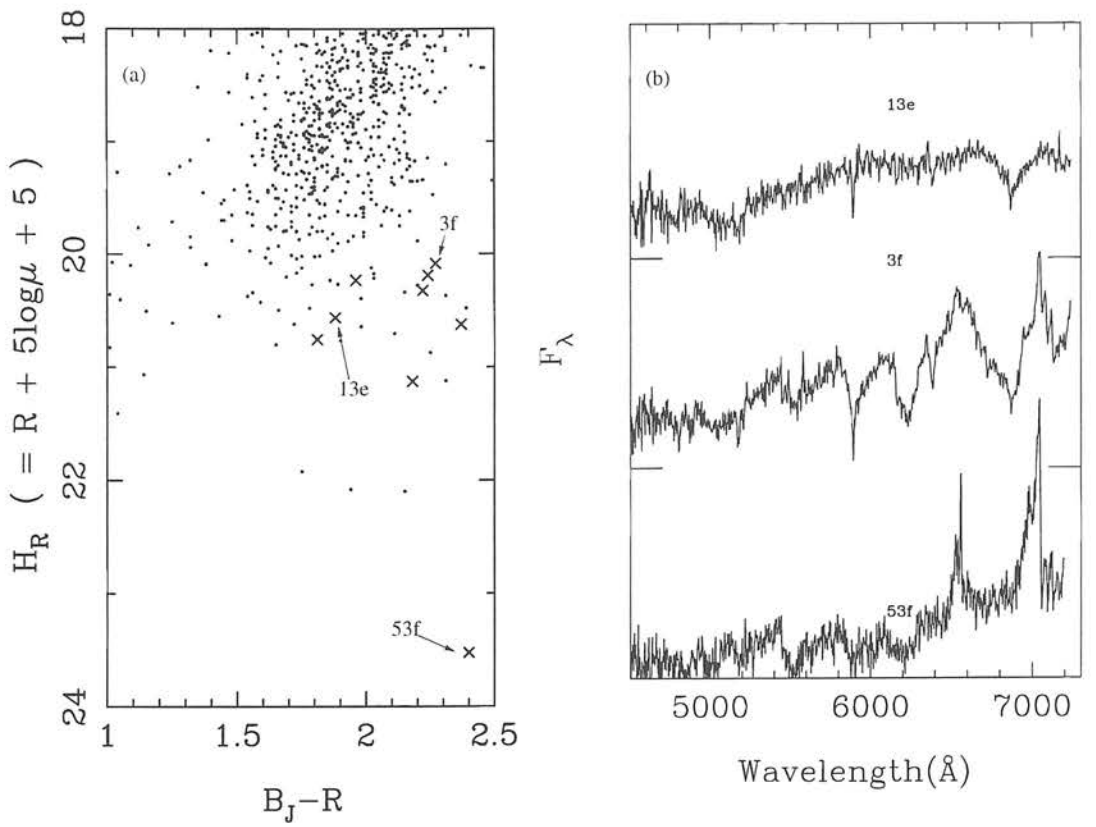

Figure 6.3: Observations in region C. The positions of the observed objects on the RPMD are shown in (a), where they are labelled and denoted by a cross. The AAT spectra obtained are shown in (b).

spectra of our candidates place them firmly within the WD regime.

Spectra of a number of objects in region C of the RPMD were obtained. Their positions on the RPMD are shown in Figure 6.3 (a). All objects observed in this region have spectra clearly distinct from the expected continuum spectra of CWDs. They appear mostly to be the 'metallic hydride dwarfs' reported by Bessell (1982), a sequence of extremely metal poor subdwarfs. Objects 3f and 13e are examples of these, their spectra (Figure 6.3 (b)) showing strong CaH and MgH features. The extreme RPM object 53f is a high velocity M-dwarf.

The majority of time at the AAT was spent observing objects in region B of the RPMD, containing both the faintest and the most promising CWD candidates. As mentioned

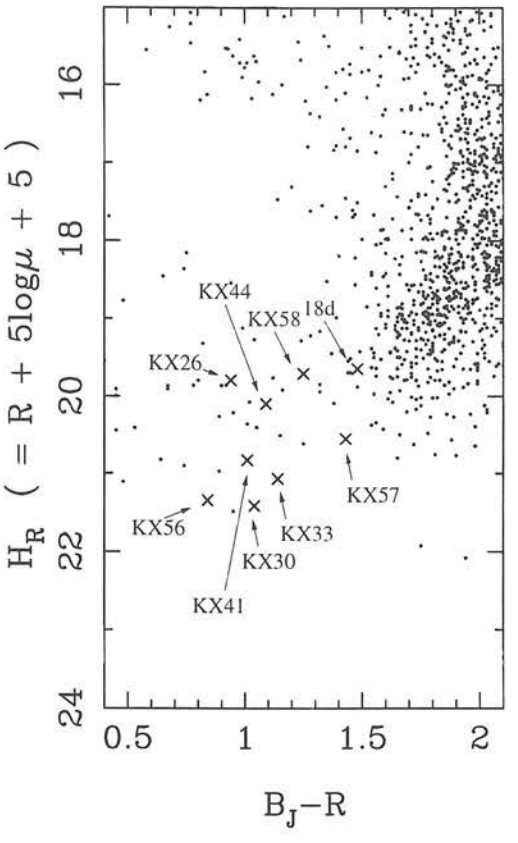

Figure 6.4: An enlargement of region B of the RPMD. Objects with usable spectroscopic observations are labelled.

above, it has not been possible to obtain high signal to noise spectra of these objects. However, a star lying near the cut-off region of the RPMD clearly showing the absence of strong metal features that would be present even in a low-metallicity subdwarf is very likely a CWD. It should be noted however that the reverse is not necessarily true, and some WDs ($\sim$ 10% of the BRL sample) show Carbon (DQ stars) or other metal (DZ stars) features (eg. Wesemael et al. 1993). However, the *absence* of subdwarf features is a good indication of WD status. This line of argument is applied to the data by selecting from the recent models of Hauschildt et al. (1998) a spectrum appropriate to a subdwarf (metallicity [M/H] ≥ -2 and [M/H] ≥ -1) of similar effective temperature to a given CWD sample object spectrum. The model spectrum is smoothed to the approximate resolution of the AAT spectra and multiplied through by a synthetic noise spectrum commensurate with the AAT CWD spectrum in question. The only features likely to be visible after this

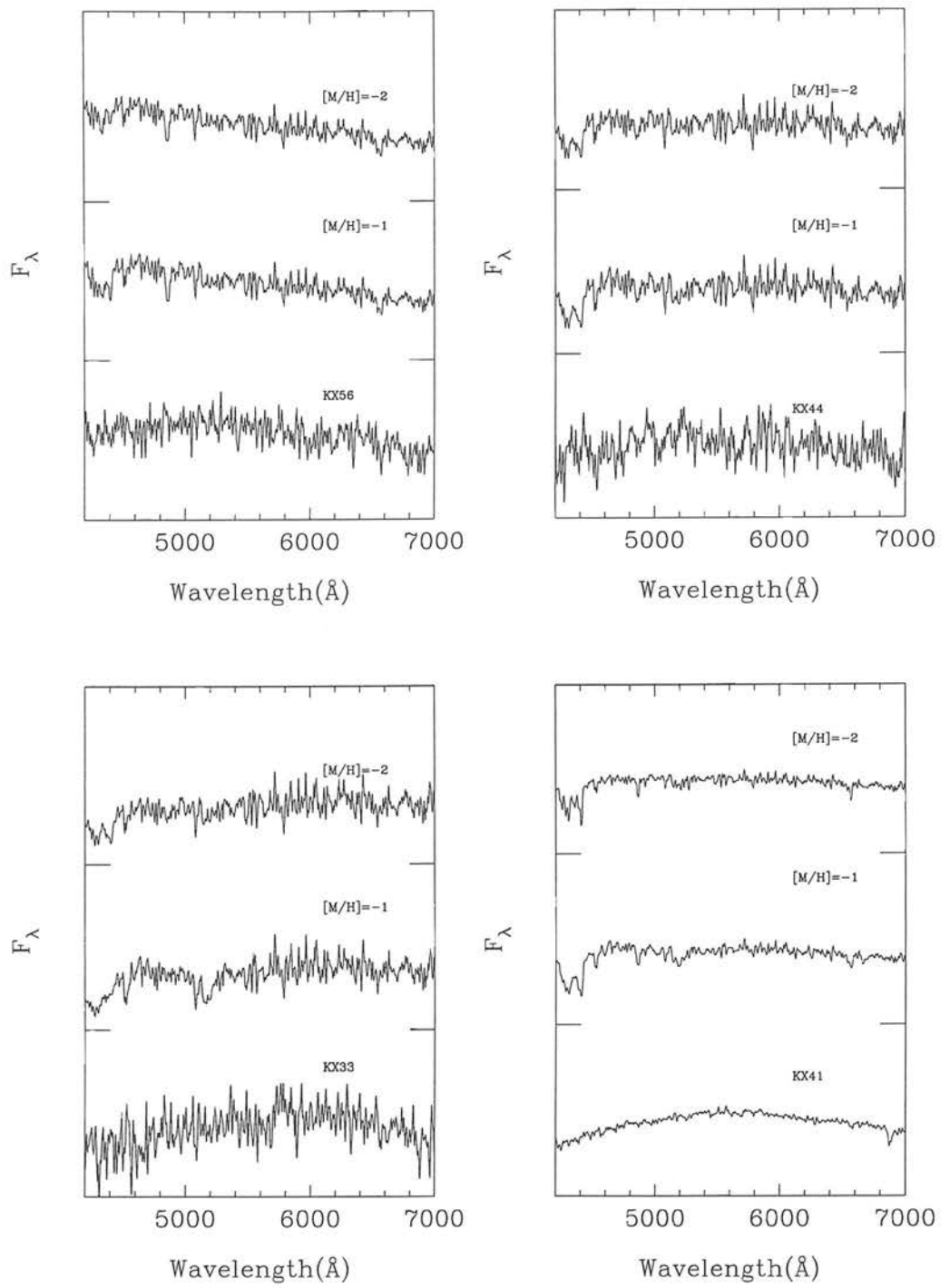

Figure 6.5: CWD candidate spectra with model subdwarf spectra for comparison. The candidate spectra are at the bottom of the plots with the [M/H] ≥ -1 model above them and the [M/H] ≥ -2 model at the top.

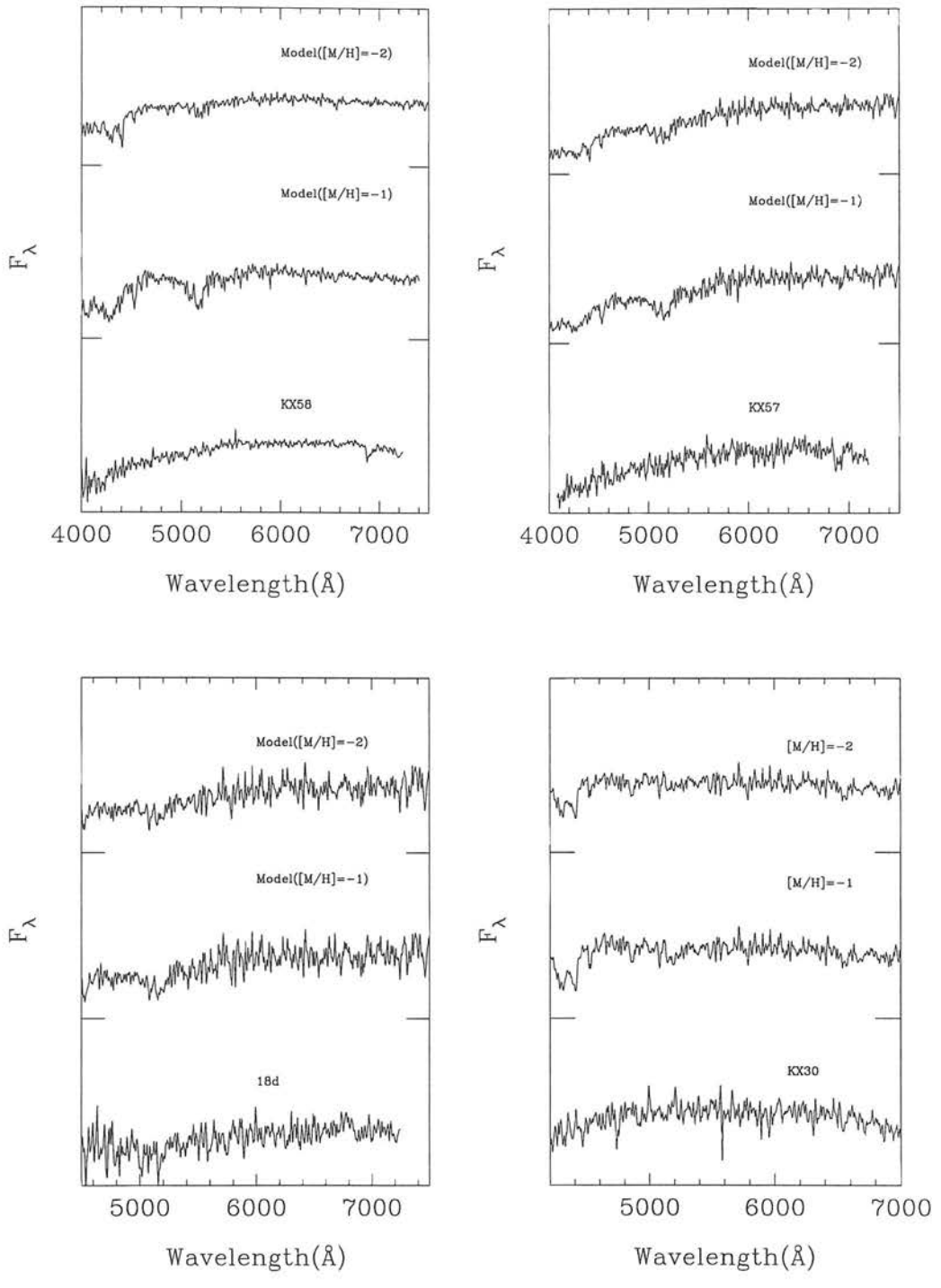

Figure 6.6: CWD candidate spectra. The candidate spectra are at the bottom of the plots with the [M/H] ≥ -1 model above them and the [M/H] ≥ -2 model at the top.

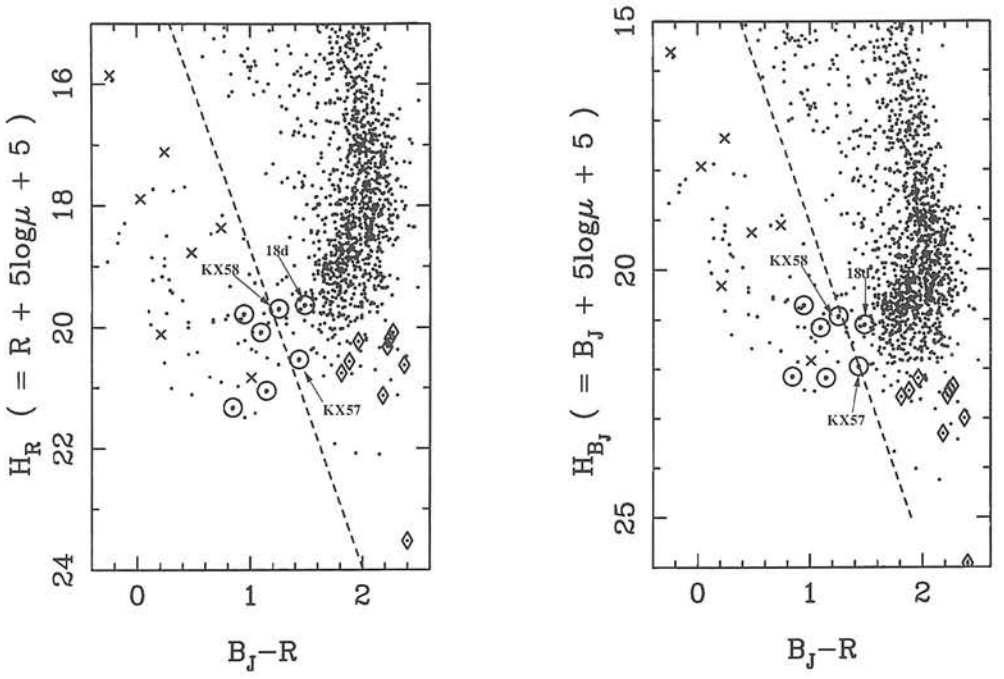

Figure 6.7: RPMD of the survey sample with spectroscopically observed objects numbered and highlighted. Diamonds denote objects identified as subdwarfs or M dwarfs, crosses an immediate firm WD identification. Dotted circles represent objects with noisier spectra (see text). The labelled objects have their spectra discussed in detail below.

procedure are $\sim$ 5200Å MgI and the $\sim$ 4300Å CH G-band, and it is in these regions that the spectra are examined for evidence that the CWD sample objects are in fact subdwarfs. Those objects in region B with usable spectra are highlighted in Figure 6.4.

In Figures 6.5 and 6.6 the (smoothed) spectra are shown with their comparison model spectra. Several of the observations are extremely noisy - notably the spectra of KX44 and KX33, whose unsmoothed spectra had signal to noise measures of 2.67 and 2.22 respectively. None of these objects , except '18d' which is discussed below, show evidence of subdwarf like spectral features, lending validity to our chosen population discrimination technique, although clearly better spectra of more of the candidates is desirable. The objects KX57, KX58 and 18d are of particular interest as they lie slightly redwards of the RPMD WD population delineator used. KX58, displayed in Figure 6.6 (top left), is a convincing CWD candidate, showing a smooth continuum spectrum with no suggestion of the metal features apparent in the model subdwarf spectra. The noisier spectrum

of KX57 in Figure 6.6 (top right) also shows no evidence of subdwarf features, although poorer signal-to-noise makes the identification less certain. The object 18d lies significantly redward of our CWD cut-off on the RPMD, and unfortunately its spectrum (Figure 6.6 bottom left) is extremely noisy. While it is difficult to draw any conclusions from such poor data, the possibility that this object is a subdwarf certainly cannot be excluded with any confidence. Thus the position of 18d on the RPMD in conjunction with the ambiguity of the spectral data means this object does not warrant inclusion in the CWD sample.

6.2.4 Summary of Spectroscopic Results

To summarise the findings of this spectroscopic survey, the only objects showing notable deviation from expected WD spectra are the objects below the M dwarf portion of the RPMD (diamonds in Figure 6.7) and the more ambiguous case of object 18d discussed above. Objects KX57 and KX58, which lie marginally outside the initial RPM WD delineator, appear to be WDs and are included in the WD sample. The fact that no observed sample member shows evidence of being a contaminant is, in the absence of further observations, taken as sufficient grounds to treat the WD sample detailed in Table 5.2 as being uncontaminated. It is therefore suitable for use in constructing a WDLF. As a cautionary note however, the lack of high quality spectra of all objects in the vicinity of the WD locus means the sample cannot be regarded as complete with total confidence. The possibility that some sample objects are either high H subdwarfs - realistic only at the cool end of the WD locus - or spurious proper motion MS contaminants cannot be excluded; although the work of the previous Chapter was aimed at minimising this possibility. A potentially more serious problem is exclusion of cool degenerates lying redwards of our RPM WD delineator, as was the case for KX57 and KX58, albeit by a small margin. This question will be addressed in the next Chapter, where some encouragement may be found, although the problem cannot be resolved satisfactorily without an extensive spectroscopic survey of all the objects around region B of the RPMD.

6.3 Photometry

CCD photometry of a subsection of the CWD sample was obtained between 29th of July and the 4th of August on the 1m telescope of the South African Astronomical Observatory in Sutherland. Over a quarter of the time was lost to cloud. Targets were chosen from the full range of colour on the WD RPM locus, although again most time was spent on the faint CWD candidates.

6.3.1 Observations and Data Reduction

Johnson-Cousins V, R, I photometry was obtained for all program stars on the Tek (512x512) CCD, with B measures also acquired for sufficiently bright objects. E-region standards were observed continuously through each usable night. The data was reduced using the method described in the IRAF Stellar CCD photometry guide (Massey & Davis 1992). Standard stars with a wide range of colour were observed at various airmasses, allowing equations of the form

$$M_{std} = M_{CCD} + c_1 + c_2 \times COLOUR_{std} + c_3 \times X \tag{6.1}$$

to provide a means of calibration for each filter. In Equation 6.1 M_{std} is the magnitude in the standard passband, M_{CCD} is the instrumental magnitude, $COLOUR_{std}$ is a measure of colour in standard passbands and X is airmass. Constants c_1, c_2 and c_3 were determined for each filter. The instrumental magnitudes were obtained using the 'phot' task, which measures the counts above sky within a given aperture. The transformation equations were tested by excluding a particular set of observations of a standard star from the calibration procedure and using the resulting solution to calibrate the excluded observations. A smaller aperture was used for the excluded star to confirm the aperture correction was correct. The resulting calibrated magnitudes had typical residuals of ~ 0.007 magnitudes from the published standard value. The calibrated magnitudes for the WD sample objects observed are tabulated in Table 6.1.

Object	B	V	R	I	Object	B	V	R	I
	σ_B	σ_V	σ_R	σ_I		σ_B	σ_V	σ_R	σ_I
KX14(1)	–	21.43	20.78	20.17	KX30	–	21.12	20.64	20.19
		0.04	0.09	0.07			0.03	0.05	0.08
KX14(2)	–	21.47	20.75	20.20	KX33	–	21.22	20.69	20.10
		0.04	0.07	0.07			0.04	0.06	0.07
KX15	19.10	18.53	18.08	17.69	KX39	–	21.19	20.66	20.18
	0.03	0.02	0.03	0.03			0.04	0.06	0.06
KX20	16.14	16.12	16.16	16.22	KX41a	20.26	19.38	18.93	18.41
	0.02	0.02	0.02	0.02		0.05	0.03	0.04	0.04
KX22	–	19.94	19.66	19.55	KX41b	20.28	19.33	18.81	18.36
		0.03	0.04	0.04		0.04	0.03	0.04	0.04
KX23	19.52	19.05	18.74	18.61	KX44	–	21.37	20.81	20.42
	0.03	0.01	0.01	0.03			0.05	0.07	0.08
KX27	–	18.15	17.97	17.91	KX53	–	20.96	20.70	20.21
		0.02	0.02	0.03			0.03	0.05	0.06
KX29	18.67	18.36	18.17	17.90	KX57	–	21.09	20.40	19.84
	0.03	0.02	0.03	0.03			0.04	0.06	0.08

Table 6.1: Johnson-Cousins CCD photometry taken at SAAO for selected members of our CWD sample. Object KX41 was resolved as a double-degenerate on the CCD frame and thus has photometry for each component. Object KX14 had two independent sets of observations, shown as (1) and (2)

6.3.2 Comparison with Photographic Photometry

These observed magnitudes provide an independent check on the accuracy of the SuperCOSMOS photographic photometry. Figure 6.8 shows the residuals between the CCD and photographic photometry as a function of colour. As may be expected given the findings of Section 3.5, the errors are at the level of tenths of a magnitude. These values allow an independent estimate of the errors on the photographic photometry, which are found to be 0.17, 0.14, 0.13 and 0.16 for B, V, R and I respectively.

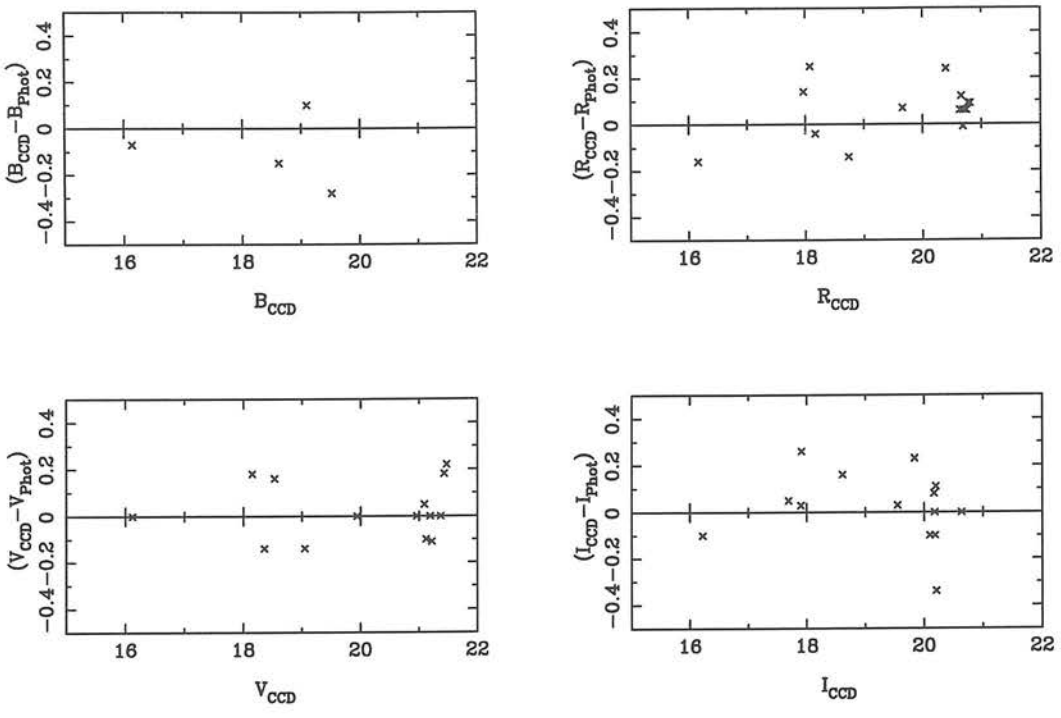

Figure 6.8: The residuals between the SAAO CCD photometry and the photographic photometry plotted as a function of CCD magnitude for the B, V, R and I passbands

Chapter 7

Sample Analysis

7.1 Introduction

The work described in the previous Chapters has enabled a sample of WDs to be extracted from Schmidt plate data knowing only their proper motions and $(B - R)$ colour. The observations described in the previous section appear to validate the RPM population discrimination technique used, since no object observed inside or near the WD sample region shows evidence of being anything other than a WD. The aims of this Chapter are twofold: firstly, stellar parameters such as luminosity and distance must be derived for each sample member in order to construct a WDLF. This work is described in Sections 7.3 and 7.4. Secondly, the sample as a whole is compared with previous observations and survey samples, and with general expectations of a complete sample. In particular, some of the questions raised in Section 6.2.4 regarding population delineation on the RPMD are addressed in Section 7.2, and a further assessment of sample completeness using the $\langle V/V_{max} \rangle$ test is described in Section 7.5. The total WD space density is discussed in Section 7.6

7.2 Comparison of Samples on the RPMD

As has been stressed before, in the absence of extensive spectroscopic observations of the proper motion sample, the RPMD remains the sole practical means of population

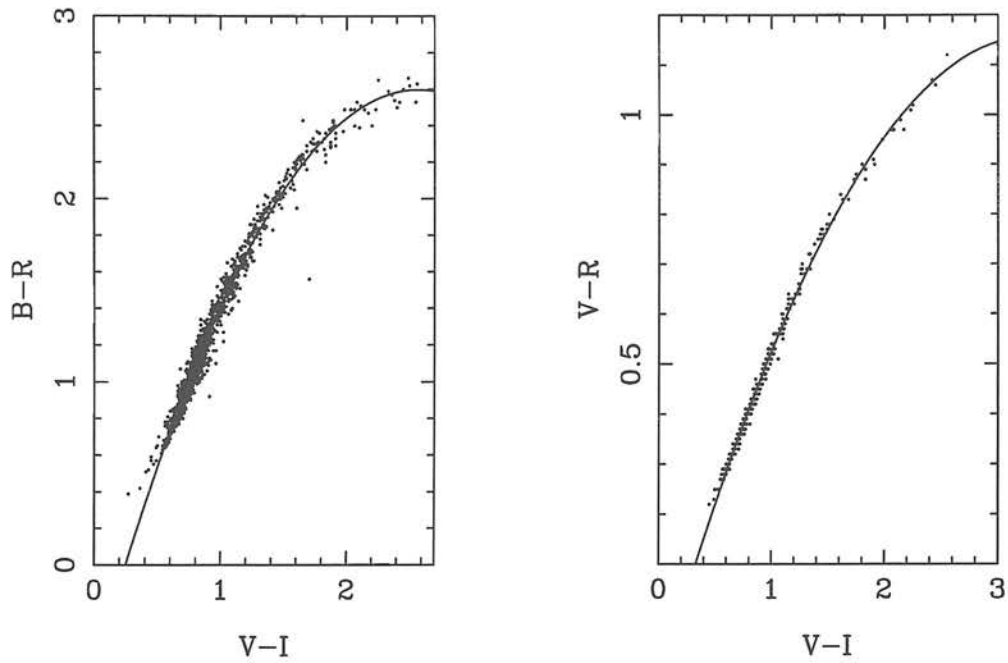

Figure 7.1: Scatter plot of $(V-I)$ against $(B-R)$ and $(V-R)$ for the Ryan subdwarfs. The lines are quadratic fits to the data, and define the colour transformations used for the Monet et al. extreme subdwarfs.

discrimination. It is therefore desirable to define as clearly as possible the distribution of stellar populations on the RPMD used. While the theoretical loci of Evans (1992) were a useful guide to sample selection in Section 5.4, they include considerations specific to that work (eg. that surveys photometric errors), making them unsuitable for direct comparison with these data. An obvious way of assessing the potential contamination or incompleteness described in Section 6.2.4 is to plot samples of previously discovered subdwarfs and CWDs alongside our data on a RPMD. BRL published observations of a sample of 110 CWDs, including most of the coolest known degenerates, which will serve as a valuable comparison to our sample. Extensive lists of extreme subdwarfs are less easily obtainable. Ryan (1989) used a RPM criterion to extract over 1000 subdwarf candidates from the NLTT catalogue. Accurate U, B, V, R, I photometry was published for these objects, providing a useful means of delineating the bluer portion of the WD RPMD locus. However, because this sample of subdwarfs is restricted to $m > 13$, it does not sample the red, higher H portion of RPMD in which contaminants to the cool end of the WD locus are expected. Monet et al. (1992) identified a subset of 17 subluminous,

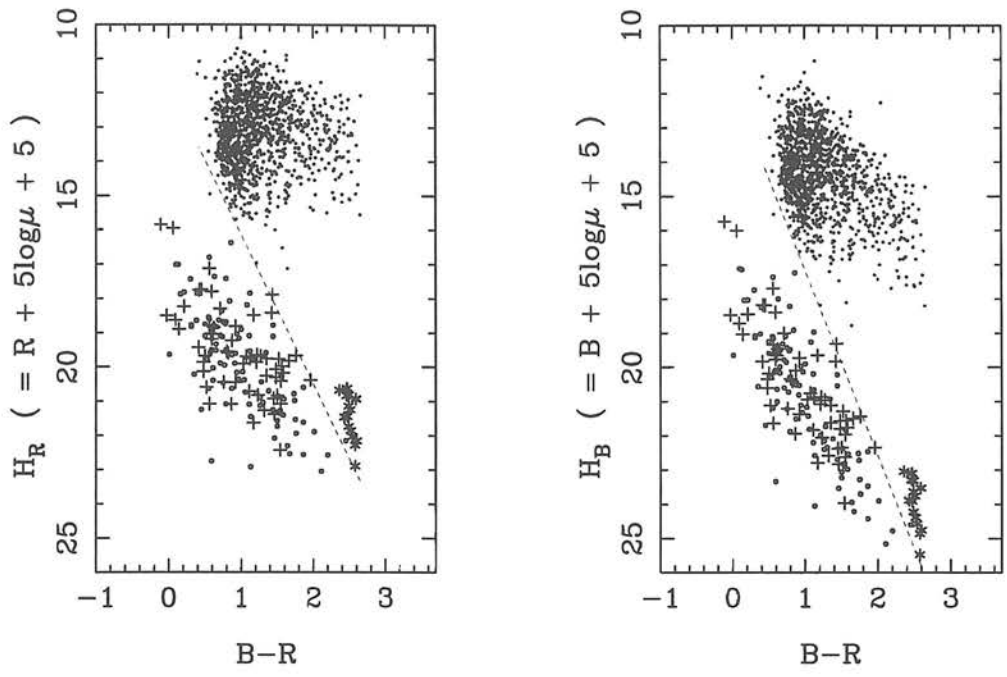

Figure 7.2: A comparison of various populations on the RPMDs: crosses denote the CWD sample from this work , large dots the BRL CWD sample, asterisks the Monet et al. extreme red subdwarfs and small dots the brighter Ryan subdwarfs

high velocity extreme subdwarfs from their CCD parallax program also involving Luyten catalogue stars. It is stars such as these that will be most likely to bridge the gap between the subdwarf and WD portion of the RPMD and contaminate a WD sample. Although only V, I photometry is published for these stars, the photometry obtained by Ryan for the brighter subdwarfs provide colour transformations allowing the extreme subdwarfs to be plotted on the $(B - R)$, RPMD planes.

These transformations are shown in Figure 7.1, where a quadratic curve was found to adequately characterise the data in both plots.

Figure 7.2 shows the two RPMD with the four samples plotted. There are several points to be made concerning this plot. Firstly, our CWD sample and the the BRL sample of previously known CWDs lie on the same region of the diagram, providing further confirmation of the validity of our survey procedure. It can also be seen that the BRL sample contains redder, cooler stars than our sample. This may be expected

since the BRL sample is rather eclectic and contains some of the coolest WDs known, whereas our sample is drawn from a rigidly defined survey in a particular ESO/SERC field. We note also that the cool portion of the BRL sample does not extend into the portion of the RPMD beyond our population discrimination cut-off shown in Figure 5.15, which may be interpreted as indicating that we are not failing to sample portions of the RPMD containing CWDs (but see Section 8.5 below). Both subdwarf samples lie in clearly distinct regions of the RPMD to our sample, although the cooler subdwarfs are all too red to directly assess contamination of the CWD sample from the direction of small RPM. However, the subdwarf RPM locus is not predicted to deviate significantly from a straight line in the CWD colour regime (Evans 1992), and if we take the high H extent of the two subdwarf samples plotted to be indicative of the limit of the extreme subdwarf locus on the RPMD, the dashed lines plotted on Figure 7.2 should be a good guide to the limit of the subdwarf locus for the intermediate colour range. It may then immediately be seen that the vast majority of our CWD sample is safely within the WD region of the RPMD. The two redder borderline stars have reasonable spectroscopic confirmation of their WD status (Figure 6.6), leaving only one potentially dubious object.

7.3 Derivation of Sample Stellar Parameters

The construction of a WDLF from a WD sample requires knowledge of luminosities and space densities for the sample members. Previous studies of CWD samples have benefited from a comprehensive and wide ranging observational database, including high quality spectra, optical and IR photometry and trigonometric parallaxes. The analysis performed by BRL used all these observed quantities where available. Their technique used accurate UBVRIJHK photometry to fit for $T_{\rm eff}$ and $(R/D)^2$ (the square of the ratio of the radius of the star to its distance from Earth) using the model atmospheres of Bergeron, Saumon & Wesemael (1995, BSW hereafter). The variable parameters in these models are $T_{\rm eff}$, $\log g$ and $N(He)/N(H)$, although it was found that constraining log g in the fitting process was not a practical possibility. If a measure of trigonometric parallax was available for a particular object however, it was possible to calculate a stellar radius from the $(R/D)^2$ determined from the fit. Cooling models (Wood 1995) were then used to obtain a WD mass, from which a value of log g ($g = GM/R^2$) was calculated. An iterative process

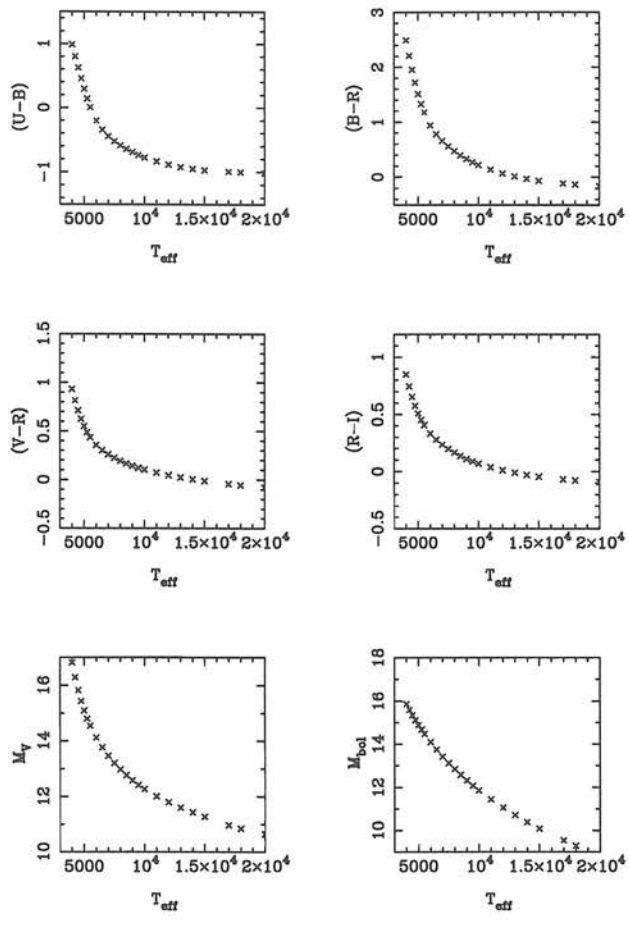

Figure 7.3: The predictions of the BSW model Helium atmospheres as a function of $T_{\rm eff}$.

was then used to obtain consistency between this value of log g and that used to produce the model atmosphere. The atmospheric composition was determined by the model atmosphere fit to the photometry. The spectroscopic data was not used as part of the fitting procedure, but served as a means of checking the results of the fits. This fitting procedure uses the extensive observations and detailed model atmosphere SEDs to obtain the effective temperature, radius, surface gravity, mass and luminosity of every star with trigonometric parallax measurements.

Such a sophisticated fitting technique is not appropriate for this survey, since in general only UBVRI photographic photometry is available, with some objects even lacking data in one or more of these passbands. It is therefore necessary to restrict the analysis, by exploiting the homogeneity of WD surface gravities by assuming a common typical log g for the entire sample. This approximation was made by OSWH, and also by BRL in the

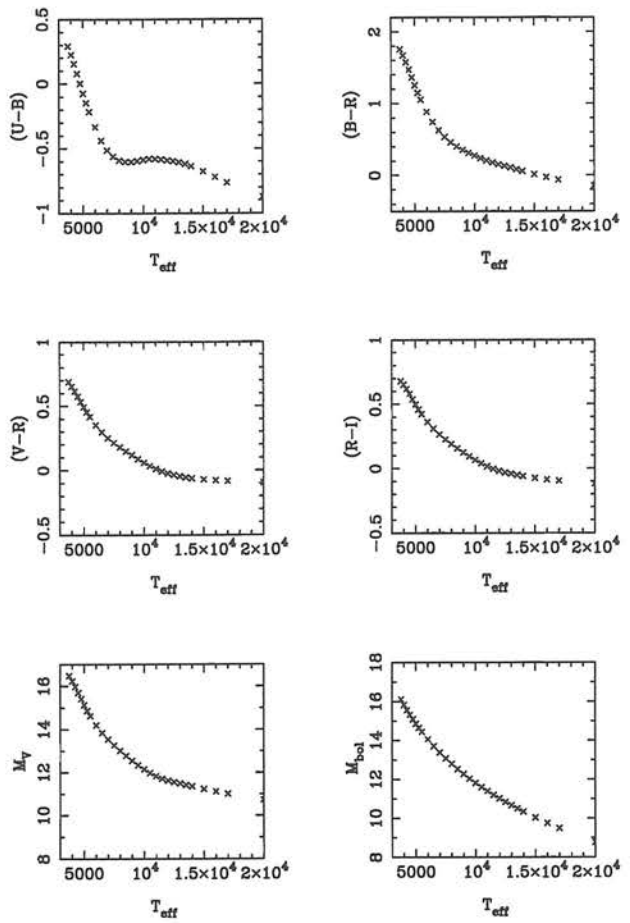

Figure 7.4: The predictions of the BSW model Hydrogen atmospheres as a function of $T_{\rm eff}$.

absence of trigonometric parallaxes. The 60 stars with measured log g in BRL have a mean surface gravity $\overline{\log g} = 8.099 \pm 0.044$, indicating the approximation is not unreasonable.

BSW have published a detailed grid of model predictions for U, B, V, R, I (and IR) photometry and bolometric corrections as a function of effective temperature and log g. This grid may be used to fit for $T_{\rm eff}$ alone, since unlike the method of BRL described above we use colour indices rather than fluxes for fitting. These models are displayed in Figure 7.3 and Figure 7.4, with $T_{\rm eff}$ varying as a function of $(U-B)$, $(B-R)$, $(V-R)$ and $(V-I)$, the colour indices used in the fitting procedure. As may be seen from the plots, the grid divisions are sufficiently small that straight lines drawn between points give an excellent approximation of continuous models. Fitting for $T_{\rm eff}$ is achieved by linearly interpolating the model grid at 10K intervals and evaluating χ^2 at each interval using all available colour indices for the object in question. The photometric errors found in

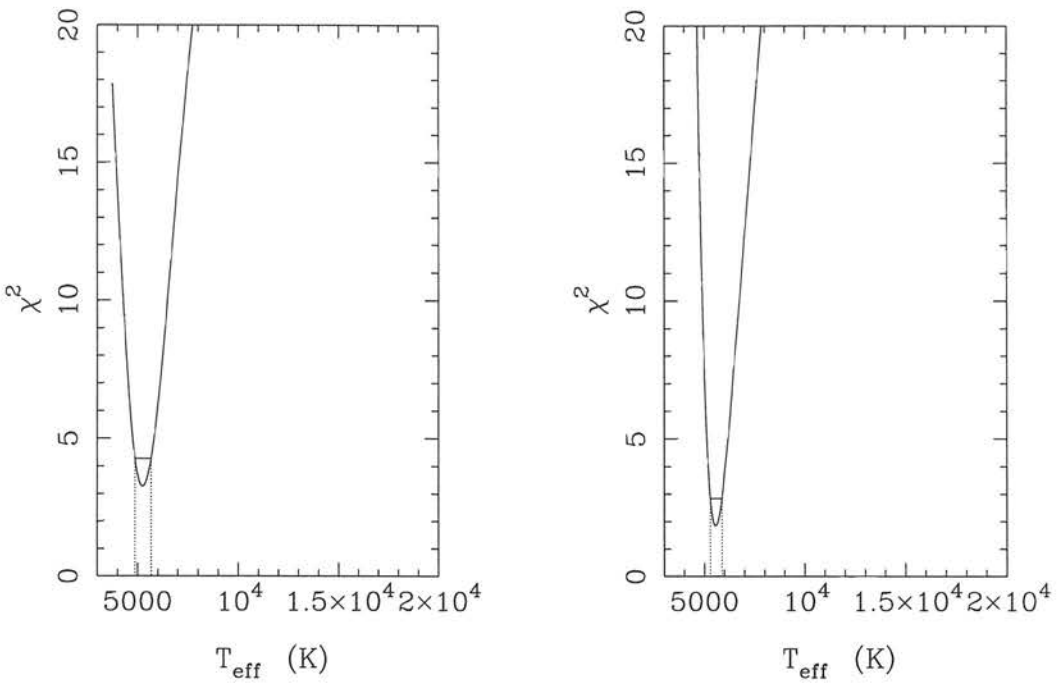

Figure 7.5: χ^2 as a function of $T_{\rm eff}$ for a fit of photographic photometry of object KX15 to BSW models (H atmosphere on the left and He on the right

Section 6.3.2 are adopted when calculating χ^2. The effect of interstellar reddening is neglected since in the maps of Burstein and Heiles (1982) $E(B-V) < 0.06$ in F287, and is less than 0.03 across most of the field.

Figure 7.5 shows an example of a fit of the BSW models to photographic photometry. Photometry in all 5 passbands is available for this object, and it can be seen that there is a well defined minimum to the fit for both H and He atmosphere models. Estimates of 1σ errors on the fitted $T_{\rm eff}$ are shown by the dotted lines. This plot is typical of the cooler WDs in the sample although the bluer objects tend to have higher errors in $T_{\rm eff}$ since, as may be seen in Figure 7.3 and Figure 7.4, for these objects $T_{\rm eff}$ is a weaker function of colour. The mean reduced χ^2 for all fits was 1.1.

Although the photographic photometry provided well constrained estimates of $T_{\rm eff}$ for all the WD sample with the exception of the very bluest objects for which the errors are large, the more accurate SAAO CCD photometry was also used for fitting as an independent comparison. The fit for the CCD photometry obtained for KX15 is shown

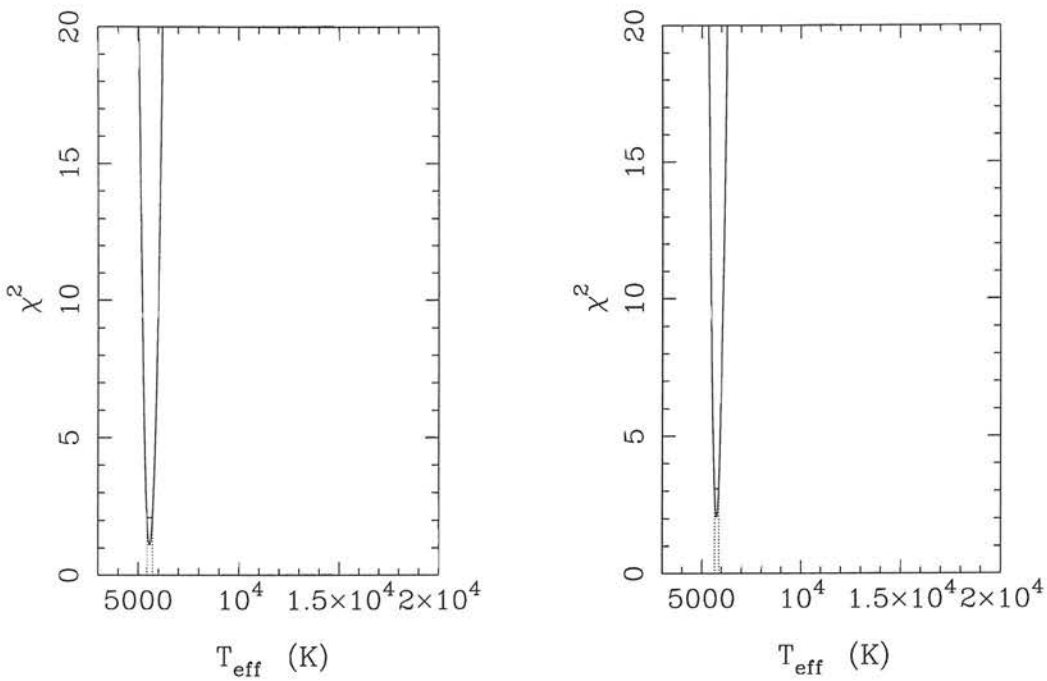

Figure 7.6: χ^2 as a function of $T_{\rm eff}$ for a fit of SAAO CCD photometry of object KX15 to BSW models (H atmosphere on the left and He on the right

in Figure 7.6. When compared to Figure 7.5, it may be seen that the CCD photometry yields fits consistent with the photographic fit but with considerably smaller errors. The BSW grid also gives absolute V magnitudes and bolometric corrections (a large source of uncertainty in LDM) as a function of $T_{\rm eff}$, allowing an $M_{\rm bol}$ and associated error to be derived for each object assuming either an H or He atmosphere. As was found by LRB, the atmospheric composition was not reliably constrained by the optical photometry (Figures 7.5 and 7.6). This analysis was therefore further restricted by treating each stars atmospheric composition as an unknown parameter whose influence on the resulting WDLF must be determined later.

7.4 Space Densities and the $1/V_{max}$ method

In order to construct a WDLF, space densities must be calculated for a survey limited by both apparent magnitude and proper motion. The CWD survey sample consists of stars with widely varying intrinsic brightness and tangential velocity, and is therefore

not volume-limited (since for example intrinsically bright objects are sampled out to greater distances than the coolest, faintest stars). The standard solution to this problem, Schmidt's (1968, 1975) $1/V_{max}$ estimator, has been extensively studied with specific reference the WDLF (Wood & Oswalt 1998). The $1/V_{max}$ method assigns each sample object a survey volume defined by the maximum distance d_{max} the object could have and satisfy the survey limit criteria. For this survey, an object at distance d with proper motion μ and magnitudes B and R has d_{max}

$$d_{max} = \min\left[d\frac{\mu}{\mu_{lim}}, d10^{0.2(R_{lim}-R)}, d10^{0.2(B_{lim}-B)}\right]. \tag{7.1}$$

The survey field solid angle Ω can then be used to calculate the corresponding V_{max}:

$$V_{max} = \frac{\Omega}{4\pi}\frac{4}{3}\pi d_{max}^3, \tag{7.2}$$

where d_{max} is assumed to be independent of position on the sky within the survey area. This prescription was adopted by LDM to produce their WDLFs, the space density in a given luminosity bin, Φ_j, was found summing over the N_j objects within that bins luminosity bounds:

$$\Phi_j = \sum_{i=1}^{N_j}\frac{1}{V_{max,i}} \tag{7.3}$$

where the $1/V_{max}$ measures were calculated according to Equation 7.2. LRB, in their redetermination of the LF from the LDM sample, used the same procedure. They explicitly discuss the effect of upper limits to the proper motion and brightness of survey members. These may be accounted for by truncating the V_{max} volume by a volume commensurate with the distance an object can be moved towards the observer before it reaches a distance d_{min}, at which it is too bright or has too large a proper motion to appear in the survey.

The procedure described above calculates space densities assuming a uniform stellar space density. However, many of the CWDs from this survey have an associated d_{max} comparable to the scale height of the Galactic Disk. It is therefore necessary to generalise the $1/V_{max}$ treatment to allow for the truncation of the survey volume by the scale height effect. Stobie, Ishida & Peacock (1989) approached this problem in the context of their galactic pole survey for M dwarfs by incorporating the scale height into the $1/V_{max}$ technique. In this prescription, a generalised volume is found by integrating over an exponentially decreasing density law with scale height h

$$V_{gen} = \Omega\int z^2\frac{\rho}{\rho_0}dz \tag{7.4}$$

where z is the distance (perpendicular to the plane of the Disc) and the density follows $\rho/\rho_0 = e^{-z/h}$. Tinney, Reid & Mould (1993) extended this treatment to observations made at arbitrary galactic latitude b by noting that an object at distance d extends a distance $z = d \sin b$ above the Disc. The density law is then written $\rho/\rho_0 = e^{-(d \sin b)/h}$ and the modified version of Equation 7.4 may be integrated by parts to give

$$V = \Omega \frac{h^3}{\sin^3 b} \{2 - (\xi^2 + 2\xi + 2)e^{-\xi}\}, \tag{7.5}$$

where $\xi = d \sin b/h$ (Equation 9 in Tinney et al. 1993).

It is Equation 7.5 that is used here to calculate space densities associated with each object. The field size, Ω, is 0.0086 steradians as used in Section 5.1. A brief assessment of the effect of image blending on the survey area available was conducted by calculating the fraction of a SuperCOSMOS scan lost in blended images. This fraction is at the level of a few percent (typically 3%), and has been neglected due to the presence of other much larger uncertainties in the space density estimates. The scale height adopted is 300 parsecs (Evans 1992). The d contained in the expression for ξ is the d_{max} found using Equation 7.1. This equation requires an estimate for the distance to an object, which is obtained using the distance moduli for the B and R photometry. The mean of the distance found via the B and R photometry is taken as the distance estimate. These distances are found to be consistent to $\sim$ 10 parsecs for objects with $d < 250$ parsecs. Three objects have inconsistencies greater than 40 parsecs in their derived distances. This is not a major cause of concern however since they are all relatively distant ($d > 230$ parsecs) and will therefore have small $1/V_{max}$ space density contributions. Tangential velocities, and the ratio of the volume out to the object, V, and the V_{max} of the object are also calculated for each object. These quantities are discussed further in the next Section.

The derived stellar parameters for the CWD sample assuming a Hydrogen atmosphere are displayed in Table 7.1. Table 7.2 shows the results assuming a Helium atmosphere.

Object	$T_{\rm eff}$ ($K^{+1\sigma}_{-1\sigma}$)	$M_{\rm bol}$	distance pc	$V_{\rm tan}$ km/s	$V_{\rm max}^{-1}$ (10^{-4}pc^{-3})	V/V_{max}
KX 1	4700^{5090}_{4320}	$15.14^{14.79}_{15.51}$	112	76	0.956	0.315
KX 2	5980^{6620}_{5470}	$14.08^{13.63}_{14.47}$	219	72	0.209	0.427
KX 3	5800^{6340}_{5340}	$14.22^{13.82}_{14.58}$	232	74	0.317	0.756

Object	$T_{\rm eff}$ ($K^{+1\sigma}_{-1\sigma}$)	$M_{\rm bol}$	distance pc	$V_{\rm tan}$ km/s	$V_{\rm max}^{-1}$ (10^{-4}pc^{-3})	V/V_{max}
KX 4	5060^{5480}_{4680}	$14.81^{14.46}_{15.16}$	84	84	0.546	0.081
KX 5	7590^{8800}_{6800}	$13.03^{12.38}_{13.51}$	290	71	0.218	0.914
KX 6	5000^{5420}_{4620}	$14.86^{14.51}_{15.21}$	160	47	1.026	0.907
KX 7	7360^{8630}_{6540}	$13.16^{12.47}_{13.68}$	306	100	0.098	0.470
KX 8	8670^{10450}_{7280}	$12.45^{11.63}_{13.21}$	337	99	0.100	0.602
KX 9	5300^{5750}_{4930}	$14.61^{14.25}_{14.93}$	204	87	0.427	0.722
KX10	4890^{5260}_{4530}	$14.96^{14.64}_{15.30}$	174	57	0.738	0.821
KX11	3970^{4370}_{3750}	$15.87^{15.45}_{16.12}$	105	42	2.892	0.803
KX12	4600^{4970}_{4240}	$15.23^{14.89}_{15.59}$	88	23	4.822	0.815
KX13	6370^{7010}_{5850}	$13.80^{13.38}_{14.18}$	277	150	0.168	0.627
KX14	3900^{4380}_{3750}	$15.95^{15.44}_{16.12}$	98	103	3.143	0.705
KX15	5560^{5710}_{5430}	$14.40^{14.28}_{14.50}$	56	36	1.330	0.060
KX16	5800^{6320}_{5360}	$14.22^{13.84}_{14.56}$	170	70	0.243	0.254
KX17	8300^{10100}_{7140}	$12.64^{11.77}_{13.30}$	82	48	0.593	0.080
KX18	7690^{9050}_{6830}	$12.97^{12.26}_{13.49}$	263	85	0.143	0.468
KX19	15620^{21150}_{9690}	$9.86^{8.54}_{11.96}$	619	167	0.033	0.783
KX20	15380^{16440}_{14450}	$9.93^{9.63}_{10.20}$	100	38	1.114	0.268
KX21	6120^{6710}_{5640}	$13.98^{13.57}_{14.34}$	225	104	0.201	0.441
KX22	6970^{7350}_{6690}	$13.40^{13.17}_{13.58}$	192	77	0.181	0.259
KX23	6570^{6750}_{6410}	$13.66^{13.55}_{13.77}$	124	57	0.384	0.169
KX24	4950^{5340}_{4600}	$14.91^{14.58}_{15.23}$	82	21	5.556	0.749
KX25	9210^{11210}_{7860}	$12.18^{11.32}_{12.88}$	401	156	0.044	0.408
KX26	5020^{5420}_{4660}	$14.85^{14.51}_{15.17}$	127	52	0.568	0.266
KX27	7340^{7640}_{7050}	$13.18^{13.00}_{13.35}$	86	117	0.107	0.017
KX28	8660^{10440}_{7340}	$12.45^{11.63}_{13.18}$	414	248	0.053	0.525
KX29	7850^{8220}_{7520}	$12.88^{12.68}_{13.07}$	118	34	1.546	0.584
KX30	5150^{5490}_{4840}	$14.74^{14.45}_{15.01}$	175	119	0.508	0.569
KX31	6640^{7430}_{6060}	$13.62^{13.12}_{14.02}$	180	44	0.775	0.943
KX32	13060^{16410}_{10400}	$10.65^{9.64}_{11.65}$	151	36	1.319	0.997
KX33	4650^{4980}_{4320}	$15.18^{14.88}_{15.51}$	144	81	1.095	0.730

Object	$T_{\rm eff}$ ($K^{+1\sigma}_{-1\sigma}$)	$M_{\rm bol}$	distance pc	$V_{\rm tan}$ km/s	$V_{\rm max}^{-1}$ (10^{-4}pc^{-3})	V/V_{max}
KX34	6940^{7860}_{6310}	$13.42^{12.88}_{13.84}$	62	37	1.222	0.074
KX35	8390^{10240}_{7240}	$12.59^{11.72}_{13.24}$	205	49	0.566	0.969
KX36	7270^{8260}_{6570}	$13.22^{12.66}_{13.66}$	267	144	0.109	0.373
KX37	20560^{27560}_{15870}	$8.65^{7.36}_{9.79}$	273	170	0.032	0.116
KX38	10250^{13600}_{8620}	$11.71^{10.47}_{12.47}$	192	82	0.155	0.224
KX39	4910^{5230}_{4600}	$14.95^{14.67}_{15.23}$	156	62	0.760	0.623
KX40	7180^{8300}_{6460}	$13.27^{12.64}_{13.74}$	260	80	0.164	0.519
KX41	4650^{4820}_{4500}	$15.18^{15.03}_{15.33}$	43	72	1.062	0.022
KX42	4680^{5050}_{4320}	$15.16^{14.82}_{15.51}$	61	54	0.926	0.053
KX43	15360^{20230}_{9990}	$9.93^{8.72}_{11.82}$	423	143	0.045	0.464
KX44	5540^{6070}_{5110}	$14.41^{14.01}_{14.77}$	231	78	0.328	0.770
KX45	7040^{8060}_{6370}	$13.36^{12.77}_{13.80}$	246	59	0.347	0.960
KX46	4760^{5130}_{4390}	$15.08^{14.75}_{15.44}$	119	102	0.863	0.333
KX47	7400^{8300}_{6670}	$13.14^{12.64}_{13.60}$	244	97	0.104	0.281
KX48	4290^{4670}_{3850}	$15.53^{15.16}_{16.01}$	115	36	2.092	0.742
KX49	5230^{5660}_{4860}	$14.67^{14.32}_{14.99}$	170	59	0.577	0.600
KX50	4860^{5230}_{4500}	$14.99^{14.67}_{15.33}$	114	45	0.711	0.249
KX51	4360^{4730}_{3950}	$15.47^{15.11}_{15.89}$	61	48	1.608	0.093
KX52	6540^{7300}_{6000}	$13.68^{13.20}_{14.06}$	216	77	0.180	0.354
KX53	6070^{6510}_{5700}	$14.01^{13.70}_{14.29}$	285	93	0.199	0.795
KX54	7350^{8330}_{6610}	$13.17^{12.62}_{13.64}$	291	72	0.210	0.890
KX55	8160^{10020}_{6980}	$12.71^{11.81}_{13.40}$	434	175	0.060	0.661
KX56	4900^{5300}_{4520}	$14.95^{14.61}_{15.31}$	121	96	0.661	0.271
KX57	3750^{3980}_{3750}	$16.12^{15.86}_{16.12}$	79	41	5.009	0.608
KX58	3750^{3930}_{3750}	$16.12^{15.92}_{16.12}$	49	28	4.411	0.134

Table 7.1: Derived stellar parameters for CWD sample assuming a Hydrogen atmosphere.

Object	$T_{\rm eff}$ ($K^{+1\sigma}_{-1\sigma}$)	$M_{\rm bol}$	distance pc	$V_{\rm tan}$ km/s	$V_{\rm max}^{-1}$ ($10^{-4}{\rm pc}^{-3}$)	V/V_{max}
KX 1	5250^{5520}_{5030}	$14.68^{14.45}_{14.86}$	151	102	0.436	0.326
KX 2	6340^{6950}_{5890}	$13.85^{13.45}_{14.18}$	255	84	0.144	0.438
KX 3	6050^{6540}_{5710}	$14.06^{13.72}_{14.31}$	263	84	0.231	0.760
KX 4	5460^{5780}_{5210}	$14.50^{14.26}_{14.71}$	104	104	0.315	0.085
KX 5	7780^{8820}_{6990}	$12.96^{12.41}_{13.43}$	310	76	0.185	0.915
KX 6	5460^{5790}_{5210}	$14.50^{14.25}_{14.71}$	204	60	0.536	0.909
KX 7	7400^{8320}_{6700}	$13.18^{12.67}_{13.61}$	318	103	0.090	0.473
KX 8	8120^{9290}_{7240}	$12.77^{12.19}_{13.27}$	305	90	0.125	0.595
KX 9	5670^{5990}_{5390}	$14.34^{14.10}_{14.56}$	245	105	0.266	0.729
KX10	5300^{5560}_{5080}	$14.63^{14.43}_{14.82}$	217	71	0.415	0.825
KX11	4720^{4940}_{4530}	$15.14^{14.94}_{15.32}$	147	59	1.156	0.808
KX12	5290^{5550}_{5050}	$14.64^{14.43}_{14.85}$	128	33	1.706	0.819
KX13	6540^{7200}_{6090}	$13.72^{13.30}_{14.03}$	301	163	0.138	0.632
KX14	4600^{4780}_{4440}	$15.25^{15.09}_{15.41}$	128	135	1.478	0.710
KX15	5750^{5860}_{5650}	$14.28^{14.20}_{14.36}$	62	39	1.015	0.061
KX16	6070^{6550}_{5730}	$14.04^{13.71}_{14.30}$	195	80	0.175	0.261
KX17	7960^{9090}_{7130}	$12.86^{12.28}_{13.34}$	77	46	0.682	0.079
KX18	7740^{8760}_{6950}	$12.98^{12.44}_{13.45}$	272	88	0.132	0.471
KX19	11830^{15400}_{9850}	$11.13^{9.97}_{11.93}$	471	127	0.058	0.760
KX20	14660^{15990}_{13740}	$10.19^{9.81}_{10.47}$	98	37	1.175	0.268
KX21	6360^{6910}_{5930}	$13.84^{13.48}_{14.15}$	251	116	0.154	0.449
KX22	7040^{7380}_{6760}	$13.39^{13.19}_{13.57}$	201	81	0.161	0.262
KX23	6640^{6820}_{6470}	$13.65^{13.53}_{13.76}$	130	60	0.338	0.171
KX24	5370^{5660}_{5140}	$14.58^{14.35}_{14.77}$	102	27	2.960	0.752
KX25	8890^{10340}_{7830}	$12.38^{11.72}_{12.93}$	378	147	0.050	0.400
KX26	5420^{5720}_{5190}	$14.54^{14.30}_{14.73}$	157	64	0.328	0.275
KX27	7230^{7550}_{6940}	$13.28^{13.09}_{13.46}$	86	117	0.107	0.017
KX28	8220^{9410}_{7320}	$12.72^{12.13}_{13.23}$	383	230	0.063	0.516
KX29	7920^{8270}_{7610}	$12.88^{12.69}_{13.06}$	122	35	1.392	0.585
KX30	5280^{5540}_{5070}	$14.65^{14.44}_{14.83}$	188	128	0.422	0.572

Object	$T_{\rm eff}$ ($K^{+1\sigma}_{-1\sigma}$)	$M_{\rm bol}$	distance pc	$V_{\rm tan}$ km/s	$V_{\rm max}^{-1}$ ($10^{-4}{\rm pc}^{-3}$)	V/V_{max}
KX31	6780^{7500}_{6250}	$13.56^{13.12}_{13.92}$	193	47	0.643	0.944
KX32	10810^{13510}_{9190}	$11.52^{10.55}_{12.23}$	121	29	2.431	0.997
KX33	4940^{5160}_{4760}	$14.94^{14.75}_{15.10}$	165	93	0.767	0.733
KX34	7080^{7920}_{6460}	$13.37^{12.88}_{13.77}$	66	39	1.019	0.075
KX35	8090^{9240}_{7230}	$12.79^{12.21}_{13.28}$	196	47	0.639	0.969
KX36	7480^{8430}_{6780}	$13.13^{12.61}_{13.56}$	290	156	0.091	0.380
KX37	14720^{26300}_{11470}	$10.17^{7.61}_{11.27}$	208	129	0.055	0.099
KX38	9910^{11890}_{8580}	$11.90^{11.11}_{12.53}$	178	76	0.187	0.220
KX39	5090^{5320}_{4910}	$14.81^{14.62}_{14.97}$	170	68	0.606	0.626
KX40	7250^{8130}_{6570}	$13.27^{12.77}_{13.70}$	272	84	0.147	0.522
KX41	5080^{5190}_{4990}	$14.82^{14.73}_{14.90}$	53	90	0.588	0.023
KX42	5180^{5420}_{4980}	$14.73^{14.54}_{14.90}$	79	71	0.459	0.056
KX43	11680^{15030}_{9760}	$11.19^{10.08}_{11.97}$	322	109	0.080	0.433
KX44	5550^{5980}_{5210}	$14.43^{14.11}_{14.71}$	236	80	0.312	0.771
KX45	7140^{7990}_{6490}	$13.33^{12.84}_{13.75}$	260	63	0.303	0.960
KX46	5260^{5520}_{5050}	$14.67^{14.45}_{14.85}$	155	133	0.425	0.344
KX47	7720^{8730}_{6950}	$12.99^{12.46}_{13.45}$	270	107	0.083	0.289
KX48	4970^{5180}_{4780}	$14.91^{14.73}_{15.09}$	162	51	0.813	0.749
KX49	5570^{5900}_{5310}	$14.42^{14.17}_{14.63}$	203	70	0.364	0.607
KX50	5350^{5630}_{5120}	$14.59^{14.37}_{14.78}$	149	59	0.359	0.259
KX51	5020^{5240}_{4830}	$14.87^{14.68}_{15.04}$	86	68	0.638	0.099
KX52	6730^{7440}_{6220}	$13.59^{13.15}_{13.94}$	235	84	0.147	0.360
KX53	6000^{6400}_{5710}	$14.09^{13.81}_{14.31}$	284	93	0.199	0.795
KX54	7570^{8540}_{6840}	$13.08^{12.55}_{13.52}$	316	78	0.173	0.892
KX55	7810^{8910}_{7010}	$12.94^{12.37}_{13.41}$	410	166	0.068	0.656
KX56	5390^{5690}_{5150}	$14.56^{14.33}_{14.76}$	157	125	0.335	0.281
KX57	4480^{4680}_{4310}	$15.37^{15.18}_{15.53}$	100	53	2.538	0.612
KX58	4570^{4750}_{4420}	$15.28^{15.11}_{15.43}$	67	39	1.824	0.138

Table 7.2: Derived stellar parameters for CWD sample assuming a Helium atmosphere.

7.5 Checks on Derived Parameters

The space densities calculated using the $1/V_{max}$ method can be used to check that the sample is consistent with being drawn from a complete survey by using the $\langle V/V_{max} \rangle$ completeness test. This test uses the prediction that a sample extracted from a survey evenly sampling a uniform distribution of stars should have $\langle V/V_{max} \rangle = 0.5$. In the past CWD surveys have not generally passed this test. For example the LRB sample has $\langle V/V_{max} \rangle = 0.37$. The OSWH sample is also incomplete ($\langle V/V_{max} \rangle = 0.324$) although the authors investigated the sample and used completeness correction factors to boost space density estimates. The fact that $\langle V/V_{max} \rangle < 0.5$ for both these samples suggests that the Luyten survey was incomplete within the limits used, failing to detect more distant objects with faint apparent magnitudes or small proper motions. Interestingly, the WD sample of Evans (1992) found using the APM plate measuring machine does pass the completeness test ($\langle V/V_{max} \rangle = 0.492$).

The $\langle V/V_{max} \rangle$ test has been applied to this sample by assuming the sample consists of either entirely H atmosphere WDs or entirely He. The calculated value of $\langle V/V_{max} \rangle$ is 0.495 in the former case and 0.497 in the latter. Disregarding the observational errors in calculating V/V_{max}, the expected errors in $\langle V/V_{max} \rangle$ for a perfectly defined sample may be used to assess whether the sample is consistent with being drawn from a complete survey. The variance of a variable x obeying probability density function $P(x)$ is given by

$$\sigma^2 = \int_{-\infty}^{\infty} (x - \overline{x})^2 P(x) \mathrm{d}x = \int_{-\infty}^{\infty} x^2 P(x) \mathrm{d}x - \overline{x}^2. \tag{7.6}$$

The probability density function of V/V_{max} for a complete survey should be

$$P(V/V_{max}) = \begin{cases} 1 & \text{if } 0 \leq V/V_{max} \leq 1 \\ 0 & \text{otherwise} \end{cases} \tag{7.7}$$

and using $\langle V/V_{max} \rangle = 0.5$ the variance is

$$\sigma^2 = \left[\frac{(V/V_{max})^3}{3} \right]_0^1 - 0.25 = 0.083. \tag{7.8}$$

A sample of N objects drawn from a complete survey should therefore have mean

$$\langle V/V_{max} \rangle = 0.5 \pm \frac{0.29}{\sqrt{N}}. \tag{7.9}$$

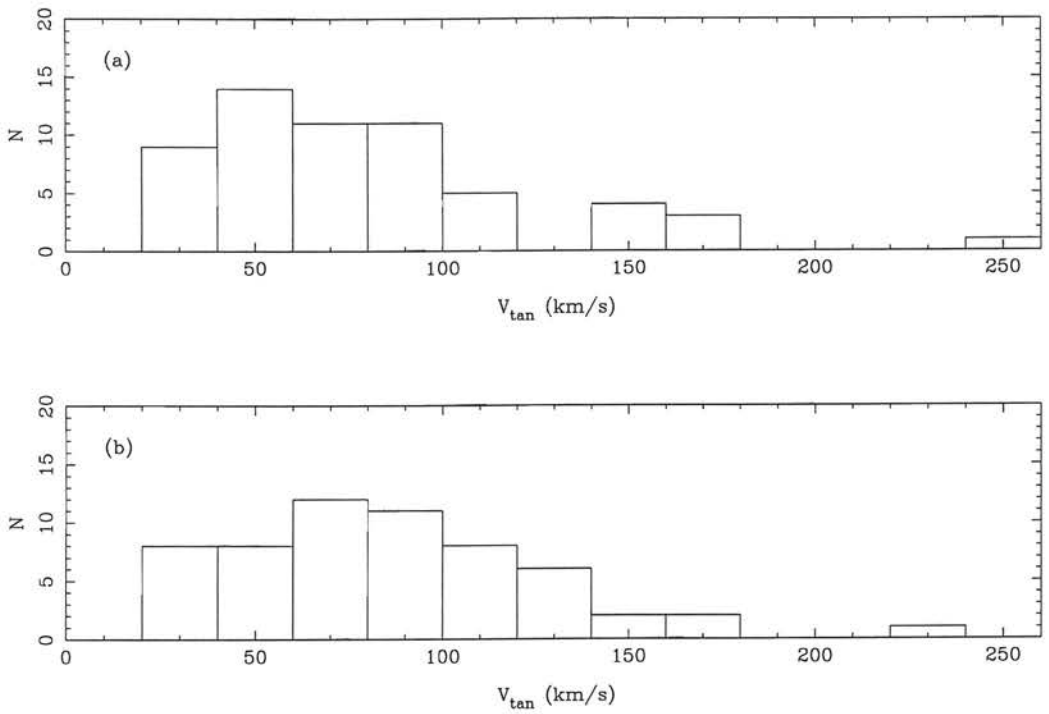

Figure 7.7: The distribution of tangential velocities for this survey sample using distances obtained assuming both a Hydrogen atmosphere (a) and Helium atmosphere (b).

which, for a sample containing 58 objects, implies $\langle V/V_{max} \rangle$ should be within 0.038 of 0.5. Since the $\langle V/V_{max} \rangle$ values given above satisfy this criterion, the survey may be said to be consistent with being complete without invoking the observational errors associated with the quantities used to calculate $\langle V/V_{max} \rangle$. Of course, this result only gives confidence that the survey is evenly sampling the survey volume, but gives no assurance that all the WDs have been discovered. The completeness concerns raised in Section 7.2 cannot be investigated with the V/V_{max} test because the test is not sensitive to the RPMD sample selection criteria.

A measure of the tangential velocities for each object have been calculated in order to confirm once more that this sample broadly agrees with expectations and results from other surveys. In a kinematical study of white dwarfs, Sion et al. (1988) plotted the distribution of V_{tan} for a large number of WDs (their Figure 1). These findings were used as the basis of the WD kinematics in the Monte-Carlo WD survey study of Wood and Oswalt (1998). The V_{tan} distribution for our sample is displayed in Figure 7.7. The plots are in remarkably good agreement with the those of Sion et al. and Wood and Oswalt.

The high velocity object with $V_{tan} \sim 250$ km/s may appear to be a candidate halo WD. However, Evans (1992) predicted that Disc stars exist with such high velocities at the tail of the V_{tan} distribution. Indeed, LDM (and LRB) include stars with even higher velocities into their Disc sample, and the star in question is therefore retained in this sample.

7.6 The Total WD Space Density

The mass density of WDs has a direct bearing on the putative dark matter distribution in the Disc of the Milky Way. Until recently estimates of the dynamically estimated mass density in the solar neighbourhood, found by analysing the motions of stars perpendicular to the Disk, often exceeded the mass density of observed matter (eg. Kuijken 1995 and references therein). Although the case for a high local mass density from dynamical arguments was far from conclusive, populations of very low luminosity stellar objects such as brown dwarfs and CWDs were natural candidates for investigation as potential dark matter components. However, new results derived from data collected by the Hipparcos satellite (Crézé et al. 1998) indicate that there is no discrepancy between the dynamically estimated mass density and the density of observed matter. This method, which avoids many of the difficulties inherent in previous work such as uncertainties in photometric distances to tracer stars, leaves little room for a population of dark CWDs which add significantly to the observed local mass density.

If the atmosphere constituents for the sample are chosen by selecting the fit with smallest χ^2, the total space density of WDs found for this survey is 0.0042 WDs per cubic parsec. A number of independent estimates of the local number density of WDs have been made in the last decade, which bear interesting comparison with this work. Since these other surveys have been described in Chapter 1, only the space density results and brief notes are displayed in Table 7.3. It should be noted firstly that Wood and Oswalt (1998) in their Monte Carlo simulations of the $1/V_{max}$ method found that total space densities calculated in this way from samples of 50 objects suffer from uncertainties of approximately 50%. The space densities found in LDM and LRB are therefore consistent with this work, although the discrepancy may arise in part from incompleteness in the LHS catalogue. Interestingly, this work does not confirm the much higher space densities found by the

Reference	Space Density pc^{-3}	N_{WDs}	Notes
LDM	0.0032	43	$1/V_{max}$; LHS stars
Ruiz (1995)	0.0080	8	high proper motion blink survey
LRB	0.0034	43	$1/V_{max}$; redetermination of LDM
Festin (1998)	0.0150	7	Volume limited sample
This Work	0.0042	58	
OSWH	0.0053	50	$1/V_{max}$; CPMB Luyten stars

Table 7.3: Previous WD space density estimates

recent studies of Ruiz and Takamiya (1995) and Festin (1998). However, these authors make only a tentative claim to detection of a high WD space density due to the small samples ($N < 10$) involved. The OSWH sample has been separated from the other surveys in Table 7.3 because it is essentially measuring a different quantity, the space density of WDs in wide-binaries. An order of magnitude calculation illustrates the insensitivity of the COSMOS survey to detection of CPMBs: assuming a typical separation of 300 AU for CPMBs and that COSMOS could resolve a binary separated by 10″, an optimally inclined CPMB could be detected at a maximum distance of 30pc. If the space density of WDs in CPMBs is $0.0053pc^{-3}$ the survey should detect < 0.4 of such objects. The OSWH findings should therefore be viewed separately, and the *real* total WD space density is the sum of binary members and single WDs. Of course this is complicated by the fact that WDs detected as single stars may in fact be members of unresolved binaries. What is clear however is that WDs represent a small fraction ($< 10\%$) of the local mass density, consistent with the recent determination of the dynamically estimated mass density.

Chapter 8

The white dwarf luminosity function and the age of the Disc

8.1 Introduction

Tables 7.1 and 7.2 contain bolometric magnitude and space density estimates for each sample object – all the basic information required for constructing a LF. Of course the principle atmospheric constituent of each sample member remains unknown, a problem which must be addressed in this Chapter. In Section 8.2 the procedure adopted for construction an observational WDLF from the sample stars is described. The desired result is a WDLF suitable for fitting to theoretical models, hopefully with attendant realistic error estimates. A brief discussion and description of the models used is given in Section 8.3. The method of fitting the data to the models is described in Section 8.4, while further potential sources of error are discussed in Section 8.5.

8.2 The Observational WDLF

The WDLF is a measure of WD space density as a function of luminosity. Traditionally, space densities have been measured in units of number per cubic parsec per bolometric magnitude interval and luminosities as a fraction of solar luminosity, $L_{\odot}$. WDLFs are

usually depicted as a log-log plot of these quantities. Construction of a LF from the sample objects is simply a matter of summing the space densities of every object in a given luminosity bin, j:

$$\Phi_j = \sum_{i=1}^{N_j} \frac{\phi_i}{b} \tag{8.1}$$

where there are N_j lying within the bin boundaries and ϕ_i is the space density associated with the i th object in the bin, taken to be the reciprocal of the volume calculated according to Equation 7.5 and tabulated in Tables 7.1 and 7.2. The factor $\frac{1}{b}$ in the summation puts space densities in a bin of size b into units of $\mathrm{pc}^{-3}\mathrm{M}_{\mathrm{bol}}^{-1}$. Thus space densities in every populated bin are derived, leaving only the problem of assigning errors to the data. LDM and subsequent authors have set the uncertainty in space density contribution associated with a single object as equal to the space density itself, and summed the errors in quadrature. This amounts to describing each object as a detection of 1 ± 1 objects. Thus in a bin j, containing N_j objects with identical associated space density ϕ, the error on the total space density Φ_j $(= N_j\phi)$ is $\sigma_{\Phi_j} = \sqrt{N_j}\phi$. In the case of approximately equal space density contributions in a bin the errors are therefore essentially Poissonian. However, in a hypothetical bin containing one space density contribution significantly larger than all the others the error on the resulting space density would be defined almost entirely by the large space density object, and this error would be larger than the optimum situation described above where all the space density contributions are equal. The LDM prescription may therefore be described as conservative, and it's applicability to the WDLF was one of the questions addressed by Wood and Oswalt (1998) in their Monte Carlo simulations of WD surveys. They found that the method of calculating errors on space densities described above was consistent with the sample to sample variations found in their simulations, and this prescription is therefore adopted here. As may be seen on inspection of Tables 7.1 and 7.2, the uncertainties in bolometric magnitude, which is related to the luminosity via

$$M_{bol} = -2.5 \log L/L_{\odot} + 4.75, \tag{8.2}$$

can be as large as $1M_{bol}$ for hotter WDs, although the errors are generally restricted to a few tenths of a magnitude. These errors are derived from the fits of the photometry to model atmospheres and are not symmetrical about the fitted value. Incorporating these errors into the LF requires a slightly different approach to that taken by previous authors who have neglected errors in luminosity and placed each point in the centre of its luminosity bin. For this work, the position of each point on the luminosity axis is

determined by the mean luminosity of the objects falling within that bin. This should lead to a more realistic LF, since for example a luminosity bin positioned near the cut-off in a LF may well be composed of objects with luminosities strongly biased towards the more populated side of the bin. In this case placing the point at the centre of the bin would artificially shift the position of the cut-off, whereas using the mean luminosity gives a truer reflection of the LF. Since the luminosity errors are asymmetrical, separate upper and lower horizontal error bars are calculated for each point. For a bin containing N objects the upper luminosity 1 sigma uncertainties, σ_u, are combined using

$$\sigma_U = \sqrt{\frac{\sum_i^N \sigma_{u_i}^2}{N}} \tag{8.3}$$

to yield an estimate for the horizontal error bar σ_U, with an analogous procedure used for the lower luminosity error bounds.

Construction of a WDLF requires selection of either a hydrogen or helium atmosphere for each sample object. Since the atmosphere constituent is not constrained by the fits to photometry a reliable choice of atmosphere cannot be made. This difficulty will be addressed in Section 8.4, and the definition of the 'first-guess' WDLF is sufficient for now. The 'first-guess' LF assigns each star the atmosphere with the lower χ^2 model fit to the photometry, with the exception of objects with $6000 > T_{\mathrm{eff_H}} > 5000$ which are deemed to be occupying the 'non-DA gap' at this temperature (BRL and Section 8.4) and are therefore automatically designated a pure H atmosphere. Since the atmospheres are not constrained however, this is effectively one arbitrarily picked example of the many LFs obtainable by changing the atmosphere constituent of each object.

The 'first-guess' LF, calculated in integer magnitude bins for WDs with $M_{\mathrm{bol}} > 12.25$, is given in Table 8.1. The luminosity errors on WDs brighter than $M_{\mathrm{bol}} = 12.25$ are sufficiently large that broader binning is appropriate, and the 6 objects that fall into this category have been placed in a larger bin spanning the range $(3 > -\log L/L_{\odot} > 2)$, which has a space density of -3.95 pc^{-3}M$_{\mathrm{bol}}^{-1}$ and mean luminosity $-2.43 \log L/L_{\odot}$. This LF is displayed in Figure 8.1, along with the LRB WDLF for comparison. Also plotted on Figure 8.1 is the LF derived by LDM from the hot WD study of Fleming, Liebert and Green (1986, henceforth FLG). A notable aspect of Figure 8.1 is the broad agreement between the datasets. The large bin containing hotter WDs from this survey is in excellent agreement with FLG, although the apparent lack of a smooth continuity between the FLG

Bin Center			Space Density	
$M_{\rm bol}$	$-\log L/L_{\odot}$	$\overline{-\log L/L_{\odot}}$	$\log\{[\sum(1/V_{max})]\,M_{\rm bol}^{-1}\}$	Number
11	2.5	2.43(1.89,2.75)	-3.94(-3.74,-4.37)	6
12.75	3.20	3.27(3.05,3.45)	-3.39(-3.23,-3.65)	14
13.75	3.60	3.62(3.44,3.76)	-3.32(-3.18,-3.51)	13
14.75	4.00	4.04(3.92,4.15)	-2.68(-2.56,-2.84)	20
15.75	4.40	4.30(4.18,4.40)	-2.97(-2.80,-3.24)	5

Table 8.1: 'First guess' Luminosity Function.

and the LRB LF is confirmed with these new data. The discrepancy is not large however, and would disappear easily if the faintest FLG bin was slightly overestimated. The WDLF from this work and the LRB LF are also fairly consistent, with this data suggesting a more peaked LF and slightly shallower cut-off. A final point regarding the observed WDLF concerns the faint cut-off at low luminosities. Although there is no data beyond the bin centred on $15.75M_{\rm bol}$, if the survey is sensitive to such faint stars then the *lack* of detected objects assumes added significance. Some idea of the predicted behaviour of very cool faint WDs is required to approach this problem, and the recent model atmospheres of Hansen (1998) provide BVR photometry for both hydrogen and helium atmosphere WDs down to effective temperatures of 2000K. It is then possible to estimate the volume sampled by the survey for a given WD luminosity by imposing the surveys photometric limits for varying WD luminosity, as shown in Figure 8.2. Analysis of this question is greatly aided by the fact that for such intrinsically faint objects the survey proper motion limits become irrelevant. To illustrate this consider a WD with $\log L/L_{\odot} = -4.8$, the next faintest bin in Table 8.1. Such an object can have a maximum distance of less than 100pc according to Figure 8.2 and thus even with a low tangential velocity of 40km/s (see Figure 7.7) the star would have a proper motion of $0.84''$/yr, well within the proper motion survey limit. The photometric survey limit then imposes an unambiguous distance limit on stars of a given magnitude, for which the survey can be said to be sampling a well defined volume (see also Figure 5.1).

It is possible to use the empty bin beyond the last occupied bin in this work because the portion of the RPMD in which fainter WDs would be expected to be found is empty. This may be seen clearly in Figure 7.2, where the cooler BRL WDs lie on a line that

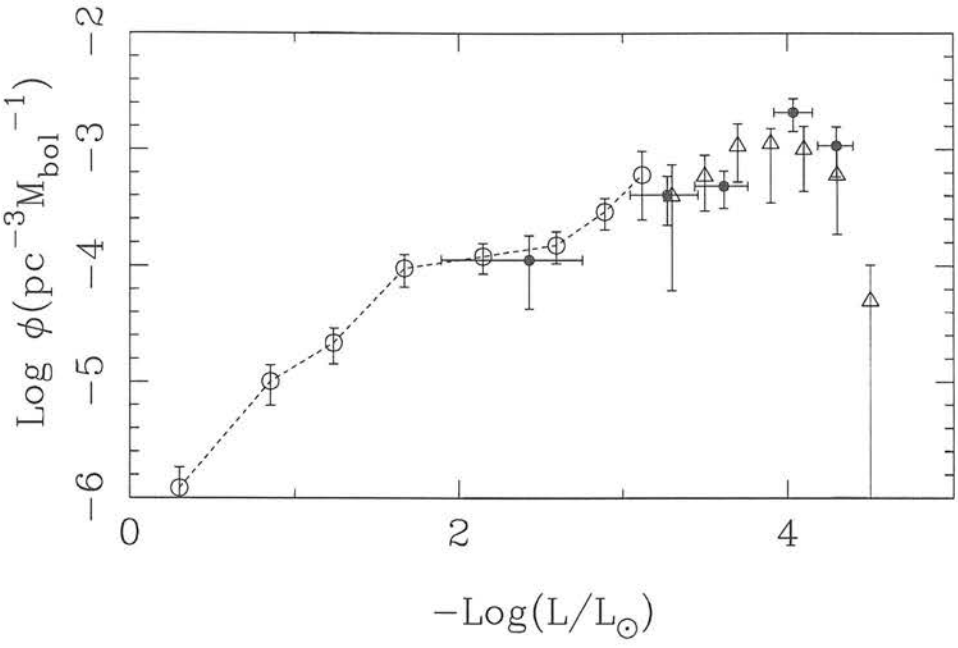

Figure 8.1: Observational LF with comparisons: this work (filled circles), hot WDLF based on Fleming, Liebert and Green (1986) from LDM (open circles) and the LRB redetermination of the LDM CWDLF (open triangles)

is a continuation of the locus of the bluer stars. Inspection of Figure 6.1 for example, shows that this region of the RPMD is empty for this surveys catalogue. In addition, the independent searches for faint and high proper motion objects detailed in Section 5.5 give further confidence that there are no cool WDs accidently omitted from the catalogue.

8.3 Theoretical WDLFs

An estimate of the Disc age may be obtained by comparing observational WDLF with expectations from theoretical models. Two sets of theoretical LFs have been used in this work. The important inputs into the model WDLFs are highlighted in this Section, and the differences between the two sets of models described.

The key inputs required to construct a theoretical WDLF are

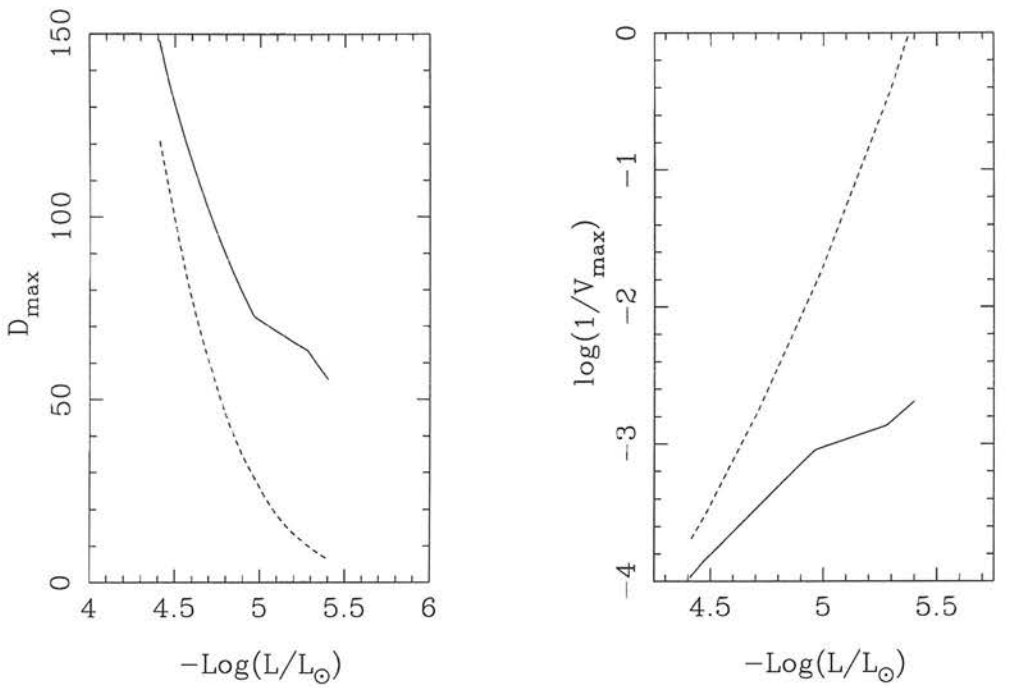

Figure 8.2: The predicted maximum distance, D_{max}, at which a WD of given luminosity will be detectable given the photometric limits of this survey. The full line represents a hydrogen atmosphere WD, the dashed line a helium atmosphere. Both curves are defined by the B passband survey limit. Also plotted on the right hand panel is corresponding space density associated with these distances.

- Realistic numerical WD model evolutionary sequences
- Main sequence progenitor lifetimes
- Main sequence progenitor mass limits
- Main sequence progenitor $\rightarrow$ WD mass relation
- The star formation rate (SFR)
- The initial mass function (IMF)
- The age of the Galactic Disc (t_{disc})

and these are combined to produce a LF in the following fashion. In a scenario where the rate of formation of WDs is constant, the distribution of number of WDs as a function of cooling time experienced, t_{cool} , is uniform. A WD cooling theory, in the form of detailed numerical evolutionary sequences, can provide a relationship between t_{cool} and

the luminosity of a WD of a given mass (and composition). Considering only WDs of a particular mass, M_{WD}, the distribution of WDs as a function of M_{bol} is simply a projection of the flat distribution in the t_{cool} plane onto the M_{bol} plane, and

$$\Phi(M_{bol}, M_{WD}) \propto \frac{dt_{cool}(M_{WD})}{dM_{bol}} \equiv \tau_{cool}(M_{WD}, M_{bol}). \tag{8.4}$$

Thus the number of WDs expected at a particular magnitude is proportional to $\tau_{cool}(M_{WD}, M_{bol})$, and adding up the contributions from the range of expected WD masses yields

$$\Phi(M_{bol}) = \int_{M_{min}}^{M_{max}} \tau_{cool}(M_{WD}, M_{bol}) \mathrm{d}M. \tag{8.5}$$

The abundance of WDs varies as a function of mass however, and is defined by the distribution of masses of the main sequence progenitors, the IMF. The rate of formation of progenitors may also vary as a function of time, and should be included in the model. For these reasons it is convenient to describe the WDLF in terms of the mass of the progenitor stars rather than the WD mass, although this obviously requires knowledge of the relationship between the progenitor and WD mass. The relevant star formation rate for a WD of given luminosity and progenitor mass is

$$\psi(t_{disc} - t_{cool}(M_{bol}, M) - t_{ms}(M)) \tag{8.6}$$

where t_{disc} is the Disc age and t_{ms} is the main-sequence life of a WD progenitor of mass M. The WDLF can now be written

$$\Phi(M_{bol}, t_{disc}) = \int_{M_{min}(M_{bol})}^{M_{max}} \tau_{cool}(M_{bol}, M)\phi(M)\psi(t_{disc} - t_{cool}(M_{bol}, M) - t_{ms}(M))dM \tag{8.7}$$

where the mass is integrated between the minimum mass, $M_{min}(M_{bol})$ constrained by the age of the disc such that

$$t_{ms}(M_{min}) + t_{cool}(M_{min}, M_{bol}) = t_{disc} \tag{8.8}$$

and the maximum WD progenitor mass ($M_{max} \sim 8M_{\odot}$ is typical). The IMF is denoted by $\phi(M)$.

The first set of model WDLFs used are those of Wood, calculated for OSWH. An earlier version of the LFs is described in detail in Wood (1992), where the effect of varying all the input parameters described above was investigated. Parameters were chosen that gave good agreement between the resulting theoretical curves and the LDM LF. The WD

Input	Wood	GB
Cooling Sequences:		
Core composition	Carbon/Oxygen	Carbon/Oxygen($M_{WD} \leq 1.0M_{\odot}$)
		Oxygen/Neon($M_{WD} > 1.0M_{\odot}$)
Crystallisation		phase separation included
Helium layer mass	$10^{-2}M_{WD}$	$10^{-4}M_{WD}$
Other Inputs:		
Pre-MS lifetime	Iben & Laughlin (1989)	Independently calculated
		(with 1% of $\hookleftarrow$)
SFR	Clayton (1988)	Constant
Progenitor mass upper limit	$8M_{\odot}$	$\sim 11M_{\odot}$

Table 8.2: Summary of principal differences between the Wood and GB theoretical WDLFs.

evolutionary models for the WDLFs used here have since been updated (Wood 1995, OSWH), and consist of mixed carbon-oxygen core WDs with hydrogen and helium surface layer masses of 10^{-4} and 10^{-2}M$_*$ respectively. These evolutionary models include the expectation that the degenerate WD core will crystallise at low temperature, with the resulting release of latent heat temporarily slowing WD cooling. Other inputs to the Wood WDLF include a Salpeter IMF and progenitor lifetimes from Iben & Laughlin (1989). Wood (1992) estimated the total error in age estimates using the earlier models arising from uncertainties in the input parameters such as the IMF and initial-final mass relation to be less than 1 Gyr.

The second set of models used are those of García-Berro, Isern & Hernanz (1997), henceforth referred to as GB models. A major difference between these models and those of Wood is the inclusion of an extra energy source at crystallisation: Hernanz et al. (1994) argued that during the phase transition in a carbon/oxygen core, the elements should separate leading to a release of gravitational binding energy. This can lengthen the cooling time of a WD by ~ 2 Gyr. Wood (1995) argued that the physics of the proposed mechanism of energy release was insufficiently understood, and that it did not warrant inclusion into his models. Indeed, the extent of the influence of the proposed element separation heating mechanism is dependent on the initial chemical stratification of the WD core, which in turn depends on the details of pre-WD evolution (Salaris et al. 1997).

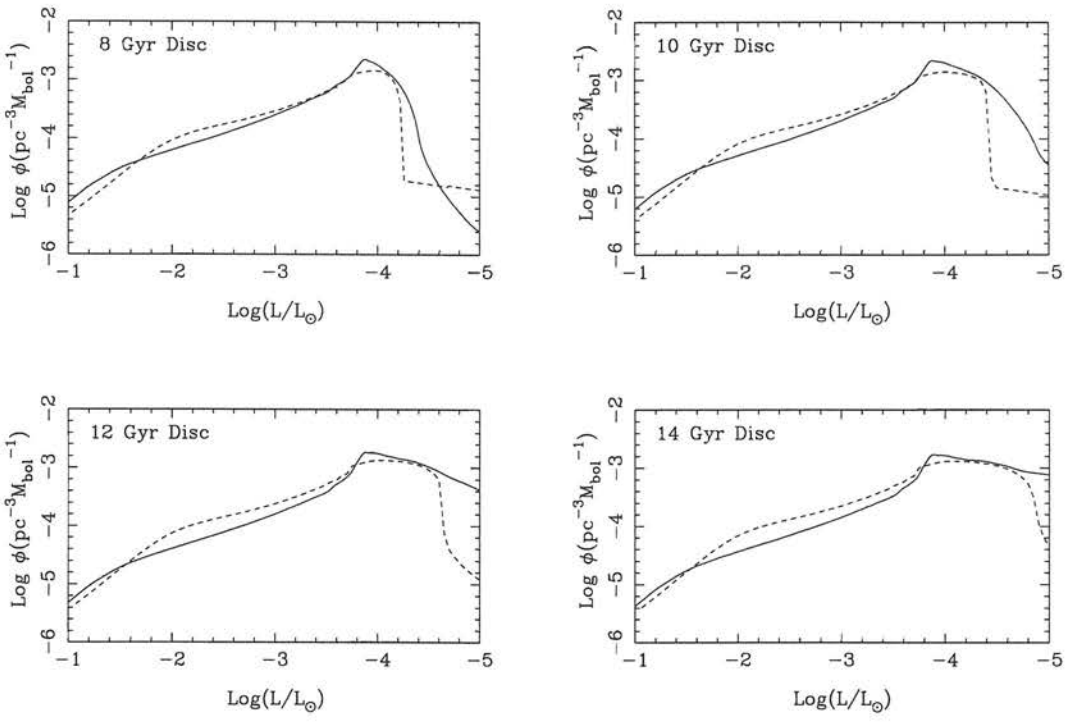

Figure 8.3: Comparison of the Wood (full line) and GB (dashed line) models

This issue represents one of the uncertainties in this method of ageing the Disc however, and highlights the importance of using more than one set of theoretical models.

A second difference in the models lies in the assumed upper limit of main sequence progenitors. Wood adopted an upper limit of $8M_{\odot}$, but but García-Berro, Isern & Hernanz (1997) point out that progenitors in the mass range $8 \leq M \leq 11M_{\odot}$ can form WDs with oxygen/neon cores. These stars cool substantially faster than CO WDs however, and the effect of including them in the treatment of the theoretical WDLF is to introduce a predicted tail of very faint WDs at space densities undetectable with this survey.

Table 8.2 summarises the chief differences between the two sets of model LFs. Wood (1995) adjusted the mass of the atmospheric layers in his models in the light of new observational evidence, increasing them by a factor of 100. The layer masses represent another disparity between the models - the increased layer masses lead to lower estimates for WD cooling ages by $\sim$ 1 Gyr. The Clayton (1988) SFR adopted by Wood shows a peak in star formation a 2-5 Gyr after the formation of the Disc, with a subsequent drop off. Wood (1992) investigated the effects of choosing various SFR schemes, and concluded

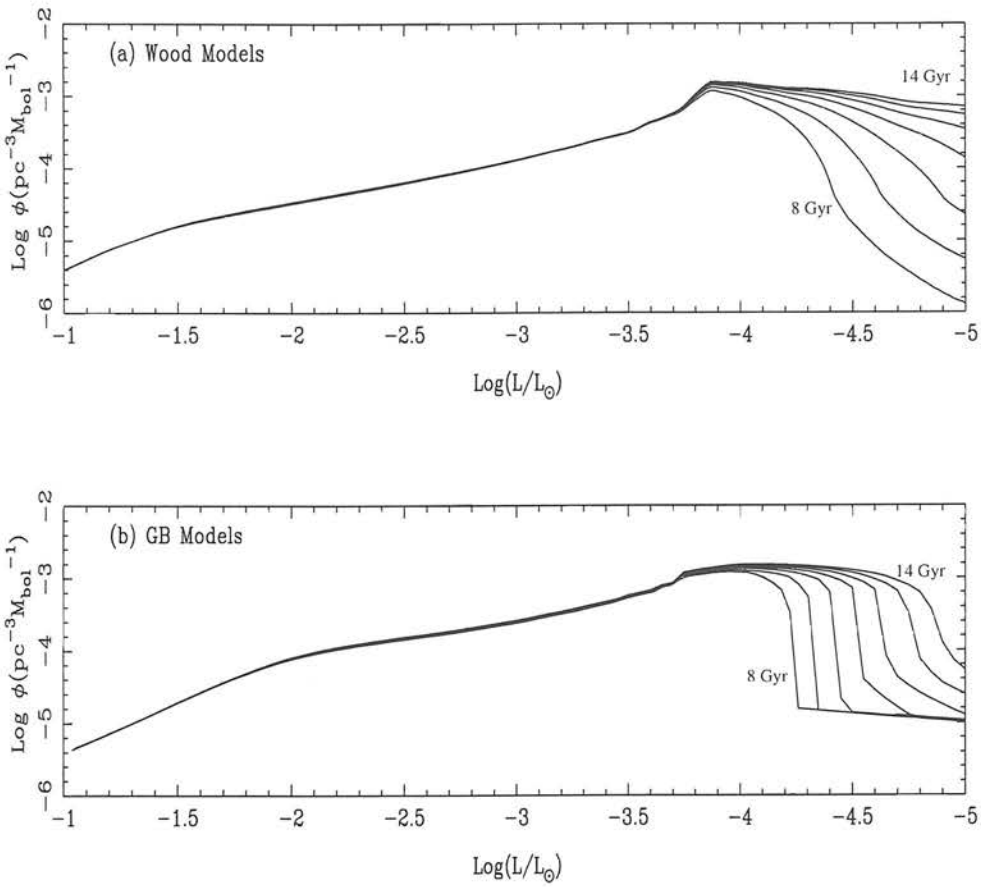

Figure 8.4: All the model WDLFs from 8 to 14 Gyrs

that the uncertainties in derived Disc age introduced by choosing eg. a constant SFR as opposed to the Clayton model were approximately 0.5 Gyr. Both models use a Salpeter (1955) IMF and choose an initial-final mass relation that produces the observed strong peak in WD masses at $\sim 0.6 M_{\odot}$. The error in the Disc age introduced by uncertainties in these inputs is small (Wood 1992).

The Wood and GB model LFs are directly compared in Figure 8.3, where LFs produced for a t_{disc} of 8, 10, 12 and 14 Gyr are displayed. The models are reasonably consistent, the notable differences being the shape of the peak in the LFs - much sharper in the Wood models, and the shape of the cut-off, which is much steeper in the GB models. The tail of ONe massive WDs is clearly visible in the 8 Gyr curves. Finally, the sets of models for 8-14 Gyrs are plotted in Figure 8.4. The models are only available for this work at 1 Gyr intervals, so these are the curves which the observational data must attempt

to distinguish between. What is immediately apparent is that the curves are virtually indistinguishable at luminosities brighter than $\log L/L_{\odot} = -4$ for both sets of models. This is of great significance to the observational astronomer, since it implies that all the useful information pertaining to the age of the Disc is in the last one or two luminosity bins. The Wood models start to diverge at a slightly higher luminosity than the GB models, which as will be seen later allows easier discrimination between Disc ages with the data.

8.4 Deriving a Disc age

The fitting procedure adopted for the WDLF should take into account the errors associated with the data points, the lack of observed objects beyond the last bin, and the ambiguity in the atmospheric constituents of the sample. The first two of these fitting criteria will be addressed first using the example of the 'first-guess' LF. The models are provided at arbitrary total space density, and the first task is to fit the curves to the data on the space density axis. The models predict relative numbers of WDs as a function of luminosity, so this fitting procedure may be thought as sliding the curves up and down the log-log LF plots on the ϕ axis to find the best fit (although the fitting is not done in log space). The fitting procedure maximises the probability of the data set. Considering only errors in one axis for the present, this probability is given by

$$P = \left[\prod_{i=1}^{N}\left\{\exp\left[-\frac{1}{2}\left(\frac{\phi_i - \phi_{model}}{\sigma_i}\right)^2\right]\Delta\phi\right\}\right] \times P_{(0)} \tag{8.9}$$

where the product term contains the probability of observed space density data points given the model prediction assuming normally distributed errors. The term $P_{(0)}$ refers to the probability of finding zero objects in the first empty bin if the model predicts space density ϕ_0. It was argued at the end of Section 8.2 that at faint luminosities the survey is sampling a well defined volume, which at the luminosity of the empty bin is denoted by V_0. The mean number of expected objects is therefore $\phi_0 V_0$ and the probability of detecting zero objects may be found using the Poisson distribution:

$$P(0) = \frac{(\phi_0 V_0)^0 e^{-\phi_0 V_0}}{0!} = e^{-\phi_0 V_0}. \tag{8.10}$$

Since the number of objects in the occupied bins is relatively small, it may be argued

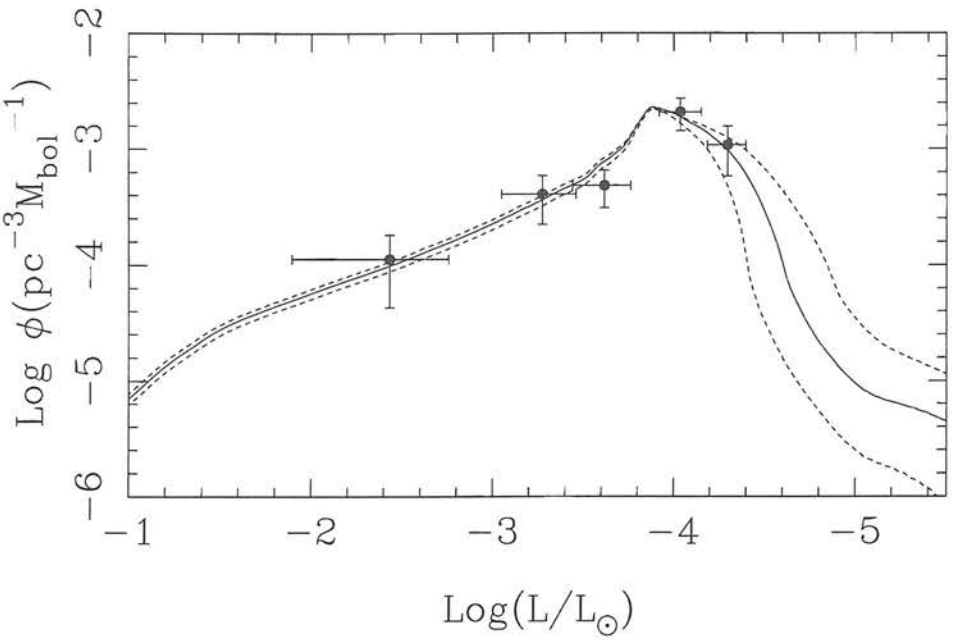

Figure 8.5: The Wood WDLF with a Disc age of 9 Gyr – the best fit to the 'first guess' LF. 8 Gyr (below) and 10 Gyr (above) curves are also shown in dashed lines.

that assuming Gaussian errors in Equation 8.9 is not ideal, and a similar approach to the one used in the empty bin should be used. The difficulty with implementing such a procedure is that for all but the faintest objects the survey is proper motion limited, and thus for a given luminosity it cannot be said to be sampling a well defined volume. The expected number of objects in a given bin cannot therefore be easily calculated, and the Equation 8.9 must serve instead. Only one bin beyond the occupied bins is used to constrain the fit. This is because in subsequent fainter bins where $\log L/L_\odot < -5$ the predicted space density is small, and more importantly the volume surveyed is small, so the expected objects will be approximately zero in any case. Moreover, the theoretical models are probably not reliable at these luminosities since they rely on extrapolations of models of hotter stars (Wood 1992).

Taking the log of Equation 8.9, the quantity minimised should be

$$\left[\sum_{i=1}^{N} \frac{(\phi_i - \phi_{model})^2}{2\sigma_i^2}\right] + \phi_0 V_0. \tag{8.11}$$

This treatment is extended to two dimensions by taking the probability of a particular

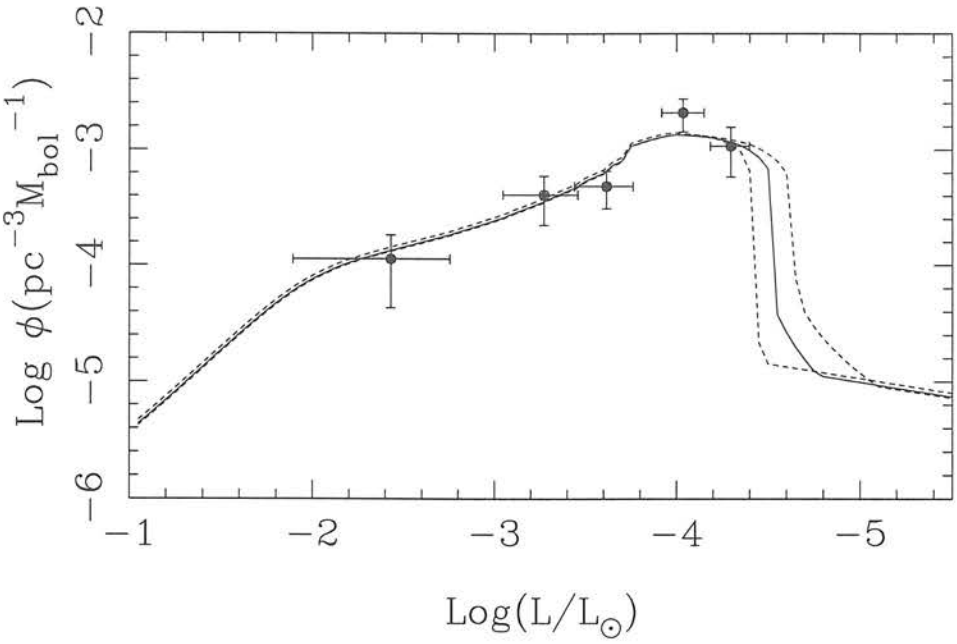

Figure 8.6: The best fit of the 'first guess' LF to the GB WDLF: a Disc age of 11 Gyr with 'adjacent' Disc age LFs shown in dashed lines as in Figure 8.5.

data point to be the probability of the point of closest approach (in terms of the error bars) of the model to the data. Each model corresponding to a given Disc age is fitted to the data by sliding the curves on the space density axis, and the best fits for each of the various Disc age models are compared. For the Wood models the 'first guess' observational LF is best fit by a 9 Gyr Disc model. The fit is shown in Figure 8.5. The GB models fit an 11 Gyr curve to the data best, as plotted in Figure 8.6. Two points to note from Figures 8.5 and 8.6 are firstly that the Wood model appears to follow the peak in the LF better than the GB models, and also that the earlier separation of the Wood models (ie. at higher luminosity) of differing Disc ages increases the discriminatory power of the data. In Figure 8.6, the difference between the 3 models plotted as seen by the data is small.

Once the fitting algorithm has been established the task of assessing the effect of changing the atmospheres of the sample WDs may be undertaken. The extremities of this atmosphere effect may be inspected by constructing either all hydrogen or all helium WD samples. Examples of these with fits to models are shown in Figure 8.7; these are limiting cases with the fitting procedure neglecting the empty bin term, and bracket the more real-

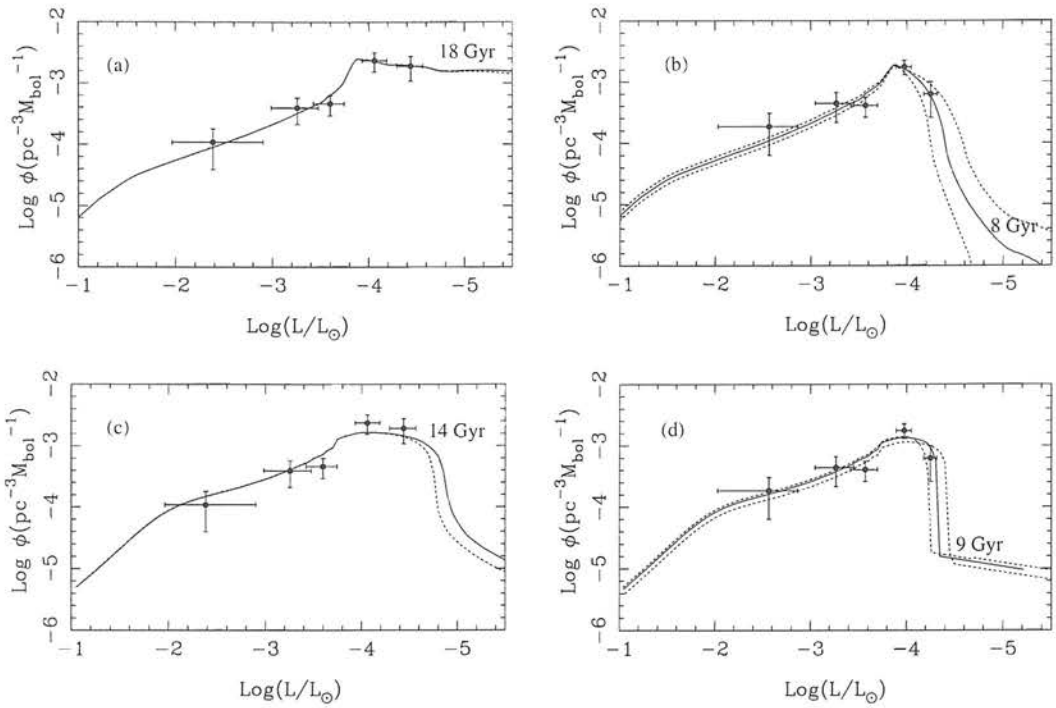

Figure 8.7: Extreme realisations of the WDLF from the sample using either only hydrogen atmosphere WDs (panels (a) and (c)) or only helium (panels (b) and (d)). The Wood (top two) and GB (bottom two) models are fit, with the best fit Disc ages written on each plot.

istic solutions sought. Two results from the study of BRL are pertinent here. Firstly, WDs with effective temperatures between 5000K and 6000K almost invariably have hydrogen rich atmospheres - the so called non-DA gap. This is a purely empirical result and is not predicted by theory. Secondly, hydrogen and helium atmosphere WDs outside the non-DA gap appear in approximately equal numbers. Although evidence for a ratio of 2:1 in favour of DA stars exists for $12000 > T_{\rm eff} > 6000$, a 1:1 ratio is a reasonable estimate, especially for the crucial region near the LF cut-off. The problem of the ambiguity in the sample WDs atmospheres has been approached by constructing a large number of realisations of the WDLF from our sample, each constructed by randomly assigning every object either a hydrogen or helium atmosphere (50% chance of each) unless the effective temperature of the WD is between 5000 and 6000K, in which case a hydrogen atmosphere is automatically assigned. Every WDLF produced is then fit to the models in the manner described above, yielding a best fit Disc age using both the Wood and GB models. A histogram of the results of constructing 1000 realisations of the WDLF is presented in Figure 8.8. The effect of binning has been investigated by producing a further 1000 WDLFs binned in 0.75

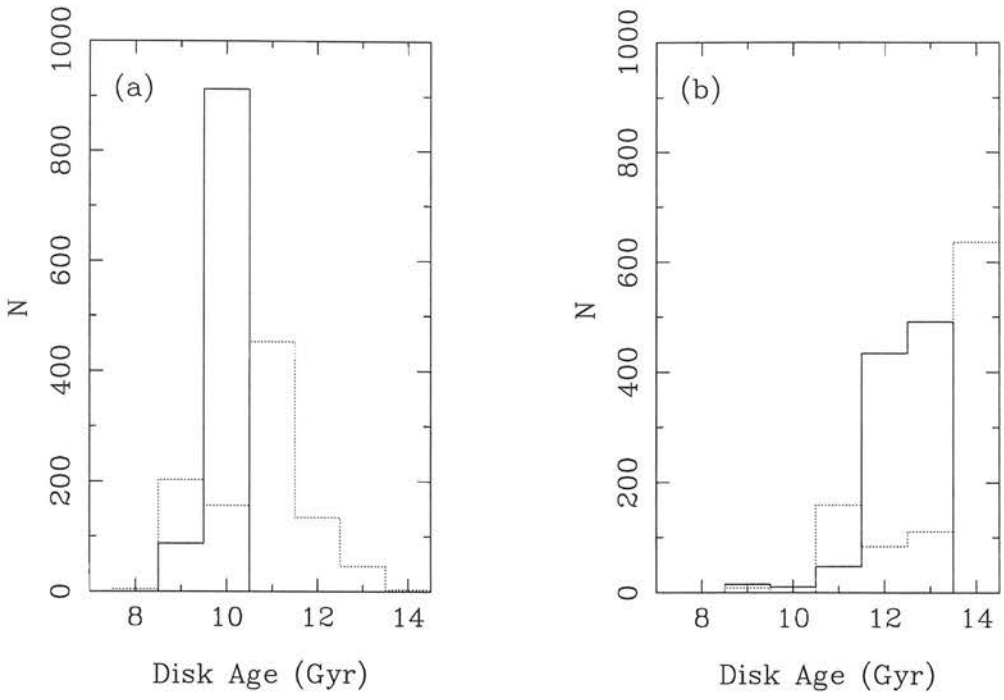

Figure 8.8: Results of constructing WDLFs from our sample by randomly assigning H or He atmospheres. Full line histograms denote 1 $M_{\rm bol}$ bins, dotted lines 0.75 $M_{\rm bol}$ bins. For each bin size 1000 realisations of the WDLF were constructed and fit to the models - the number of times each Disc age was the best fit is displayed. Graph (a) shows fits to the Wood models, graph (b) fits to GB.

M_{bol} bins.

The 1 $M_{\rm bol}$ binned LFs give rise to well constrained Disc ages with both sets of models, with the Wood models strongly favouring a 10 Gyr Disc and the GB models a 12-13 Gyr Disc. The effect that variations in binning can have on the fits is demonstrated in Figure 8.8 (b). The major contributor to this problem seems to be that the GB model curves are sufficiently indistinct in the region of our sample dataset (as can be seen clearly in Figure 8.6) that changes in observational LF binning can have a significant bearing on the result of the fit. This effect is apparent in Figure 8.8 (b), where a bin size of 0.75 $M_{\rm bol}$ yields a strong preference of a Disc age of 14 Gyr, in contrast to the 12-13 Gyr Disc age selected by the other binning regime (note also that 14 Gyr was the oldest curve available for fitting). Although it is difficult to resolve this matter satisfactorily with the current data set, there are two points to raise. The problem does not apply to the Wood models, the fits to which are extremely difficult to dislodge from the 9–11 Gyr region indicated by

Figure 8.8 (a). Secondly, Wood and Oswalt (1998), as a result of their Monte Carlo analysis of the WDLF, recommend choosing a binning in which the crucial lowest luminosity bin contains ~ 5 objects; giving a reasonable compromise between the requirements of good signal to noise in the final bin and having that bin as faint as possible to provide maximum information on the position of the cut off. This means a bin size of 1 $M_{\rm bol}$ for our data set, for which the fitted Disc age is well constrained for both models.

An overview of all the various fittings to both sets of models points firmly to a Disc age between 9 and 11 Gyr using the Wood models, and an age of 12-14 Gyr using the GB models. This discrepancy is expected (LRB, García-Berro et al. 1997) and indicates the extent of errors introduced by uncertainties in the WD crystallisation process; the Wood model Disc ages indicate a lower limit however, and Figure 8.8 demonstrates the difficulty in obtaining a Disc age of less than 9 Gyr from our data. Since internal errors in the models should amount to no more that ~ 1 Gyr (Wood 1992), Figure 8.8 is indicative of the extents of the error in the Disc age determination, which arises from the differences between the models and scatter introduced by the undetermined atmosphere constituents. The adopted Disc age estimation is 10^{-1}_{+3} Gyr. The upper and lower bounds are not strict 1σ error bars, and are simply chosen to include the likely values of the Disk age given all the uncertainties. The peak at 14 Gyr in Figure 8.8 (b) is neglected because it arises solely from the $0.75M_{\rm bol}$ fits which tend to have only one or two objects in the influential last data bin, and also because the 1 $M_{\rm bol}$ fits totally exclude a 14 Gyr Disc.

8.5 Discussion

A comparison of the various Disc ages derived using the WDLF method is presented in Figure 8.9. All the ages are consistent within the error bounds given, and the age estimates from this work and that of LRB are the most discrepant. None of the other estimates include the results of fitting to more than one model in their error bounds. For example, LRB state that fitting their data to an earlier version of the GB models leads to a Disk age estimate of 9 Gyr, bringing the LRB work much more into line with the rest in Figure 8.9. Having established that the results of this work are broadly consistent with previous studies, some further possible sources of error in this work are discussed.

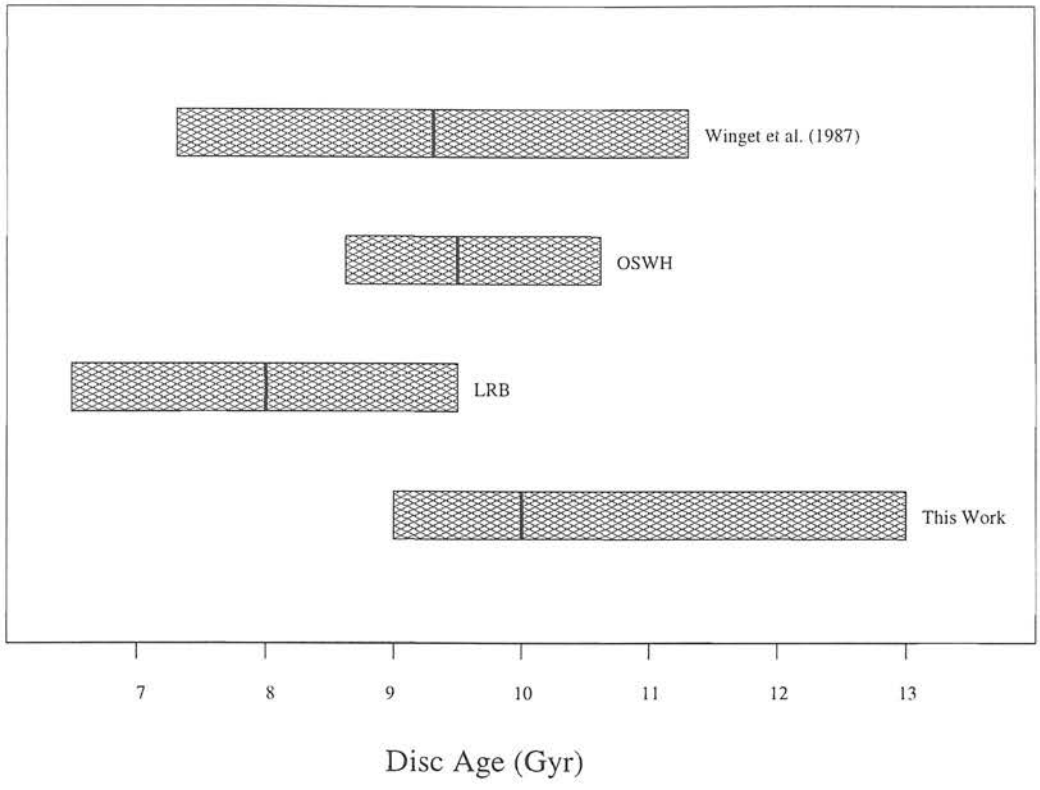

Figure 8.9: The four estimates of the Disc age found using the WDLF compared.

One important source of error in the WDLF is again concerned with completeness. Inspection of Figure 6.4 will show that there is a small group of objects lying just beyond our RPMD cut-off that have not been included in our CWD sample. Although the distribution of known WDs on the RPMD (the BRL objects in Figure 7.2) indicates a population of CWDs is not expected in this region, the reason for this may be that many of the known CWDs have been themselves selected on the basis of RPM criteria (Luyten 1970). It may be that the region of the RPMD just beyond our cut-off has not been adequately investigated before, since in the presence of noisier data from blink comparators and eye-measure photometry it would be hopelessly confused. The investigation of the Luyten WD catalogue on the $(H_V, (B-V))$ plane by Jones (1972b) highlighted the weak dependence of Luytens eye measured colour class on $(B-V)$ colour, and the fact that stellar sequences are 'hopelessly intermingled' as a consequence. Indeed, an analogous problem was encountered in this work, where the use of precious telescope time on faint marginal candidates beyond our cut-off was not practical. These considerations argue strongly for a wholesale spectroscopic survey using multi-fibre instruments of the entire population below $H_R = 19$ for complete confidence that our sample does not exclude any

CWDs. For the present, the possibility that a few more CWDs exist in our catalogue but do not satisfy our RPMD survey criteria cannot be ruled out. Such objects would certainly be very cool, resulting in a higher Disc age estimate. Responding to this source of error by introducing some form of completeness correction to the final LF bin was considered but finally not implemented. The obvious reason for this is that Figure 7.2 suggests WDs redder than KX57 and KX58 and at the same RPM are unlikely. In addition, the interest in an estimate for the Disc age, notably in terms of constraining cosmological models, is in a lower limit. Therefore putting in an essentially arbitrary factor into the LF that would increase the derived lower limit is not desirable, and in the absence of further observations it must suffice simply to bear in mind the potential for omission of CWDs due to the ambiguity of the RPM method when assessing the significance of the Disc age derived here. It is worth reiterating however that other CWD samples are also likely to suffer from this source of contamination, being culled from catalogues with less well defined photometry and proper motions.

A constrasting source of error, the possibility of sample contamination by non-degenerates, cannot be discounted without spectroscopic identification of the entire sample. Probably the most serious source of potential contamination arises from spurious proper motion objects, since several objects passing the proper motion survey criteria had to be rejected on inspection of their proper motion plots. Of the five objects making up the crucial last bin in the 'first guess' LF, two (KX57 and KX58) have spectroscopic identifications. The proper motion plots for the other three, KX11, KX14 and KX51, are displayed in Figure 8.10. The KX14 and KX51 data is convincing, whereas the KX11 plot is considerably noisier. The values of reduced χ^2 for the various fits, shown in Table 8.3, do not suggest the KX11 data is inconsistent with a real motion however. If, for the sake of argument, KX11 did turn out to be a contaminant, the best fit to the 'first guess' LF would still be 9 Gyr as shown in Figure 8.11, although the space density in the final bin has clearly decreased when compared to Figure 8.5, and is closer to the 8 Gyr curve.

A brief investigation of the effect of altering the Disc scale height in Equation 7.5 revealed that for any scale height between 250 and 400 pc the alterations in space densities for a LF binned as in Table 8.1 are restricted to a few hundredths in $\log \phi$. Variations at this level have a negligible effect on the fits to model LFs.

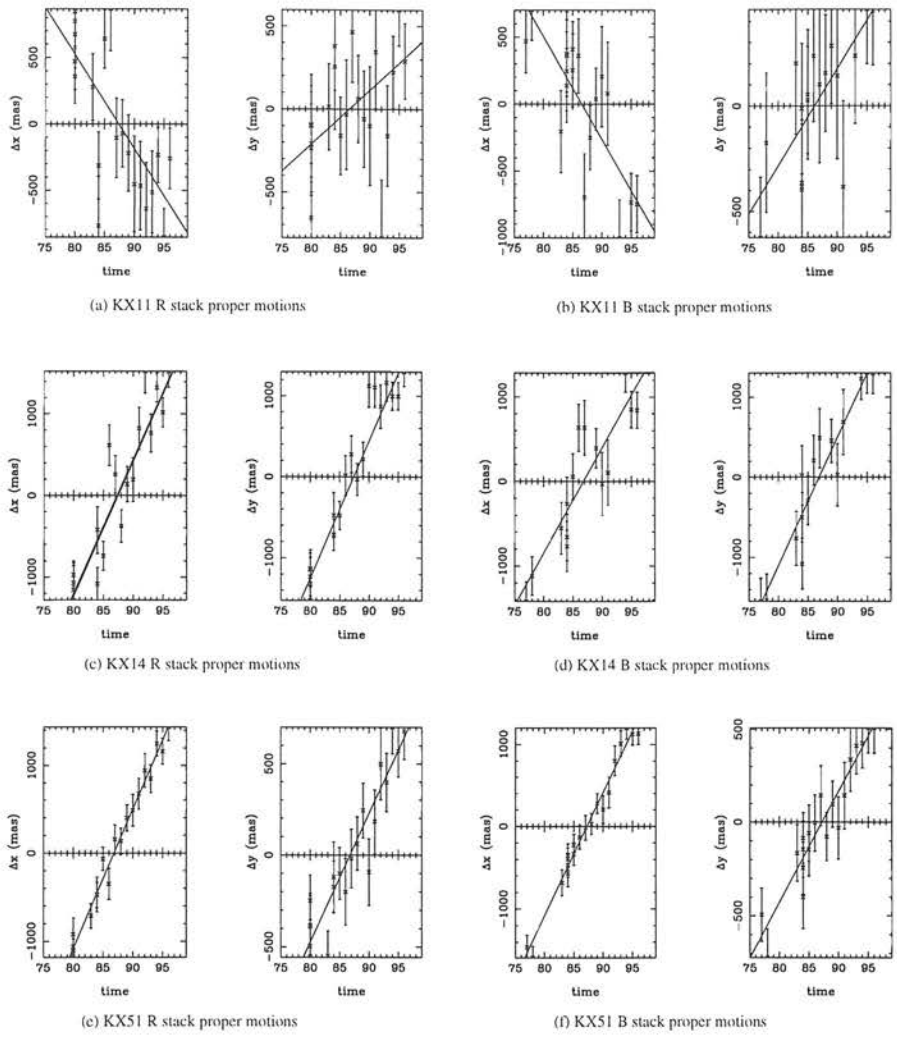

Figure 8.10: The proper motion plots for three objects in the final bin of the 'first guess' luminosity function

Another effect is concerned with the question of WD mass. The difficulty is amply demonstrated by the case of CWD ESO 439-26 (Ruiz et al. 1995), which was observed to have a luminosity fainter by 1 magnitude than the WDLF cut off. Analysis of the objects optical energy distribution in conjunction with a measure of trigonometrical parallax allowed the authors to conclude that the objects low luminosity was in fact due to its large mass, or small radius. Again, ideally it would be desirable to extend the observations to include trigonometric parallaxes and CCD optical and IR photometry of the entire sample, obviating the need to assume a mass of $0.6M_{\odot}$ (and allowing the surface composition to be constrained). When investigating the effect of mass on their derived Disc age OSWH constructed two LFs, one composed entirely of WDs of mass $0.5M_{\odot}$, the other with masses of

Object	Reduced χ^2			
	R stacks		B stacks	
	μ_x	μ_y	μ_x	μ_y
KX11	1.67	1.15	1.07	0.43
KX14	1.98	1.24	1.60	0.72
KX51	0.49	0.74	0.63	0.45

Table 8.3: Reduced χ^2 for the fits displayed in Figure 8.10

$0.7M_\odot$. The dispersion of WD masses about the mean value of $\sim 0.6M_\odot$ is small – Liebert and Bergeron (1995) measured a mean of $(0.590 \pm 0.137)M_\odot$ – and LFs composed entirely of WDs deviating by $0.1M_\odot$ from the mean mass may justifiably be described as extreme. OSWH found these test LFs only shifted the estimated the Disc age by 0.3 Gyr or less, and since the their method of constructing the LF is the same as used here the extent of the effect of WD mass deviations should be the same.

Photometric surveys must often be corrected for systematic bias introduced by uncertainties in measuring absolute magnitudes. This so called Malmquist Bias (Mihalas and Binney 1981) arises when colours are used to infer absolute magnitudes. The bias is caused by the scatter in absolute magnitude at a given colour, the source of which may be intrinsic to the stellar population or due to measurement errors. All previous studies of the WDLF have neglected this bias since its effect will be dominated by the LF measurement errors (Evans 1992). This is especially true in this work, where the uncertainty in absolute magnitude arises principally from the undefined atmosphere constituents, and the effect of this uncertainty has been investigated independently in the LF realisations described in the previous section. An order of magnitude assessment of the effect of the bias was made on the crucial last point of the 'first guess' LF using the prescription of Stobie et al. (1989). It was estimated to reduce the point by $\sim 0.1 \log L/L_\odot$, much less than the size of the error bar. This bias has therefore not been corrected for, although it will become more important for larger samples with better defined stellar parameters.

The extent of binarity in the survey sample is difficult to ascertain from the data available. All that can be said for certain is that no sample member was detected as part of a proper motion binary system from the COSMOS data - an expected result (recall

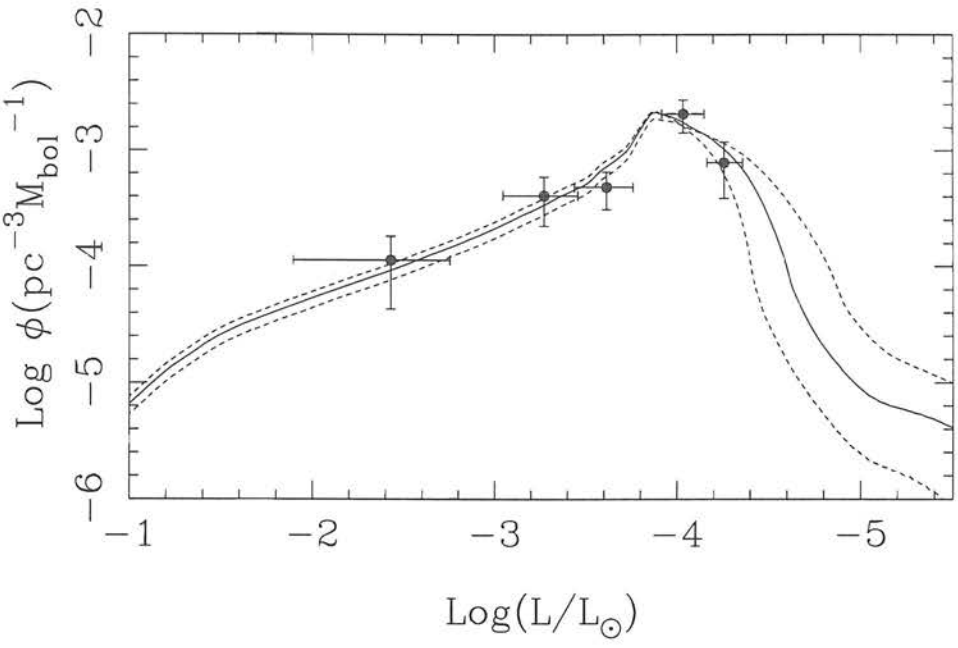

Figure 8.11: Best fit of the Wood models to a version of the 'first guess' LF with object KX11 removed, to illustrate the effects of potential contamination in the faintest bin. The best fit curve is still 9 Gyr.

Section 7.6). In addition, one of the objects (KX41) observed as part of the SAAO photometry programme was resolved as a double degenerate on the CCD frame. This object appears to be a normal point source on the stack data. Object KX41 was only discovered to be a binary because of its relatively small distance ($\sim$ 50 pc) and because it happened to be included as a target for photometric observations. Including both components in the sample would thus appear to be giving this particular system unwarranted special treatment. Double degenerate binary candidates can be found by plotting trigonometric parallax determined absolute magnitudes against colour, and searching for overluminous objects (BRL). If the low mass (large radius) implied for such candidates is not confirmed by more refined analysis the object is likely to be a double degenerate. Clearly, it is not feasible to allow for binarity in the sample given the present extent of observational material.

Finally, in the context of current cosmochronometry, our Disc age estimate is consistent with current Globular cluster age estimates of 13-14Gyr (Vandenberg 1998). When combined only with a conservative 1 Gyr value for the halo–Disc formation interval (Burkert,

Truran & Hensler 1992, Pitts & Tayler 1992) and a further 1 Gyr for the big bang–halo formation interval, a 10 Gyr Disc excludes $\Omega = 1$, $\Lambda = 0$ cosmologies based on current estimates for $H_\circ$ of 60-80 (Freedman 1998).

Chapter 9

Summary

The principal aim of this work has been the construction of a white dwarf luminosity function by undertaking a new survey for CWDs using digitised Schmidt plate data. The following Chapter summarises the survey procedure and the main results obtained. The suggestions for future work which have been made several times in the preceding pages are reiterated below and some potential new avenues of interest are also outlined.

An investigation into the optimum method of stacking SuperCOSMOS digitised Schmidt plate data has been undertaken. The criteria of optimising the signal to noise ratio in the resultant stack while rejecting spurious signal was found to be best served by adopting the described weighting scheme in conjunction with an 'average sigma clipping' pixel rejection algorithm. The gain in depth as a function of number of plates included in the stack was tested and found to be in good agreement with the expected $\Delta M \sim 2.5 \log_{10} n^{\frac{1}{2}}$ relation.

Both COSMOS and SuperCOSMOS scanned data of the large collection of plates taken in ESO/SERC field 287 have been used to compile proper motion measures and B and R photometry for every detected object. UVI photographic photometry is also available for most objects. The proper motions were measured by arranging the B and R plate data into stacks of four plates. 20 such stacks were available in each of the B and R passbands, allowing two independent measures of proper motion to be made. The time baseline in both passbands is approximately 20 years, and the proper motions calculated by simple linear regression fit to position as a function of time. The COSMOS photometry was

found to be self consistent at the level of a few hunderedths of a magnitude, although the real error on the photometry was found to be closer to 0.1 magnitudes when COSMOS magnitudes were compared to the CCD sequence. The same behaviour was noted for SuperCOSMOS derived magnitudes, possibly indicating the errors arise from the CCD sequence.

From the list of objects obtained from the stack data was drawn a complete catalogue of objects with genuine proper motions within well defined survey limits. Detection on at least 15 stacks in both the B and R passbands was a requirement for an object to be included in the catalogue. The photometric survey limits of 22.5 in B and 21.2 in R were obtained from number counts as a function of magnitude, where a clear cut off at the stack limit was clearly identifiable. Defining the survey proper motion limit was more problematic since a real compromise had to be struck between maximising the sample size and eliminating contamination from spurious proper motions arising from machine measurement error. The availability of two independent measures of proper motion for each object was of great assistance in this regard. A combination of approaches to this problem (described below) led to the adoption of a proper motion limit of $0\farcs05$ yr^{-1} for objects brighter than 20^{th} magnitude in R, and $0\farcs06$ yr^{-1} for the remaining fainter objects with larger positional errors.

The method of population discrimination employed was the reduced proper motion diagram. It was found that the locus of white dwarfs was clearly distinct from other populations on this diagram for almost all colours. This allowed a sample of white dwarfs to be extracted from the catalogue simply by defining a portion of the diagram inhabited by white dwarfs. The correct region to use was clear and unambiguous for all but the red extremity of the white dwarf locus, where a small region of uncertainty between the white dwarf and main sequence loci was encountered. White dwarf candidates isolated using the reduced proper motion criterion were subject to further scrutiny, notably via their distribution of position against epoch. Ten objects were rejected on inspection of these distributions, where it was clear that the detected displacement with time was not characteristic of a constant motion, but tended to be an abrupt shift where no motion was previously discernable. The remaining 56 objects constituted the preliminary survey sample. A search for very faint or very high proper motion stars was made using 16 plate

stacks and independent 'multiple-pass' software. The results of this search indicated that no white dwarf candidate with R $<$ 22 and proper motion less than several arcseconds per year exist in the field, confirming that the cut-off in the white dwarf locus is real and not an artefact of incompleteness arising from the faintness of white dwarfs and that colour.

Spectroscopic observations of a subset of the white dwarf sample were obtained to confirm their status as degenerates. In addition, redder stars with high reduced proper motion were observed, both to test for extremely cool white dwarfs and to aid population discrimination on the reduced proper motion diagram. The apparent faintness and poor weather conditions at the AAO combined to make high signal to noise spectra of many of the reddest white dwarf candidates unobtainable. Several observed stars were clearly cool white dwarfs however, including two objects appearing just redwards of the imposed reduced proper motion criteria, and were thus included in the sample. No white dwarf sample object observed was found to be anything other than a degenerate. The redder objects observed tended to be subdwarfs with high proper motions.

The expanded white dwarf sample, supplemented by the two spectroscopically observed objects, was then used to construct a luminosity function. Stellar parameters for the sample objects were derived by fitting UBVRI photometry to a published grid of model atmospheres, yielding estimates of effective temperature, absolute magnitude and bolometric magnitude. The $1/V_{max}$ method was used to construct the luminosity function, which was in good agreement with previous estimates, although the space density of the coolest white dwarfs was found to be slightly higher. Unfortunately, the dominant atmospheric constituent of the sample members could not be reliably inferred from comparison of the data available to model atmospheres, which lead to an extra large uncertainty in the fitting of the luminosity function to model curves. The data was fitted to two different sets of theoretical models, the ambiguity in the atmospheres accounted for by randomising each stars atmosphere and constructing many luminosity functions, and fitting each to the model curves. The fits to the models of Wood (1995, 1992) strongly indicated a Disc age of 10 Gyr. Since these models are currently the most widely used by authors publishing fits to observational white dwarf luminosity functions (LRB, OSWH), the best fit age of 10 Gyr is adopted for this work to facilitate comparison with the results of others. The models of García-Berro, Isern & Hernanz (1997), which include treatment of an extra heat

source at white dwarf crystallisation, yield larger Disc ages if 12-13 Gyr when fit to the data however. This discrepancy is incorporated into the findings of this work by quoting the derived age as 10^{-1}_{+3} Gyr.

Finally, since sample completeness and contamination are of central importance to this work, it is worthwhile briefly recapping the various sources of error related to these issues and the precautions taken to combat them.

The source of potential sample contaminants are twofold. Firstly, inclusion in the proper motion catalogue may arise from a spurious proper motion measurement, since every detected object has a calculated proper motion. This source of contamination was investigated in three ways. The distribution of proper motions arising from machine errors may be estimated, and a prediction of the the number of contaminants as a function of of survey proper limit calculated, taking into account the various survey criteria imposed in objects included in the catalogue. This analysis assumes Gaussian distributed positional errors about zero from the machine. While this assumption should be reasonable for the bulk of objects, it neglects contamination arising from other types of error, such as miss-paired images or emulsion flaws, which may cause sudden jumps in object position and large spurious motions. The results of this analysis suggested a sample with proper motion limit $0''.04\ \mathrm{yr}^{-1}$ should be free of contamination arising from normally distributed positional measurement errors. Since positional errors increase with magnitude, this analysis also split the catalogue into magnitude bins, with the unsurprising result that fainter objects can exhibit higher spurious motion measures. A plot of cumulative number counts as a function of proper motion gives a second indication of the contamination as a function of magnitude. An excess of objects above the expected -3 law indicates the onset of contamination, and is sensitive to spurious motions arising from any source of error. As expected, this plot indicated the onset of contamination at the slightly higher limit of $0''.05\ \mathrm{yr}^{-1}$, although the result was reassuringly close the the findings of the previous analysis. The reduced proper motion diagram itself may also be used to detect spurious proper motion objects. As the sample proper motion limit is lowered, spurious motions appear first in a reduced proper motion locus populated by the most numerous objects at the stack limit, which also have the largest measurement errors. This locus happens to appear in the region of confusion on the reduced proper motion diagram between the

white dwarf locus and the main sequence stars. This is unfortunate in the sense that spurious objects making it through the finally imposed survey limits may be likely to be included in any white dwarf sample. However, since the contaminant locus is in a region where few stars are expected, it is possible to simply raise the proper motion limit until the contaminant locus disappears. The adopted survey limits were in compliance with the three tests described.

The second source of potential contamination is due to imperfect population discrimination on the reduced proper motion diagram. This well known problem may arise partly from poorly determined proper motions and colours, but also from the natural merging of the white dwarf and subdwarf reduced proper motion loci. In part because the colours are relatively well determined (in contrast to the 'colour classes' of Luyten), the white dwarf locus is unambiguous for all but the reddest potential candidates. The confusion in this region is impossible to fully resolve without comprehensive observations of all objects, although the existing observational results, theoretical predictions of population loci and notably overplotting of previously published cool white dwarf and extreme subdwarf samples indicate that the white dwarf region adopted on the reduced proper motion diagram for this work is unlikely to be contaminated by non-degenerates.

The completeness of the sample has been tested in two ways. Firstly, the cumulative proper motion number counts discussed above with regard to spurious motion contamination are also a test for completeness. The expected slope of -3 in these plots for a complete sample is in excellent agreement with this data until the onset of contamination, indicating the proper motion catalogue is complete. Secondly, the sample passes the $\langle V/V_{max} \rangle$ completeness test (in contrast to samples drawn from the Luyten catalogues), indicating that the survey is evenly sampling the survey volume. The most serious source of potential incompleteness is again concerned with population discrimination on the reduced proper motion diagram. It is possible that cool white dwarfs are excluded from the sample because they lie redwards of the reduced proper motion cut-off. However, the main astrophysical interest in this work is the lower limit on the age of the Disc. For this reason, given the limited observational material available, it is preferable to obtain a conservative sample with a small probability of contamination from which a firm lower Disc age limit may reliably be drawn.

Astronomers experienced in the field of cool white dwarf surveys will justifiably regard any conclusions based on a sample without full spectroscopic confirmation with some scepticism. They will also point to the example of ESO 439-26, and insist on trigonometric parallax measurements of the sample members. These worries will particularly apply to the coolest white dwarfs, on which the Disc age estimate is most dependent and for which concerns over the reduced proper motion diagram population discrimination method are most applicable. While the author is fully sympathetic to these reservations, it is hoped that the preceding material has convinced the reader that the sample members are very likely to be degenerates, and that therefore the space density of the coolest white dwarfs is higher than previously thought.

The obvious first step in furthering the work of this thesis is extending the observational material available on the white dwarf sample. The most pressing priority must be firm spectroscopic identifications of all sample members to finally resolve contamination concerns. Trigonometric parallax and CCD optical and infra red photometry should also be obtained where possible to constrain stellar masses and luminosities. These observations would also allow the samples' atmosphere constituents to be determined. To be fully confident of the completeness of the sample, it is also crucial to undertake a spectroscopic survey of all objects lying close to the white dwarf region on the reduced proper motion diagram, obviating the current requirement to impose a sharply defined white dwarf region. The above observations would put this sample on equal footing with the most extensively observed white dwarf sample to date (LRB), with the important difference that this sample would be drawn from a demonstrably complete proper motion catalogue. Given the results of the experiments in this work with 16 plate stacks, it appears unlikely that a significant increase in the sample size is possible by further exploiting the plate material in F287.

The priority for observational astronomers in the near future will be to produce significantly larger samples of white dwarfs from which to produce luminosity functions. This is of particular importance at the faint end of the luminosity function, where well populated bins with small errors bars should allow tight constraints to be placed on models. This work has shown that surveying large areas of sky is not necessarily a prerequisite for obtaining large samples. If digitised Schmidt plate data is to be used, it is likely to prove

more profitable to concentrate on fields with reasonably large plate collections than to opt for all sky two epoch surveys with their attendant contamination difficulties. It is possible however that new projects such as the proposed 4×4m liquid mirror telescope, which could provide deep CCD photometry, proper motions *and* parallaxes across an entire strip of the sky, will soon supercede Schmidt plate work altogether in terms of obtaining large, complete samples of faint stars.

Glossary

AAT Anglo-Australian Telescope

BC bolometric correction

BRL Bergeron, Ruiz and Leggett (1997)

BSW Bergeron, Saumon and Wesemael (1995)

CCD charge coupled device

CPMB common proper motion binary

CWD cool white dwarf

CWDLF cool white dwarf luminosity function

DA denotes hydrogen atmosphere white dwarf

F287 ESO/SERC field 287

FLG Fleming, Liebert and Green (1986)

GB model described in García-Berro, Isern and Hernanz (1997)

HR Hertzsprung-Russell

IAM COSMOS 'image analysis mode' data

IMF initial mass function

LDGS Liebert et al. (1979b)

LDM Liebert, Dahn and Monet (1988)

LF luminosity function

LHS Luyten half second (catalogue)

LRB Legget, Ruiz and Bergeron (1998)

MS main sequence

OSWH Oswalt et al. (1995)

PISA ' Position, Intensity and Shape Analysis' Starlink software package

RPM reduced proper motion

RPMD reduced proper motion diagram

SAAO South African Astronomical Observatory

SFR star formation rate

UKST United Kingdom Schmidt Telescope

VLL very low luminosity

WD white dwarf

WDLF white dwarf luminosity function

References

Adams W.S., 1914, PASP, 26, 198

Adams W.S., 1915, PASP, 27, 236

Altmann J.H., 1977, In: The Theory of the Photographic Process, ed. T.H. James (MacMillan:New York), 481

Bahcall J.N., 1984, ApJ, 287, 926

Beard S.M., MacGillivray H.T., Thanisch P.F., 1990, MNRAS, 247, 311

Bergeron P., Saumon D., Wesemael F., 1995, ApJ, 443, 764

Bergeron P., Wesemael F., Beauchamp A., 1995, PASP, 107, 1047

Bergeron P., Ruiz M.T., Leggett S.K., 1997, ApJS, 108, 339

Bessell M.S., 1982, Proc.ASA 4(4), p.417-419

Bessell M.S., 1986, PASP, 98, 1303

Blair M., Gilmore, G., 1982, PASP, 94, 742

Bland–Hawthorn J., Shopbell P.L., 1993, in: IAU Commission 9: Working Group on Wide–Field Imaging, Newsletter No. 3, 52

Burkert A., Truran J.W., Hensler G., 1992, ApJ, 391, 651

Burstein D., Heiles C., 1982, AJ, 87, 1165

Carter D, 1993, Gemini, No. 39. p14

Chiu, L-T.G., 1980, ApJS, 44, 31

Clayton D.D., 1988, MNRAS, 234, 1

Crézé M., Chereul E., Bienaymé O., Pichon C., 1998, A&A, 329, 920

D'Antona F., Mazzitelli I., 1990, ARA&A, 28, 139

D'Antona F., Caloi V., Mazzitelli I., 1997, ApJ, 477, 519

Dawson P.C., 1986, ApJ, 311, 984

Draper P.W., Eaton N.,1996, Starlink User Note 109: PISA: Position, Intensity and Shape

Analysis

Dunlop J., Peacock J., Spinrad H., Dey A., Jimenez R., Stern D., Windhorst R., 1996, Nature, 381, 581

Eggen O.J., 1983, ApJS, 51, 183

Evans D.W., 1988, PhD Thesis, Cambridge University

Evans D.W., 1989, A&AS, 78, 249

Evans D.W., 1992, MNRAS, 255, 521

Festin L., 1998, A&A, 336, 883

Fleming T.A., Liebert J., Green R.F., 1986, ApJ, 308, 176

Fowler R.H., 1926, MNRAS, 87, 114

Freedman W.L., 1998, in Turok N., ed., Proceedings for "Critical Dialogs in Cosmology", in press (Princeton University Press) (preprint astro-ph 9612024)

Furenlid I., Schoening W.E., Carder B.E., 1977, AAS Photo–Bulletin No. 16

García-Berro E., Isern J. , Hernanz M., 1997, MNRAS, 289, 973

Giclas H.L., Burnham R., Thomas N.G., 1971, Lowell Proper Motion Survey, Northern Hemisphere Catalogue (Flagstaff: Lowell)

Giclas H.L., Burnham R., Thomas N.G., 1978, Lowell Proper Motion Survey, Southern Hemisphere Catalogue Lowell Obs. Bull. 164, Vol VIII, p.89

Green R.F., Schmidt M., Leibert J., 1986, ApJS, 61, 305

Greenstein J.L., 1976, AJ, 81, 323

Greenstein J.L., Liebert, J., 1990, ApJ, 360, 662

Hamada T., Salpeter E.E., 1961, ApJ, 134, 683

Hambly N.C., Smartt S.J., Hodgkin S.T., 1997, ApJ, 489, L157

Hambly N.C., Miller L., MacGillivray H.T., Herd J.T., Cormack, W.A., 1998, MNRAS, 298, 897

Hambly N.C., on-line SuperCOSMOS guide:http://www.roe.ac.uk/cosmos/

Hansen B.M.S., 1998, Nature, 394, 860

Hauschildt P.H., Allard F., Baron E., 1998, ApJ, in press

Hawkins M.R.S., 1983, MNRAS, 202, 571

Hawkins M.R.S., 1986, MNRAS, 223, 845

Hawkins M.R.S., Bessell M.S., 1988, MNRAS, 234, 177

Hawkins M.R.S., 1991, in: IAU Commission 9: Working Group on Wide–Field Imaging, Newsletter No. 1, 23

Hawkins M.R.S., Ducourant, C., Jones, H. R. A., Rapaport, M., 1998 , MNRAS, 294, 505

Hoaglin D.C., Mosteller F., & Tukey J.W., 1983, *Understanding Robust and Exploratory Data Analysis*, Wiley, Chp 11.

Iben I., Laughlin G., 1989, ApJ, 341, 312

Irwin M.J., 1996, "Detectors and Data Analysis Techniques for Wide Field Optical Imaging" in *7th Canary Islands Winter School*, Ed. Espinosa, J.M., Cambridge University Press,p59

Isern J, Garci-Berro E, Hernanz M., Mochkovitch R, Torres S, 1998, ApJ,503, 239

Jaschek C., Jaschek M., 1987, *The Classisification of Stars*, Cambridge University Press

Jimenez R., Flynn C., Kotoneva E., 1998, MNRAS, 299, 515

Jones E.M., 1972a, ApJ, 173, 671

Jones E.M., 1972b, ApJ, 177, 245

Kaprandis S., 1985, ApJ, 294, 634

Kemp S.N., Meaburn J., 1993, A&A, 274, 19

Kilkenny D., O'Donoghue D., Koen C., Stobie R.S., Chen A., 1997, MNRAS, 287, 867

Kovetz A., Shaviv G., 1976, A&A, 52, 403

Kuijken K., 1995, Stellar Populations, IAU Symp. 164, 195

Leggett S.K., Ruiz M.T., Bergeron P., 1998, ApJ, 497, 294

Liebert J., Dahn C.C., Gresham M., Hege E.K., Moore R.L., Romanishin W., Strittmatter P.A., 1979a, 229, 196

Liebert J., Dahn C.C., Gresham M., Strittmatter P.A., 1979b, 233, 226

Liebert J., Dahn C.C., Sion E.M., 1983, in: IAU Colloquium 53, The Neary Stars and the Stellar Luminosity Function, ed A.G.D. Philip and A.R.Upgren (Schenactady:Davis, p103

Liebert J., Dahn C.C., and Monet D.G., 1988, ApJ, 332, 891

Liebert J., Bergeron P., 1995, in: White Dwarfs (eds. Koester, D. and Werner, K.), p.12(Springer, Berlin)

Luyten W.J., 1958, Vistas in Astronomy, 2, 1048

Luyten W.J., 1963, in *Basic Astronomical Data*, ed K. A. Strand (Chicago: University of Chicago Press), p.46

Luyten W.J., 1969, Proper Motion Survey with the 48" Schmidt Telescope XXI (U. Minn)

Luyten W.J., 1970, *White Dwarfs* (U. Minn)

Luyten W.J., 1974, Proper Motion Survey with the 48" Schmidt Telescope XXXVIII (U.

Minn)

Luyten W.J., 1977, *White Dwarfs* (U. Minn)

Luyten W.J., 1979, Proper Motion Survey with the 48" Schmidt Telescope LII (U. Minn)

Luyten W.J., 1979, LHS Catalogue (U. Minn)

MacGillivray H.T., Stobie R.S., 1984, Vistas in Astronomy, 27, 433

MacGillivray H.T., Thomson E.B., 1992, Digitised Optical Sky Surveys, Astrophysics and Space Science Library Proceedings volume 174 (Kluwer:Dordrecht)

Malin D.F., 1988, In: Proc. IAU Workshop on Astrophotography, ed. S. Marx (Springer: Berlin), 125

Massey P., 1992, *A Users Guide to CCD Reductions with IRAF*

Massey P., Valdes F., Barnes, J., 1992, *A Users Guide to Reducing Slit Spectra with IRAF*

Massey P., Davis L.E., 1992, *A Users Guide to Stellar CCD Photometry with IRAF*

Méndez R., Ruiz M.T., Maza J., Wischnjewsky M., 1992, AJ, 103, 904

Mestel L., 1952, MNRAS, 112, 583

Mihalas D., Binney J., 1981, *Galactic Astronomy Structure and Kinematics*, W.H. Freeman

Miller L., Cormack W.A., Paterson M., Beard S.M., Lawrence L., 1992, see MacGillivray & Thomson (1992), p. 133

Monet D.G., Dahn C.C., Vrba F.J., Harris H.C., Pier J.R., Luginbuhl C.B., Ables H.D., 1992, AJ, 103, 638

Morgan D.H., Tritton S.B., Savage A., Hartley M., Cannon R.D., 1992, see MacGillivray & Thomson (1992), p. 11

Nutting P.G., 1913, Phil. Mag., 26, 423

Oswalt T.D., Hintzen P., Luyten W.J., 1988, ApJS, 66, 391

Oswalt T.D., Smith J.A., 1995, in: White Dwarfs (eds. Koester, D. and Werner, K.), p.24(Springer, Berlin)

Oswalt T.D., Smith J.A, , Wood M.A., Hintzen P., 1996, Nature, 382, 692

Pitts E., Tayler R.J., 1992, MNRAS, 255, 557

Reid N., 1997, In: ASP Conference Vol 127 'Proper Motions and Galactic Astronomy' (ed Humphreys R.M.), p63

Ruiz M.T., Maza J., Wischnjwesky M., González, 1986, ApJ, 304, L25

Ruiz M.T., Bergeron P., Leggett L.K., Anguita C., 1995, ApJ, 455, L159

Ruiz M.T., Takamiya M.Y., 1995, AJ, 109, 2817

Ruiz M.T., 1996, AJ, 111, 1267

Ryan S.G., 1989, AJ, 98, 1693

Salaris M., Domínguez I., García-Berro E., Hernanz M., Isern J., Mochkovitch R., 1997, ApJ, 486 413

Salpeter E.E., 1955, ApJ, 121, 161

Schmidt M., 1959, ApJ, 129, 243

Schmidt M., 1968, ApJ, 151, 393

Schmidt M., 1975, ApJ, 202, 22

Schwartzenberg J.M., Phillipps S., Parker Q.A., 1996, A&AS, 117, 179

Selwyn E.W.H., 1935, Photogr. J., 75, 571

Sion E.M., Liebert J., 1977, 213, 468

Sion E.M., 1984, ApJ, 282, 612

Sion E.M., Fritz M.L., McMullin J.P., Lallo M.D., 1988, AJ, 96, 251

Smith J.A., Oswalt T.D., 1994, in: The Lower Main Sequence - and Beyond, ed. C. Tinney, Spriger-Verlag, p.113

Stobie, R.S., 1986, Pattern Recognition Letters, 4, 317

Stobie R.S., Ishida K., Peacock J.A., 1989, MNRAS, 238, 709

Tinney C.G., Reid I.N., Mould J.R., 1993, ApJ, 414, 254

Tritton S.B., 1983, UKSTU Handbook, Royal Observatory Edinburgh

Vandenberg D.A., 1998, Bedding T. R., Booth A. J. & Davis J., eds., in IAU Symp Fundamental Stellar Properties: The Interaction between Observation and Theory, Kluwer, Dordrecht, p.439

Véron, P., Hawkins, M.R.S., 1995, A&A, 296, 665

Wanner J.F., 1972, MNRAS, 155, 463

Weidemann V., 1967, Zs. Ap., 67, 286

Wesemael F., Greenstein J.L., Liebert J., Lamontagne R., Fontaine G., Bergeron P., Glaspey J.W., 1993, PASP, 105, 761

Winget D.E., Hansen C.J., Liebert J., Van Horn H.M., Fontaine G., Nather R.E., Kepler S.O., Lamb D.Q., 1987, ApJ, 315, L77

Wood M., 1992, ApJ, 386, 539

Wood M.A., , 1995, Koester D. & Werner K., eds., in White Dwarfs, Springer, Berlin, p.41

Wood M., Oswalt T.D., 1998, ApJ, 497, 870

Acknowledgements

During the course of my PhD studies I have benefited from the advice and experience of many of the staff at both the ATC and the IfA, especially those working with SuperCOSMOS and in the UK Schmidt Library. Particular and special thanks must go to the indefatigable Nigel Hambly, whose generous and unstinting assistance it is a pleasure to acknowledge, and without whom my time at the Observatory would have been considerably less rewarding and enjoyable. This work would not have been possible without the key input of my main supervisor Mike Hawkins - a reliably stimulating interlocutor on any subject.

I would like to thank John Cooke for being a supportive second supervisor, and for helpful comments on the manuscript. Thanks are due also to my father and brother for taking the time to proof read the draft version. Other notably helpful people at the Observatory were Alison Stirling and Andy Taylor (help with hard sums), Liz Gibson (help with large forms) and any of the multitude of people I have pestered about computers.

Thanks to all the people, inside and outside the Observatory, who have made my time in Edinburgh such fun; and finally many thanks to my family for continual support and occasional visits.

Mon. Not. R. Astron. Soc. 297, 839–848 (1998)

Digital stacking of photographic plates with SuperCOSMOS

R. A. Knox,[1] N. C. Hambly,[2] M. R. S. Hawkins[2] and H. T. MacGillivray[2]

[1]*Institute for Astronomy, University of Edinburgh, Blackford Hill, Edinburgh EH9 3HJ*
[2]*Royal Observatory, Blackford Hill, Edinburgh EH9 3HJ*

Accepted 1998 February 12. Received 1998 February 6; in original form 1997 December 5

ABSTRACT

Photographic Schmidt plates are among the most effective tools in wide-field astronomy. One of the principal difficulties of photographic plates when compared to modern detectors is lack of image depth. We present a technique for stacking plates digitized using the SuperCOSMOS microdensitometer, aimed at maximizing the signal-to-noise ratio in faint images. The efficacy of several image combination algorithms is tested by stacking plate frames in the presence of spurious images. We find that an 'average sigma clipping' type pixel rejection in conjunction with our weighting scheme is most effective in delivering a clean, high signal-to-noise ratio stack. The gain in limiting magnitude obtained from stacking is found to be consistent with that expected: $\Delta M \sim 1.5$ for a stack of 16 good-quality plates.

Key words: instrumentation: miscellaneous – methods: data analysis – techniques: image processing.

1 INTRODUCTION

Continually improving CCD technology inevitably means that the case for using photographic Schmidt plates in survey work will become progressively less compelling with time. However, the unrivalled field of view of Schmidt telescopes coupled with the advent of high-speed scanning machines such as SuperCOSMOS (Miller et al. 1992; Hambly et al. 1998) still allow Schmidt plates to provide a wealth of information in wide fields (MacGillivray & Thomson 1992). The chief disadvantage of photography compared with modern CCD imaging is that the quantum efficiency of the photographic emulsion is typically between one and two orders of magnitude smaller than that of the CCD. In this paper we address the problem of lack of depth in photographic imaging by demonstrating a technique for stacking digitized Schmidt plates. This is not a new idea – previously, plate stacking has been done both photographically (e.g. Malin 1988, and references therein) and digitally (e.g. Hawkins 1991; Kemp & Meaburn 1993; Schwartzenberg, Phillipps & Parker 1996), generally in faint galaxy and quasar projects. There are still many fields with large numbers of plates where the stacking process will yield valuable data on all manner of faint objects. In addition, where sufficient plate material exists, stacking may be done at several epochs, yielding information on time-dependent phenomena, e.g., long-term variability and proper motions. Table 1 shows a 'top ten' of United Kingdom Schmidt Telescope (UKST) fields having sufficient suitable plates for stacking in the three photographic passbands *J*, *R* and *I*. The SuperCOSMOS machine is currently scanning all the UKST survey plates (Morgan et al. 1992) and is routinely archiving pixel data for subsequent analysis. Many private projects are also underway, scanning collections of plates in small numbers of fields.

Plate stacking has been approached in several different ways in the past. In Section 2 we describe the philosophy behind our choice of technique, and the arguments behind our weighting algorithm. Section 3 goes into some detail describing the stacking procedure. Example results are shown in Section 4, and discussed in Section 5. We present our conclusions in Section 6.

2 THEORETICAL BACKGROUND AND THE STACKING TECHNIQUE

Since astrometric and photomeric data for bright objects are readily available from scans of single plates, the primary purpose of plate stacking must be to maximize the signal-to-noise ratio of faint images. We also wish to devise a stacking scheme that accounts for the often large variations in plate quality, the sources of which are many and varied (Tritton 1983), but the effects of which may be quantified by analysis of the scanned plates' pixel data. Furthermore, it is advantageous in many circumstances to implement bad-pixel rejection algorithms to avoid spurious photographic image

Table 1. 'Top ten' UKST fields for plate stacking.

Rank	Field Centre		No. of plates available (as at 4 February 1998)		
	RA	DEC	J	R	I
1	21 28	−45 00	99	100	40
2	00 54	−73 00	29	5	59
3	05 20	−66 48	2	2	67
4	18 24	−33 58	31	30	3
5	05 30	−72 12	2	2	56
6	10 38	+00 08	12	33	13
7	05 12	−70 00	37	7	3
8	20 48	−35 00	22	19	4
9	06 04	−70 00	4	6	32
10	04 20	−70 00	5	6	29

defects (e.g., due to satellite trails or emulsion flaws) propagating through the stacking procedure (note that time-dependent information, e.g., positions of high proper motion objects, will be destroyed by such rejection).

The action of photons on the photographic emulsion is to produce dark grains (after development) as a function of exposure time. The photographic process is highly non-linear (e.g., Altman 1977) – a plot of the density of dark grains versus log(exposure) typically shows a 'toe', a linear part with gradient conventionally denoted γ, and a 'shoulder' where saturation due to the finite number of available grains in the emulsion is approached. Sky-limited astronomical photographs are usually exposed so as to yield a background density towards the lower end of the linear part of the characteristic curve, along with good contrast (i.e., high γ). Plate scanning in general produces a transmission value T for each pixel. Photographic densities D are, by definition (see, e.g., Altman 1977), the logarithm of the reciprocal transmission values, i.e. $D=\log_{10}(1/T)$. Calibration of transmission T to relative intensity I is achieved via the step-wedge region of the plate, where spots of known relative intensity are exposed for the duration of the main exposure. Valid stacking procedures could be performed in T, D or I units, provided that the noise characteristics of the data in those units are correctly quantified and taken into account. However, for simplicity we ideally want to work in units whose associated error distribution is Poissonian. Then errors propagate naturally in the stacking process when adding data values.

It can be shown that a density measurement is essentially a count of the number of dark grains (Nutting 1913). Fluctuations in measured density arise both from photon shot noise and the distributions in grain size and position. While fluctuations arising from grain properties are not Gaussian, the fluctuations in observed density do follow a normal distribution closely, as may be expected from the central limit theorem. Modelling by Selwyn (1935) also predicted Gaussian behaviour for density fluctuations, with the distribution rms (henceforth σ_D) proportional to the inverse square root of the aperture size. In the specific case of the science-grade emulsions used on Schmidt plates, Furenlid, Schoening & Carder (1977) have verified the Gaussian nature of the fluctuations in D. The non-linear relationships between T and D or D and I should then lead to skewed distributions for fluctuations in T and I. Stacking in units of T or I would therefore require cumbersome non-linear weights as a function of data value to propagate the errors correctly. We therefore choose to co-add pixel data in densities $[\log_{10}(1/T)]$ and, since the associated errors are normally distributed, we can use the following simple plate-weighting algorithm.

Consider a faint image on two plates to be co-added. Plate one has background noise σ_1 and our image has signal above background H_1, with plate two having corresponding characteristics σ_2 and H_2. We shall simply add our pixel data such that

$$(-\log_{10}T)_{\rm stack}=w_1(-\log_{10}T)_1+w_2(-\log_{10}T)_2, \tag{1}$$

and define our weights such that $w_1+w_2=1$. We make the (very good) approximation for faint images that the noise is constant across the profile of the image, and find the signal-to-noise ratio at the peak of the stacked image to be

$$s{:}n=f(w_1,w_2)=\frac{w_1H_1+w_2H_2}{\sqrt{w_1^2\sigma_1^2+w_2^2\sigma_2^2}}, \tag{2}$$

assuming normally distributed errors adding in quadrature. Putting $w_2=1-w_1$, we maximize the signal-to-noise ratio by setting $\partial f/\partial w_1=0$ and find

$$w_1=\frac{(\sigma_2^2/H_2)}{(\sigma_1^2/H_1)+(\sigma_2^2/H_2)}=\frac{(H_1/\sigma_1^2)}{(H_1/\sigma_1^2)+(H_2/\sigma_2^2)}. \tag{3}$$

Bland-Hawthorn & Shopbell (1993) have argued that due to the presence of threshold and saturation limits in photographic emulsions, density fluctuations obey a limited Poisson distribution which introduces skewness that must be corrected for in the weights. However, since we are only concerned with enhancing faint images lying safely in the linear region of the characteristic curve (demonstrated to be least affected by this effect), we argue that this source of error is negligible for our purposes.

The weighting scheme described here optimizes the signal-to-noise ratio by taking the mean, but takes no account of potential contamination by spurious images and bad pixels. In the presence of bad data, the median is a more robust (but less efficient) estimator of the 'true' mean, and will yield a cleaner stacked image than the weighted mean but with lower signal-to-noise ratio. Tukey and others (e.g., Hoaglin, Mostleler & Tukey 1983) have developed more elaborate techniques for stacking images which provide more of the efficiency of a mean estimator while retaining the 'pixel rejection' characteristics of a robust median estimator. A detailed discussion of the theory of image stacking and these estimators in particular may be found in Carter (1993) and Irwin (1996), and references therein. Tukey's biweight function is reported to be one of the best of these robust estimators, and we apply it to our plate data as a comparison to the conventional weighted average/pixel rejection combination algorithms.

3 THE STACKING PROCEDURE

3.1 Details of pixel weighting

A high-quality plate from our stacking sample was chosen to be used as a master or reference plate. A small section (1280×1280 10-μm pixels) of the pixel data from the centre of this plate was extracted for analysis, in which five blank

regions of sky (50×50 pixels) were identified. Values of σ_D and the background density D were calculated for each individual sky region, using iterative 3σ rejection in the log T distribution to discard non-sky pixels arising from plate defects or images. The global plate value of each parameter was taken to be the median average across the sky regions.

In order to obtain a well-defined faint-image signal value (corresponding to the H parameter discussed in Section 2), a 'mini-stack' of some 50 objects near the plate limit was used. Objects lying about 1 mag above the plate limit were identified in the small (1280×1280) section of pixel data used to determine the background parameters described above. These faint images were inspected, and spurious or extended objects were rejected; in addition, the stellar magnitude parameter was examined over the full run of plates to be stacked, and any object showing variation at a level greater than 3σ above the measured plate-to-plate differences was rejected. Pixel data of the good images were then extracted, and the plate background-subtracted. Positions for these objects accurate to ~ 1 μm, calculated using the SuperCOSMOS image analysis software (e.g. Beard, MacGillivray & Thanisch 1990), were used to co-add the objects, registering the images with one another on a 1-μm grid to create a finely sampled stacked array. Orthogonal strips were extracted from the centre of this combined image, which in general fit a Gaussian profile well (Fig. 1). The average height of these Gaussian fits was taken to be our parameter H for the master plate.

Both plate stacking and the weighting technique described here require that all slave plates be re-sampled on to the coordinate system of the master plate. Standard SuperCOSMOS software achieves this by dividing each plate pixel map into a 16 by 16 grid and using all object images within each subsection to define a geometric transformation (rotation, translation and scale) between coordinate systems. The (2-cm) grid size was chosen so that jumps in pixel position across grid boundaries were limited to a small fraction of a pixel and were thus negligible compared to other sampling errors. After coordinate transformation and bilinear interpolation to re-sample the data the above analysis was then simply repeated using the same blank sky regions and faint objects on the remaining plates. The resulting σ_D and H values for each slave plate were used to assign a weight relative to the master according to equation (3).

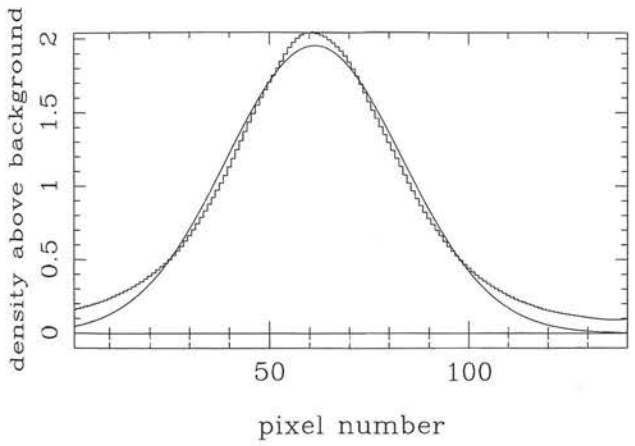

Figure 1. Histogram of a cut through a stack of faint images with a Gaussian fit overplotted.

3.2 Details of bad pixel rejection

A comprehensive set of image-combining algorithms incorporating weighting and bad pixel rejection are provided in the task 'imcombine' running under the IRAF[1] environment. In this section we present the results of using these various algorithms in conjunction with the weighting scheme described above on a set of 16 IIIaJ UKST Schmidt plates (see Table 2).

The small field used in these experiments was carefully chosen to contain plate blemishes and spurious images on one of the plates (see Fig. 2), features which would ideally be removed in any stacking process. The problem of bad pixel rejection should become progressively less serious as the number of plates to be stacked increases, and the most effective pixel-rejection algorithm may also change. The 16 plates have therefore also been analysed in substacks of four and eight plates.

The image-combination algorithms used were as follows:

(1) no rejection;
(2) median taken at each pixel;
(3) minmax rejection (one high, one low);
(4) sigma clipping (3σ rejection);
(5) average sigma clipping (3σ rejection);
(6) no weighting, no rejection;
(7) Tukey's biweight.

All except (2), (6) and (7) combined unrejected pixels by simple co-addition using weights, and any rejection was on a purely pixel-by-pixel basis, except for (5). The average sigma-clipping algorithm uses an entire strip of image data to calculate a noise model as a function of signal, which is then applied to each pixel in turn (see the online help pages for 'imcombine' for details).

Table 2. The 16 IIIaJ UK Schmidt plates used in this work.

Plate Number	Date	Exposure Time(mins)	Grade	Relative Weight
15563	24/05/93	65	bI	0.53
15795	05/10/93	60	bU	0.46
15796	06/10/93	100	bU	0.68
15801	07/10/93	90	aU	0.93
16177	06/07/94	110	a	0.84
16180	07/07/94	110	a	0.62
16183	08/07/94	110	a	0.53
16230	10/08/94	110	a	0.67
16700	29/07/95	60	aHD	0.31
16728	20/08/95	60	cXD	0.24
16731	23/08/95	60	aE	0.67
16741	25/08/95	70	aD	0.53
17117	25/05/96	90	aU	0.83
17167	07/08/96	60	aI	0.52
17173	11/08/96	60	a	1.0 (master plate)
17189	13/08/96	60	aDE	0.45

[1]IRAF is distributed by the National Optical Astronomy Observatories, which is operated by the Association of Universities for Research in Astronomy Inc., under contract with the National Science Foundation of the United States of America.

Correct application of these algorithms, of course, requires that the images have the same noise parameters. We therefore scale the data both additively and multiplicatively such that the global noise fluctuations in each plate are equal, allowing rejection of bad pixels. We note, however, that, due to sometimes large differences in seeing between plates, data in the presence of images can never be scaled to look identical. We therefore expect there to be variations in signal at the peak of faint images, inevitably resulting in a reduction of signal-to-noise ratio by the action of any pixel-rejection algorithm.

4 EXAMPLE RESULTS

The weighting algorithm was tested by stacking two plates with weights varying around those calculated using our technique. The weights we calculate were found to maximize the signal-to-noise ratio in faint images.

The relative merit of these stacking methods was assessed by considering both the signal-to-noise ratio in the resultant stack and the success of the pixel rejection in removing unwanted features. Each stack was reanalysed using the technique described in Section 3.1, and its signal-to-noise ratio was taken to be H/σ_D. The results are shown in Table 3. While the performances of the various rejection algorithms are assessed in Section 5, we answer the fundamental question of whether spurious features are likely to contaminate stacked data by simulating the action of the SuperCOSMOS image analysis software on our data. The 'pisafind' task in PISA (Draper & Eaton 1996) performs isophotal analysis on image data and is equivalent to the analogous SuperCOSMOS routine. We adopt the SuperCOSMOS norm of defining a 2.5σ detection as a signal and defining eight connected signal pixels as an object detection.

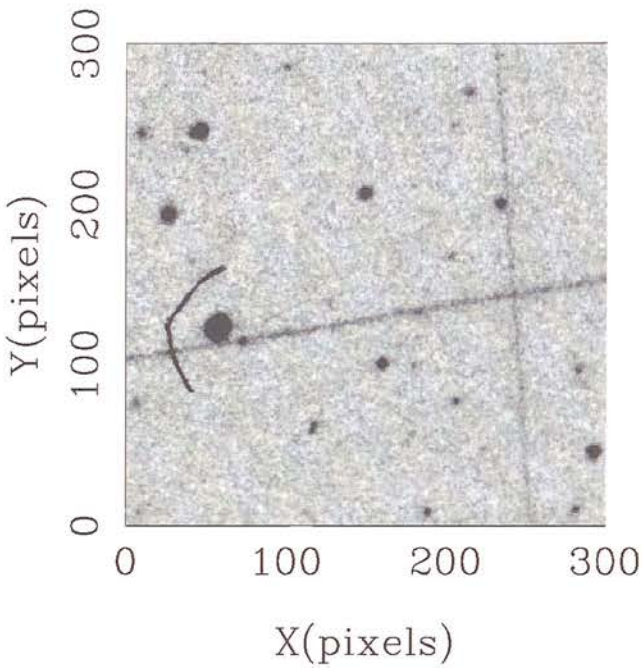

Figure 2. Pixel map of a region of plate J15796 containing two satellite trails crossing and a dust speck.

Table 3. Results of signal-to-noise ratio analysis on stacks (*note:* plate J15796 containing the image defects had a signal-to-noise ratio of 5.0 and the master plate had a signal-to-noise ratio of 8.9).

Stacking algorithm	4 plate stack s:n	8 plate stack s:n	16 plate stack s:n
(1) No rejection	12.8	18.7	23.3
(2) Median	10.3	14.9	18.1
(3) Minmax	10.3	16.6	21.4
(4) Sigma clipping	12.1	17.6	22.0
(5) Average sigma clipping	11.0	16.8	21.7
(6) No weighting, no rejection	11.1	16.8	20.9
(7) Tukey's biweight	–	–	18.8

Pixel and PISA thresholded image ellipse plots are shown for selected stacks. The results of stacking four plates are shown in Figs 3–10. The results of sigma-clipping rejection in eight-plate stacks and the full 16-plate stacks are shown in Figs 11–14. The full-stack results with no rejection are shown in Figs 15 and 16.

Certain applications of image-analysis software may require a relaxation of the criteria for object detection. Fig. 17 shows the ellipse plot for four plates stacked with no pixel rejection, with the object detection criteria relaxed to six interconnected 2σ signal detections. The result of applying the same detection criteria to a four-plate stack with average sigma-clipping rejection is shown in Fig. 18.

The weighting algorithm itself was tested by stacking the same two plates several times with various relative weightings. The signal-to-noise ratio in each resultant stack (measured as described above) is plotted against plate weight in Fig. 19, with the prediction for optimum weighting from our algorithm also plotted.

5 DISCUSSION

All rejection algorithms inevitably lead to a reduction in signal-to-noise ratios, since they can only *reduce* the signal at the peak of faint images as discussed in Section 3.2. It is clear from Table 3 that simply taking the median compromises the stack quality, while with the expected exception of minmax rejection being poor for a small number of plates the remaining rejection algorithms tend to perform equally well in terms of signal to noise.

Although Tukey's biweight is effective in removing spurious features from the stack, the stack signal-to-noise ratio is only marginally better than the median for 16 input images. The biweight technique may be improved by using a noise model to calculate sigma (as average sigma clipping does), although since the biweight always incorporates all data values into the final image (however weighted down), it cannot perform as well as an algorithm that efficiently rejects bad data outright.

Close inspection of the ellipse plots reveals that even with a four-plate stack both minmax and average sigma clipping remove both the satellite trails and the dust speck very effectively. The latter is to be preferred, however, since data are not automatically discarded, leading to increased signal-to-noise ratios in the final stack. In the case of no rejection the spurious features are propagated through the stacking procedure as expected, and are plainly visible even in the 16-plate stack in both the pixel and ellipse plots. The simple sigma-clipping algorithm is unsurprisingly very poor at rec-

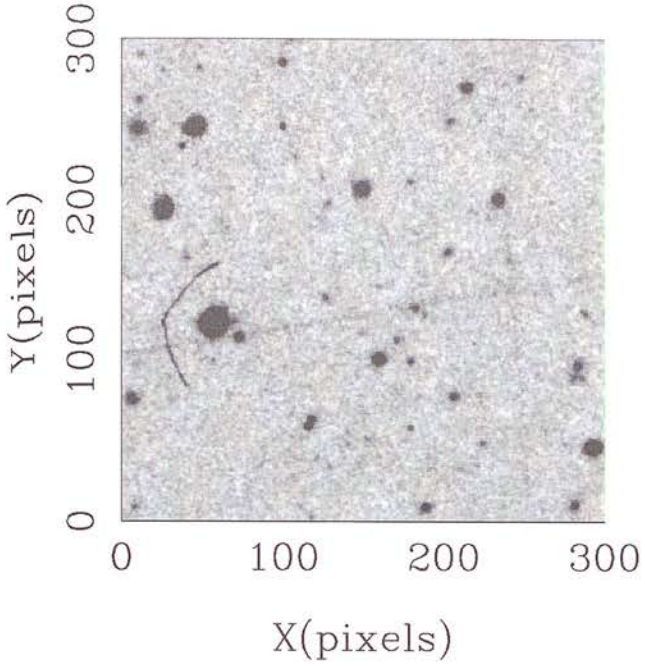

Figure 3. Four-plate-stack pixel map – no rejection used.

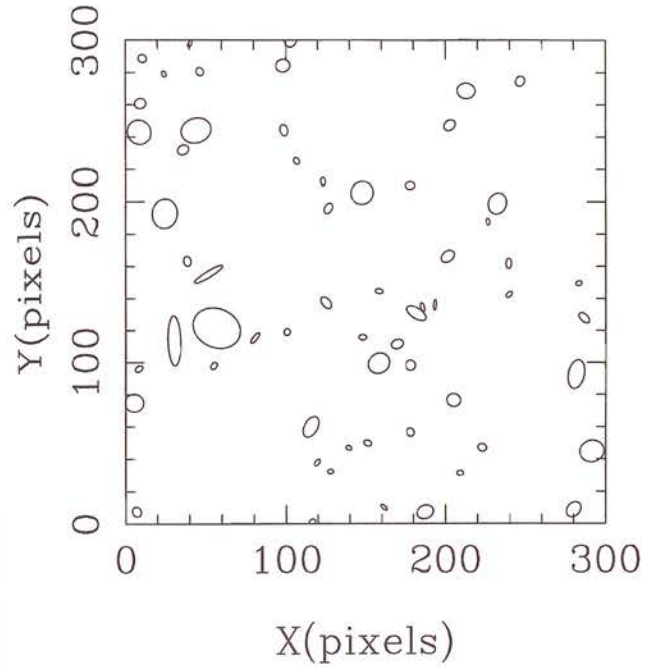

Figure 4. PISA ellipse plot of Fig. 3 pixel map – no rejection.

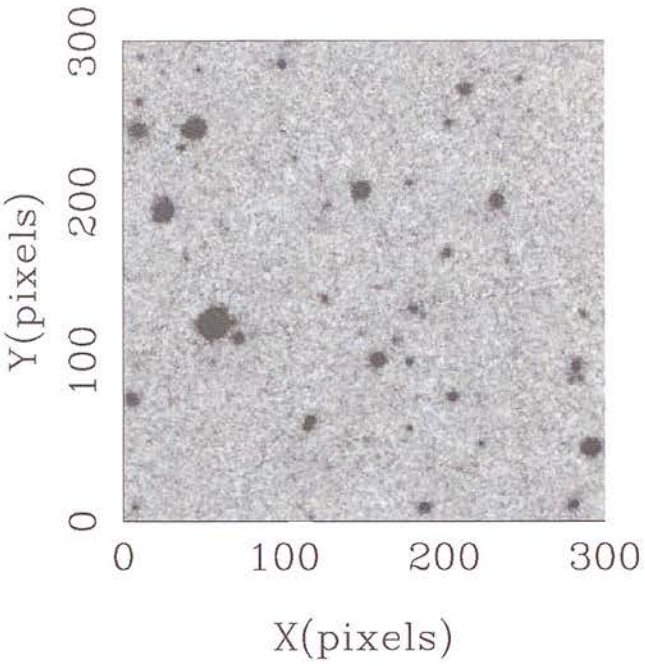

Figure 5. Four-plate-stack pixel map – average sigma-clipping rejection.

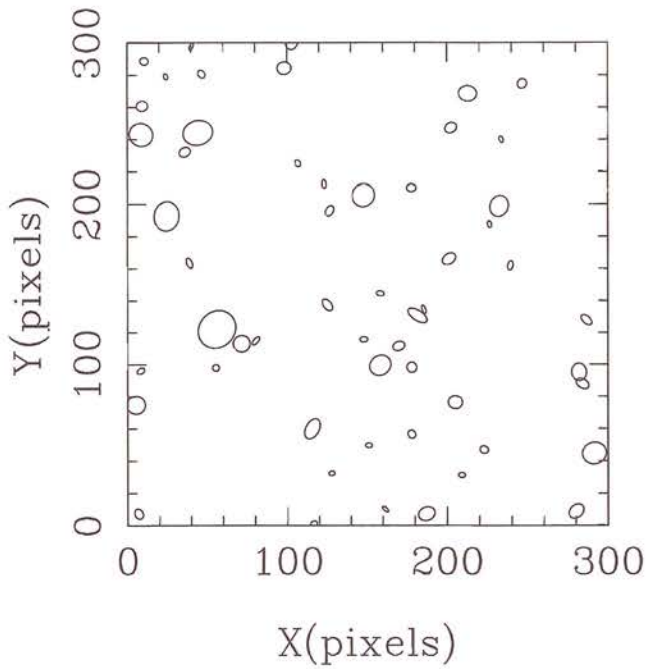

Figure 6. PISA ellipse plot of Fig. 5 pixel map – average sigma-clipping rejection.

ognizing spurious pixels in both the 4 and 8 plate stacks, although 16 plates appears to be sufficient for the 'pixel-by-pixel' technique to work adequately.

The performance of the various rejection algorithms can be assessed more quantitatively by subtracting the various stacked images from the purely weighted optimal signal-to-noise stack (number 1 in Table 3). The resulting image is zero where no pixel rejection has occurred, thus showing the regions where the rejection algorithm has been active very clearly. A 12 000-pixel area (containing no bright stars but several spurious images) has been extracted from these subtracted (16-plate) images for each rejection algorithm, plus the median and Tukey's biweight images. For a perfect algorithm, a histogram of the data values from this sub-image should have a large peak at zero, corresponding to the optimum signal-to-noise ratio where no rejection is required. There should also be a group of outlying points (generally at $\Delta D < 1$, since spurious images are more com-

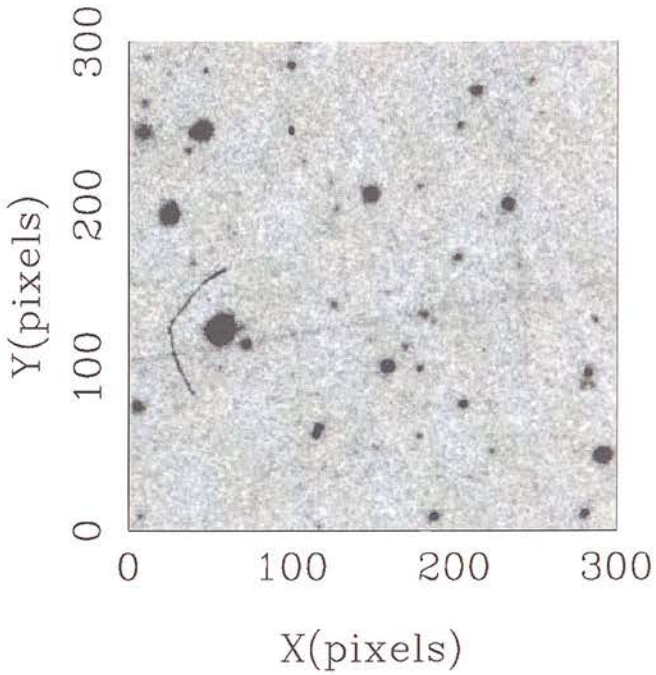

Figure 7. Four-plate-stack pixel map – sigma-clipping rejection.

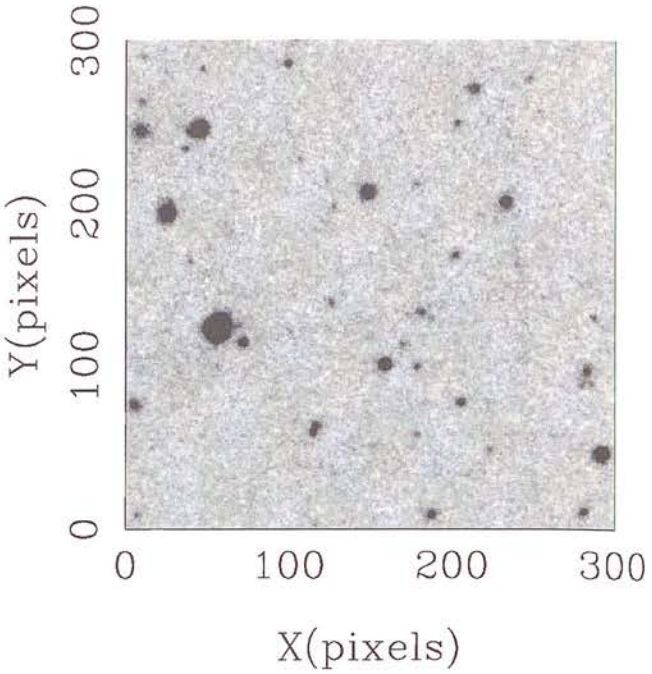

Figure 9. Four-plate-stack pixel map – minmax rejection.

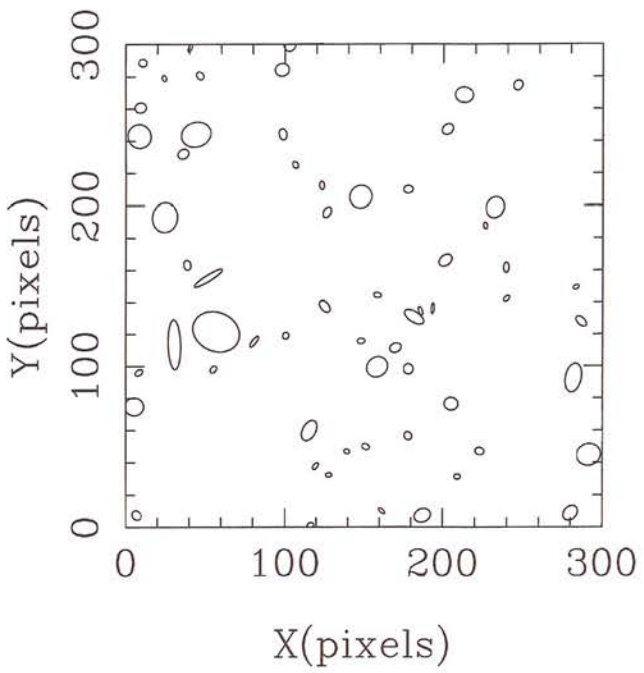

Figure 8. PISA ellipse plot of Fig. 7 pixel map – sigma-clipping rejection.

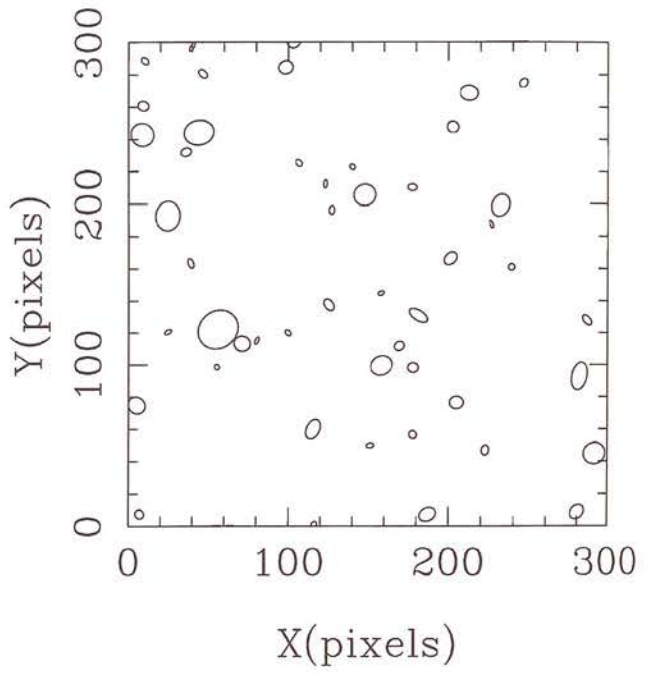

Figure 10. PISA ellipse plot of Fig. 9 pixel map – minmax rejection.

mon than emulsion scratches) where the rejection algorithm has discarded a bad data value. The 'average sigma clipping' algorithm emulates this behaviour most effectively (see Fig. 20), although the population with positive ΔD indicates that some rejection of good data is occurring (as expected for 3σ clipping). The straight sigma-clipping algorithm (Fig. 21) has been less effective in eliminating the large body of bad data at $\Delta D = -1 \times 10^{-3}$ in Fig. 20, although rejection of good data is perhaps less of a problem. The other three algorithms successfully reject deviant data (Figs 22, 23 and 24), but the plots show clearly that the stack signal-to-noise ratio has suffered as a result of the action of these algorithms, since all the good data points have been shifted to varying extents from their optimum value.

The relaxed detection criteria used in producing Fig. 17 have resulted in a clear increase in satellite trail images when compared to Fig. 4. Spurious images introduced by random sky fluctuations have also increased in number. The

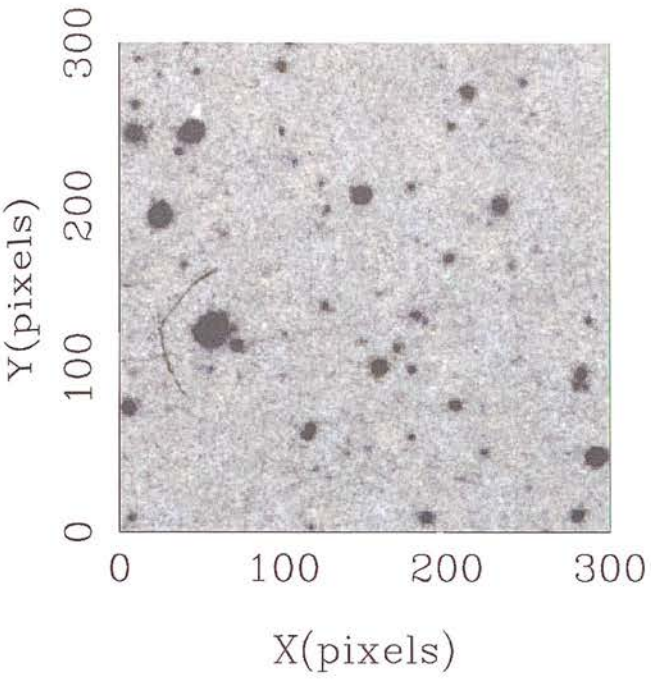

Figure 11. Eight-plate-stack pixel map – sigma clipping rejection.

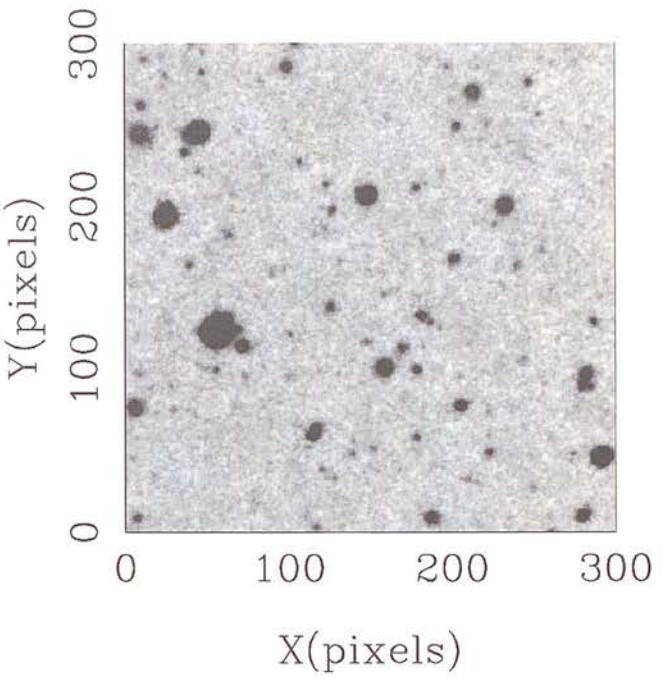

Figure 13. 16-plate-stack pixel map – sigma-clipping rejection.

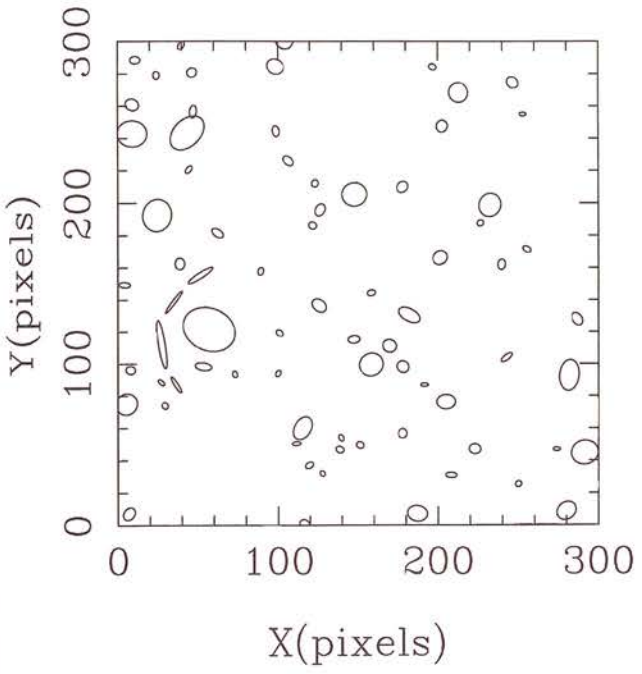

Figure 12. PISA ellipse plot of Fig. 11 pixel map – sigma-clipping rejection.

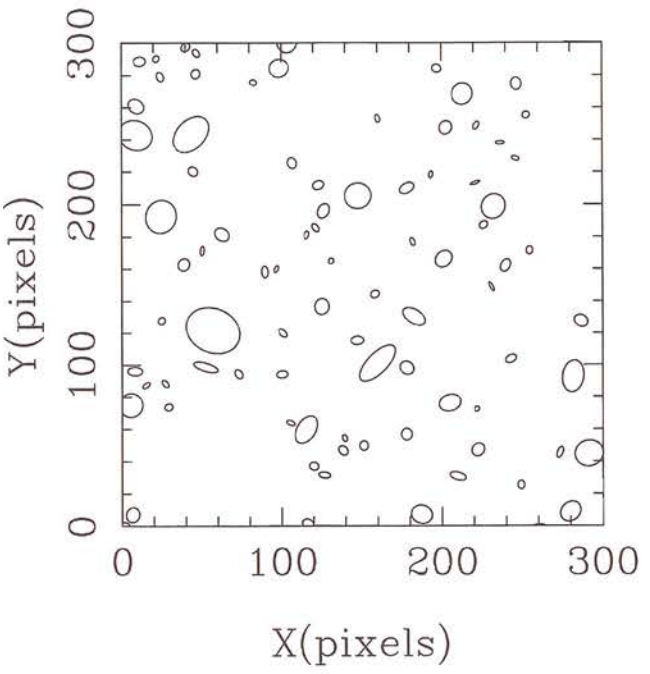

Figure 14. PISA ellipse plot of Fig. 13 pixel map – sigma-clipping rejection.

average sigma-clipping rejection performs well in eliminating bad images even in this case.

The validity of our weighting algorithm has been confirmed by our two-plate stacking experiment. Fig. 19 shows a broad maximum on the weighting axis providing optimum stack signal-to-noise ratios, which our algorithm locates successfully.

Table 3 appears to indicate that near-optimal signal-to-noise ratios are obtainable by a simple no-weighting stacking procedure. This will generally be true if, as in this paper, one is working with a universally high-quality plate collection. It should be emphasized, however, that weighting becomes increasingly important for more heterogenous plate material, where a single low-quality plate added at equal weight can seriously compromise stack quality.

Finally, we address the question of the increase in depth attainable by stacking plates. Assuming Poissonian counting errors, the signal-to-noise ratio should go as $n^{1/2}$ for identi-

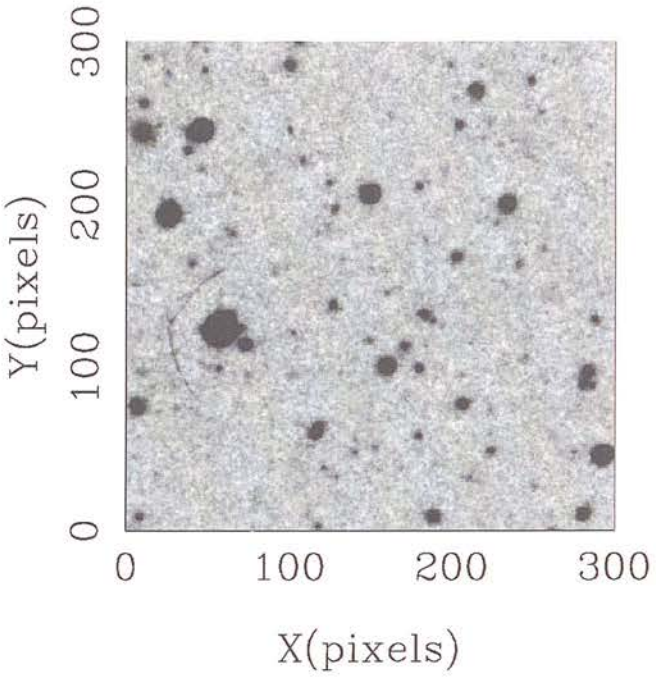

Figure 15. 16-plate-stack pixel map – no rejection.

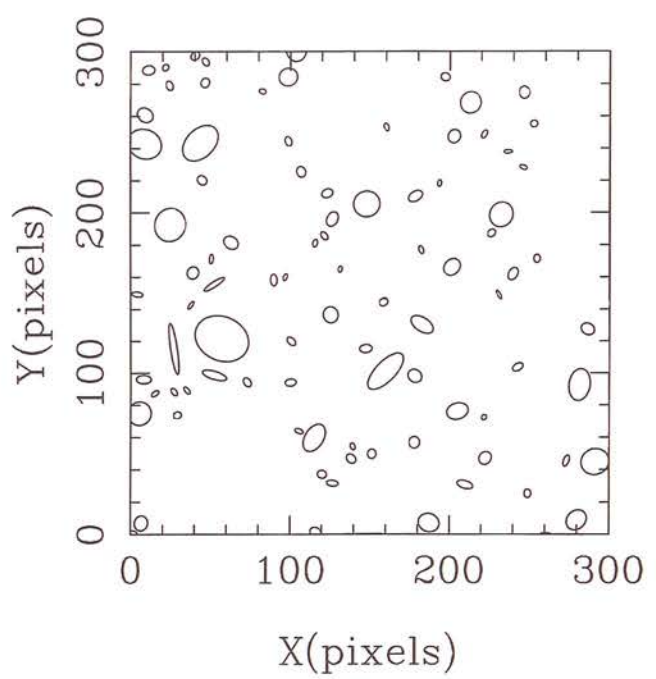

Figure 16. PISA ellipse plot of Fig. 15 pixel map – no rejection.

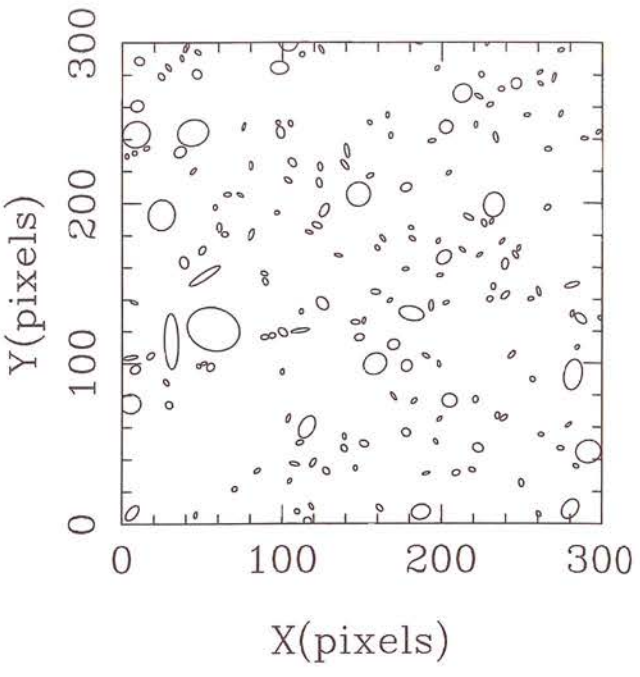

Figure 17. Four-plate-stack with no rejection PISA ellipse plot using relaxed object detection criteria.

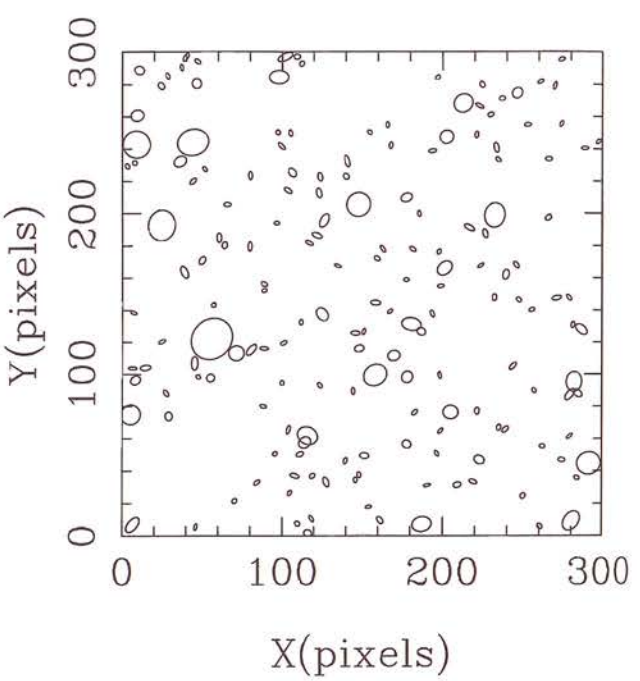

Figure 18. Four-plate-stack with average-sigma-clipping rejection PISA ellipse plot using relaxed object detection criteria.

cal plates, and therefore the increase in limiting magnitude will be 2.5 $\log_{10} n^{1/2}$. In Fig. 25 we show number–magnitude counts for a single plate, and also for a four-, eight- and 16-plate stack. Taking the 100 per cent completeness limit to be the point at which a given number–magnitude count turns over, the single plate reaches $B_J \sim 22$. This is around 0.5 mag brighter than the nominal 'limiting magnitude' quoted in the UKSTU Handbook (Tritton 1983). Following an $n^{1/2}$ law, the four-, eight- and 16-plate stack limits should be $B_J^4 \sim 22.8$, $B_J^8 \sim 23.1$, $B_J^{16} \sim 23.5$ respectively. This is in good agreement with Fig. 25, given that the 16 plates in question are not identical in terms of their signal-to-noise ratios (e.g., see the relative plate weights in Table 2).

6 CONCLUSIONS

The use of any pixel-rejection algorithm leads to reduction in signal-to-noise ratio in faint images in the resultant stack;

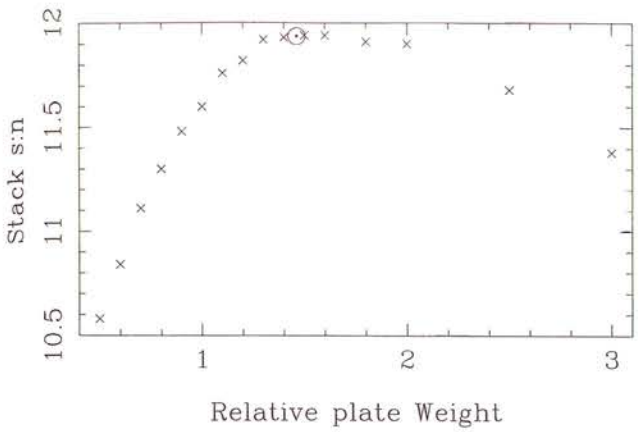

Figure 19. Resulting signal-to-noise ratio as a function of plate weighting for a stack of two test plates. Our weighting algorithm calculated an optimum relative weight shown by the dotted circle.

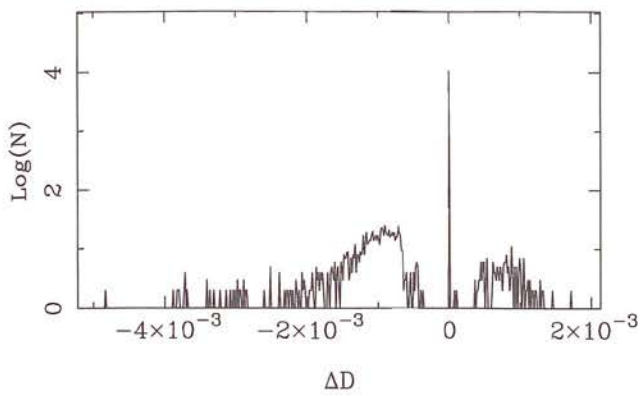

Figure 20. Rejection histogram (see text) for the 'average sigma-clipping' algorithm.

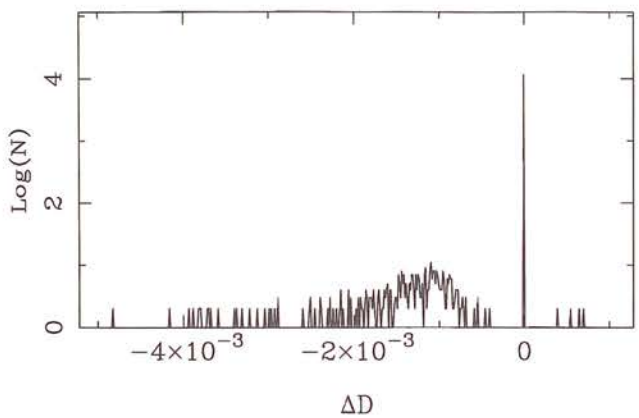

Figure 21. Sigma-clipping-rejection histogram.

thus pixel rejection should only be used in applications where spurious images are likely to pose a serious problem. In addition, while all rejection algorithms tend to work reasonably effectively for a stack of many plates, there is little need for pixel rejection in large stacks since a deviant point in one plate is unlikely to be significant when averaged into all the other plate data.

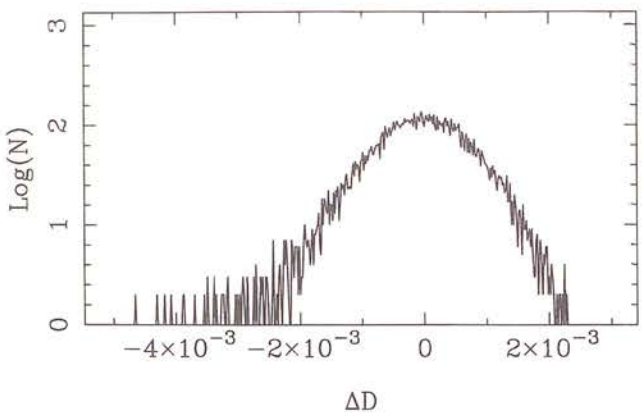

Figure 22. Median-image-rejection histogram.

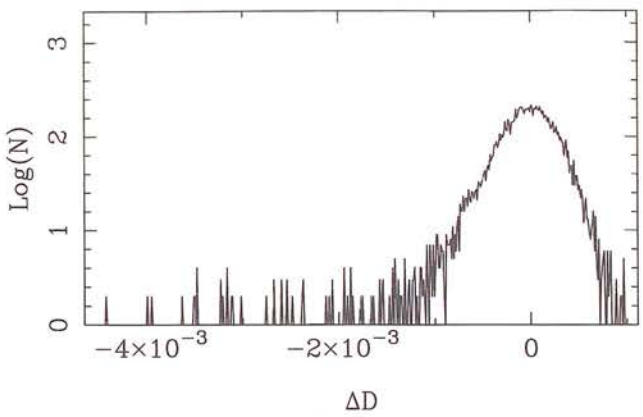

Figure 23. Minmax-rejection histogram.

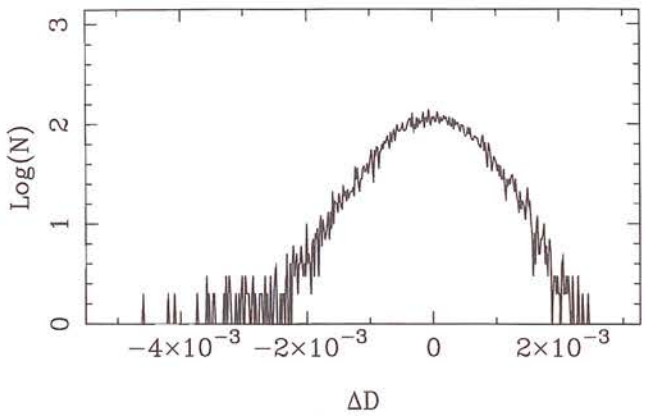

Figure 24. Tukey's biweight-rejection histogram.

The prime motivation for stacking digitized Schmidt plates is to detect faint objects over a wide field of view. The plate-stacking regime described here optimizes the signal-to-noise ratio in faint objects by analysing the noise characteristics of each plate and weighting them accordingly. We find that these weights used in conjunction with an 'average sigma clipping' bad pixel rejection algorithm yield a stacked image of near-optimal depth and free of spurious contaminant images. The gain in depth is found to be in accordance with the expected $\Delta M \sim 2.5 \log_{10} n^{1/2}$ law.

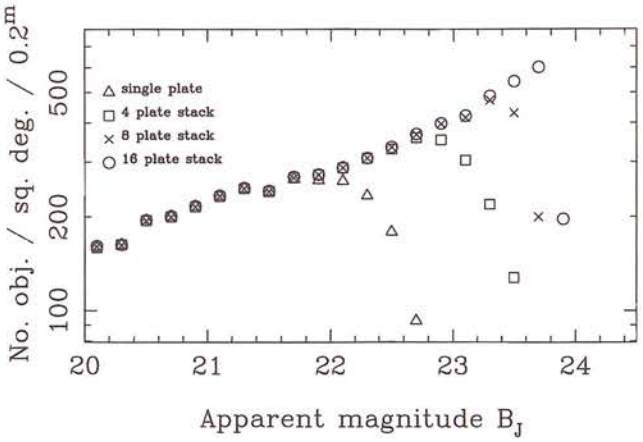

Figure 25. Number counts versus magnitude for various stacks, all with weighting but no rejection.

ACKNOWLEDGMENTS

Many people have contributed to the success of the SuperCOSMOS project. Among them are Bill Cormack, Lance Miller, Dennis Kelly, Steven Beard, Clive Davenhall, Bernard McNally, Magnus Paterson, John Cooke, Tom Paul, Joel Sylvester, Steven Stewart, Richard Bennett, John Harris and Eve Thomson. Thanks are due to David Carter for supplying the biweight code, and to Mike Irwin for helpful suggestions as a referee. We also thank the UK Schmidt Telescope Unit for obtaining and loaning the high-quality Schmidt plate material used here. Richard Knox acknowledges a PPARC post-graduate studentship.

REFERENCES

Altman J. H., 1977, in James T. H., ed., The Theory of the Photographic Process. MacMillan, New York, p. 481
Beard S. M., MacGillivray H. T., Thanisch P. F., 1990, MNRAS, 247, 311
Bland-Hawthorn J., Shopbell P. L., 1993, in IAU Commission 9: Working Group on Wide-Field Imaging, Newsletter No. 3, 52
Carter D., 1993, Gemini, No. 39, p. 14
Draper P. W., Eaton N., 1996, Starlink User Note 109: PISA: Position, Intensity and Shape Analysis
Furenlid I., Schoening W. E., Carder B. E., 1977, AAS Photo-Bulletin No. 16
Hambly N. C., Miller L., MacGillivray H. T., Herd J. T., Cormack W. A., 1998, MNRAS, in press
Hawkins M. R. S., 1991, in IAU Commission 9: Working Group on Wide-Field Imaging, Newsletter No. 1, 23
Hoaglin D. C., Mosteller F., Tukey J. W., 1983, Understanding Robust and Exploratory Data Analysis, Wiley, Chapter 11
Irwin M. J., 1996, in Espinosa J. M., ed., 7th Canary Islands Winter School, Detectors and Data Analysis Techniques for Wide Field Optical Imaging. Cambridge Univ. Press, Cambridge, p 59
Kemp S. N., Meaburn J., 1993, A&A, 274, 19
MacGillivray H. T., Thomson E. B., 1992, Digitised Optical Sky Surveys, Astrophysics and Space Science Library Proceedings, Vol. 174. Kluwer, Dordrecht
Malin D. F., 1988, in Marx S., ed., Proc. IAU Workshop on Astrophotography. Springer, Berlin, p. 125
Miller L., Cormack W. A., Paterson M., Beard S. M., Lawrence L., 1992, see MacGillivray & Thomson (1992), p. 133
Morgan D. H., Tritton S. B., Savage A., Hartley M., Cannon R. D., 1992, see MacGillivray & Thomson (1992), p. 11
Nutting P. G., 1913, Phil. Mag., 26, 423
Schwartzenberg J. M., Phillipps S., Parker Q. A., 1996, A&AS, 117, 179
Selwyn E. W. H., 1935, Photogr. J., 75, 571
Tritton S. B., 1983, UKSTU Handbook, Royal Observatory Edinburgh

Mon. Not. R. Astron. Soc. 000, 000–000 (0000) Printed 23 March 1999 (MN LATEX style file v1.4)

A Survey for Cool White Dwarfs and the age of the Galactic Disc

R.A. Knox[1], M.R.S. Hawkins[1,2], N.C. Hambly[1,2]
[1]*Institute for Astronomy, University of Edinburgh, Blackford Hill, Edinburgh, EH9 3HJ*
[2]*Royal Observatory, Blackford Hill, Edinburgh, EH9 3HJ*

Accepted —. Received —; in original form —

ABSTRACT

We describe a new multi–colour proper motion survey for cool white dwarfs (CWDs). The observational database consists of $\sim$ 300 digitally scanned Schmidt plates in ESO/SERC field 287. The entire survey procedure, from the raw Schmidt plate data to final white dwarf luminosity function (WDLF) is described, with special emphasis on completeness concerns.

We obtain a sample of 58 WDs, for which we have follow up CCD photometry and spectroscopy of a representative sub–sample. Effective temperatures and luminosities of our sample objects are determined by comparing photometry with the model atmosphere predictions of Bergeron, Saumon and Wesemael. Space densities are calculated using an adaptation of Schmidts ($1/V_{max}$) method, from which a WDLF is constructed. Comparison of our observational LF with the models of both Wood and García-Berro et al. indicate an age for the local Galactic Disc of 10^{-1}_{-3} Gyr. Importantly, we find no evidence of incompleteness in our survey sample. Proper motion number counts imply the survey is complete, and the WD sample passes the (V/V_{max}) completeness test.

Key words: surveys – stars: luminosity function – white dwarfs

1 INTRODUCTION

A reliable age for the local Galactic Disc places a valuable constraint on both globular cluster ages and cosmological models. A number of independent methods of investigating this problem have been employed in the past (eg. Jimenez 1998 and references therein), resulting in a broad consensus that the lower limit for the Disc age lies between 8 and 12 Gyr. Potentially one of the most reliable means of estimating the Disc age is via cool white dwarf (CWD) stars. These estimates use the idea, first proposed by Schmidt (1959), that in a galaxy of finite age there will be a temperature beyond which the oldest, coolest white dwarfs (WDs) have not had time to cool. This predicted cut-off in the luminosity function (LF) of WDs, if satisfactorily observed, can then be used in conjunction with WD cooling models to derive the Disc age.

CWDs are difficult to find, being both extremely faint and of similar colour to the numerous K and M-type dwarfs; and are almost exclusively discovered by means of their proper motion. The cut-off in the WDLF was observed (Liebert, Dahn & Monet 1988, hereafter LDM) after thorough follow up observations of CWD candidates drawn from the Luyten Half Second (LHS) Catalogue (Luyten 1979). Although at that time a Disc age of 9.3 $\pm$ 2 Gyr was derived from this sample (Winget et al. 1987), further observations and improvements in model atmospheres (Bergeron, Ruiz & Leggett 1997, hereafter BRL) and theoretical LFs (Wood 1992, 1995) has prompted a recent redetermination of the Disc age for the same sample (Leggett, Ruiz & Bergeron 1998, hereafter LRB), yielding a value of 8 $\pm$ 1.5 Gyr. While the existence of the cut-off in the LDM WDLF has not been challenged by subsequent observational work, the details of its precise position and shape have. A sample of CWDs found using common proper motion binaries (CPMBs), again culled from the Luyten surveys, suggest that there are $\sim$ 5 times more very faint CWDs than found by LDM (Oswalt et al. 1996, hereafter OSWH). A Disc age of 9.5 $\pm$ 1 Gyr was found using this sample. and the factor of $\sim$ 5 increase in the faintest WDs has been confirmed by an independent search for CWDs in the south (Ruiz and Takamiya 1995).

Until now, the proper motion catalogues used to extract samples of CWDs have been produced by 'blink' comparison. While these surveys have clearly been successful in picking up individual stars of low luminosity and high proper motion, the use of such a subjective survey technique raises worries concerning completeness. The advent of high precision micro-densitometers such as SuperCOSMOS (Hambly 1998 and references therein) allow proper motions

and magnitudes to be calculated objectively using a series of plates in the same field. Hambly et al. (1997) have recently discovered in Taurus perhaps the coolest known WD using just such a procedure. This object, WD 0346+246, should certainly appear in the LHS Catalogue, and would then presumably have been included in the LDM sample since it fulfills the given criteria. This object was discovered serendipitously from work in a particular $6 \times 6^{\circ}$ Schmidt field. and therefore casts further doubt on the completeness of the Luyten catalogue.

In this work we exploit both the extensive collection of over 300 plates in ESO/SERC field 287 and the power of the SuperCOSMOS measuring machine to produce a deep, complete multi-colour proper motion survey from which a sample of CWDs has been extracted. Much attention was given to the critical question of completeness, with specific reference to the choice of survey limits and the sources of potential contaminants. The paper is organised as follows: the plate database and reduction of the digitally scanned data is described in Section 2; the choice of survey limits to combat sample contamination and the method of WD sample selection are discussed in Section 3; in Section 4 the important question of the high proper motion limit is addressed by independent tests; some follow up observations of our WD candidates are presented in Section 5; stellar parameters are calculated for our sample in Section 6, which also includes a discussion of potential contaminant populations; the WDLF from our sample is presented in Section 7, and the derived Disc ages discussed in Section 8.

2 SCHMIDT PLATE DATA REDUCTION

In the course of a long term quasar variability study (eg. Véron & Hawkins 1995) over 300 Schmidt plates have been taken in ESO/SERC field 287. Figure 1 shows the distribution over time of the plate collection in this field in the two principal passbands available. B_J and R_F . Additional plate material exists in the U (19 plates), V (11 plates) and I (40 plates) passbands. All these plates have been digitally scanned by either the SuperCOSMOS plate measuring machine or its predecessor COSMOS (MacGillivray and Stobie, 1984). As described in Appendix A, a CWD survey utilising the reduced proper motion (RPM) population discrimination technique requires photometry in at least two passbands and proper motion data. Although for most stellar types a survey of this sort will be proper motion limited, for extremely intrinsically faint objects such as cool degenerates the photometric survey limits also become important. A principal concern in this work is therefore to maximise the survey depth.

The technique of stacking digitised Schmidt plates has been in existence for some time (eg. Hawkins 1991; Kemp & Meaburn 1993; Schwartzenberg et al. 1996), and has recently been thoroughly investigated with SuperCOSMOS (Knox et al. 1998). The database presented in Figure 1 is an obvious candidate for stacking in a proper motion survey, since at least 4 plates are available in most years and the use of 4 plate stacks rather than single plate data will yield deeper photometric survey limits with no reduction in the proper motion time baseline. The data has therefore been grouped into 4 plate stacks according to Table 1.

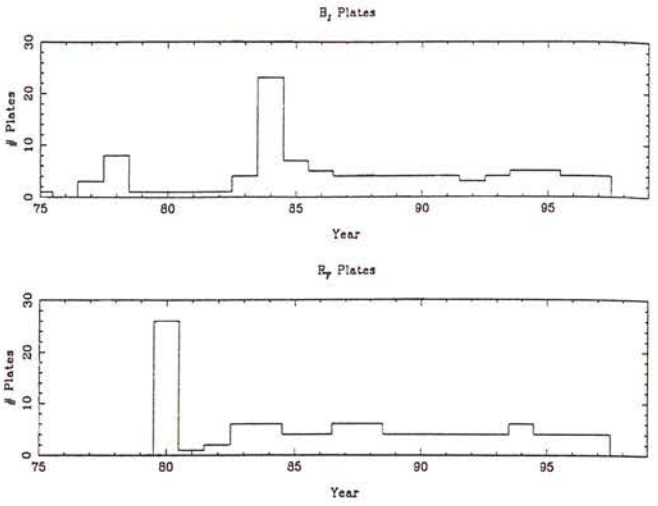

Figure 1. Number of plates per year in ESO/SERC Field 287 in the B_J (top) and R_F (bottom) passbands

Year	B_J	R	Year	B_J	R	Year	B_J	R
1977	1		1984	4	2	1991	1	1
1978	1		1985	2	1	1992	1	1
1979			1986	1	1	1993	1	1
1980		5	1987	1	1	1994	1	1
1981			1988	1	1	1995	1	1
1982			1989	1	1	1996	1	1
1983	1	1	1990	1	1			

Table 1. The number of B_J and R 4 plate stacks per annual epoch.

In order to track objects through epochs and calculate relative proper motions, all the stacks have been shifted to a common co-ordinate system corresponding to a measure of the high quality B_J plate J3376. This is achieved by a global transformation followed by local transformations (translation, rotation and scale), performed by splitting the stack area into a grid of 16x16 small areas (Hawkins 1986). Every object in each area is used to define the local transformation (since fainter objects are more numerous, they essentially define the astrometric coordinate system). Objects are then paired up between epochs. The software used in this work operates using a fixed 'box size' (13arcecs) in which it looks for a pair, thus in the first instance a high proper motion limit is imposed on the survey – this issue will be addressed in detail later. The pairing procedure yields a list of x and y coordinates for each object, one set for each stack the object is found on. Calculating proper motions is then simply a matter of performing a linear regression fit to each object's x and y coordinates as a function of time. However, erroneous pairing inevitably occurs between stacks, and we therefore wish to perform some form of bad point rejection to reduce contamination by spurious proper motions. In order to reject deviant points (and calculate parameters such as σ_μ and χ^2) an estimate of the error associated with each measure of position is required. We assume this error is simply a function of magnitude and that it will vary from stack to stack, but not across the survey area. This error is calculated using the

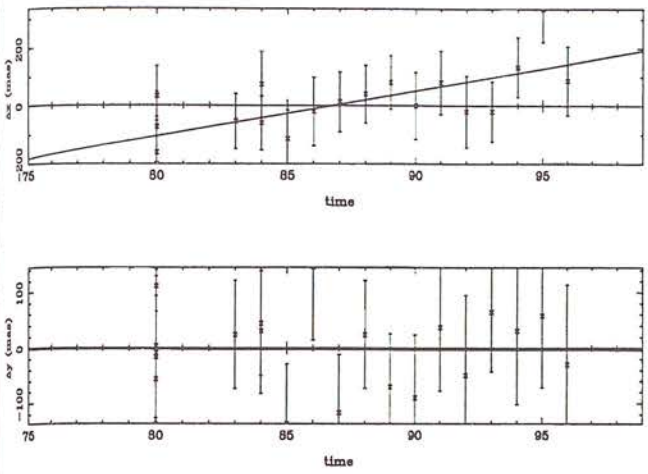

Figure 2. An example of a linear regression fit to a set of object positions. The vertical axis is deviation of measured position on a given stack from the mean object position, with year this century on the horizontal axis

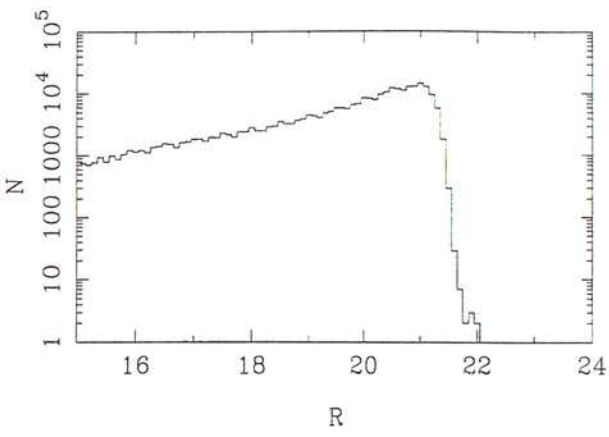

Figure 3. Number counts as a function of apparent R magnitude

deviation of an object's position on a particular stack from the mean position over the 20 stacks used, and is determined over 10 magnitude bins. A 3σ iterative rejection procedure is implemented to reject spurious pairings or high proper motion objects which are not reflecting the true positional errors sought. The calculated errors are much as one might expect: decreasing for brighter objects until factors such as saturation and blended images makes positional measures more uncertain.

A straight line fit can now be applied to the x and y data for each object, the gradient of which is taken to be the measured proper motion, μ_x and μ_y respectively. An example is shown in Figure 2, the points showing the deviation at each epoch from the average object position with error bars calculated as above. Deviant points arising from spurious pairings often lie far from the other data and will give rise to spurious high proper motion detections if not removed. We therefore iteratively remove points lying 3σ from the fitted line. This can occasionally lead to further problems if there are several bad points associated with the object, and the result of several iterations can be a larger spurious motion detection. This source of contamination is generally eliminated by insisting sample objects are detected on virtually every stack. The validity of the positional error estimation scheme described above has been verified by confirming that scatter plots of log reduced χ^2 as a function of magnitude cluster around zero for all magnitudes in all regions of the survey area.

Instrumental magnitudes are calculated for every object detected on each stack in the standard COSMOS/SuperCOSMOS fashion (Beard et al. 1990 and references therein). Briefly, an object detection is defined by a given number of interconnected pixels with intensity above a given threshold (eg. 8 interconnected pixels with intensity above a 2.5σ sky noise threshold for SuperCOSMOS data). An object's instrumental magnitude is then calculated as the log of the sum of the intensity above background across the object area. This quantity varies monotonically with true magnitude, and is therefore suitable for use in constructing calibration curves using a CCD sequence. A sequence of $\sim$ 200 stars with CCD magnitudes measured in a variety of passbands exists in field 287 (Hawkins et al. 1998) , yielding U, B, V, R and I photometry to a typical accuracy of 0.15 magnitudes (see Section 5.2). Significantly smaller errors are theoretically obtainable from photographic material, and the larger uncertainties we find appear to be caused by systematic deviations of sequence objects from the calibration curve. This is not a colour or field effect, and is probably caused by differences in detection media.

3 SURVEY LIMITS AND SAMPLE SELECTION

The 'catalogue' resulting from the implementation of the procedure described in the previous section consists of astrometric and photometric measures for over 200,000 objects. Criteria for inclusion in this preliminary sample is merely detection in both B_J and R passbands (since these are required for construction of the reduced proper motion diagram (RPMD)) and a measure of proper motion in both these passbands. It is from these objects that an uncontaminated proper motion sample is to be drawn; and we require well defined universal survey limits so that space densities can be calculated from the final survey sample.

Number count plots from this survey data increase linearly with increasing magnitude, as shown for the R data in Figure 3, before dropping precipitously. This cut-off is attributed to the survey detection limit, and the position of the turnover is used to determine photometric survey limits. The limits used are 21.2 in R and 22.5 in B.

The proper motion distribution for all objects in our survey area detected on at least 15 stacks in both B and R is shown in Figure 4. Low proper motions are generally an artifact of measuring machine error, thus the distribution indicates a typical error in measured proper motions of $\sim$ 10mas/yr. Our criteria for choosing a survey proper motion limit are elimination of contaminant spurious proper motions from the sample and , with this in mind, maximising the size of the final proper motion sample extracted. The deterioration of positional accuracy with magnitude means

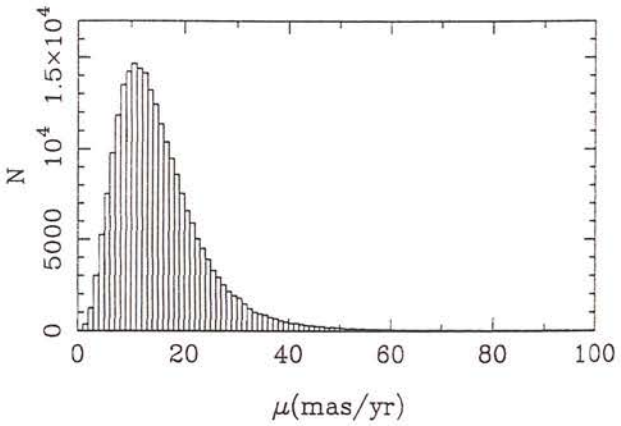

Figure 4. Proper motion frequency distribution

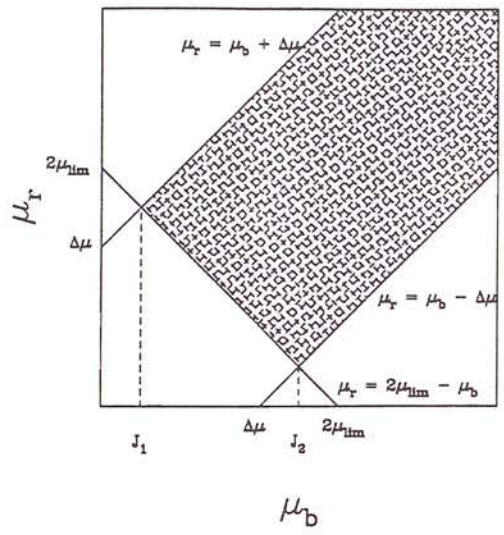

Figure 5. Objects will only be selected for the survey sample if their proper motions lie in the hatched region of the diagram.

that fainter objects also have more uncertain proper motion determinations. The peak of the proper motion distribution therefore moves to higher proper motions with object samples drawn from progressively fainter magnitude bins. For this reason, we consider the survey proper motion limit as a function of magnitude.

Three independent methods of determining an appropriate proper motion limit have been investigated for this dataset:

(1) analysis of proper motion error distribution
(2) cumulative proper motion number counts
(3) RPMD inspection

all of which are described here.

The characteristics of the 'noise' in the proper motion distribution can be analysed by assuming all objects are 'zero proper motion objects' and the calculated proper motions arise purely from random measurement error. The 'true' values of μ_x and μ_y measured by linear regression are therefore zero, and the random measurement errors give rise to a normal error distribution in μ_x and μ_y about zero with common σ. We are of course interested in the total proper motion, which follows a Rayleigh distribution of the form

$$P(\mu) = \frac{\mu}{\sigma^2} e^{-\frac{\mu^2}{2\sigma^2}}. \quad (1)$$

This survey utilises two independent measures of proper motion in the same field, one from the stacks of B plates and the other from the R stacks. A useful means of reducing the final proper motion survey limit will be to compare these two measures and reject inconsistent motions. Comparison of independent measures of proper motion needs to be incorporated into this analysis if it is to be useful in predicting sample contamination later. The measured B and R motions and their associated error distributions are therefore characterised

$$P(\mu_b) = A_b \mu_b e^{-C_b \mu_b^2} \quad (2)$$

and

$$P(\mu_r) = A_r \mu_r e^{-C_r \mu_r^2} \quad (3)$$

respectively. The algorithm used to select sample objects on the basis of proper motions will use three sequential cuts to eliminate spurious motions. Firstly, the averaged proper motion must exceed the proper motion limit μ_{lim} , ie:

$$\frac{\mu_r + \mu_b}{2} > \mu_{lim}. \quad (4)$$

Secondly, the difference in proper motion must not exceed a second survey parameter ($\Delta\mu$):

$$|\mu_b - \mu_r| < (\Delta\mu), \quad (5)$$

and finally the difference in position angle must not exceed a third survey parameter (Δo):

$$|\phi_j - \phi_r| < (\Delta\phi). \quad (6)$$

An object must satisfy all three of these criteria to be included in the sample. The desired outcome of this analysis is the ability to predict the expected contamination from spurious motions for a survey with parameters μ_{lim}, ($\Delta\mu$) and ($\Delta\phi$) given the 'zero proper motion object' error distribution described by equations 2 and 3. In order to do this we consider the combined probability distribution $P(\mu_b)P(\mu_r)$ on the $\mu_b - \mu_r$ plane. The survey criteria described above effectively limit the selected sample to a specific area on the $\mu_b - \mu_r$ plane, shown in Figure 5. Given a realistic estimate of the (normalised) $P(\mu_b)$ and $P(\mu_r)$ distributions an integration over the hatched region is Figure 5 yields an estimate for the fraction of objects, X, belonging to the error distribution likely to contaminate the sample. The integral

$$X = \int_{J_1}^{J_2} \int_{2\mu_{lim}-\mu_b}^{\mu_b+(\Delta\mu)} P(\mu_b)P(\mu_r)\mathrm{d}\mu_r\mathrm{d}\mu_b + \int_{J_2}^{\infty} \int_{2\mu_b-(\Delta\mu)}^{\mu_b+(\Delta\mu)} P(\mu_b)P(\mu_r)\mathrm{d}\mu_r\mathrm{d}\mu_b \quad (7)$$

where

$$J_1 = \frac{2\mu_{lim} - (\Delta\mu)}{2} \quad (8)$$

and

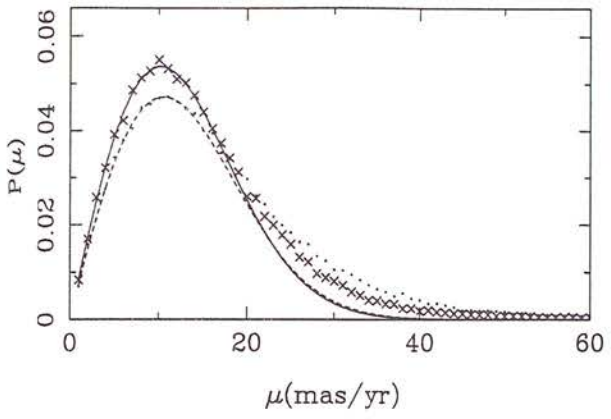

Figure 6. Normalised B (dashed line and dots) and R (solid line and crosses) measured data(points) and fitted error distributions (lines). This example uses the first 15 data points to determine the error distribution.

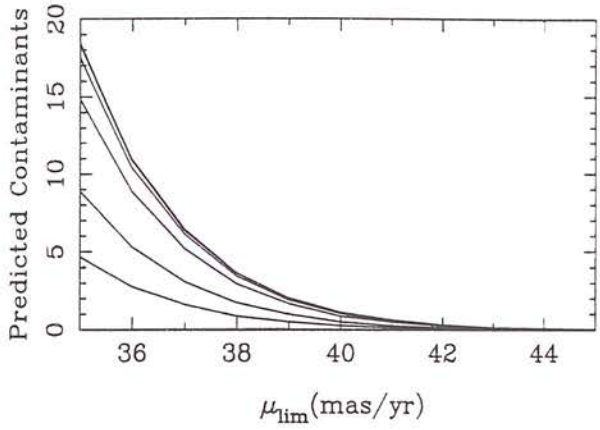

Figure 7. The results of numerical integration predicting the number of contaminant objects in the survey sample as a function of survey proper motion limit. The lower of the lines used a $(\Delta\mu)$ of 5 mas/yr, with $(\Delta\mu)$ rising to 50 mas/yr for the top line ($(\Delta\phi)$ was set to 90 throughout). These calculations were based on error distributions determined from the first 15 proper motion bins of the measured μ_b and μ_r distributions.

$$J_2 = \frac{2\mu_{lim} + (\Delta\mu)}{2} \tag{9}$$

is easily calculated numerically for arbitrary μ_{lim} and $(\Delta\mu)$. Since this analysis concerns zero proper motion objects whose spurious motion arises purely from machine measurement error, we may assume no preferred position angle, and the resulting fraction X will be cut by a further $(2(\Delta\phi))/360$ ($(\Delta\phi)$ in degrees) by the position angle selection criterion, ie.

$$X_{final} = \frac{X}{2(\Delta\phi)/360}. \tag{10}$$

The calculation described above requires knowledge of the $P(\mu_b)$ and $P(\mu_r)$ 'zero proper motion' error distributions. If equation 7 is to be used to calculate numbers of contaminants it is important that $P(\mu_b)$ and $P(\mu_r)$ can be simultaneously rescaled from normalised distributions. The B and R data are therefore paired so that $P(\mu_b)$ and $P(\mu_r)$ contain the same objects and thus the same number of objects. For the purposes of this analysis this proper motion data is thought of as consisting of two distinct distributions: the 'zero proper motion object' error distribution, on which a distribution of real proper motions is superposed. Any attempt to determine the error distribution from the measured distribution must use only the low proper motion data where the random errors of interest dominate systematics introduced by real proper motions. In the example to be shown here the first 15 bins (1mas/yr bins) of the normalised proper motion distribution is taken to be representative of the error distribution.

The first 15 data points in both B and R are fitted with an assumed error distribution like equation 3. These fits are shown along with the measured data in Figure 6, with the real data rising above the error fits representing real proper motions. Since the error distributions exclude real motions they must be renormalised before use in equation 7. The rescaling factor to be used in calculating numbers of contaminants is taken to be the number of objects contained in the error distributions. This number will in general be different for the B and R data, so the average is used. Numerical methods can now be used to predict the number of contaminant spurious proper motions for a range of μ_{lim}, $(\Delta\mu)$ and $(\Delta\phi)$ using equations 7 and 10. The result of a series of calculations is shown in Figure 7. The predicted contamination falls rapidly below one object as μ_{lim} exceeds $\sim$ 42mas/yr. Care must be taken however that the error distributions are not overly sensitive to the number of points in the measured μ_b and μ_r distributions used in their calculation. The error distributions were therefore recalculated using the first 30 bins in the measured μ_b and μ_r distribution and the predicted contamination plot redrawn using these new distributions . The two calculations prediction of the μ_{lim} at which the survey contamination drops to below 1 object are consistent to within $\sim$ 3mas/yr. Presented in Table 2 are the results of calculating the μ_{lim} at which the predicted number of contaminant objects falls below one for a range of magnitude cuts, $(\Delta\mu)$ and derived $P(\mu_b), P(\mu_r)$ distributions. Table 2 indicates that the $(\Delta\mu)$ survey parameter has a small bearing on the μ_{lim} where $N_{contam} \sim 1$. The $(\Delta\mu)$ criterion can therefore be relaxed substantially to ensure no real motions are rejected. A similar argument is applicable to the $(\Delta\phi)$ parameter, where the small advantage gained by tightening the $(\Delta\phi)$ criterion again becomes increasingly outweighed by the potential for rejection of real proper motions. To conclude comment on this analysis, any μ_{lim} greater than $\sim$ 45mas/yr should eliminate contamination arising from normally distributed positional measurement errors, although thus far no account has been taken of spurious motions arising from other sources (eg. erroneous pairings).

The second means of investigating the proper motion limit is via proper motion number counts. Assuming the local Disc has constant stellar density and that Disc kinematics give rise to an approximate inverse correlation between distance and proper motion, a plot of log cumulative number count (from large to small μ) versus log μ should fol-

R magnitude cut	No. of μ_b,μ_r data points used	μ_{lim} (mas/yr) for varying ($\Delta\mu$)			
		($\Delta\mu$)=5	($\Delta\mu$)=10	($\Delta\mu$)=30	($\Delta\mu$)=50
$R > 20.5$	15	40	41	42	43
	25	41	43	44	44
$20.5 > R > 20$	15	34	35	36	36
	25	34	35	36	36
$20 > R > 17$	15	30	31	32	32
	22	32	33	33	33
$R < 17$	15	31	32	33	33
	25	34	35	36	36

Table 2. Calculated μ_{lim} where predicted number of contaminants falls below 1 object. Column two represents the number of bins in the measured μ_b and μ_r distributions used to derive the $P(\mu_b)$, $P(\mu_r)$ distributions.

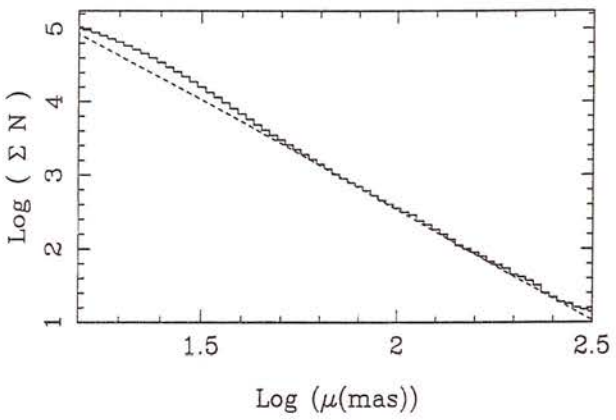

Figure 8. Cumulative number counts plot showing deviation from simple model at $\mu \sim 50mas/yr$.

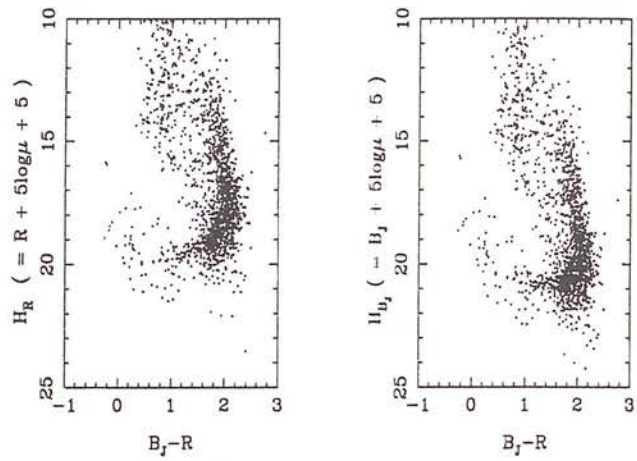

Figure 9. A RPMD of a sample with μ_{lim}= $50mas/yr$ for all objects.

low a straight line of gradient -3 (ie. $\log \sum N \propto -3 \log \mu$). In principle a proper motion limit for this survey could be obtained by determining the point at which our measured proper motions deviate from this relation due to the existence of spurious motions. In Figure 8 the cumulative number counts are plotted as a histogram. If the points between $\log \mu = 1.9$ and $\log \mu = 2.5$ are fit with a straight line the resulting gradient is (-2.998 ± 0.071), in excellent agreement with the idealised predicted slope of -3. The fit is shown as a dashed line. This finding compares favourably with a similar analysis of Luyten (1969, 1974, 1979) and Giclas (1971, 1978) common proper motion binary stars, which on an analogous plot describe a straight line of significantly shallower gradient that the expected -3 indicating increasing incompleteness with decreasing proper motion (Oswalt & Smith 1995). Towards lower proper motions our data rises above the line, indicating the onset of contamination at $\mu \sim 50$ mas/yr, lending credence to the findings of the previous analysis.

The final means of assessing the effects of varying μ_{lim} is the RPMD. The RPMD is, for all sample objects lacking follow up observations, the sole means of stellar population discrimination. For this reason it is worthwhile inspecting the RPMD of samples produced using various survey limits. The principal concern is that the white dwarf locus be

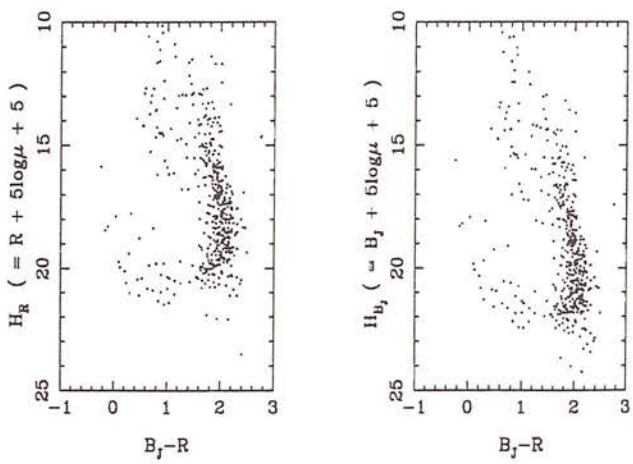

Figure 10. A RPMD of a sample with μ_{lim}= $80mas/yr$ for all objects.

as distinct as possible at all colours while maximising the sample size.

It can be argued that there is little purpose in lowering μ_{lim} for bright objects to anything near the level of potential contamination. Consider searching for an intrinsi-

cally faint star such as a reasonably cool white dwarf, with an absolute R magnitude of $\sim$ 14. amongst survey objects with apparent R magnitudes as faint as $\sim$ 19. Such an object, having a (conservative) tangential velocity of 40km/s, would have a proper motion of $\sim$ 80mas/yr - well beyond the predicted contamination limit. This argument becomes even more forceful for both intrinsically fainter and apparently brighter objects, implying that a conservative μ_{lim} is desirable for all but the faintest survey objects.

Figure 9 is a RPMD produced with a μ_{lim} of 50 mas/yr at every magnitude. The main sequence and white dwarf loci are visible, as is a dense group of objects between the two at $H_R \sim 19.5$. This group of objects probably consists of two sub-groups. Firstly of course, the most likely sample contaminants are faint objects creeping through just over the proper motion limit at this point. Secondly, one would expect a large population of objects to lie on the RPMD where the μ and R distributions are most populated , ie. at μ_{lim} and at faint R (an object with μ = 50 mas/yr and R=21 has H_R = 19.5), and it should therefore not be automatically assumed that every object lying at this point in the RPMD is suspect. A cause for concern however, is the way this population bridges the gap between the main sequence and the white dwarf population, a property one would expect from a contaminant locus rather than the detection of bona fide proper motions. If a more conservative limit of μ_{lim}=60 mas/yr is adopted for objects with $R > 20.5$ the RPMD (Figure 11) looks more promising, with the 'contaminant locus' all but gone, leaving only the expected mild confusion (Evans 1992) between populations at their faint extremity. The adoption of an extremely conservative μ_{lim} of 80 mas/yr for all objects leads to an even more well defined RPMD (Figure 10), where the white dwarf population discrimination is almost without exception unambiguous.

The survey parameters to be used to select the preliminary sample (ie. a sample subject to further object-by-object scrutiny and potential rejection, with the possibility of further objects being included the sample which lie just outside the RPM cut on one or both RPMDs) have been chosen with reference to the findings in this section.

Error analysis and number counts suggest a μ_{lim} of 50 mas/yr, a $(\Delta\mu)$ of 50 mas/yr and a $(\Delta\phi)$ of 90 degrees should essentially eliminate contamination arising from normally distributed measurement errors. It was found, however, that the white dwarf locus is insufficiently distinct in the RPMD obtained using these survey parameters. A slight restriction of μ_{lim} for objects with R $\geq$ 20.5 does much to solve the population discrimination problem. Therefore the survey parameters given above, with the exception of a μ_{lim} of 60 mas/yr for object with R $\geq$ 20.5, appears to be an acceptable compromise between sample maximisation and potential contamination and population discrimination problems.

The RPM can be expressed in terms of tangential velocity ,V_T ,and absolute magnitude, M :

$$H = M + 5\log_{10} V_T - 3.379. \qquad (11)$$

Evans (1992) has produced theoretical RPMDs by using expected $5\log_{10} V_T$ distributions and absolute magnitude - colour relations for various populations. Although these theoretical predictions were made for specific fields and incorporated error estimates peculiar to that work, they serve

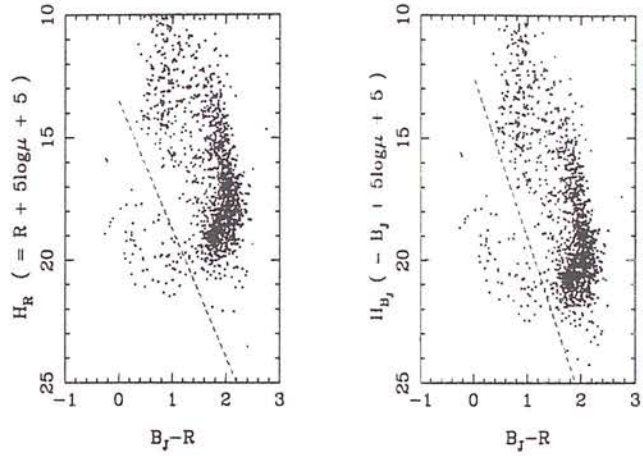

Figure 11. RPMD of the survey sample showing the white dwarf population divider used.

as a useful guide to the expected distribution of stellar populations on the RPMD. The RPMD white dwarf population locus is found to be an unambiguous population discriminator for all colours blue-wards of $(O - E) \sim 1.8$, with an increasing chance of contamination from the spheroid main sequence population red-wards of this colour. Transforming from $(O - R)$ to $(B - R)$ (Evans, 1989 - equation 13), spheroid population contamination should become a problem red-wards of $(B-R) \sim 1.6$ which in turn corresponds to $(B_J - R) \sim 1.2$. Indeed on inspection of Figure 11, the white dwarf locus does begin to become confused at this colour. This contamination occurs solely from the direction of small RPM, and the RPMD can still be used with some confidence as a population discriminator for objects with high measured RPM red-wards of $(B_J - R) \sim 1.2$. In order to accommodate these contamination considerations, the preliminary survey white dwarf sample is defined as those objects blue-wards (in both plots) of the lines in Figure 11. The lines cut the top of the white dwarf locus at $(B_J - R) \sim 1.2$ but allow slightly redder objects with higher RPMs into the sample. The white dwarf locus is unambiguous blue-wards of $(B_J - R) \sim 1.2$.

Every object in the sample must appear in at least 15 stacks in each passband. The positional data as a function of time have been scrutinised for every object selected as a white dwarf candidate, and those with dubious motions rejected. While such a process may seem rather arbitrary, it was necessary to incorporate this screening stage in the sample extraction because simple automated rejection algorithms such as the 3σ rejection routine used here cannot be guaranteed to eliminate spurious motions. Some examples are shown in Figures 12 and 13. All three objects shown successfully satisfied all the survey criteria. The object plotted at the top of Figures 12 and 13 (KX27) shows a clear, genuine motion in both x and y in both passbands and was included in the final sample without hesitation. The middle object (KX18) has larger positional uncertainties and a smaller overall motion, but still shows consistent, smooth motions and was also included. The final object shows evidence of large non-linear deviations in the last four epochs of the x measures in both passbands. Although the bad-point rejection algorithm has removed at least one datum from

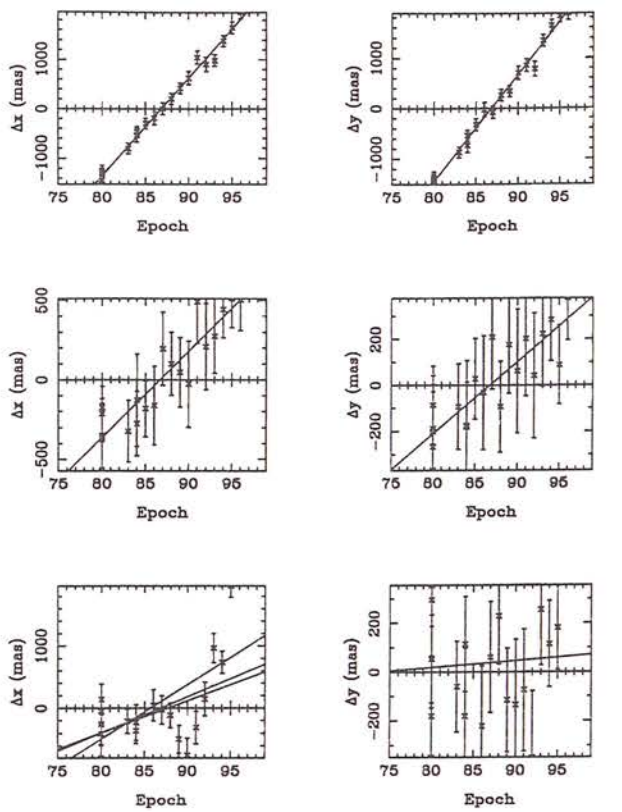

Figure 12. Some example proper motion plots from the R plate stacks. The top plot shows data for object KX27, the middle for KX18 and the lower for a rejected object

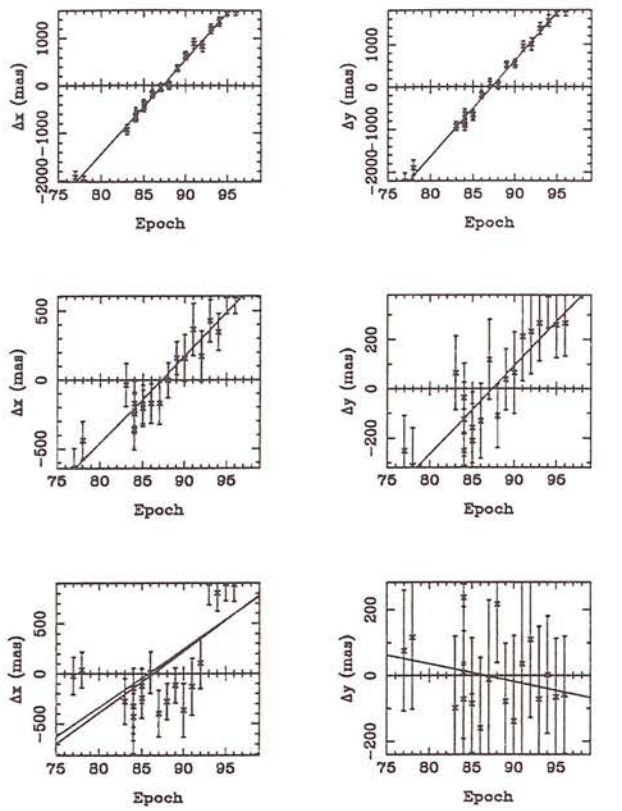

Figure 13. Proper motion plots complementary to Figure 12 from the B_J plate stack data

each x plot (as shown by the multiple straight line fits), this object shows no evidence of proper motion based on the first 16 data points and certainly cannot be considered a reliable proper motion object candidate. This object, along with 9 others, were rejected from the final WD sample. These rejected objects tended either to have large offsets from a positional distribution otherwise consistent with zero motion at either the first or last few epochs, as is the case with the rejected object described above; or the positional measures had an unusually large scatter around the mean position, indicating the error in position was larger than the objects magnitude would suggest. The reasons for these larger errors may be unusual image morphology or the effect of proximity to a neighbouring object. While this final rejection procedure is unsatisfactory in terms of its lack of objectivity, it is certainly preferable to inclusion of such objects in the final sample, or the introduction of extremely stringent survey limits which would doubtless exclude genuinely interesting objects. The digitised images have also been inspected.

The final sample consists of 56 objects which fully satisfy the photometric, proper motion and RPM/colour survey limits. A further two objects, which satisfy the photometric and proper motion limits but fall marginally outside the RPM/colour cut shown in Figure 11 have also been included after favourable follow up observations detailed in Section 5.

4 VERY HIGH PROPER MOTION, FAINT OBJECT SENSITIVITY LIMITS

In the previous Section, we discussed in some detail the checks made to establish a clean astrometric and photometric catalogue. The availability of plates over such a wide epoch range as detailed in Table 1 allowed us to search for faint and/or very high proper motion objects in this field. This is important for a number of reasons. For example, it is crucial to firmly establish what the upper limit of detectable proper motion is for the methods used, and also to check if significant numbers of objects have been missed because of this limit or because of the pairing algorithm used. Also, it is important to check at fainter magnitudes for very dim, high proper motion objects since it is the coolest (and therefore faintest) objects that constrain the age determination based on the turn–over in the WDLF. It is also interesting to search for very faint, high proper motion halo WDs in the light of the current debate concerning the origin of the dark lensing bodies detected in microlensing experiments (eg. Isern et al. 1998 and references therein).

We performed three experiments to investigate high proper motion and/or faint objects:

(i) Within the restricted epoch range 1992 to 1996, ie. five separate epochs, each consisting of a stack of four R plates, we used completely independent software employing a 'multiple–pass' pairing technique aimed specifically at detecting high proper motion objects. This software has successfully detected a very cool, high proper motion degenerate WD 0346+246 elsewhere (Hambly, Smartt & Hodgkin 1997). The pairing algorithm described previously used a 200μm

search radius over 19 yr resulting in an upper limit of ~ 1 arcsec yr^{-1}, whereas in the multiple–pass test we used a maximum search radius of 650μm over a 4 yr baseline, theoretically enabling detection of objects with annual motions as high as $\sim$ 10 arcsec. The highest proper motion object detected in the catalogue was relatively bright (R $\sim$ 14), with $\mu \sim 0.8$ arcsec yr^{-1}. This experiment revealed two $\mu \sim 0.8$ arcsec yr^{-1} objects , the one mentioned above and another slightly fainter object (R $\sim$ 15) ; no objects were found with motions larger than this. The colours and reduced proper motions of the two objects indicate that they are M-type dwarfs. The second object was undetected in the catalogue due to a spurious pairing, an increasingly likely scenario for high proper motion objects detected without a multiple pass algorithm since they move substantially from their master frame position. We note that all the expected objects having $\mu > 0.2$ arcsec yr^{-1} detected in the catalogue were also found by this procedure.

(ii) Using the procedure described in the previous Section, but with a relaxed minimum number of epochs, high proper motion objects were searched for. With a 200μm pairing requirement over a maximum epoch separation of 7 yr, the upper limit of proper motion was ~ 1.9 arcsec yr^{-1}. The two objects having $\mu \sim 0.8$ arcsec yr^{-1} found in the previous experiment were also recovered here; again, no objects were found with motions larger than this.

(iii) To investigate the possibility of fainter objects, we stacked up the R band material in groups of 16 plates at epochs 1980, 1983 to 1986, 1987 to 1991 and 1992 to 1996. Obviously, over any individual four year period an object having a proper motion greater than $\sim$ 1 arcsec yr^{-1} will have an extended image and will not be detected to the same level of faintness as a stationary star; nonetheless, the $\sim 0.75^{\rm m}$ increase in depth afforded by going from 4 to 16 plate stacks (eg. Knox et al. 1998) at least allows us to investigate the possible existence of objects having $\mu \sim 0.5$ arcsec yr^{-1} down to R $\sim$ 23 (100% complete to R $\sim$ 22) over an area of 25 square degrees. In this experiment, all the objects expected from the catalogue were recovered; in addition, one star was found having R $\sim$ 20, $\mu = 0.47$ arcsec yr^{-1} at PA = 179° and RA,DEC = 21h30m8.553s, −44°46'24.09 (J2000.0). This object is the M–type dwarf 'M20' discovered in the photometric survey of Hawkins & Bessell (1988) and has $B_J \sim 23$. The faintness in the blue passband is the reason that this object is absent from the catalogue. Once more, no other high proper motion, fainter stars were found.

These three experiments allow us to be confident that there is no large population of objects having $\mu \gtrsim 1$ arcsec yr^{-1} down to faintness limits of R $\sim$ 22 and $B_J \sim 23$. Furthermore, the cut–off in the WD sequence seen in the reduced proper motion diagrams is real, and not an artefact of incompleteness.

5 FOLLOW UP OBSERVATIONS

While the RPMD technique is a powerful population discriminator, it is desirable to obtain follow up observations of a sub-set of sample members. The principle motivation for this is to explicitly demonstrate the applicability of our survey technique by confirming the WD status of the sample objects via spectroscopy. Spectroscopic observations redwards of the WD cut in the RPMD may also be used to investigate the possibility of ultra-cool white dwarfs existing in the sample; and as a corollary to this, such observations allow clearer population delineation in the RPMD. In addition, photometric observations through standard filters ensure confidence in photographic-to-standard photometry transformations, provide useful independent checks of stellar parameters (eg $T_{\rm eff}$) derived from fits to photometry and may in future allow alternative population discrimination via eg. colour-colour plots.

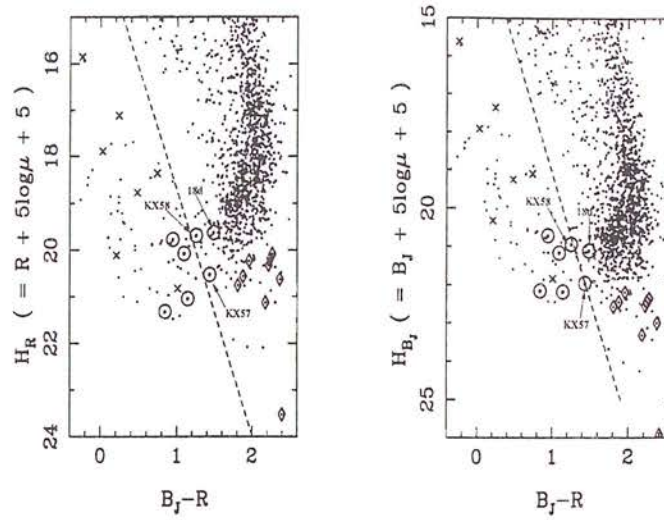

Figure 14. RPMD of the survey sample with spectroscopically observed objects numbered and highlighted. Diamonds denote objects identified as subdwarfs or M dwarfs, crosses an immediate firm WD identification. Dotted circles represent objects with ambiguous spectra (see text).The labelled objects have their spectra discussed in detail below.

5.1 Spectroscopy

This project was allocated 3 nights of observing time in 1996 between the 8th and 10th of August, and a further 3 nights in 1997 between the 5th and 7th of August on the 3.9m Anglo-Australian Telescope. A spectral coverage of 4000-7500Å was obtained with the RGO spectrograph and 300B grating in conjunction with the Tek CCD. Various standards were observed throughout each usable night and CuAr lamp exposures used for wavelength calibration. The data were reduced following standard procedures within the IRAF * environment.

The strategy behind these observations was to define as clearly as possible the constituents of the lower portion of the RPMD, from the blue end of the WD locus down to the extremely high H objects below the M stars. The spectroscopically observed proper motion sample objects are shown in

* IRAF is distributed by the National Optical Astronomy Observatories, which is operated by the Association of Universities for Research in Astronomy Inc., under contract with the National Science Foundation of the United States of America.

Figure 14. Both the unambiguous bluer region of the WD locus and the portion of RPMD lying red-ward of our WD cut generally consist of fairly bright objects. These regions have been probed spectroscopically, albeit more sparsely than the cool WD region consisting of mostly very faint objects. A combination of poor weather conditions at the AAT and the faintness of our CWD sample has rendered high signal-to-noise spectra of these objects unobtainable thus far.

The bluest objects have clearly defined Hydrogen Balmer lines with equivalent widths equal to or in excess of those typical for DA white dwarfs of similar colour (Greenstein and Liebert, 1990). The objects red-wards of our sample cut below the main sequence (MS) show spectra clearly distinct from cool WDs. Both subdwarfs and high velocity M dwarfs have been identified in this region of the RPMD.

A star lying near the cut-off region of the RPMD clearly showing the absence of strong metal features that would be present even in a low-metallicity subdwarf is very likely a CWD. We apply this line of argument to our data by selecting from the recent models of Hauschildt et al. (1998) a spectrum appropriate to a subdwarf (metallicity $[M/H] \geq -2$) of similar effective temperature to a given CWD sample object spectrum. The model spectrum is smoothed to the approximate resolution of the AAT spectra and multiplied through by a synthetic noise spectrum commensurate with the AAT CWD spectrum in question. The only features likely to be visible after this procedure are $\sim$ 5200Å MgI and the $\sim$ 4300Å CH G-band, and it is in these regions that we look for any evidence that our CWD sample objects are in fact subdwarfs.

This procedure has been undertaken for all CWD candidate spectra. Of these, the spectra of the three objects lying within the region of serious potential subdwarf contamination are displayed, and we restrict comment on the investigation of the bluer objects to the statement that none show any evidence of subdwarf like spectral features. KX58, displayed in Figure 15, is a convincing CWD candidate, showing a smooth continuum spectrum with no suggestion of the metal features apparent in the model subdwarf spectra. The noisier spectrum of KX57 in Figure 16 also shows no evidence of subdwarf features, although poorer signal-to-noise makes the identification less certain. The object 18d lies significantly red-ward of our CWD cut-off on the RPMD, and unfortunately its spectrum (Figure 17) is extremely noisy. While it is difficult to draw any conclusions from such poor data, the dip at $\sim$ 5200Å is a reasonable indication that this object is a subdwarf or MS star. Thus the position of 18d on the RPMD in conjunction with the spectral data evidence means this object does not warrant inclusion in our CWD sample.

To summarise the findings of our spectroscopic survey, the only objects showing notable deviation from expected WD spectra are the objects below the M dwarf portion of the RPMD (diamonds in Figure 14) and the more ambiguous case of object 18d discussed above.

5.2 Photometry

CCD photometry of a subsample of our CWD sample was obtained between 29th of July and the 4th of August 1997 on the 1m telescope of the South African Astronomical Observatory in Sutherland. Johnson-Cousins V, R, I photometry was obtained for all program stars on the Tek (512x512) CCD, with B measures also acquired for sufficiently bright objects. E-region standards were observed continuously through each usable night. Observed magnitudes with associated errors are displayed in Table 3.

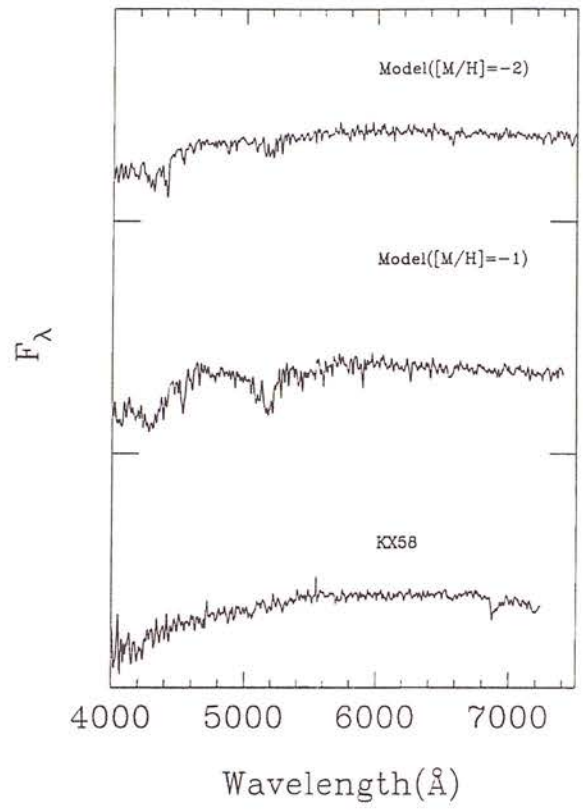

Figure 15. Spectrum of KX58 with comparison model subdwarf spectra

These observed magnitudes provide an independent check on the accuracy of the SuperCOSMOS photographic photometry, and we use the deviations of $m_{photographic}$ from m_{CCD} to obtain errors on the B, V, R, I photographic photometry of 0.17, 0.14, 0.13 and 0.16 respectively. The CCD photometry also allowed tighter estimates of effective temperature to be derived for observed objects, although they did not provide the hoped for useful constraints on log g.

6 SAMPLE ANALYSIS

Previous studies of CWD samples (eg LDM, BRL) have often benefited from a comprehensive and wide ranging observational database, including high quality spectra, optical and IR photometry and parallaxes. These observations, in conjunction with detailed WD models, allow determinations of stellar parameters such as effective temperature, log g, atmospheric composition, mass and bolometric luminosity. However, since this is a relatively new project and is concerned with stars of unusually faint apparent magnitude, such a database does not yet exist for this sample. It is therefore necessary for us to restrict our analysis, in the

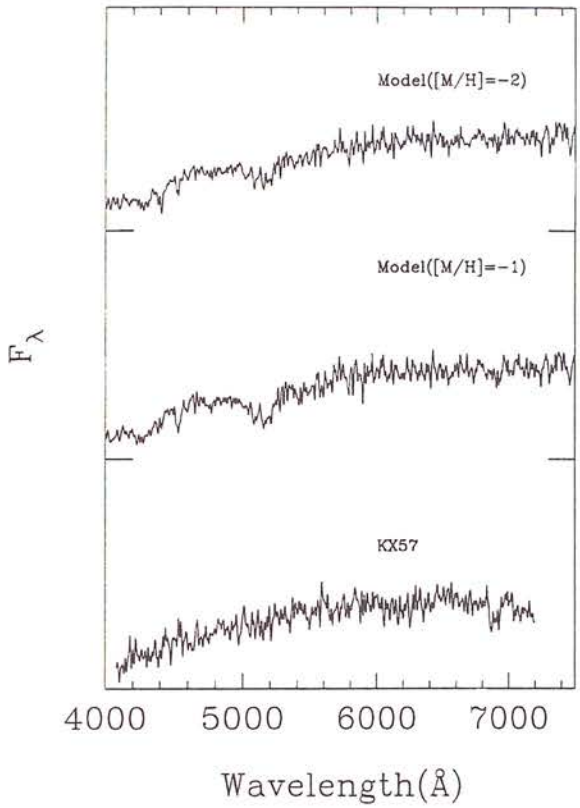

Figure 16. Spectrum of KX57 with comparison model subdwarf spectra

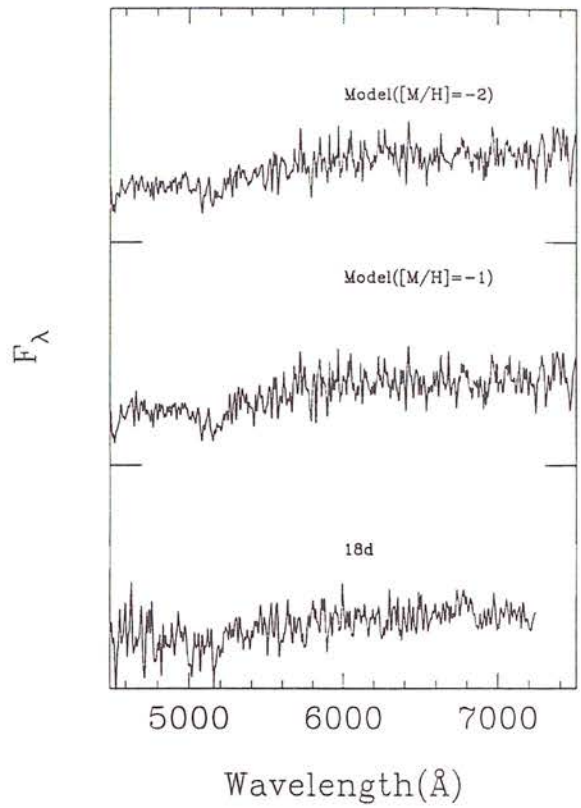

Figure 17. Spectrum of 18d with comparison model subdwarf spectra

first place by exploiting the homogeneity of WD masses by assuming a common typical log g for our entire CWD sample (the 60 stars with measured log g in BRL have a mean surface gravity $\overline{\log g} = 8.099 \pm 0.044$), and secondly by treating the atmospheric constituent of each star as an unknown parameter whose influence on the resulting WDLF must be determined later.

Bergeron et al. (1995) have published a detailed grid of model predictions for Johnson-Cousins U, B, V, R, I (and IR) photometry and bolometric corrections as a function of effective temperature and log g. Making our assumption that log g is always equal to 8, values for effective temperature and bolometric luminosity assuming both a H and He atmosphere can be calculated for every sample object.

Fitting for $T_{\rm eff}$ is achieved by interpolating the model grid at 10K intervals for the colour indices $(U-B)$, $(B-R)$, $(V-R)$ and $(V-I)$. We then evaluate χ^2 at each $T_{\rm eff}$ interval using all available colour indices for the object in question. While the photographic photometry is effective in adequately constraining $T_{\rm eff}$, smaller errors are obtainable with the SAAO CCD photometry, and it is used where available. The resulting χ^2, $T_{\rm eff}$ distribution yields a fitted value for $T_{\rm eff}$ and an estimate of the associated error, which can be used to read off interpolated values of absolute V magnitude and bolometric luminosity. This procedure is performed for each object for both an assumed H and He atmosphere.

Distance moduli obtained from these fits allow calculation of tangential velocities via the SuperCOSMOS proper motion measures. The distribution of derived tangential velocities is consistent with expectations for a sample of Disc stars (Evans 1992), and shows no evidence of contamination from high velocity halo objects. A summary of the results of the fitting procedure is shown in Table 4, including $T_{\rm eff}$ and $M_{\rm bol}$ with associated errors and $V_{\rm tan}$ values. Space density values for each object are also presented in Table 4; these are discussed in the following section.

An independent check on the validity of our initial CWD sample parameters (SuperCOSMOS photometry and astrometry) can be made by comparing known CWD samples with our data on the RPMD. Since the RPMD is the original means of population discrimination it is also interesting to overplot known subdwarf samples on our RPMD to further address the question of potential contamination. BRL published observations of a sample of 110 CWDs, including most of the coolest known degenerates. Extensive lists of extreme subdwarfs are less easily obtainable. Ryan (1989) used a RPM criterion to extract over 1000 subdwarf candidates from the NLTT catalogue. Accurate B and R photometry was published for these objects, providing a useful means of delineating the bluer portion of the WD RPMD locus. Monet et al. (1992) identified a subset of 17 extreme subdwarfs from their CCD parallax program also involving Luyten catalogue stars. Although only V, I photometry is published for these stars, we use the photometry published in Ryan (1989) to define colour transformations allowing the 17 subdwarfs from Monet et al. (1992) to be plotted on

Atmosphere:	H				He			
Object	$T_{\rm eff}$ ($K^{+1\sigma}_{-1\sigma}$)	$M_{\rm bol}$	$V_{\rm tan}$ km/s	$V_{\rm max}^{-1}$ (10^{-4}pc^{-3})	$T_{\rm eff}$ ($K^{+1\sigma}_{-1\sigma}$)	$M_{\rm bol}$	$V_{\rm tan}$ km/s	$V_{\rm max}^{-1}$ (10^{-4}pc^{-3})
KX 1	4700^{5090}_{4320}	$15.14^{14.79}_{15.51}$	76.0	0.956	5250^{5520}_{5030}	$14.68^{14.45}_{14.86}$	102.2	0.436
KX 2	5980^{6620}_{5470}	$14.08^{13.63}_{14.47}$	72.5	0.209	6340^{6950}_{5890}	$13.85^{13.45}_{14.18}$	84.4	0.144
KX 3	5800^{6340}_{5340}	$14.22^{13.82}_{14.58}$	73.7	0.317	6050^{6540}_{5710}	$14.06^{13.72}_{14.31}$	83.5	0.231
KX 4	5060^{5480}_{4680}	$14.81^{14.46}_{15.16}$	83.7	0.546	5460^{5780}_{5210}	$14.50^{14.26}_{14.71}$	103.5	0.315
KX 5	7590^{8800}_{6800}	$13.03^{12.38}_{13.51}$	71.2	0.218	7780^{8820}_{6990}	$12.96^{12.41}_{13.43}$	76.2	0.185
KX 6	5000^{5420}_{4620}	$14.86^{14.51}_{15.21}$	47.2	1.026	5460^{5790}_{5210}	$14.50^{14.25}_{14.74}$	60.2	0.536
KX 7	7360^{8630}_{6540}	$13.16^{12.47}_{13.68}$	99.6	0.098	7400^{8320}_{6700}	$13.18^{12.67}_{13.61}$	103.3	0.090
KX 8	8670^{10450}_{7280}	$12.45^{11.63}_{13.21}$	98.9	0.100	8120^{9290}_{7240}	$12.77^{12.19}_{13.27}$	89.6	0.125
KX 9	5300^{5750}_{4930}	$14.61^{14.25}_{14.93}$	87.4	0.427	5670^{5990}_{5390}	$14.34^{14.10}_{14.56}$	105.2	0.266
KX10	4890^{5260}_{4530}	$14.96^{14.64}_{15.30}$	57.4	0.738	5300^{5560}_{5080}	$14.63^{14.43}_{14.82}$	71.5	0.415
KX11	3970^{4370}_{3750}	$15.87^{15.45}_{16.12}$	42.2	2.892	4720^{4940}_{4530}	$15.14^{14.94}_{15.32}$	58.8	1.156
KX12	4600^{4970}_{4240}	$15.23^{14.89}_{15.59}$	22.5	4.823	5290^{5550}_{5050}	$14.64^{14.43}_{14.85}$	32.6	1.707
KX13	6370^{7010}_{5850}	$13.80^{13.38}_{14.18}$	149.7	0.168	6540^{7200}_{6090}	$13.72^{13.30}_{14.03}$	162.8	0.138
KX14	3900^{4380}_{3750}	$15.95^{15.44}_{16.12}$	102.9	3.147	4600^{4780}_{4440}	$15.48^{15.30}_{15.64}$	123.7	1.883
KX15	5560^{5710}_{5430}	$14.40^{14.28}_{14.50}$	35.7	1.330	5750^{5860}_{5650}	$14.55^{14.50}_{14.59}$	32.6	1.716
KX16	5800^{6320}_{5360}	$14.22^{13.84}_{14.56}$	70.3	0.243	6070^{6550}_{5730}	$14.04^{13.71}_{14.30}$	80.2	0.175
KX17	8300^{10100}_{7140}	$12.64^{11.77}_{13.30}$	48.3	0.593	7960^{9090}_{7130}	$12.86^{12.28}_{13.34}$	45.8	0.682
KX18	7690^{9050}_{6830}	$12.97^{12.26}_{13.49}$	84.6	0.144	7740^{8760}_{6950}	$12.98^{12.44}_{13.45}$	87.7	0.132
KX19	15620^{21150}_{9690}	$9.86^{8.54}_{11.96}$	166.7	0.033	11830^{15400}_{9850}	$11.13^{9.97}_{11.93}$	126.8	0.058
KX20	15380^{16440}_{14450}	$9.93^{9.63}_{10.20}$	38.2	1.118	14660^{15990}_{13740}	$11.08^{10.93}_{11.23}$	32.0	1.802
KX21	6120^{6710}_{5640}	$13.98^{13.57}_{14.34}$	104.2	0.201	6360^{6910}_{5930}	$13.84^{13.48}_{14.15}$	116.3	0.154
KX22	6970^{7630}_{6690}	$13.40^{13.17}_{13.58}$	76.9	0.181	7040^{7760}_{6760}	$13.68^{13.46}_{13.88}$	68.0	0.246
KX23	6570^{6750}_{6410}	$13.66^{13.55}_{13.77}$	57.0	0.384	6640^{6820}_{6470}	$13.96^{13.84}_{14.08}$	49.5	0.556
KX24	4950^{5340}_{4600}	$14.91^{14.58}_{15.23}$	21.4	5.556	5370^{5660}_{5140}	$14.58^{14.35}_{14.77}$	26.8	2.960
KX25	9210^{11210}_{7860}	$12.18^{11.32}_{12.88}$	155.8	0.044	8890^{10340}_{7830}	$12.38^{11.72}_{12.93}$	146.9	0.050
KX26	5020^{5420}_{4660}	$14.85^{14.51}_{15.17}$	51.6	0.568	5420^{5720}_{5190}	$14.54^{14.30}_{14.73}$	63.8	0.328
KX27	7340^{7640}_{7050}	$13.18^{13.00}_{13.35}$	117.2	0.107	7230^{7550}_{6940}	$13.56^{13.35}_{13.75}$	99.4	0.158
KX28	8660^{10440}_{7340}	$12.45^{11.63}_{13.18}$	248.4	0.053	8220^{9410}_{7320}	$12.72^{12.13}_{13.23}$	230.0	0.063
KX29	7850^{8220}_{7520}	$12.88^{12.68}_{13.07}$	33.8	1.547	7920^{8270}_{7610}	$13.13^{12.93}_{13.32}$	30.7	2.023
KX30	5150^{5490}_{4840}	$14.74^{14.45}_{15.01}$	119.3	0.508	5280^{5540}_{5070}	$14.84^{14.63}_{15.03}$	109.8	0.632
KX31	6640^{7430}_{6060}	$13.62^{13.12}_{14.02}$	43.7	0.775	6780^{7500}_{6250}	$13.56^{13.12}_{13.92}$	46.8	0.643
KX32	13060^{16410}_{10400}	$10.65^{9.64}_{11.65}$	35.9	1.323	10810^{13510}_{9190}	$11.52^{10.55}_{12.23}$	28.7	2.437
KX33	4650^{4980}_{4320}	$15.18^{14.88}_{15.51}$	81.4	1.095	4940^{5160}_{4760}	$15.15^{14.95}_{15.32}$	80.7	1.119
KX34	6940^{7860}_{6310}	$13.42^{12.88}_{13.84}$	36.9	1.222	7080^{7920}_{6460}	$13.37^{12.88}_{13.77}$	39.4	1.019
KX35	8390^{10240}_{7240}	$12.59^{11.72}_{13.24}$	49.1	0.566	8090^{9240}_{7230}	$12.79^{12.21}_{13.28}$	46.9	0.639
KX36	7270^{8260}_{6570}	$13.22^{12.66}_{13.66}$	143.8	0.109	7480^{8430}_{6780}	$13.13^{12.61}_{13.56}$	155.8	0.091
KX37	20560^{27560}_{15870}	$8.65^{7.36}_{9.79}$	169.5	0.032	14720^{26300}_{11470}	$10.17^{7.61}_{11.27}$	129.3	0.055
KX38	10250^{13600}_{8620}	$11.71^{10.47}_{12.47}$	81.9	0.155	9910^{11890}_{8580}	$11.90^{11.11}_{12.53}$	75.9	0.187
KX39	4910^{5230}_{4600}	$14.95^{14.67}_{15.23}$	62.4	0.760	5090^{5320}_{4910}	$15.01^{14.81}_{15.17}$	58.5	0.903
KX40	7180^{8300}_{6460}	$13.27^{12.64}_{13.74}$	80.1	0.164	7250^{8130}_{6570}	$13.27^{12.77}_{13.70}$	83.8	0.147
KX41	4650^{4820}_{4500}	$15.18^{15.03}_{15.33}$	72.0	1.062	5080^{5190}_{4990}	$15.02^{14.92}_{15.10}$	77.4	0.874
KX42	4680^{5050}_{4320}	$15.16^{14.82}_{15.51}$	54.2	0.926	5180^{5420}_{4980}	$14.73^{14.54}_{14.90}$	70.6	0.459
KX43	15360^{20230}_{9990}	$9.93^{8.72}_{11.82}$	143.3	0.045	11680^{15030}_{9760}	$11.19^{10.08}_{11.97}$	109.0	0.080
KX44	5540^{6070}_{5110}	$14.41^{14.01}_{14.77}$	78.2	0.328	5550^{5980}_{5210}	$14.63^{14.45}_{14.90}$	68.0	0.471
KX45	7040^{8060}_{5370}	$13.36^{12.77}_{13.80}$	59.3	0.347	7140^{7990}_{6490}	$13.33^{12.84}_{13.75}$	62.6	0.303
KX46	4760^{5130}_{4390}	$15.08^{14.75}_{15.44}$	101.9	0.863	5260^{5520}_{5050}	$14.67^{14.45}_{14.85}$	133.2	0.425
KX47	7400^{8300}_{6670}	$13.14^{12.64}_{13.60}$	97.2	0.104	7720^{8730}_{6950}	$12.99^{12.46}_{13.45}$	107.5	0.083
KX48	4290^{4670}_{3850}	$15.53^{15.16}_{16.01}$	36.4	2.093	4970^{5180}_{4780}	$14.91^{14.73}_{15.09}$	51.4	0.813
KX49	5230^{5660}_{4860}	$14.67^{14.32}_{14.99}$	58.5	0.577	5570^{5900}_{5310}	$14.42^{14.17}_{14.63}$	69.8	0.364
KX50	4860^{5230}_{4500}	$14.99^{14.67}_{15.33}$	45.1	0.711	5350^{5630}_{5120}	$14.59^{14.37}_{14.78}$	58.5	0.359
KX51	4360^{4730}_{3950}	$15.47^{15.11}_{15.89}$	48.1	1.608	5020^{5240}_{4830}	$14.87^{14.68}_{15.04}$	67.7	0.638
KX52	6540^{7300}_{6000}	$13.68^{13.20}_{14.06}$	77.0	0.180	6730^{7440}_{6220}	$13.59^{13.15}_{13.94}$	83.8	0.147
KX53	6070^{6510}_{5700}	$14.01^{13.70}_{14.29}$	92.8	0.199	6000^{6400}_{5710}	$14.44^{14.14}_{14.56}$	73.4	0.359
KX54	7350^{8330}_{6610}	$13.17^{12.62}_{13.64}$	72.3	0.211	7570^{8540}_{6840}	$13.08^{12.55}_{13.52}$	78.4	0.173
KX55	8160^{10020}_{6980}	$12.71^{11.81}_{13.40}$	175.5	0.060	7810^{8910}_{7010}	$12.94^{12.37}_{13.41}$	165.8	0.068
KX56	4900^{5300}_{4520}	$14.95^{14.61}_{15.31}$	96.1	0.661	5390^{5690}_{5150}	$14.56^{14.33}_{14.76}$	124.7	0.335
KX57	3750^{3980}_{3750}	$16.12^{15.86}_{16.12}$	41.2	5.010	4480^{4680}_{4310}	$15.37^{15.18}_{15.53}$	52.5	2.538
KX58	3750^{3930}_{3750}	$16.12^{15.92}_{16.12}$	28.4	4.411	4570^{4750}_{4420}	$15.28^{15.11}_{15.43}$	38.9	1.824

Table 4. Derived stellar parameters for CWD sample assuming either a H or He atmosphere.

Object	B σ_B	V σ_V	R σ_R	I σ_I
KX14(1)	–	21.43	20.78	20.17
		0.04	0.09	0.07
KX14(2)	–	21.47	20.75	20.20
		0.04	0.07	0.07
KX15	19.10	18.53	18.08	17.69
	0.03	0.02	0.03	0.03
KX20	16.14	16.12	16.16	16.22
	0.02	0.02	0.02	0.02
KX22	–	19.94	19.66	19.55
		0.03	0.04	0.04
KX23	19.52	19.05	18.74	18.61
	0.03	0.01	0.01	0.03
KX27	–	18.15	17.97	17.91
		0.02	0.02	0.03
KX29	18.67	18.36	18.17	17.90
	0.03	0.02	0.03	0.03
KX30	–	21.12	20.64	20.19
		0.03	0.05	0.08
KX33	–	21.22	20.69	20.10
		0.04	0.06	0.07
KX39	–	21.19	20.66	20.18
		0.04	0.06	0.06
KX41a	20.26	19.38	18.93	18.41
	0.05	0.03	0.04	0.04
KX41b	20.28	19.33	18.81	18.36
	0.04	0.03	0.04	0.04
KX44	–	21.37	20.81	20.42
		0.05	0.07	0.08
KX53	–	20.96	20.70	20.21
		0.03	0.05	0.06
KX57	–	21.09	20.40	19.84
		0.04	0.06	0.08

Table 3. Johnson-Cousins CCD photometry taken at SAAO for selected members of our CWD sample. Object KX41 was resolved as a double-degenerate on the CCD frame and thus has photometry for each component. Object KX14 had two independent sets of observations, shown as (1) and (2)

the $(B-R)$, RPMD planes. These objects define a portion of the RPMD marginally red-wards of the faintest CWDs where the most extreme contaminants may be expected to lie.

Figure 18 shows the two RPMD with the four samples plotted. There are several points to be made concerning this plot. Firstly, our CWD sample and the the BRL sample of previously known CWDs lie on the same region of the diagram, providing further confirmation of the validity of our survey procedure. It can also be seen that the BRL sample contains redder, cooler stars than our sample. This may be expected since the BRL sample is rather eclectic and contains some of the coolest WDs known, whereas our sample is drawn from a rigidly defined survey in a particular ESO/SERC field. We note also that the cool portion of the BRL sample does not extend into the portion of the RPMD beyond our population discrimination cut-off shown in Figure 11, which may be interpreted as indicating that we are not failing to sample portions of the RPMD containing CWDs (but see Section 8 below). Both subdwarf samples lie in clearly distinct regions of the RPMD to our sample, although the cooler subdwarfs are all too red to directly

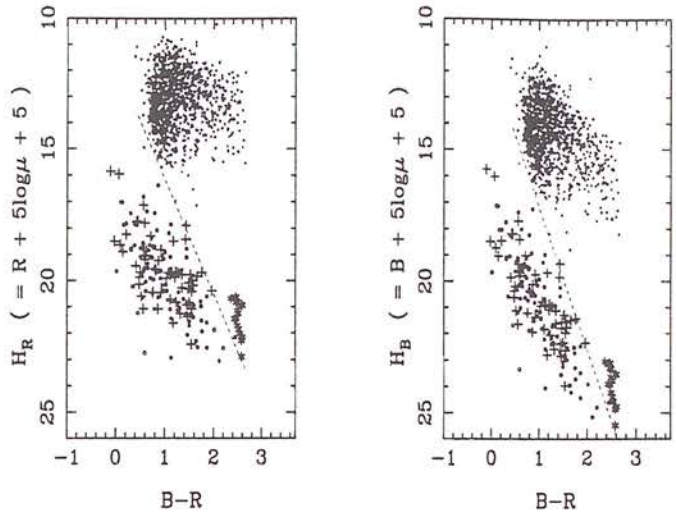

Figure 18. A comparison of various populations on the RPMDs: crosses denote our CWD sample , circles the BRL CWD sample, asterisks the Monet et al. extreme red subdwarfs and dots the brighter Ryan subdwarfs

assess contamination of the CWD sample from the direction of small RPM. However the subdwarf RPM locus is not predicted to deviate significantly from a straight line in the CWD colour regime (Evans 1992), and if we take the high H extent of the two subdwarf samples plotted to be indicative of the limit of the extreme subdwarf locus on the RPMD, the dashed lines plotted on Figure 18 should be a good guide to the limit of the subdwarf locus for the intermediate colour range. It may then immediately be seen that the vast majority of our CWD sample is safely within the WD region of the RPMD. The two redder borderline stars have reasonable spectroscopic confirmation of their WD status (Figures 16 and 15), leaving only one potentially dubious object.

7 THE WDLF

In order to construct a WDLF, space densities must be calculated for a survey limited by both apparent magnitude and proper motion. The CWD survey sample presented in Table 4 consists of stars with widely varying intrinsic brightness and tangential velocity, and is therefore not volume-limited (since for example intrinsically bright objects are sampled out to greater distances than the coolest, faintest stars). The standard solution to this problem, Schmidt's (1968, 1975) $1/V_{max}$ estimator, has been extensively studied with specific reference to the WDLF (Wood & Oswalt 1998). The $1/V_{max}$ method assigns each sample object a survey volume defined by the maximum distance d_{max} the object could have and satisfy the survey limit criteria. For this survey, an object at distance d with proper motion μ and magnitudes B and R has d_{max}

$$d_{max} = \min\left[d\frac{\mu}{\mu_{lim}}, d10^{0.2(R_{lim}-R)}, d10^{0.2(B_{lim}-B)}\right]. \quad (12)$$

For the simple case of uniform stellar space density, the survey field solid angle Ω can then be used to calculate the

corresponding V_{max} ($= \Omega d_{max}^3/3$) . However, many of the objects in our CWD sample yield a d_{max} comparable to the scale height of the Disc, and we follow the method of Tinney, Reid & Mould (1993) in generalising our calculation of V_{max} to allow for the truncation of the survey volume by the scale height effect. In this prescription, the volume is found by integrating over an exponentially decreasing density law (Stobie, Ishida & Peacock 1989) with scale height h at galactic latitude b, yielding the modified expression for the volume out to a distance d:

$$V = \Omega \frac{h^3}{\sin^3 b}\{2 - (\xi^2 + 2\xi + 2)e^{-\xi}\}, \quad (13)$$

where $\xi = d \sin b/h$ (Equation 9 in Tinney et al. 1993). Each object is thought of as a sampling of the survey volume V_{max}, and thus contributes a space density of V_{max}^{-1} to its particular LF bin. We adopt the convention of LDM in assigning the uncertainty in each space density contribution as being equal to that contribution (ie. 1 ± 1 objects per sampling). We may therefore construct a LF simply by summing the individual space density contributions in each luminosity bin, and the error obtained by summing the error contributions in quadrature. A true reflection of the LFs observational uncertainties should also allow for the uncertainties inherent in photometric fits to model atmospheres described in the previous section. The errors in $M_{\rm bol}$ detailed in Table 4 suggest the introduction of horizontal error bars in any observational LF is necessary. When converting our sample $M_{\rm bol}$ values into luminosity units via

$$M_{bol} = -2.5 \log L/L_\odot + 4.75 \quad (14)$$

we also calculate the upper and lower 1 sigma luminosity uncertainties for each object. For a bin containing N objects we then combine eg. the upper luminosity 1 sigma uncertainties, σ_u, using

$$\sigma_U = \sqrt{\frac{\sum_i^N \sigma_{u_i}^2}{N}} \quad (15)$$

to yield an estimate for the horizontal error bar σ_U, with an analogous procedure for the lower luminosity error bounds. In addition, to give the most realistic estimate for the LF in magnitude bins containing a very few objects, we plot the binned data at the mean luminosity of the objects in the bin, rather than at the mid-point of that bin.

Table 5 gives the LF calculated in this fashion for integer magnitude bins. Only the cool end of the LF is given here ($M_{\rm bol} > 12.25$), and a field size of 0.0086 steradians and Disc scale height of 300 parsecs were used in calculating space densities. Columns 3 and 4 give the plotted (Figure 19) LF with upper and lower error bounds in parenthesis. The hot WD data point not detailed in Table 5 represents the 6 stars with ($3 > -\log L/L_\odot > 2$). These hotter objects tend to have large errors in fitted $M_{\rm bol}$, and the resulting large horizontal error bars makes broader binning appropriate. It is necessary to choose either a pure hydrogen or helium atmosphere for each object to construct the LF. We use our 'best guess' atmospheres for the LF described here: for each object we choose the atmosphere with the lower χ^2 model fit to the photometry, with the exception of objects with $6000 > T_{\rm eff_H} > 5000$ which are deemed to be occupying the 'non-DA gap' at this temperature (BRL) and are therefore automatically designated a pure H atmosphere. Note

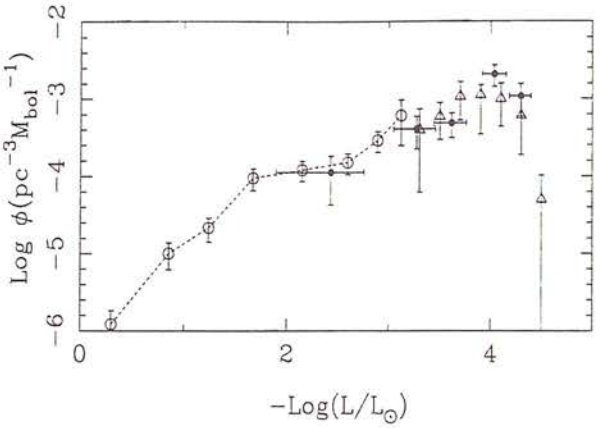

Figure 19. Observational LF with comparisons: this work (filled circles), hot WDLF based on Fleming, Liebert and Green (1986) from LDM (open circles) and the LRB redetermination of the LDM CWDLF (open triangles)

however that the photometry does not adequately constrain atmospheric composition and this 'best guess' LF is only one arbitrary realisation of the data (see Section 8 below).

The standard means of assessing the completeness of a sample analysed using the $1/V_{max}$ method is to calculate the mean value of the ratio of V_{obs}, the volume out to an object, to V_{max}. A complete survey evenly sampling the survey volume should yield $\langle V_{obs}/V_{max} \rangle = \frac{1}{2}$. This is generally not the case for published CWD samples, although some authors have incorporated completeness corrections into their analyses to account for the effects of the original survey incompleteness (OSWH). The $\langle V_{obs}/V_{max} \rangle$ calculated for this sample is 0.495 or 0.496 choosing either all H or He atmospheres. From a complete sample containing 58 objects we expect $\langle V_{obs}/V_{max} \rangle = 0.5 \pm 0.038$, indicating our sample is consistent with being drawn from a complete survey. It should be emphasised however that this result cannot be regarded as proof of completeness, since clearly an incomplete survey sample may also exhibit $\langle V_{obs}/V_{max} \rangle \sim \frac{1}{2}$.

The total space density determined from our 'best guess' sample is 4.16×10^{-3} WDs per cubic parsec, approximately 25% greater than that found by LRB. These results are certainly consistent, since the simulations of Wood and Oswalt (1998) predict errors of $\sim 50\%$ in total space density estimates from samples of 50 CWDs using the $1/V_{max}$ technique and additional uncertainties are introduced by our lack of knowledge of the WD atmospheric constituents. Our findings reiterate that WDs represent only a small fraction ($\sim 1\%$) of the local dynamically estimated mass density. Interestingly, we do not confirm the much higher total WD space densities found recently by two independent studies. We note however that these studies (Ruiz & Takamiya 1995, Festin 1998) make only a tentative claim to detection of a high WD space density due to the small samples ($N < 10$) involved. A third study (OSWH) searched exclusively for WDs in CPMBs, and found a total space density of 5.3×10^{-3} for these objects. At this space density, and given our survey area and the resolution of the COSMOS data, we would not expect to find any CPMB WDs. It is therefore not surpris-

Bin Center			Space Density	
M_{bol}	$-\log L/L_\odot$	$\overline{-\log L/L_\odot}$	$\log\{\left[\sum(1/V_{max})\right] M_{bol}^{-1}\}$	Number
12.75	3.20	3.27(3.05,3.45)	-3.39(-3.23,-3.65)	14
13.75	3.60	3.62(3.44,3.76)	-3.32(-3.18,-3.51)	13
14.75	4.00	4.04(3.92,4.15)	-2.68(-2.56,-2.84)	20
15.75	4.40	4.30(4.18,4.40)	-2.97(-2.80,-3.24)	5

Table 5. Luminosity Function

ing that no object in our sample is a CPMB member, since the survey technique is only sensitive to lone WDs or double degenerate binary systems.

8 DISCUSSION

An estimate of the Disc age may be obtained by comparing our WDLF with expectations from theoretical models. We compare our data with two sets of models, which are available in the form of curves at integer 1 Gyr Disc age intervals. Since we are fitting to a cut-off in space density, the *lack* of detected objects beyond our faintest observational bin assumes added significance. We can calculate the probability of detecting zero objects in the next faintest luminosity bin because we have well defined survey limits: at given faint luminosity the proper motion survey limit is irrelevant and the survey is sampling a known volume defined by the photometric survey limits. This volume was calculated using B and R magnitudes for very cool WDs from the recent models of Hansen (1998), which combined with the photometric survey limits yield a d_{max} for both an H and an He atmosphere WD. The minimum d_{max} defines the survey volume at that magnitude. We have assumed the LF at any given luminosity consists of equal numbers of H and He WDs, in which case the H WD survey volume provides the best constraint on the LF and is adopted for fitting. Using Poisson statistics, the probability of detecting zero objects in a volume V in which a model predicts space density ρ is simply $e^{-\rho V}$. We assume the errors on the data points are normally distributed, and derive best fits by maximising the probability of the dataset for each curve and comparing the fits for the various Disc ages.

The various inputs to the first set of WDLFs we use, those of Wood, were described in detail in Wood (1992). Careful consideration was given to the various inputs to the WDLF, such as initial mass function, star formation rates and initial-final mass relation. The Wood WD evolutionary models for the WDLFs have since been updated (Wood 1995, OSWH), and consist of mixed carbon-oxygen core WDs with hydrogen and helium surface layer masses of 10^{-4} and $10^{-2}M_*$ respectively, and also utilise revised opacities and neutrino rates. It is these more recent model WDLFs that are used here.

The best fit of our 'best guess' LF to the Wood model WDLFs is for a Disc age of 9 Gyr, and is shown in Figure 20. Although this gives a reasonable first indication of the Disc age implied by our sample, further investigation is necessary since the photographic photometry fitting procedure used to estimate T_{eff} (as described in Section 6) does not reliably constrain the atmospheric constituent of the stars in our sample. We have addressed this question by constructing a large number of WDLF 'realisations' from our sample data, each time giving each star a 50% probability of having either a H or He atmosphere. Every resulting WDLF was fit to the models and the best fit Disc age recorded. We have also used this analysis to assess the effect of binning on the fitting procedure. Figure 21 (a) displays the results of fits to 1000 realisations binned in 1.0 M_{bol} bins and a further 1000 in 0.75 M_{bol} bins. These results give a fairer indication of the Disc age and associated errors than Figure 20, which is effectively one arbitrarily picked realisation.

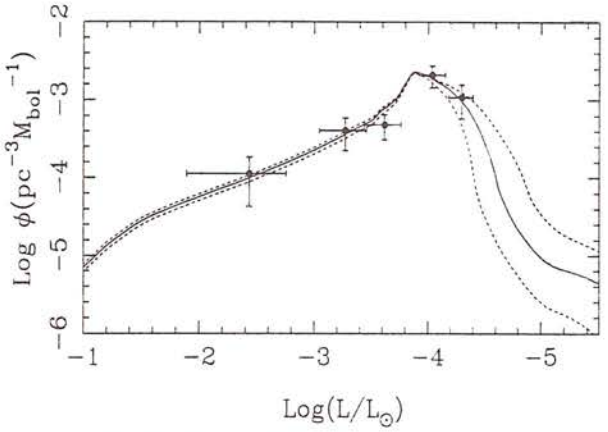

Figure 20. The Wood WDLF with a Disc age of 9 Gyr – the best fit to our 'best guess' LF. 8 Gyr (below) and 10 Gyr (above) curves are also shown in dashed lines.

The second set of theoretical WDLFs we use are described in García-Berro et al. (1997) (henceforth GB models). These LFs include the expectation that the progenitors of the faintest WDs are likely to have been massive stars since these stars evolve more quickly and the resulting (Oxygen-Neon) massive WDs also cool faster. These models also include a predicted delay in Carbon-Oxygen WD cooling induced by the separation of C and O at crystallization (Hernanz et al. 1994). The incorporation of these considerations into the theoretical WDLF leads to a broader predicted peak at the tail of the LF. We find a best fit of 11 Gyr to our sample, as shown in Figure 22. Again, we have investigated the effect of our poor knowledge of our samples atmospheres in the same way as above. The results, shown in Figure 21 (b), highlight the effect that variations in binning can have on the fits for this second set of models.

The major contributor to this problem seems to be that the model curves are sufficiently indistinct in the region of

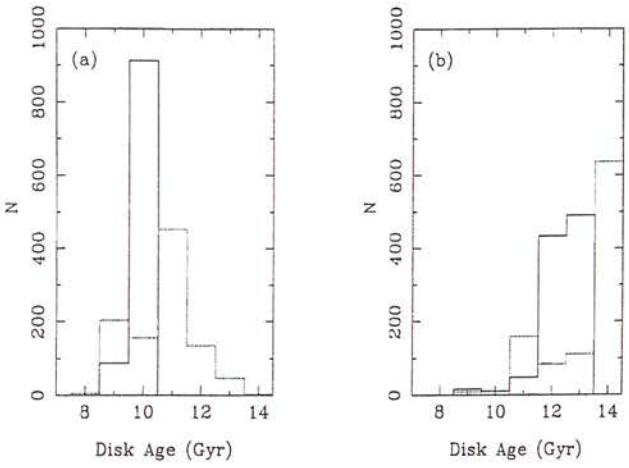

Figure 21. Results of constructing WDLFs from our sample by randomly assigning H or He atmospheres. Full line histograms denote 1 M_{bol} bins, dotted lines 0.75 M_{bol} bins. For each bin size 1000 realisations of the WDLF were constructed and fit to the models - the number of times each Disc age was the best fit is displayed. Graph (a) shows fits to the Wood models, graph (b) fits to GB.

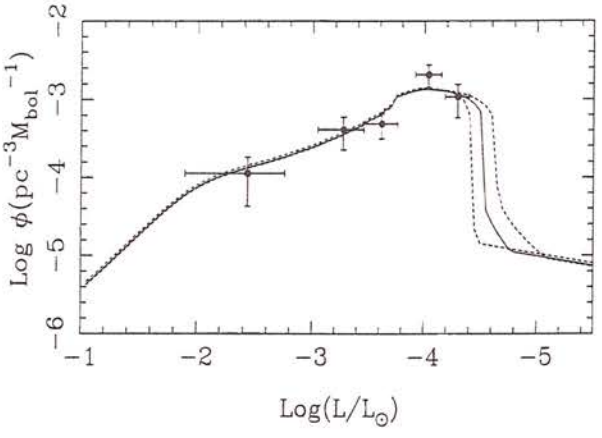

Figure 22. The best fit of our 'best guess' LF to the GB WDLF: a Disc age of 11 Gyr with 'adjacent' Disc age LFs shown in dashed lines as in Figure 20.

our sample dataset (as can be seen clearly in Figure 22) that changes in observational LF binning can have a significant bearing on the result of the fit. This effect is apparent in Figure 21 (b), where a bin size of 0.75 M_{bol} yields a strong preference of a Disc age of 14 Gyr, in contrast to the 12-13 Gyr Disc age selected by the other binning regime (note also that 14 Gyr was the oldest curve available for fitting). Although it is difficult to resolve this matter satisfactorily with the current data set, there are two pertinent points to raise. The problem does not apply to the Wood models, the fits to which are extremely difficult to dislodge from the 9–11 Gyr region indicated by Figure 21 (a). Secondly, Wood and Oswalt (1998), as a result of their Monte Carlo analysis of the WDLF, recommend choosing a binning in which the crucial lowest luminosity bin contains $\sim$ 5 objects; giving a reasonable compromise between the requirements of good signal to noise in the final bin and having that bin as faint as possible to provide maximum information on the position of the cut off. This means a bin size of 1 M_{bol} for our data set, for which the fitted Disc age is well constrained for both models.

A brief investigation of the effect of altering the Disc scale height in Equation 13 revealed that for any scale height between 250 and 400 pc the alterations in space densities for a LF binned as in Table 5 are restricted to a few hundredths in $\log\phi$. Variations at this level have a negligible effect on the fits to model LFs. This behaviour is to be expected , since it is objects with large d_{max} which are most affected by changes in the scale height, and these make the smallest contributions to the space density when using the $1/V_{max}$ prescription.

An overview of all the various fittings to both sets of models points firmly to a Disc age between 9 and 11 Gyr using the Wood models, and an age of 12-14 Gyr using the GB models. This discrepancy is expected (LRB, García-Berro et al. 1997) and indicates the extent of errors introduced by uncertainties in the WD crystallisation process; the Wood model Disc age should be a reliable lower limit however, and Figure 21 demonstrates the difficulty in obtaining a Disc age of less than 9 Gyr from our data. We note that the Wood models seem to represent our data better, the GB models not following the peak in the observed LF. Wood (1992) reported that the uncertainties in the inputs to model WDLFs lead to a further $\sim$ 1 Gyr contribution to the total error. Further insight into the error associated with the Disc age may be gained by considering the extremities of the distribution of atmosphere types within the sample. The 50% probability assigned to the H and He atmosphere is adopted in the absence of strong evidence for a dominant atmospheric type amongst the crucial coolest WDs (see eg. the coolest bin in Figure 1 of BRL), and has no physical basis. Adopting all H atmospheres leads to high space density estimates in the final LF bins and arbitrarily old Disc age estimates. More interestingly, a LF composed of all He atmosphere WDs is still incompatable with Disc ages below 8 Gyr, regardless of the model WDLF used. This reiterates the important point that the cosmologically interesting lower Disc age limit appears to be 8 Gyr, and that even a Disc as young as this must be considered unlikely (Figure 21). Our adopted Disc age estimation is therefore 10^{-1}_{+3} Gyr.

There are at least two possible effects arising from our present lack of extensive follow up observational data that could affect the derived Disc age. First, as may be seen in Figure 14 there is a small group of objects lying just beyond our RPMD cut-off that have not been included in our CWD sample. Although the distribution of known WDs on the RPMD (the BRL objects in Figure 18) indicates a population of CWDs is not expected in this region, the reason for this may be that many of the known CWDs have been themselves selected on the basis of RPM criteria (Luyten 1970). It may be that the region of the RPMD just beyond our cut-off has not been adequately investigated before, since in the presence of noisier data from blink comparators and eye-measure photometry it would be hopelessly confused. These considerations argue strongly for a wholesale spectroscopic survey using multi-fibre instruments of the entire population below $H_R = 19$ for complete confidence that our sample does

not exclude any CWDs. For the present, the possibility that a few more CWDs exist in our catalogue but do not satisfy our RPMD survey criteria cannot be ruled out. Such objects would certainly be very cool, resulting in a higher Disc age estimate. The second effect concerns the question of mass. The difficulty is amply demonstrated by the case of CWD ESO 439-26 (Ruiz et al. 1995), which was observed to have a luminosity fainter by 1 magnitude than the WDLF cut off. Analysis of the object's optical energy distribution in conjunction with a measure of trigonometric parallax allowed the authors to conclude that it's low luminosity was in fact due to its large mass, or small radius. Again, ideally it would be desirable to obtain parallaxes and CCD optical and IR photometry of our entire sample, obviating the need to assume a mass of $0.6M_{\odot}$ (and allowing the surface composition to be constrained).

In summary, our WD sample has passed every test for completeness applied to it. The calculated space density of WDs is slightly higher than that for the LDM sample, however we do not detect the much higher total space densities found by more recent authors (Ruiz 1995, Festin 1998). Our WDLF yields a Disc age estimate of 10^{-1}_{+3} Gyr, older but still consistent with previous estimates (Winget 1987, LRB, OSWH). In the context of current cosmochronometry, our Disc age estimate is consistent with current Globular cluster age estimates of 13-14Gyr (Vandenberg 1998). Finally, when combined only with a conservative 1 Gyr value for the halo–Disc formation interval (Burkert, Truran & Hensler 1992, Pitts & Tayler 1992) and a further 1 Gyr for the big bang–halo formation interval, a 10 Gyr Disc excludes $\Omega = 1$, $\Lambda = 0$ cosmologies based on current estimates for $H_{\circ}$ of 60-80 (Freedman 1998).

9 CONCLUSIONS

(i) Using a large collection of COSMOS/SuperCOSMOS digitised Schmidt plate data in ESO/SERC field 287 we have extracted a sample of proper motion objects. Number counts indicate this sample is complete down to the survey proper motion limit, which was chosen with care to exclude contaminant spurious proper motion measures.

(ii) A sample of cool white dwarfs have been culled from our proper motion objects using the reduced proper motion technique. By overplotting samples of known extreme subdwarfs we show our CWD sample is unlikely to be contaminated by other stellar population groups. We have confirmed the WD status of a number of our sample with AAT spectroscopy. The sample passes the (V/V_{max}) completeness test.

(iii) We calculate a total WD space density of 4.16×10^{-3} WDs per cubic parsec using Schmidt's $(1/V_{max})$ method. Careful comparison of luminosity functions constructed from our sample and theoretical models indicate an age for the local Galactic Disc of 10^{-1}_{+3} Gyr, older than previous estimates using this technique.

ACKNOWLEDGMENTS

We would like to thank M. Wood and E. García-Berro for access to theoretical WDLFs, and P. Bergeron, P. Hauschildt and B. Hansen for supplying model atmosphere predictions. Thanks also to S. Ryan for supplying lists of subdwarfs, and to Andy Taylor for useful discussions concerning statistics. This work would not have been possible without the time and expertise of the SuperCOSMOS and UK Schmidt Library staff. Particular thanks to Harvey MacGillivray, Mike Read and Sue Tritton. Richard Knox acknowledges a PPARC postgraduate studentship.

REFERENCES

Beard S.M., MacGillivray H.T., Thanisch P.F., 1990, MNRAS, 247, 311
Bergeron P., Wesemael F., Beauchamp A., 1995, PASP, 107, 1047
Bergeron P., Ruiz M.T., Leggett S.K., 1997, ApJS, 108, 339
Burkert A., Truran J.W., Hensler G., 1992, ApJ, 391, 651
Evans D.W., 1989, A&AS, 78, 249
Evans D.W., 1992, MNRAS, 255, 521
Festin L., 1998, A&A, 336, 883
Fleming T.A., Liebert J., Green R.F., 1986, ApJ, 308, 176
Freedman W.L., 1998, in Turok N., ed., Proceedings for "Critical Dialogs in Cosmology", in press (Princeton University Press) (preprint astro-ph 9612024)
García-Berro E., Isern J. , Hernanz M., 1997, MNRAS, 289, 973
Giclas H.L., Burnham R., Thomas N.G., 1971, Lowell Proper Motion Survey, Northern Hemisphere Catalogue (Flagstaff: Lowell)
Giclas H.L., Burnham R., Thomas N.G., 1978, Lowell Proper Motion Survey, Southern Hemisphere Catalogue Lowell Obs. Bull. 164, Vol VIII, p.89
Greenstein J.L., Liebert J., 1990, ApJ, 360, 662
Hambly N.C., Smartt S.J., Hodgkin S.T., 1997, ApJ, 489, L157
Hambly N.C., Miller L., MacGillivray H.T., Herd J.T., Cormack, W.A., 1998, MNRAS, 298, 897
Hansen B.M.S., 1998, Nature, 394, 860
Hauschildt P.H., Allard F., Baron E., 1998, ApJ, in press
Hawkins M.R.S., 1986, MNRAS, 223, 845
Hawkins M.R.S., Bessell M.S., 1988, MNRAS, 234, 177
Hawkins M.R.S., 1991, in IAU Commission 9: Working Group on Wide–Field Imaging, Newsletter No. 1, 23
Hawkins M.R.S., Ducourant C., Jones H. R. A., Rapaport M., 1998, MNRAS, 294, 505
Hernanz M., García-Berro E., Isern J. ,Mochkovitch R., Segretain L., Chabrier G., 1994, ApJ, 434, 652
Isern J, Garci-Berro E, Hernanz M., Mochkovitch R, Torres S, 1998, ApJ,503, 239
Jimenez R., Flynn C., Kotoneva E., 1998, MNRAS, 299, 515
Kemp S.N., Meaburn J., 1993, A&A, 274, 19
Knox R.A., Hambly N.C., Hawkins M.R.S., MacGillivray H.T., 1998, MNRAS, 297, 839
Leggett S.K., Ruiz M.T., Bergeron P., 1998, ApJ, 497, 294
Liebert J., Dahn C.C., and Monet D.G., 1988, ApJ, 332, 891
Luyten W.J., 1969, Proper Motion Survey with the 48" Schmidt Telescope XXI (U. Minn)
Luyten W.J., 1970, White Dwarfs, U. Minn
Luyten W.J., 1974, Proper Motion Survey with the 48" Schmidt Telescope XXXVIII, U. Minn
Luyten W.J., 1979, Proper Motion Survey with the 48" Schmidt Telescope LII, U. Minn
Luyten W.J., 1979, LHS Catalogue, U. Minn
MacGillivray H.T., Stobie R.S., 1984, Vistas in Astronomy, 27, 433
Monet D.G., et al., 1992, AJ, 103, 638
Oswalt T.D., Smith J.A., 1995, Koester D. & Werner K., eds., in White Dwarfs, Springer, Berlin, p.24

Oswalt T.D., Smith J.A, , Wood M.A., Hintzen P., 1996, Nature, 382, 692
Pitts E., Tayler R.J., 1992, MNRAS. 255. 557
Ruiz M.T., Takamiya M.Y., 1995, AJ. 109, 2817
Ruiz M.T., Bergeron P., Leggett S.K., Anguita C., 1995, ApJ, 455, L159
Ryan S.G., 1989, AJ, 98, 1693
Schmidt M., 1959, ApJ, 129, 243
Schmidt M., 1968, ApJ, 151, 393
Schmidt M., 1975, ApJ, 202, 22
Schwartzenberg J.M., Phillipps S., Parker Q.A., 1996, A&AS, 117, 179
Stobie R.S., Ishida K., Peacock J.A., 1989, MNRAS, 238, 709
Tinney C.G., Reid I.N., Mould J.R., 1993, ApJ, 414, 254
Vandenberg D.A., 1998, Bedding T. R., Booth A. J. & Davis J., eds., in IAU Symp Fundamental Stellar Properties: The Interaction between Observation and Theory, Kluwer, Dordrecht, p.439
Véron P., Hawkins M.R.S., 1995, A&A. 296, 665
Winget D.E., Hansen C.J., Liebert J., Van Horn H.M., Fontaine G., Nather R.E., Kepler S.O., Lamb D.Q., 1987, ApJ, 315, L77
Wood M.A., 1992, ApJ, 386, 539
Wood M.A., , 1995, Koester D. & Werner K., eds., in White Dwarfs, Springer, Berlin, p.41
Wood M.A., Oswalt, T.D., 1998, ApJ, 497, 870

APPENDIX A: REDUCED PROPER MOTION DIAGRAMS

The reduced proper motion (RPM) is defined by

$$H = m + 5\log_{10}\mu + 5 \qquad \text{(A1)}$$

where m is apparent magnitude and μ proper motion. A reduced proper motion diagram (RPMD) is a plot of colour against RPM. It is a powerful way of combining proper motions and photometry to distinguish stellar population groups. Equation A1 can be re-written using the relationships $m = M - 5 + 5\log d$ and $\mu = V_T/4.74d$ to give

$$H = M + 5\log_{10} V_T - 3.379 \qquad \text{(A2)}$$

where M is the absolute magnitude, V_T the transverse velocity (in kms^{-1}) and d the distance. Since M and V_T are both intrinsic properties of the star, so too is H.

To see the significance of H, suppose that every star had an identical V_T; H would then clearly be simply M plus a constant and the distribution of a particular population group in H at a particular colour would depend solely on the spread of the populations' colour-magnitude relation at that colour. Of course there is a distribution in $5\log_{10} V_T$ for each population, but since the tangential velocities are distributed around a most probable value the RPM serves as an estimate of M, ie. $M = a + bH$ (a and b constants). The resulting locus for each population in the RPMD is then the convolution of its colour magnitude distribution with its $5\log_{10} V_T$ distribution over the diagrams colour range. To allow population discrimination in some colour region we therefore only require that the various population loci do not overlap significantly in that region of the RPMD. In effect the RPMD is analogous to the Hertsprung-Russell diagram, and in both plots the white dwarf population is quite distinct in most colours.

This paper has been produced using the Royal Astronomical Society/Blackwell Science LaTeX style file.